Performance of the Upgraded Surface Detector of the Pierre Auger Observatory

For the attainment of the academic degree of

Doctorate in Science

from the
Karlsruher Institut für Technologie (KIT)
and the
Universidad Nacional de San Martín (UNSAM)

accepted

Dissertation

of

M.Sc. Alexander Streich

from Stade

Date of the exam: 06.05.2022

Referee: Prof. Dr. Dr. h.c. Johannes Blümer

Co-referee: Prof. Dr. Hernán Asorey

Advisors: Prof. Dr. Ralph Engel, Dr. Darko Veberič, Dr. Markus Roth

Performance of the Upgraded Surface Detector of the Pierre Auger Observatory

Zur Erlangung des akademischen Grades eines

Doktors der Naturwissenschaften

von der KIT-Fakultät für Physik des
Karlsruher Instituts für Technologie (KIT)
und der
Universidad Nacional de San Martín (UNSAM)

genehmigte

Dissertation

von

M.Sc. Alexander Streich

aus Stade

Tag der mündlichen Prüfung: 06.05.2022

Referent: Prof. Dr. Dr. h.c. Johannes Blümer

Korreferent: Prof. Dr. Hernán Asorey

Betreuer: Prof. Dr. Ralph Engel, Dr. Darko Veberič, Dr. Markus Roth

Performance of the Upgraded Surface Detector of the Pierre Auger Observatory

Para optar por el grado académico de

Doctor en Astrofísica

del Instituto de Tecnología Sabato de la
Universidad Nacional de San Martín (UNSAM)
y del
Karlsruher Instituts für Technologie (KIT)

Tesis

de

M.Sc. Alexander Streich

de Stade

Día de la defensa: 06.05.2022

Director: Prof. Dr. Dr. h.c. Johannes Blümer

Co-director: Prof. Dr. Hernán Asorey

Colaboradores: Prof. Dr. Ralph Engel, Dr. Darko Veberič, Dr. Markus Roth

Abstract

Until the present day, the physics of ultra-high energy cosmic rays is one of the greatest unsolved puzzles in science. With the Pierre Auger Observatory, currently the world's largest observatory for the detection of ultra-high energy cosmic rays, significant progress in the understanding of these exceptional particles has been achieved since its start of data acquisition in 2004. Although certain properties of the ultra-high energy cosmic rays have been determined and confirmed with a very high precision, for example the suppression of the flux of particles with energies above 10^{20} eV, numerous open questions remain unanswered, for instance the origin of these particles or their acceleration mechanisms. Furthermore, recent unexpected observations, e.g., the tendency towards a heavier mass composition at the highest energies, raise even more questions which have to be addressed by the current and future ultra-high energy cosmic ray experiments.

The Pierre Auger Collaboration will participate in the future ultra-high energy cosmic ray research with the upcoming AugerPrime upgrade, which will enhance the sensitivity of the detectors towards the determination of the mass composition on an event-by-event level. In this thesis, we present extensive studies of the performance of the current and new detectors of the Surface Detector of the Pierre Auger Observatory, focusing on the evaluation of the AugerPrime components. Thereby, we follow the evolution of the upgrade process, beginning with the first test measurements during the detector production and ultimately reaching the use of the new detectors in the reconstruction of air showers.

In the analysis of the performance of the newly constructed Surface Scintillator Detectors under laboratory conditions, we investigate the signal quality of the new detector components and further explore their full potential. Therein, we demonstrate the stable and high-quality detector production of more than 660 units at the Karlsruhe Institute of Technology, and we are able to validate the fulfillment of the initially defined requirements.

Furthermore, we evaluate the readiness of the most crucial detector components in detailed studies of the performance of the new electronics boards for the upgraded Surface Detector stations under the measurement conditions in the Observatory. With the comparison of the various hardware versions regarding their general properties and noise levels, the fulfillment of the minimum requirements are tested and the finally chosen type of electronics boards which will be deployed in all Surface Detector stations is characterized.

Besides the hardware evaluations, we present the extensive analysis of the currently implemented calibration procedures for the main sub-detectors of the Surface Detector station, the water-Cherenkov detector and the Surface Scintillator Detector. Due to the poor

performance of the current procedure when applied to the signals of the upgraded detectors, a new algorithm is developed in the scope of this thesis. This optimized algorithm offers an enhanced flexibility towards changes in the measured data, resulting in a superior calibration efficiency for the events obtained with the non-upgraded Surface Detector stations, as well as with the AugerPrime detectors. Furthermore, the accessibility and interpretation of the data obtained with the AugerPrime stations is significantly improved. This enables a direct comparison of the reconstruction performance of the different Surface Detector array configurations providing an outlook for the forthcoming measurements of air showers at the Pierre Auger Observatory.

In summary, we propose the new calibration procedure to replace the currently implemented algorithm in the analysis software framework of the Pierre Auger Collaboration. The new algorithm can serve as a basis for the development of new methods for the determination of the mass composition of ultra-high energy cosmic rays.

Zusammenfassung

Bis zum heutigen Tag ist die Physik der ultrahoch-energetischen kosmischen Strahlung eines der größten ungelösten Rätsel der Wissenschaft. Seit dem Beginn der Datenerfassung im Jahr 2004, hat das Pierre-Auger-Observatorium, das gegenwärtig weltweit größte Observatorium für die Messung von ultrahoch-energetischer kosmischer Strahlung, bedeutende Fortschritte beim Verständnis dieser außergewöhnlichen Teilchen erzielt. Trotz der präzisen Festlegung und Bestätigung bestimmter Eigenschaften der ultrahoch-energetischen kosmischen Strahlung, wie beispielsweise die Unterdrückung des Flusses von Teilchen mit Energien über 10^{20} eV, bleiben zahlreiche der offenen Fragen unbeantwortet, wie die Erklärung des Ursprungs dieser Teilchen oder ihre Beschleunigungsmechanismen. Darüber hinaus werfen die neuesten unerwarteten Beobachtungen, z.B. die Tendenz hin zu einer schwereren Massenzusammensetzung bei den höchsten Energien, weitere Fragen auf, die von den derzeitigen und zukünftigen Experimenten für die Messung von ultrahoch-energetischer kosmischer Strahlung beantwortet werden müssen.

Die Pierre-Auger-Kollaboration wird sich dabei mit der bevorstehenden AugerPrime-Aufrüstung der Detektoren an der zukünftigen Erforschung der ultrahoch-energetischen kosmischen Strahlung beteiligen. Das Ziel dieser Aufrüstung ist dabei die Verbesserung der Detektor-Empfindlichkeit für die Bestimmung der Massenzusammensetzung auf Basis einzelner Ereignisse. In diesem Kontext präsentieren wir in dieser Doktorarbeit umfangreiche Studien über die Leistungsfähigkeit der aktuellen und neuen Detektoren des Oberflächendetektors des Pierre-Auger-Observatoriums, wobei der Schwerpunkt auf der Bewertung der AugerPrime-Komponenten liegt. Dabei verfolgen wir die Entwicklung des Aufrüstungsprozesses, beginnend mit den ersten Testmessungen während der Detektorproduktion, bis hin zum späteren Einsatz der Detektoren in der Rekonstruktion von Luftschauern.

Durch die Analyse der Leistungsfähigkeit der neu gebauten Szintillator-Oberflächendetektoren unter Laborbedingungen ist es uns möglich, die Signalqualität der neuen Detektorkomponenten zu untersuchen und ihr volles Leistungspotenzial zu erforschen. Dabei können wir zeigen, dass eine stabile und qualitativ hochwertige Detektorproduktion mit mehr als 660 Stück am Karlsruher Institut für Technologie durchgeführt werden konnte, und zudem bestätigen, dass die im Vorfeld definierten Anforderungen erfüllt wurden.

Darüber hinaus bewerten wir die Einsatzbereitschaft der wichtigsten Detektorkomponenten unter den Messbedingungen im Observatorium durch detaillierten Studien zur Leistungsfähigkeit der neuen Elektronikplatinen für den Einsatz in den aufgerüsteten Oberflächendetektorstationen. Durch den Vergleich verschiedener Hardwareversionen hinsicht-

lich ihrer allgemeinen Eigenschaften und Rauschpegel, werden deren Mindestanforderungen genauer untersucht und eine Charakterisierung des finalen Typs der Elektronikplatinen für den Einsatz in allen Oberflächendetektorstationen erreicht.

Neben der Evaluierung der Hardware präsentieren wir zudem eine umfangreiche Analyse der gegenwärtig implementierten Kalibrierungsverfahren für die wichtigsten Subdetektoren der Oberflächendetektorstation, dem Wasser-Cherenkov-Detektor und dem Szintillator-Oberflächendetektor. Aufgrund der schwachen Leistung des derzeitigen Verfahrens für die Kalibrierung der aufgerüsteten Detektoren, wird im Rahmen dieser Arbeit ein neuer Algorithmus entwickelt. Dieser optimierte Algorithmus bietet eine erhöhte Flexibilität gegenüber Veränderungen in den gemessenen Daten, was zu einer verbesserten Kalibrierungseffizienz der Ereignisse führt, sowohl für Daten, die mit den nicht-aufgerüsteten Oberflächendetektorstationen gemessen wurden, als auch im Falle der AugerPrime-Detektoren. Zudem wird die Zugänglichkeit und Interpretation der Daten, die mit den AugerPrime-Stationen aufgenommen wurden, deutlich verbessert. Dies ermöglicht einen direkten Vergleich der Leistungsfähigkeit der Ereignisrekonstruktion für die verschiedenen Konfigurationen der Oberflächendetektorstationen und bietet zudem einen Ausblick auf die bevorstehenden Messungen von Luftschauern am Pierre-Auger-Observatorium.

Zusammenfassend unterbreiten wir den Vorschlag, den derzeitig implementierten Algorithmus in der Analysesoftware der Pierre-Auger-Kollaboration durch das neue Kalibrierungsverfahren zu ersetzen. Der neue Kalibrierungsalgorithmus kann dabei als spätere Grundlage für die Entwicklung neuer Methoden zur Bestimmung der Massenzusammensetzung der ultrahoch-energetischen kosmischen Strahlung dienen.

Resumen

Hasta la fecha, la física de los rayos cósmicos ultraenergéticos es uno de los mayores enigmas sin resolver de la ciencia. Desde 2004, con el inicio de la adquisición de datos del Observatorio Pierre Auger, el cual es actualmente el mayor observatorio del mundo para la detección de rayos cósmicos de ultra-altas energías, se han logrado avances significativos en la comprensión de estas partículas excepcionales. A pesar de que algunas propiedades de los rayos cósmicos ultra energéticos, tal como la abrupta caída del flujo de partículas con energías por encima de 10^{20} eV, se han determinado y confirmado con una precisión muy alta, numerosas preguntas continúan sin respuesta, por ejemplo, el origen de estas partículas o sus mecanismos de aceleración. Asimismo, recientes resultados inesperados como la tendencia a una composición más pesada a energías más altas plantean aún más interrogantes que deberán ser abordados por los experimentos de rayos cósmicos actuales y futuros.

En los próximos años, la Colaboración Pierre Auger contribuirá a la investigación de los rayos cósmicos ultra energéticos con la inminente actualización del Observatorio denominada AugerPrime, la cual tiene como objetivo mejorar la sensibilidad de los detectores para determinar la composición individual de cada evento. En esta tesis, presentamos estudios exhaustivos del rendimiento de los detectores actuales y nuevos del Detector de Superficie del Observatorio Pierre Auger, centrándonos en la evaluación de los componentes de AugerPrime. Con este objetivo, seguimos la evolución del proceso de actualización, desde la primera medición de prueba durante la producción de los detectores, hasta su uso final en la reconstrucción de las cascadas atmosféricas.

En el análisis del rendimiento en condiciones de laboratorio de los detectores de centelleo de superficie recién construidos, investigamos la calidad de la señal de los nuevos componentes del detector y exploramos todo su potencial en profundidad. En este sentido, demostramos la estabilidad y la alta calidad de los más de 660 detectores producidos en el Instituto Tecnológico de Karlsruhe, así como también corroboramos que los requisitos previamente definidos se satisfagan.

Además, evaluamos la aptitud de los componentes más cruciales del detector en las condiciones de medición del Observatorio mediante estudios detallados del rendimiento de los nuevos tableros electrónicos en las estaciones actualizadas del detector de superficie. Por medio de la comparación de las propiedades generales y los niveles de ruido de varias versiones de hardware chequeamos en detalle los requisitos mínimos de los detectores y caracterizamos el tipo final de tableros electrónicos que se instalarán en todas las estaciones del Detector de Superficie.

Además de las evaluaciones del hardware, presentamos el análisis exhaustivo de los procedimientos de calibración actualmente implementado para los principales subdetectores del Detector de Superficie: el detector Cherenkov y el Detector de Centelleo de Superficie. Debido al pobre rendimiento del procedimiento de calibración actual, desarrollamos un nuevo algoritmo en el contexto de esta tesis. La optimización lograda del algoritmo proporciona una mayor flexibilidad, alcanzando así una eficiencia de calibración superior para los datos obtenidos con los detectores Cherenkov antes de la actualización y mejorando la accesibilidad e interpretación de los datos adquiridos con las estaciones de AugerPrime. De este modo, se pueden comparar el rendimiento de la reconstrucción realizada con diferentes configuraciones del arreglo de detectores de superficie, proporcionando un gran aporte para las futuras mediciones de cascadas atmosféricas con el Observatorio Pierre Auger.

Finalmente, proponemos un nuevo procedimiento de calibración para reemplazar el algoritmo actualmente implementado en el marco del programa de análisis de la Colaboración Pierre Auger. El nuevo algoritmo sirve de base para el desarrollo de nuevos métodos para la determinación de la composición de rayos cósmicos de ultra-altas energías.

Acronyms

This is a list of acronyms used within this work sorted alphabetically according to the short version.

AERA   Auger Engineering Radio Array

AGASA   Akeno Giant Air Shower Array

AMIGA   Auger Muon Detectors for the Infill Ground Array

AMS-02   Alpha Magnetic Spectrometer

ANITA   Antarctic Impulsive Transient Antenna

BLF   Balloon Launching Facility

CDAS   Central Data Acquisition System

CLF   Central Laser Facility

CMB   cosmic microwave background

CR   cosmic ray

CREAM   Cosmic Ray Energetics and Mass

DAMPE   Dark Matter Particle Explorer

EA   Engineering Array

EAS   extensive air shower

Elog   electronic logbook

EPS   expanded polystyrene

FADC   flash analog-to-digital converter

FD   Fluorescence Detector

FNAL   Fermi National Accelerator Laboratory

FoV   field of view

FPGA   field-programmable gate array

FRAM   F/Photometric Robotic Atmospheric Monitor

GPS   Global Positioning System

GW	gravitational waves
GZK	Greisen–Zatsepin–Kuzmin
HEAT	High Elevation Auger Telescopes
HiRes	High Resolution Fly's Eye
ISS	International Space Station
KASCADE	Karlsruhe Shower Core and Array Detector
KIT	Karlsruhe Institute of Technology
LDF	lateral distribution function
LED	light-emitting diode
LHC	Large Hadron Collider
LIDAR	Light Detecting And Ranging
LIV	Lorentz invariance violation
LPDA	logarithmic periodic dipole antenna
LPMT	large photomultiplier tube
LSD	Layered Surface Detector
LST	limited-streamer tube
MARTA	Muon Array with RPC for Tagging Air showers
MIP	minimum ionizing particle
MoPS	multiplicity-of-positive-steps
MTD	muon tracking detector
NKG	Nishimura-Kamata-Greisen
PAMELA	Payload for Antimatter Matter Exploration and Light-nuclei Astrophysics
PMMA	poly(methyl methacrylate)
PMS	Parts Management System
PMT	photomultiplier tube
POEMMA	Probe Of Extreme Multi-Messenger Astrophysics
PVC	polyvinyl chloride
RD	Radio Detector
RFI	radio-frequency interference
RPC	resistive plate chamber
SALLA	short aperiodic loaded loop antenna
SD	Surface Detector
SiPM	silicon photomultiplier
SNR	supernova remnant
SPE	single photoelectron
SPMT	small photomultiplier tube
SSD	Surface Scintillator Detector
SSD PPA	Surface Scintillator Detector pre-production array
STAS	streamer tube acquisition system

TA	Telescope Array
ToT	time-over-threshold
ToTd	time-over-threshold deconvolved
UB	Unified Board
UHECR	ultra-high energy cosmic ray
UMD	Underground Muon Detector
UUB	Upgraded Unified Board
UUB PPA	Upgraded Unified Board pre-production array
UV	ultraviolet
VEM	vertical-equivalent muon
WCD	water-Cherenkov detector
WLS	wavelength-shifting
XLF	Extreme Laser Facility
XPS	extruded polystyrene

Contents

xx

Chapter

1

Introduction

The Universe we observe appears mostly dark and empty, with objects and environments far beyond our understanding. To explore the unknown space and reveal the mysteries of the Cosmos, different types of particles created in cosmic processes serve as the main messengers when they reach the Earth. Some of these types of particles are the so-called cosmic rays (CRs) which consist of charged nuclei with large varieties in their properties like energy and mass. Although CRs have been already discovered more than hundred years ago, their sources and acceleration mechanisms, as well as the propagation from their origins to the Earth remain as open questions. Especially, the ultra-high energy cosmic rays (UHECRs) are messengers from the most violent and extreme environments we can imagine. Various models have been proposed to describe potential source environments and define acceleration processes for these particles with energies above 10^{18} eV, energies which are still unreachable for the current and future artificial accelerators. Until the present day, the sources of UHECRs are controversially discussed, especially at energies of the expected transition from the Galactic to the extra-galactic CRs, as well as when searching for potential candidates at the upper end of the energy spectrum [1].

Over the last century and mainly in the last decades, many of these open questions have been addressed with immense efforts leading to an impressive number of breakthrough discoveries on two scales, the small world of the particles and the large world of astrophysics. Since the start of its data acquisition in 2004, one of the leading global players in the CR research is the Pierre Auger Observatory, representing the currently world's largest experiment to measure UHECRs [2]. The Observatory is designed to address the mysteries of UHECRs by measuring extensive air showers (EASs) produced by the primary particles entering the Earth's atmosphere. Due to the low CR flux at the highest energies, the Pierre Auger Observatory covers an immense area of more than $3000\,\mathrm{km}^2$ with a Surface Detector (SD) utilizing particle-sampling stations that measure the lateral distributions of air showers on the ground. In combination, the telescopes of the Fluorescence Detector (FD) determine the longitudinal profile of the air shower developing in the atmosphere, and thereby providing a precise calorimetric detection of EASs. With the Observatory, the features of the UHECR energy spectrum have been determined including the confirmation of the suppression of the particle flux at energies of 10^{20} eV and above [3]. Until recently, this feature was explainable assuming a proton dominated CR composition interacting with the photons of the cosmic microwave background (CMB). With recent observations leaning towards a heavier mass

composition [4], other mechanisms such as photo-disintegration and the maximum rigidity of nearby extra-galactic sources stepped into the foreground as possible explanations. Thereby, the mass composition not only influences the interpretation of the features of the energy spectrum, but also interferes with the arrival directions of the CRs. These arrival directions depend on deflections in the propagation of the CRs caused by magnetic fields whose strengths and orientations are not well constrained. Despite the fact that significant progress has been achieved, the detectors in their current configuration are not able to reach the necessary sensitivity to further examine the properties of UHECRs.

For this reason, after nearly two decades, the Observatory has currently entered the transition phase towards the next measurement stage to increase the capability and the precision of detecting EAS events and thereby obtaining the physical properties of UHECRs [5]. Especially, with the enhancement of the sensitivity to determine the mass composition, new opportunities in the analysis of UHECRs will be provided. The transition is realized with an extensive detector upgrade, named AugerPrime, which includes the addition of new sub-detectors, e.g., scintillation detectors and radio antennas, providing complementary responses to the different air-shower components, as well as major enhancements of the electronics capabilities of the current detectors. Since 2016, various components and detectors have been assembled, tested, and deployed in the Observatory resulting in different detector configurations and several upgrade stages.

In this Dissertation, extended studies of the performance of the current and the new detectors of the Pierre Auger Observatory are presented. Therein, the new AugerPrime hardware components have been analyzed to test their readiness for the deployment on a large scale. This includes checks if preliminary defined requirements are matched, as well as the exploration of their full performance potential when compared to the current detector configuration. The results of these analyses are crucial to secure the success of the AugerPrime upgrade and the upcoming decade of measurements at the Pierre Auger Observatory.

As an introduction, the physics and phenomenology of CRs including the discussion about their origin, acceleration, and propagation through the Universe is provided in Chapter 2. Additionally, we present an overview on the methods to detect CRs in space or on Earth, focusing on the techniques to measure the particles of EASs initialized by UHECRs arriving at the Earth's atmosphere. Furthermore, the major discoveries and latest results in the UHECR research are discussed, including the remaining open questions and the future plans to address them. In the following Chapter 3, a detailed description of the current detectors and facilities of the hybrid design of the Pierre Auger Observatory is given. In addition, the different components and detectors of the AugerPrime upgrade are introduced. One main component of the Upgrade is the installation of the newly assembled Surface Scintillator Detectors (SSDs) on top of the existing water-Cherenkov detector (WCD) stations of the SD. To guarantee a high quality standard during the detector production, various validation measurements and tests have been performed at the Karlsruhe Institute of Technology (KIT) production site which are presented in Chapter 4. This Chapter commences with the detailed description of the set-up for the validation tests, followed by the presentation of the test results of the more than 660 detector units. Additionally, we compare in this Chapter the laboratory measurement data with detector simulations. Afterwards, we analyze in Chapter 5 the performance of the different versions of the electronics boards for the upgrade of the SD stations. Furthermore, a description of the configurations and operation status of the different AugerPrime SD arrays since the deployment of the first components in 2016 is given, including the impact of environmental effects on the measured signals. With the new electronics boards and additional detection devices, modifications and adaptations in the calibration procedure became necessary. For this reason, Chapter 6 contains a description of the current SD calibration procedure, together with a summary of its long-term behavior and performance using events from the 18 years of data acquisition. This Chapter also provides

the development of a modified algorithm to generally improve the calibration process and its application to the data acquired with the non-upgraded SD and AugerPrime stations. Thereby, the algorithms are compared on a single device level, as well as on the stage of the determined detector signals. In addition, we analyze the performance of the newly developed calibration procedure applied to the devices installed in the AugerPrime stations. Subsequently to the calibration, the procedure of air-shower event reconstruction with the SD is presented in Chapter 7. Therein, the effects of the calibration-algorithm modifications on the reconstruction of the energy estimators are analyzed. Furthermore, comparisons of the reconstruction performance of the different array configurations are carried out. This includes mass-composition sensitive analyses of the signals of the different sub-detectors. Finally, Chapter 8 provides a summary and conclusion of the previously presented analyses, as well as an outlook for the potential of the upgraded detectors of the Pierre Auger Observatory.

Chapter

2

Physics of Cosmic Rays

To this day, the fascinating world of cosmic rays (CRs) provides a large number of mysteries and unknowns and defines the research of numerous scientists all over the globe. This fascination already started in the beginning of the 20th century with the discovery of the CRs and their effects on the Earth's atmosphere. More than 100 years later, the determination of the properties and the origins of the CRs is still an enormous challenge and various approaches have been developed over the last century to access the physics of these exotic particles. Especially at the highest energies, i.e., particle energies above $\sim 10^{18}$ eV, the so-called ultra-high energy cosmic rays (UHECRs) are providing an unique possibility to search for new particle physics, far beyond the accessibility of the current generation of accelerator experiments on Earth.

This Chapter introduces the nature of CRs by describing their measured properties including their composition, arrival rate at the Earth, and potential origin. In addition, an overview of the detection methods for particles of different energy ranges is given. The identification of the particles at the highest energies is only possible through an indirect procedure utilizing the interactions of UHECRs with nuclei of the atmosphere. These interactions commence the creation of extensive air showers (EASs) which can be measured by large ground-based observatories, as of one is the Pierre Auger Observatory. For this reason, we present in the second part of this Chapter the properties and concepts of EASs and their detection techniques, together with certain experiments which define milestones in the research field of UHECRs. Finally, with the latest generation of EAS observatories, remarkable results concerning the determination of the mass composition, the energy spectrum, or the arrival directions of UHECRs have been achieved, significantly improving the understanding of the physical behavior of these remarkable particles. Despite the fact that an immense research progress has been achieved, a large number of mysteries still remain in the world of UHECRs, as for example, what are their sources, or how are they accelerated. The last part in this Chapter summarizes the most important results in the UHECR research and the open questions therein which will be addressed by the upcoming upgrades of the current EAS observatories and possible future experiments.

2.1   Properties of cosmic rays

In the first decade of the 20th century, scientists discovered that the air is ionized to a certain degree and concluded that the radiation from radioactive decays in the ground has to be the source of this ionization. This hypothesis was ruled out when Victor Hess measured during several balloon flights in 1911 and 1912 an increase of ionization with raising altitude [6]. Hess was able to demonstrate that the ionization of the air was, against the common consensus, the result of a type of penetrating radiation entering the atmosphere from above, and therefore named the new observation "Höhenstrahlung". Approximately 15 years later, Robert Millikan defined the term "cosmic rays" by describing their origin from cosmic processes, but still assuming a mostly electromagnetic radiation, thus the use of the word "ray" [7]. This picture then changed when succeeding experiments measured that CRs mostly consist of positively charged massive particles with very high energies, and only a very small fraction, i.e., approximately 1 %, of electrons and photons can be observed. With these observations, the CRs became natural sources for the newly forming high-energy particle physics leading to a large amount of discoveries of new particles and to the combination of the two major disciplines astrophysics and particle physics into one, the astroparticle physics.

Nowadays, the CRs are known as atomic nuclei with masses ranging from the lightest particle, the proton, up to the heaviest element from nuclear fusion processes in stars, the iron, propagating through the Universe with nearly the speed of light [1]. Thereby, ~90 % of the CRs are assumed to be protons, and ~9 % helium nuclei, also called alpha particles. The remaining percent of particles are assumed to be heavier nuclei. These mass fractions are not static, but depend on the energy distribution of the CRs defining the flux of the cosmic particles. In the following, the most important properties of CRs are presented. Subsequently to the CR energy spectrum, we describe conditions on the potential sources of CRs, as well as propagation effects, especially for UHECRs. Finally, various detection techniques for CRs are introduced which strongly differ depending on the targeted energy range.

2.1.1   Particle flux and origin

To characterize a CR particle, two major properties have to be determined, the mass of the nucleus and its kinetic energy. The measured energies of CRs span a large range of over 12 orders of magnitude, starting at energies around ~10^9 eV and reaching values above ~10^{20} eV [9]. While CRs with energies close to the lower energy threshold are assumed to be created by solar activities, the medium energy particles are expected to originate from Galactic sources, e.g., supernova remnants (SNRs) [1]. For the high-energy CRs the situation is still under debate. Especially the transition from the Galactic to the extra-galactic origin, as well as the potential sources of the particles at the highest possible energies remain unclear.

The flux of charged particles arriving at Earth is not constant over the whole energy range, but follows a certain energy correlation forming the so-called CR energy spectrum. The observed cosmic particle flux J can be described with a falling power law which is defined by the scaling power γ of the energy, i.e., can be written as

$$J \propto \frac{\mathrm{d}N}{\mathrm{d}E} \propto E^{-\gamma} \tag{2.1}$$

with N as the number of arriving particles and E defining the particle energy. In Fig. 2.1, the CR flux measured by various experiments with different energy sensitivities is shown. When the particle flux is scaled with a factor similar to the average power law exponent, in the diagram by a factor of $E^{2.6}$, we can observe that the slope of the energy spectrum is not constant over the total energy range. Various features become visible that mark transition energies at which the slope of the spectrum changes, and thereby divide the total spectrum into individual power laws in-between the inflection points. These features are expected to
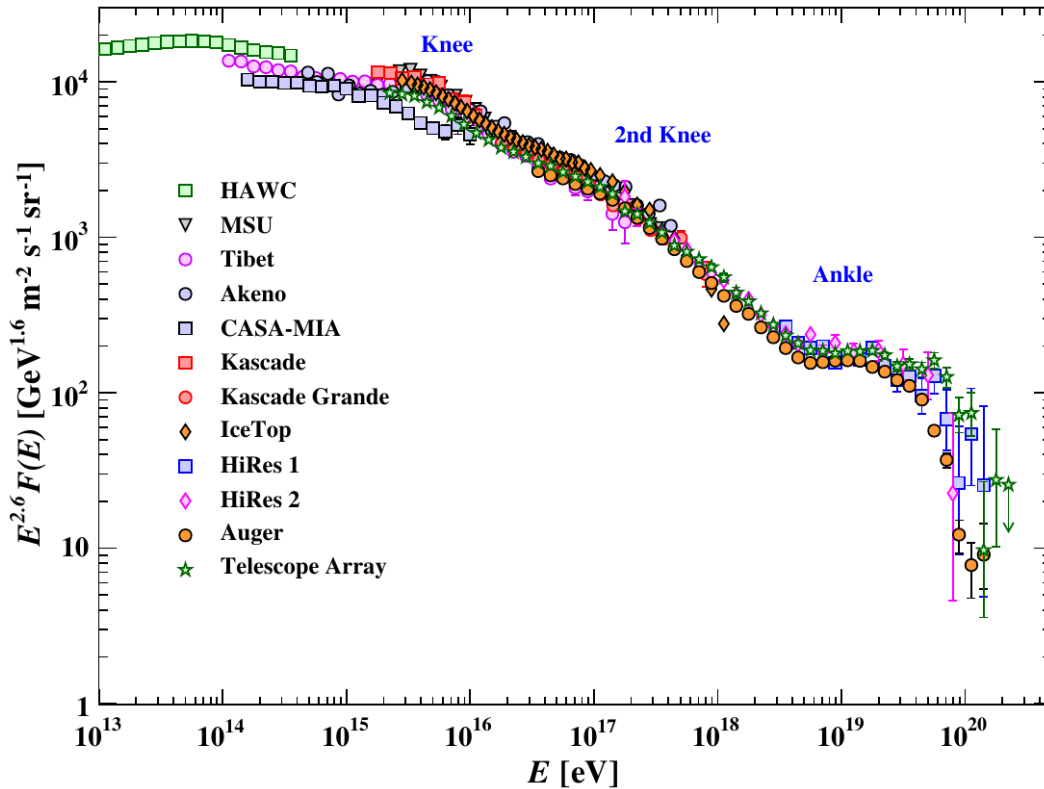
Figure 2.1: Flux of CRs measured by various experiments at different energy ranges and scaled with the energy $E^{2.6}$ to emphasize certain features. Taken from Ref. [8].

represent the phenomenology of the CR physics and have been studied by a multitude of CR experiments. In the diagram, several of the most evident features are highlighted whose terminology follows the anatomy of a human leg resembling the shape of the spectrum:

- At 4×10^{15} eV a steepening of the flux is visible, called the "knee", which can be related with the reaching of the maximum energies of acceleration mechanisms for particles with low masses originating from sources in our Galaxy, e.g., SNRs.

- For energies above the knee, the CR spectrum is expected to be dominated by Galactic heavy elements which fade out when their maximum acceleration energy is reached at $\sim 2 \times 10^{17}$ eV, defining a further steepening of the energy spectrum, named the "second knee".

- At 5×10^{18} eV the slope of the particle flux increases significantly leading to a flattening of the spectrum called the "ankle". At this energy, the transition from CRs of Galactic to extra-galactic origin can be assumed due to the deficiency of source candidates in our Galaxy.

- Finally, a fourth feature is visible at the highest energies, i.e., for energies above $\sim 5 \times 10^{19}$ eV. At this inflection point a strong suppression of the particle flux can be observed.

While the origin of the knee and the second knee seem to be understood, the explanation of the ankle and the flux suppression are still under discussion. For the interpretation of the spectrum in the ankle region various different scenarios have been proposed depending on the expected CR mass composition.

In the case of the flux suppression, one possible explanation might be the effect of the extra-galactic sources reaching their maximum acceleration potential and defining the
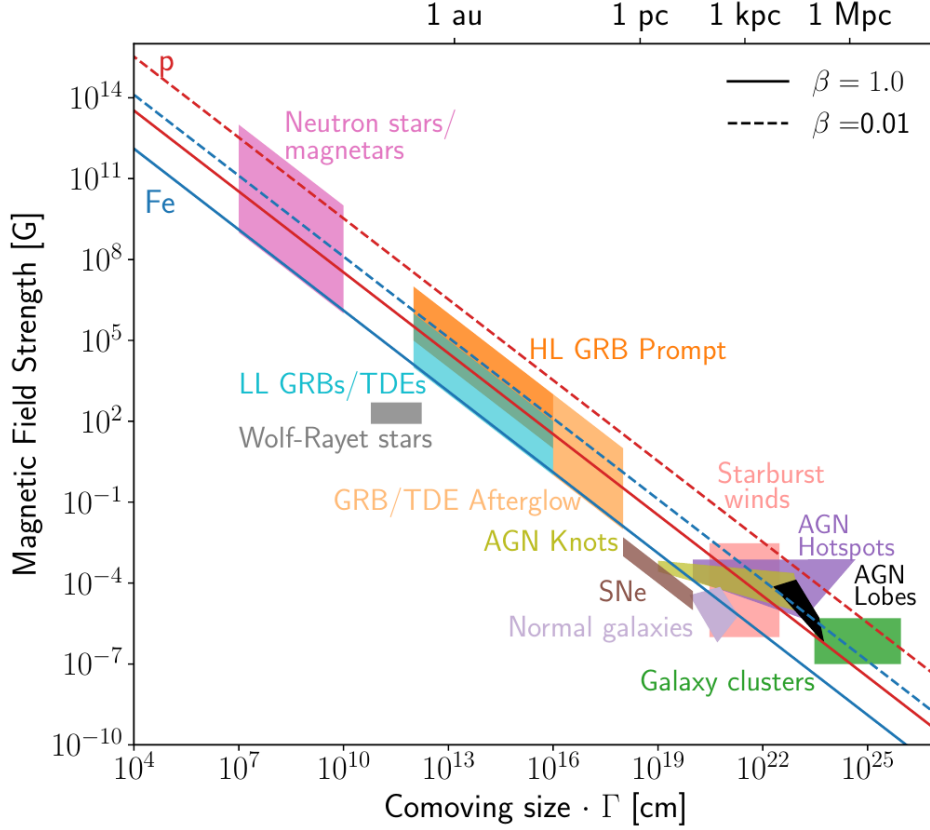
Figure 2.2: Hillas diagram containing various source classes depending on their average size *L* and magnetic field strength *B*. The diagonal lines represent the required limits to accelerate protons (red) or iron nuclei (blue) up to energies of 10^{20} eV under the condition of fast shocks ($\beta = 1.0$) shown by the solid lines and slower shocks ($\beta = 0.01$) depicted by the dashed lines. Taken from Ref. [14].

energy spectrum by the superposition of the suppression of the different CR masses [10]. This resembles the effect that can be observed for the Galactic CRs at the knee and the second knee. Another explanation to describe the particle flux suppression is the so-called Greisen–Zatsepin–Kuzmin (GZK) effect [11, 12]. This effect characterizes the interaction of ultra-high energy protons with photons of the cosmic microwave background (CMB) resulting in a Δ^+-resonance which then decays in two channels,

$$p + \gamma_{\text{CMB}} \rightarrow \Delta^+ \rightarrow p + \pi^0, \tag{2.2}$$

$$p + \gamma_{\text{CMB}} \rightarrow \Delta^+ \rightarrow n + \pi^+. \tag{2.3}$$

Due to the fact that the GZK effect works only for protons, a high fraction of protons needs to be assumed to describe the flux suppression. The GZK effect also constrains the mean free path of ultra-high energy protons, and thereby defines the energy-dependent GZK horizon.

If the CR composition tends towards heavier elements, the photo-disintegration effect of the nuclei in the ambient photon fields becomes relevant [13]. In Section 2.4, the different scenarios to describe the shape of the UHECR spectrum are introduced in more detail. Furthermore, additional spectrum features are presented in this section, e.g., a potential steepening between the ankle and the suppression region which has been observed recently.

2.1.2 Acceleration and source candidates

To produce particles with ultra-high energies, the existence of sources with unimaginably violent environments is necessary. In these sources, processes are present which accelerate charged particles to the highest energies. One potential process was proposed by Enrico Fermi who explained the acceleration of particles by iterative scattering in moving magnetized clouds [15]. The resulting energy after n scattering processes can be written with the second-order Fermi equation

$$E_n \approx E_0 \left(1 + \frac{4}{3}\beta^2\right)^n \tag{2.4}$$

with the initial energy E_0 and the velocity of the clouds $\beta = v/c$. If the particles are passing a shock front instead, the energy gain is more efficient and the energy after n passages of the shock front can be summarized with the first-order Fermi acceleration, defined as

$$E_n \approx E_0 \left(1 + \frac{4}{3}\beta\right)^n. \tag{2.5}$$

Here, the velocity β describes the speed of the shock front. The resulting particle energy spectrum can then be described with a power law function.

The maximum energies which can be reached with these processes are limited by two main source properties, the size of the source and the strength of the surrounding magnetic fields [16]. Thereby, the Hillas criterion describes the maximum energy E_{max} that CR particles can obtain in cosmic accelerators and can be written as

$$E_{\mathrm{max}} \sim eZBL \tag{2.6}$$

with Z as the charge of the particle. B and L are the magnetic field strength and the size of the cosmic source, respectively. To search for candidate sources, various source classes can be placed in a Hillas diagram as shown in Fig. 2.2. Therein, various source classes are arranged by their average magnetic field strength and size. The minimum source requirements to accelerate protons and iron nuclei up to energies of 10^{20} eV are given by the diagonal lines. These limits depend on the efficiency of the acceleration processes which is related to the velocity of the shocks β. Sources that are located below the limit lines do not satisfy the Hillas criterion. A recent correlation analysis of UHECRs with different candidate source classes is introduced in Section 2.4.

2.1.3 Detection techniques

In over more then 100 years since their first observation, the search for CRs of all energies has lead to the development of various detection techniques and methods. Thereby, the utilized techniques depend on the flux of particles which itself strongly depends on the energy of the CRs [1]. While for particles with energies of a few GeV the flux is approximately $1\,\mathrm{m}^{-2}\,\mathrm{s}^{-1}$, and therefore the measurement can be performed directly, the arrival rate of particles with the highest energies is reduced by several orders of magnitude. Particles with energies above 10^{20} eV are observed with a flux of one particle per square kilometer per century. To detect these particles, enormous efforts are required which can be achieved by increasing the observation time and the size of the experiment, i.e., ultimately the exposure.

Due to the interaction capability with matter, the direct detection of individual CR particles can only be realized above the Earth's atmosphere. Thereby, technologies commonly utilized in accelerator experiments are necessary to determine the properties of the particles [8]. These include spectrometers such as calorimeters, drift chambers, time-of-flight detectors, transition radiation detector, etc. To enhance the sensitivity, modern experiments use a combination of different detector types precisely determining the particle properties, e.g., its

Primary Particle
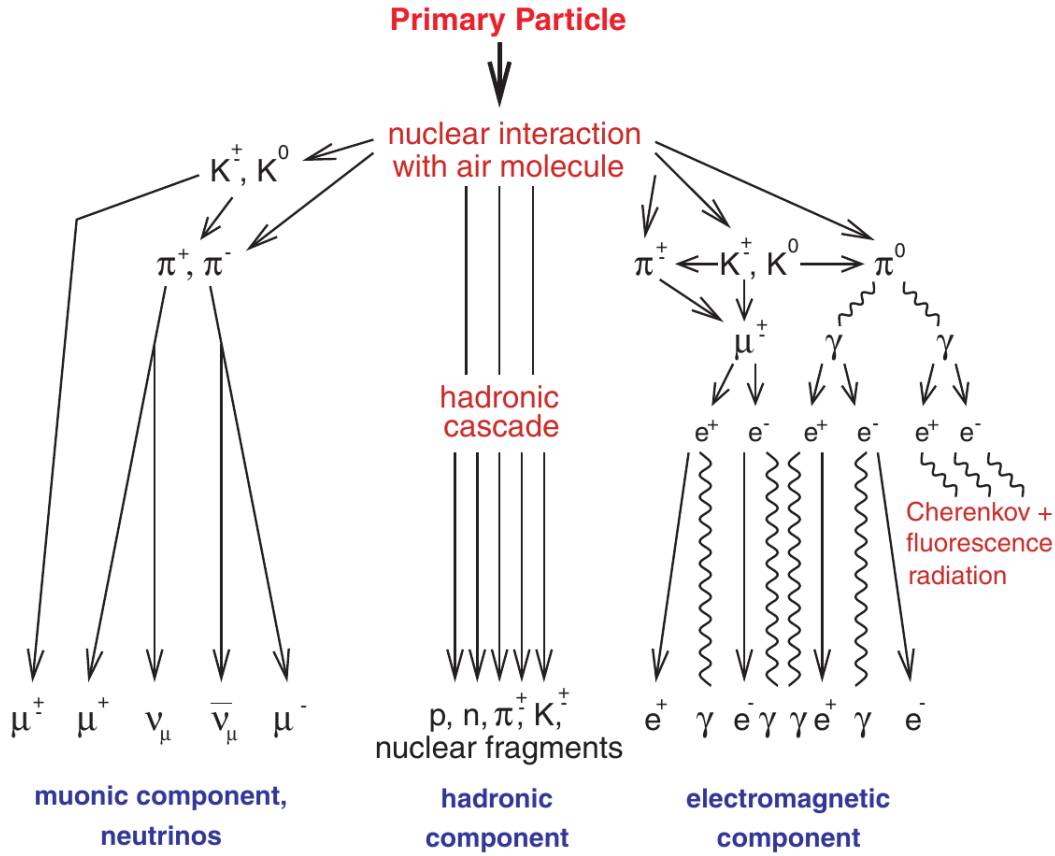
Figure 2.3: Schematic of the different EAS components, the hadronic, the muonic, and the electromagnetic particles. Taken from Ref. [21].

kinetic energy, charge, and mass. Due to the necessity to fit on balloons or satellites, the scale of direct CR detection experiments is constrained and correlates with high costs, a limited flight time, as well as restrictions of the size which cannot exceed the transport devices. Balloon experiments like the Cosmic Ray Energetics and Mass (CREAM) experiment [17] and satellites such as the Payload for Antimatter Matter Exploration and Light-nuclei Astrophysics (PAMELA) [18] or the Dark Matter Particle Explorer (DAMPE) [19], together with the Alpha Magnetic Spectrometer (AMS-02) detector at the International Space Station (ISS) [20], are providing precise measurements of the CR spectrum and mass composition up to energies of $\sim 10^{14}$ eV.

Above this energy, the flux of arriving particles at these detectors falls below the sensitivity threshold and a different technique is necessary to measure CRs. Instead of a direct detection of the incoming particles, the capability of the CRs interacting with the atmosphere can be utilized. The interactions appear in the outer layers of the Earth's atmosphere resulting in the generation of the air showers which develop down to the Earth's surface. In the following, the nature, as well as the detection methods of the phenomena are presented.

2.2   Extensive air showers

When primary CRs with energies above $\sim 10^{15}$ eV reach the outer layers of the atmosphere, they initiate the creation of extensive air showers (EASs) [1, 21]. These phenomena can be described with cascades of secondary particles raining down on the Earth, from the outer to the inner atmosphere layers, and spanning over several kilometers in size. Thereby, the atmosphere serves as a giant calorimeter which converts the energy of the primary particle

through interactions with air nuclei into numerous secondary particles and radiation. The initiation of EASs or just shortly called "air showers" depends on the type of the primary particle and its energy. Statistically, heavy nuclei like iron interact earlier with atoms in the atmosphere due to their higher cross section, i.e., shorter mean free path, compared to lighter nuclei like protons. This leads to an increased altitude for the first interaction for heavier primaries, and therefore in an earlier development of the air shower. Additionally, the cross section depends on the energy of the primary particle. Particles with a lower energy statistically penetrate deeper into the atmosphere before the first interaction appears, implying that the cross section increases with a higher primary energy.

In general, the secondary particles of an EAS consist of three main components, a hadronic, a muonic, and an electromagnetic part which are displayed in the diagram in Fig. 2.3. Thereby, the hadronic component defines the first particles in the early development of an air shower. The component consists of a variety of hadrons, mostly pions or kaons, as well as baryons like protons and neutrons. These hadrons contribute only a very small fraction to the total number of secondary particles, but initiate the development of the muonic and electromagnetic components through particle decay processes and the production of sub-showers.

The muonic component represents 1 to 2 % of the air-shower particles and consists of muons and anti-muons, as well as neutrinos from the decay of charged pions and kaons. Despite the fact that these particles have the probability to decay into electrons or positrons, the majority of muonic particles propagate through the atmosphere and reach the ground without interacting due to their average energy being several GeV.

Finally, the third and largest EAS component are the electromagnetic particles, i.e., electrons, positrons, and photons, which define ~98 % of the cascade particles. These particles carry on average a kinetic energy of several MeV and are produced in decays of neutral pions, as well as by interaction processes like pair production and bremsstrahlung. The electromagnetic particles form rather wide cascades caused by scattering effects and develop at higher altitudes compared to the muonic component.

Generally, the development of a purely electromagnetic cascade can be described with a simple model introduced by Walter Heitler [22]. This model assumes a simple symmetric branching structure including two main processes, the production of electrons and positrons through pair creation and the generation of photons by bremsstrahlung. After each collision length λ the model assumes that the energy of a single particle is after the interaction equally distributed into the two resulting particles. Therefore the number of particles after n iterations is

$$N(X) = 2^n = 2^{X/\lambda}. \tag{2.7}$$

Here, X describes the slant depth. The energy of each particle is then given by the initial energy divided by the number of created particles

$$E(X) = E_0/N(X). \tag{2.8}$$

The branching process continues until the particles reach a critical energy E_c and no further particles can be produced, but only energy losses and decays occur. In air, this critical energy is $E_c \approx 87\,\text{MeV}$. The maximum number of particles that can be produced is then limited to

$$N_{\text{max}} = N(X_{\text{max}}) = E_0/E_c \tag{2.9}$$

and the slant depth at which the air-shower maximum is reached can be formulated as

$$X_{\text{max}} = \lambda \frac{\ln{(E_0/E_c)}}{\ln 2}. \tag{2.10}$$

The electromagnetic cascade model was generalized and extended to the hadronic air-shower component by James Matthews [23] using a similar branching approach. In the

Heitler-Matthews model the production of pions define the main processes which can be split with a probability of two-third for the production of charged pions representing the hadronic component and a probability of one-third for the immediate production of neutral pions that promptly decay and define the electromagnetic cascade. Assuming a hadronic interaction length λ_{int}, which is larger than the interaction length of the electromagnetic cascade for the charged particles, the particle energies are then given as

$$E_{\text{had}} = \left(\frac{2}{3}\right)^n E_0 \quad \text{and} \quad E_{\text{em}} = \left[1 - \left(\frac{2}{3}\right)^n\right] E_0. \tag{2.11}$$

The depth of the shower maximum can be calculated from the point of the first hadronic interaction λ_{int} with

$$X_{\text{max}} \sim \lambda_{\text{int}} + X_0 \ln\left(\frac{E_0}{2n_{\text{tot}}E_{\text{c}}}\right), \tag{2.12}$$

with the total number of produced pions n_{tot}. The charged pions decay into the muonic component of the air shower so that the number of muons can be derived from the critical decay energy E_{dec} with

$$N_\mu = \left(\frac{E_0}{E_{\text{dec}}}\right)^\alpha \quad \text{with} \quad \alpha = \frac{\ln n_{\text{ch}}}{\ln n_{\text{tot}}} \approx 0.82 \text{ to } 0.9. \tag{2.13}$$

Therein, n_{ch} describes the number of the produced charged pions. Due to the negligible binding energy, if the primary particle is a nucleus with mass A, the interactions can be assumed to be produced by a superposition of A independent nucleons with energies of E_0/A. This leads to an increased production of muons for heavier nuclei following

$$N_\mu^A = A^{1-\alpha} \left(\frac{E_0}{E_{\text{dec}}}\right)^\alpha. \tag{2.14}$$

Additionally, up to ~10 % of the total energy can be carried away by the neutrinos which are produced in the hadronic interactions. This energy cannot be measured calorimetrically due to the extremely small cross section of the neutrinos, and therefore is lost as "invisible" energy.

In general, the air shower can be described with the longitudinal particle distribution which contains the information of the number of particles N in the shower at a given penetration depth X. The functional shape of this profile has been phenomenologically obtained and can be written as the Gaisser-Hillas function [24], i.e.,

$$N(X) = N_{\text{max}} \left(\frac{X - X_0}{X_{\text{max}} - X_0}\right)^{\frac{X_{\text{max}} - X_0}{\lambda}} \exp\left(\frac{X_{\text{max}} - X}{\lambda}\right) \tag{2.15}$$

with X_0 describing the depth of the first interaction. The parameters thereby depend on the mass and the energy of the primary particles and N_{max} is driven by the electromagnetic component. If the air shower develops higher in the atmosphere, i.e., with a smaller X_{max}, the majority of electromagnetic particles are already absorbed before reaching the ground. This effect can also be observed for inclined EASs, i.e., air showers which develop under a large angle to the normal vector of the Earth's surface. In these air showers, the particles have to propagate through a significantly longer distance in the atmosphere before reaching the ground.

The understanding of the geometry of EASs is of high importance for their reconstruction and thereby for the determination of the properties of the primary particles. The air-shower direction can be described by its central axis created by the arrival direction of the primary particle. This can be achieved with the definition of two angles in the coordinate system

above the Earth's surface. In this Dissertation, we use the term "zenith" angle, or the letter θ, to define the angle between the air-shower axis and the normal vector of the Earth's surface. In addition, for the angle relative to the geographical orientation of the experiment, the term "azimuth" angle, or the letter ϕ, is used.

Despite the fact that the majority of particles are propagating semi-parallel to the central axis, energy dependent scattering effects can be observed leading to a certain fraction of particles arriving on the ground multiple kilometers away from the impact position of the air-shower axis. Thereby, the size of these footprints depend on the energy and the mass of the primary particle, as well as its arriving angle. Additionally, the number and types of secondary particles that reach the ground depend on these parameters. The highest density of particles can be seen in the proximity of the center of the air shower, i.e., inside the so-called core around the air-shower axis. The particle density then radially decreases with distance to the core providing detectable information about the geometry of the EAS. Generally, the radial distribution of secondary particles can be described by the lateral particle density which can be expressed with the Nishimura-Kamata-Greisen (NKG) function [25, 26, 27].

Besides the lateral particle density, the arrival time of the particles can be used to analyze EASs. When the air shower develops through the atmosphere, all particles propagate with approximately the speed of light creating a thin and flat front of particles which is oriented perpendicularly to the air-shower core. Farther away from the core, the front appears to be slightly curved, i.e., particles with larger distances to the air-shower core are delayed. Finally, when the particles reach the ground, the impact position is defined as the intersection point between the shower core and the Earth's surface.

In general, EASs can be measured by determining the longitudinal or the lateral air-shower profile depending on the used method and detector. For an improvement of the measurement, both profiles can be obtained at the same time leading to a more precise analysis of the properties of the primary CR. The measurements can be realized with different detection types and methods introduced in the following section.

2.3 Detection of air showers

For the measurement of EASs, different types of ground-based detectors are used to observe the sky and measure the signals of the secondary particles propagating through the atmosphere and finally reaching the ground. Thereby, the detectors are designed to analyze the electromagnetic radiation of different wavelengths created by interactions of relativistic particles with matter. In Fig. 2.4 a schematic of different detection techniques of air-shower particles is provided. Besides the installation on the ground, new proposals of EAS measurements with cameras and telescopes mounted on satellites or space stations observing the atmosphere from above have been developed, e.g., the Probe Of Extreme Multi-Messenger Astrophysics (POEMMA) experiment [28].

When an air shower develops through the atmosphere, the electromagnetic particles excite and ionize the nitrogen molecules in the air which then isotropically emit fluorescence light in the ultra-violet and blue wavelength between 300 and 400 nm [1]. Due to the fact that the electromagnetic component represents the dominating majority of the particles, the intensity of the emitted fluorescence light can be assumed to be proportional to the total number of particles, i.e., the radiation describes the size of the air shower which can be related to the energy and mass of the arriving primary particle. The fluorescence light can be detected with photon-sensitive devices like telescopes which observe air showers propagating through the air and measure their longitudinal profile. By utilizing the Gaisser-Hillas function, the depths of the air-shower maxima X_{max} can be determined. The necessary vertical field of view (FoV) of the telescopes depends on the examined energy range, more accurately, the on depth of the air-shower maximum relative to the height at which the CR entered the atmosphere.
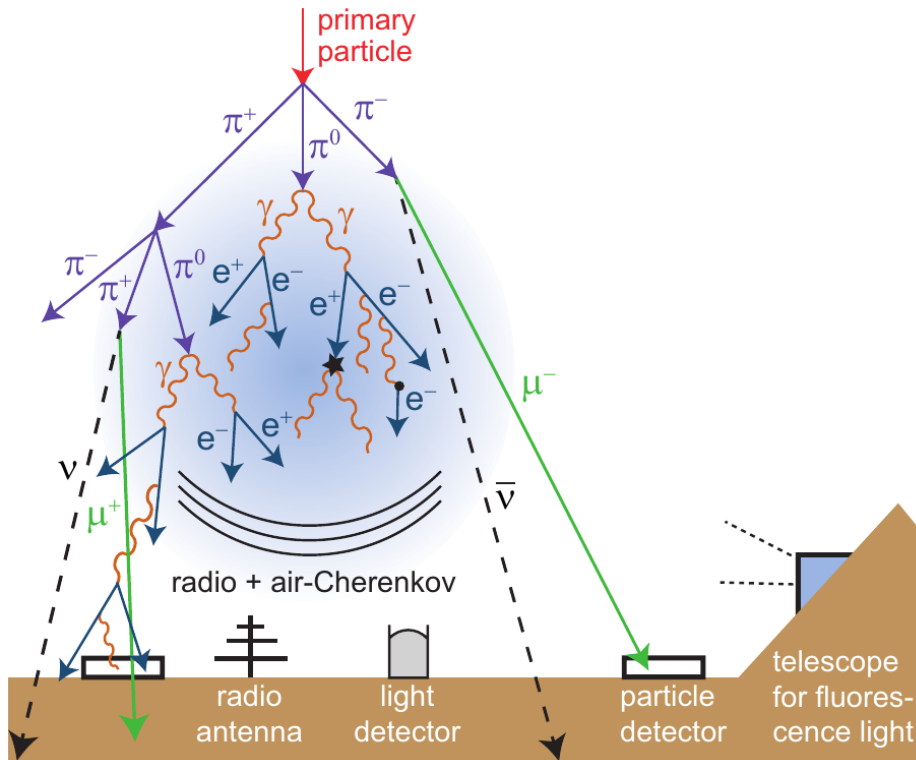
Figure 2.4: Schematic of several ground-based techniques for the detection of EAS particles. The different detector types are sensitive to different air-shower components. Taken from Ref. [29].

Telescopes with a vertical FoV starting at the ground level and raising up to several tens of degrees are designed for air showers created by primaries with the highest energies. For lower CR energies, elevated FoVs are needed to observe the air showers developing at high altitudes in the atmosphere.

In addition, the Cherenkov effect of the particles propagating superluminally through the air produces blue light as very short and faint light pulses in a very narrow beamed light cone around the air-shower axis. The relativistic charged particles, e.g., muons or electrons, propagate through an electrically polarizable medium and generate the emission of radiation. The reason for this is the high propagation velocity which exceeds the phase velocity of light in the respective medium. The passing charged particle polarizes the surrounding medium which then radiates a coherent shock wave called Cherenkov radiation. This radiation, for air typically in the blue or ultraviolet (UV) part of the spectrum, is emitted in a cone around the traveling particle with a maximum opening angle of $\sim1°$. The energy of the particle also defines the intensity of this radiation. To measure the Cherenkov radiation of secondary particles, similar telescopes than for the fluorescence-light measurements can be utilized. Due to the beamed emission with a very small angles to the air-shower axis, the aperture of the telescope has to be elevated, and preferably inclined air showers with large zenith angles are observed.

Both optical detection techniques use highly sensitive and fragile telescope components to measure the electromagnetic component of the EASs. Therefore, they are usable only during nights without intense moon light or deep clouds due to their strong sensitivity to background light. Additionally, these telescopes usually are not operated during nights with unfavorable weather conditions, e.g., strong winds, rain, or snow. These restrictions substantially limit the detection rate of EASs, especially for the events created by primary CRs with ultra-high energies.

When the air-shower particles finally reach the ground, they can be detected with arrays of surface detectors that sample the through-going particles. These surface detectors can be designed to be rather simple and robust and are usually self-sufficient concerning their power supply to provide an independent operation of each detector unit. Due to the large footprints of air showers, it is impossible to cover the total air-shower area with detectors. In addition, the majority of particles arrive inside a few hundreds of meters around the core demanding detectors with a very close spacing and the ability to measure very high signal intensities. These requirements are contrary to the general concept of simple detector stations which are distributed over a maximum possible area to increase the detection rate of the ultra-high energy primary particles. As a compromise, individual devices regularly distributed over a large area are used to measure the particle densities at different distances to the air-shower core. Then, the general lateral distribution of the air shower can be determined. Thereby, the spacing between the individual detectors defines the lower energy limit of the primary CRs to which the experiment is sensitive to. The optimal spacing for surface sampling detectors depending on the targeted energy range has been empirically determined from the results of experiments and detector simulations.

To measure the signals of the particles reaching the ground, different methods are used utilizing the interaction of charged particles with matter [8]. Thereby, radiation from processes like excitation or ionization is detected which provides information about the properties of the arriving particles, e.g., their energy and charge. In the case of the muonic particles in the GeV range, the ionization of the surrounding matter is the leading energy-loss process. To detect EAS particles, various types of detectors have been used and proposed. In the past, Geiger counters or ionization chambers filled with gas molecules have been the standard tools to analyze the incoming particles. Current experiments consists of Cherenkov detectors containing dense media like water or ice, which provide significantly increased opening angles of the Cherenkov radiation cones (~43° in water), and therefore an enhanced possibility of light detection. Besides Cherenkov detectors, plastic scintillators can be used to measure the density of air-shower particles. For both types of detectors, photon-sensitive devices are utilized to read out the optical signals, for instance photomultiplier tubes (PMTs) or silicon photomultipliers (SiPMs).

Additionally to the determination of the particle density, with the timing information of the individual surface detectors, the air-shower geometry can be determined and thereby the arrival direction of the incoming primary particles reconstructed. After the lateral distribution is obtained, the general shower size can be described which then can be used as an estimate of the number of particles in the air shower, and hence serves as estimator of the energy of the primary CRs.

The mass composition of the primary CRs can be accessed with an analysis of the general shapes of the pulses in the signal traces. These shapes depend on the type of particles which produced the pulses, and therefore provide an estimation of the ratio of the electromagnetic and muonic component. With the determination of the respective dominating component, especially the amount of muons in the EAS, conclusions on the original mass of the primary can be drawn. Thereby, the estimation of the CR masses is strongly limited when only a single type of sampling detector is used, but can be significantly improved when several different detectors with varying signal responses are installed. In contrast to the fluorescence telescopes, the surface detectors provide the advantage to be independent of the ambient light, i.e., measurements during the daytime are possible. For this reason, a robust and simple design is necessary to withstand the harsh environmental conditions, and at the same time ensure low material costs for a production in large quantities.

In the recent decades, a third major detection technique has been designed and implemented. This method measures the radio signal majorly created by the charged air-shower particles propagating in the Earth's magnetic field [29]. The signal can be observed with

radio antennas, distributed on the ground analogously to the particle sampling detectors and profits from their cheap and simple design.

The measurement era of EASs started in 1939 with the first experiment by Pierre Auger, the pioneer of ground-based air-shower detection [30]. By installing Geiger counters in a regularly spaced grid, Auger was able for the first time in history to measure the particles of air shower reaching the Earth's surface. In the decades after Pierre Auger, several experiments have been built to further improve the determination of EASs with the goal to gain knowledge on the mysterious CRs reaching Earth. Some of these experiments have been realized with surface sampling detectors to search for UHECRs, e.g., the Volcano Ranch experiment [31], the surface detector array at Haverah Park [32], or the Akeno Giant Air Shower Array (AGASA) experiment [33]. Other collaborations chose the fluorescence telescopes as primary detection technique, for example the Fly' Eye experiment and its successor the High Resolution Fly's Eye (HiRes) experiment [34]. At the Karlsruhe Institute of Technology (KIT), the Karlsruhe Shower Core and Array Detector (KASCADE) and its extension KASCADE-Grande have been operated for more than a decade to reconstruct lateral distribution of air showers and measure their muon content at the ground level [35, 36]. Thereby, the targeted energy range of KASCADE was below the energies of UHECRs to measure the CR energy spectrum in the region between the knee and the ankle. In the middle of the 1990s, discrepancies in the results of the leading UHECR experiments, the AGASA and the HiRes experiment have been observed, visible in diverging CR energy spectra. To resolve the correct shape of the energy spectrum, it was necessary to enhance the reconstruction sensitivities. This was achievable by developing hybrid experiments combining the detection of EASs with telescopes and ground detectors.

Currently, two main experiments are using hybrid techniques for the detection of EAS, one on each of the Earth's hemispheres. The Telescope Array (TA) located in the northern hemisphere at the HiRes experiment site in Utah in the USA combines the fluorescence telescopes of HiRes with 500 particle sampling detectors [37]. To detect particles reaching the ground, plastic scintillators are installed in each surface detector station spanning a total detection area of $\sim\!800\,\mathrm{km}^2$.

On the other side of the world, a second hybrid EAS experiment observes the southern hemisphere. The Pierre Auger Observatory, the currently world's largest experiment to measure EASs, is located in Argentina at the foot of the Andes [2]. With the combination of fluorescence telescopes, ground-based sampling detectors, and additional radio antennas, a precise measurement of air showers is realized. The experiment, in detail introduced in Chapter 3, is named after the pioneer of EAS detection and has strongly contributed to the research and understanding of the nature of UHECRs in the last two decades. In the subsequent Section, we present the major and most recent results in the UHECR research provided by the current experiments and outline the remaining open questions, which will be addressed by the Pierre Auger Observatory and the TA, which currently undergo major upgrades phases, as well as by future EAS experiments.

2.4   Ultra-high energy cosmic rays: Research and future aims

With the latest generation of hybrid air-shower experiments, outstanding discoveries and measurements for the determination of the physics of UHECRs have been achieved [14]. Nevertheless, various open questions remain unanswered until today which will be crucial in the understanding of the origin and behavior of these particles. In the following, the most recent results and unknowns concerning the energy spectrum, the mass composition, and the arrival direction of UHECRs are described.
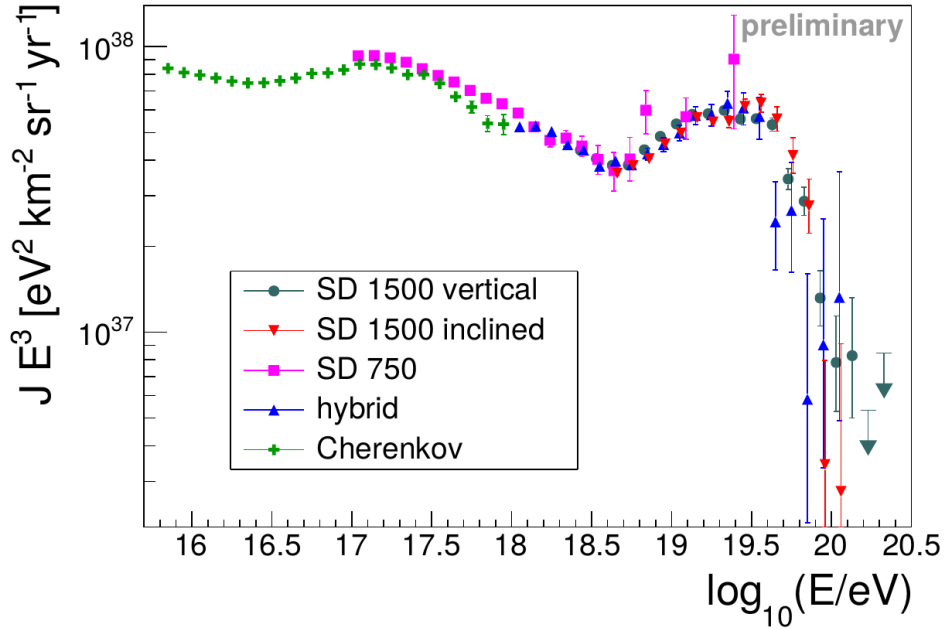
Figure 2.5: Flux of UHECRs measured by the detectors of the Pierre Auger Observatory scaled with an energy of E^3 to emphasize certain features. Taken from Ref. [38].

2.4.1 Energy spectrum

With the measurement of the energy dependent CR flux using the different detectors of the Pierre Auger Observatory, the energy spectrum of UHECRs and CRs below the ankle can be described precisely [3, 39, 40, 38]. With the latest measurement results shown in Fig. 2.5, the appearance of the two characteristic features for CRs with energies above 10^{18} eV, introduced in Section 2.1.1, has be confirmed. In the ankle region, an increase of the particle flux can be observed leading to a positive slope in the diagram. At the highest energies, the strong flux suppression is unambiguously confirmed leading to a non-detectable flux of UHECRs above energies of $10^{20.5}$ eV. In addition to the known features, another inflection point in-between the ankle and the suppression region has been proposed. This characteristic is called "instep" and describes the moderate steepening of the energy spectrum after the ankle at $\sim 2 \times 10^{19}$ eV and before the strong steepening of the suppression appears at $\sim 5 \times 10^{19}$ eV. A similar feature at the same energy has been confirmed by the TA experiment [41].

Despite the fact that the shape of the UHECR energy spectrum is measured to a high precision, the interpretation of the physics behind the characteristic curvature remains unclear. A strong interconnection of the energy distribution with the mass composition of the arriving particles is expected. Thereby, the correlation depends on the selection of the source models and the estimation of propagation effects. Different scenarios have been proposed to explain the shape of energy spectrum from 10^{18} eV to the highest energies:

- The classical model utilizes two propagation effects to predict the UHECR flux [42]. With a combination of a pair production process at the ankle region and the previously mentioned GZK effect for CRs with the highest energies, this scenario describes the energy spectrum well for the case that for all energies the largest fraction of CR nuclei are hydrogen, i.e., protons, as shown in the top diagram in Fig. 2.6.

- With the indication of an increase of the mass of CRs above the ankle, the proton-dependent scenario has been less favored for models which include contributions of heavier nuclei. One proposal defines the maximum rigidity of the cosmic sources as cause for the shape of the energy spectrum [10]. In this model, the acceleration processes
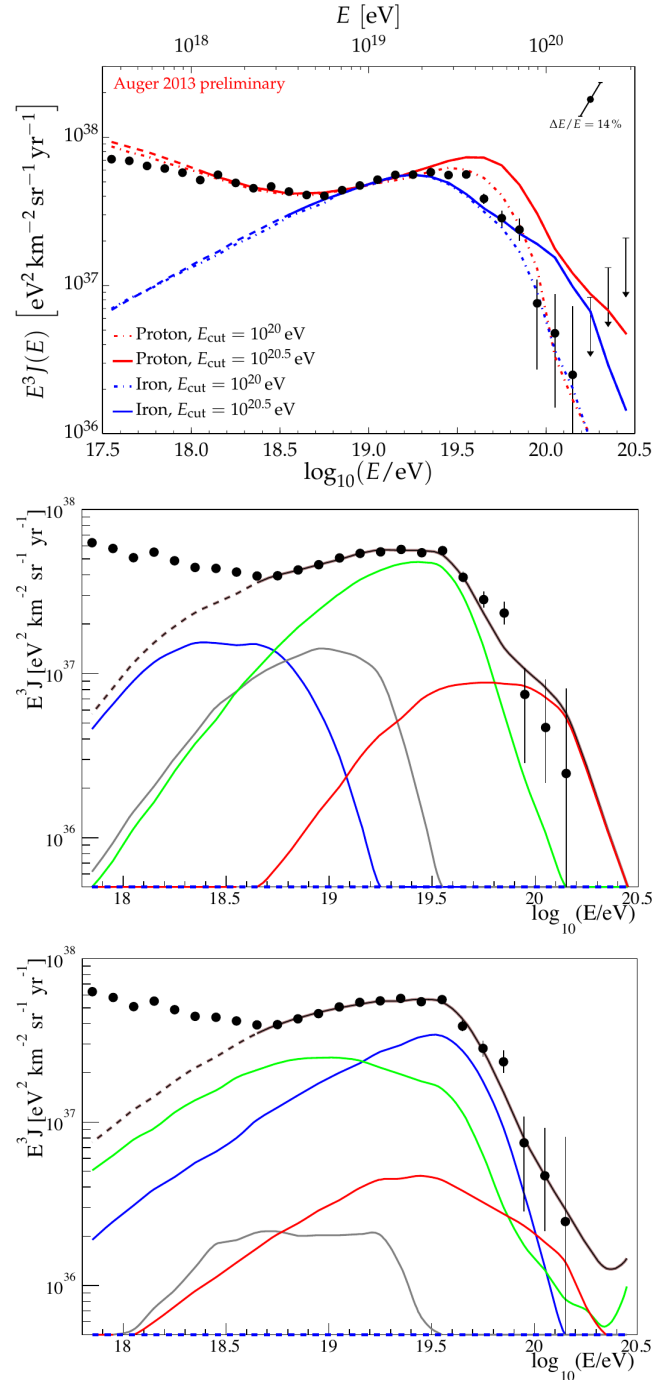
Figure 2.6: Mass composition dependent scenarios for the description of the UHECR energy spectrum. The classical approach describes the spectrum with a combination of a pair production mechanism and the GZK effect assuming a pure proton composition (top). For the other scenarios, a mixed mass composition is used as the starting point, and the total energy spectrum is obtained by the superposition of the individual spectra. The colors indicate the individual mass groups: blue for hydrogen, gray for helium, green for nitrogen, and red for iron. In the maximum rigidity scenario (center) the particle acceleration is charge dependent, i.e., higher charged nuclei can reach higher energies. Contrarily, the third scenario is based on the photo-disintegration of heavier nuclei during their propagation, resulting in individual spectra for different mass groups (bottom). Taken from Ref. [5].
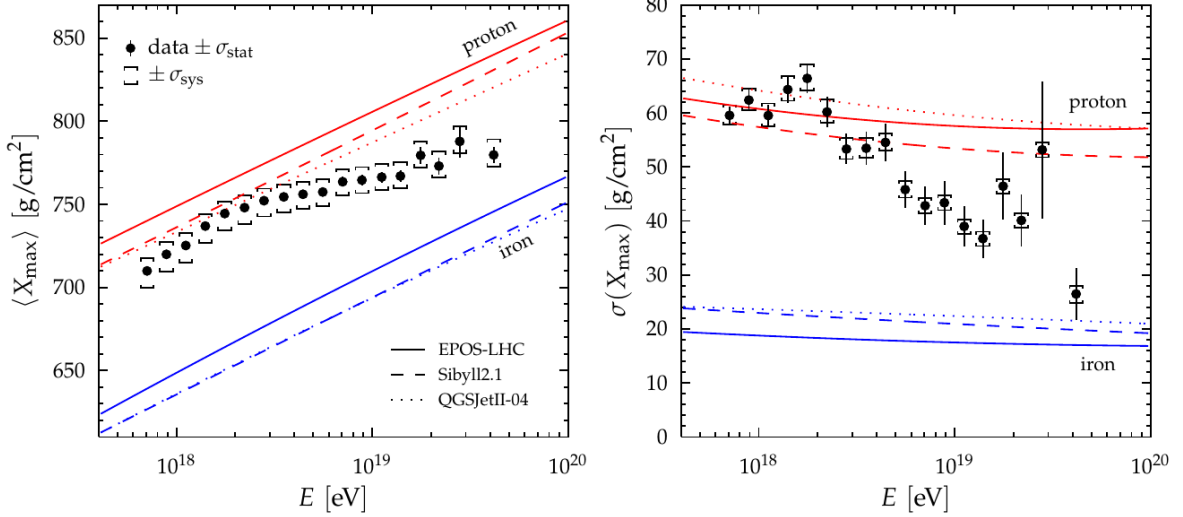
Figure 2.7: Measurement of the depth of the shower maximum X_{max} by the Pierre Auger Observatory compared to the expected distributions from simulations of a pure proton (red) or iron (blue) composition. *Left:* Mean of the depth of the shower maximum $\langle X_{max} \rangle$. *Right:* Dispersion (standard deviation) of the maximum depth $\sigma(X_{max})$. Taken from Ref. [5].

in the sources are charge dependent, and therefore different nuclei can be accelerated up to different maximum energies, ordered by the charge. The total energy spectrum is then defined by the superposition of the individual nuclei spectra. In the center diagram in Fig. 2.6, the maximum-rigidity scenario is displayed.

- Similarly, a third scenario also assumes a total energy spectrum created by the superposition of the individual nuclei, but the individual spectra are not ordered by the charges or masses of the nuclei [13]. In the so-called photo-disintegration scenario, the propagation effect of the heavy elements is accounted which interact with photons of the CMB and suffer from fragmentation. The resulting individual energy spectra are then defined by the ratio of the mass numbers of the respective parent and daughter nuclei. The results of a potential photo-disintegration model can be seen in the bottom diagram in Fig. 2.6.

To answer this open question of the explanation of the UHECR flux, the knowledge of the mass composition, especially at energies above $10^{19.5}$ eV, is crucial to distinguish between the various proposed scenarios or search for a combination of them. For this reason, the Pierre Auger Observatory is undergoing a major upgrade phase enhancing the mass sensitivity at the highest energies by the installation of new detector components. With the upgrade, extensively presented in Section 3.2, the exposure of the Observatory will be significantly increased and the measurement precision improved.

2.4.2 Mass composition

As already mentioned previously, the measurements of the average and the dispersion of the depth of the shower maximum X_{max} with the fluorescence telescopes of the Pierre Auger Observatory indicate a change of the mass composition over the energy range of UHECRs [4, 43, 44]. In the diagrams in Fig. 2.7, the energy dependence of these two mass-sensitive quantities is shown. To compare the results with simulations, the red and blue lines describe the expected behavior depending on the hadronic interaction model for a pure proton and pure iron estimate, respectively. The measured data shows a trend towards a lighter composition
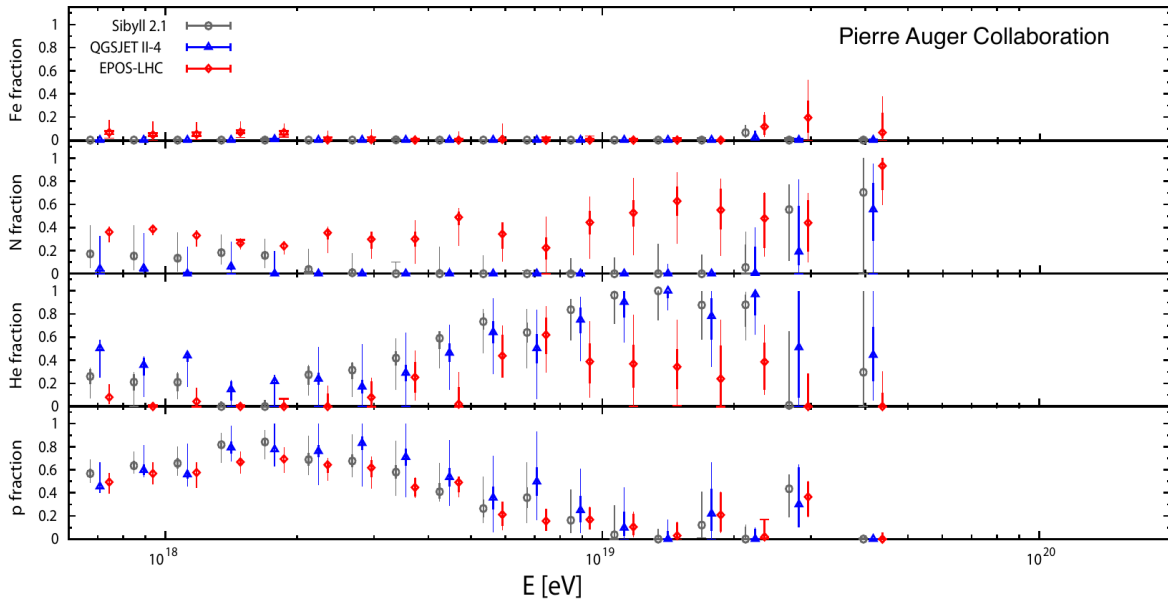
Figure 2.8: Energy-dependent fractions of four different mass groups, hydrogen, helium, nitrogen, and iron, for three different hadronic interaction models. Above CR energies of $10^{19.5}$ eV the limited detection statistics of the FD prohibits the estimation of the mass fractions. Taken from Ref. [5].

at energies around 10^{18} eV which then changes to favor nuclei of intermediate masses at the highest measured energies. A similar interpretation of the data can be observed, when the energy dependent mass fractions are analyzed, as can be seen in Fig. 2.8. Despite the fact that large fluctuations from the applied hadronic interaction models are visible, all models favor a maximum proton fraction at $\sim 10^{18}$ eV and a transition towards heavier elements with increasing energy. Both results disfavor a proton dominated CR flux at energies between the ankle and the suppression region, but the interpretation of the mass composition above CR energies $10^{19.5}$ eV is prohibited by the limited detection statistics of the Fluorescence Detector (FD).

Here, the upgrade of the Pierre Auger Observatory with additional detector components and advanced analysis methods will provide a measurement of the CR masses at even higher energies and will thereby provide an improved resolution of the actual proton content. This proton fraction defines the possibility to utilize CRs for astronomy and is strongly linked to the flux predictions of ultra-high energy photons and neutrinos, e.g., created by the GZK effect.

In parallel to the determination of X_{max} by the fluorescence telescopes, other detectors of the Pierre Auger Observatory are capable to determine the muon content in EASs, often referred to as R_μ [45]. With this observable, information about the UHECR mass composition can be derived and the model-dependent air-shower simulations can be analyzed. When comparing the measurement results and simulations, an excess of muons can be observed in the measured data, i.e., the hadronic interaction models tuned with the most recent Large Hadron Collider (LHC) results show a clear deficit in the estimated muon fractions [46].

To further investigate the differences between data and simulations, the upgraded detectors of the Observatory will in the near future provide a precise determination of the muon content of EAS on an event-to-event level, leading to an improved understanding of the air-shower development and potential modifications of the hadronic interaction models.
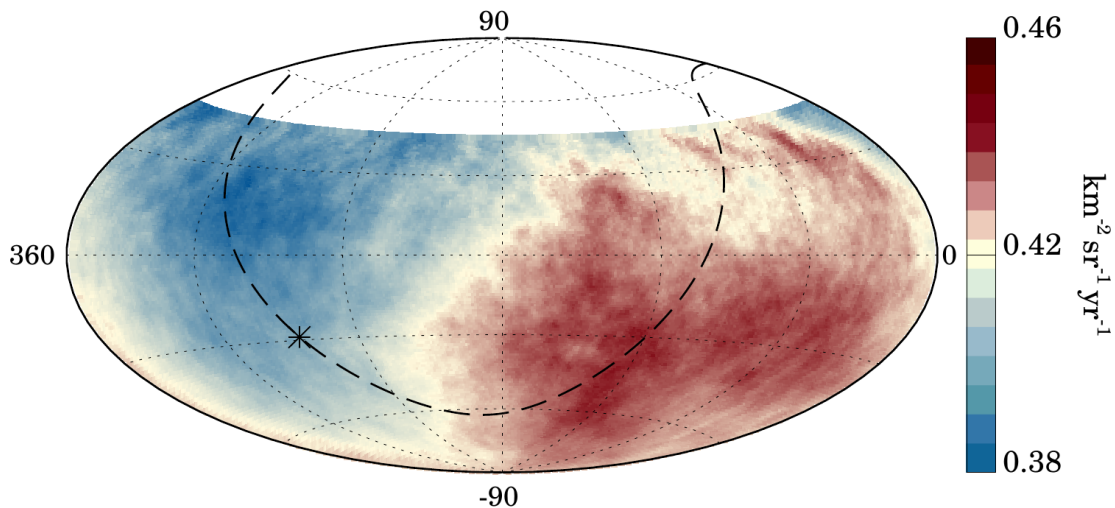
Figure 2.9: Measured particle fluxes in equatorial coordinates. A large-scale dipolar anisotropy at CR energies above 8×10^{18} eV can be observed. The Galactic plane is indicated by the black dashed line, the single black marker represents the Galactic center. Taken from Ref. [47].

2.4.3 Arrival directions

Besides the energy spectrum and mass composition, major results in the analysis of the arrival directions of UHECRs have been achieved in the recent years. With a significance above 5σ, the Pierre Auger Observatory has measured a large-scale dipolar structure with an amplitude of 6.5 % above the isotropic level for CRs with energies above 8×10^{18} eV [47]. The measured arrival directions of UHECRs are shown in Fig. 2.9 in the equatorial coordinate system. This observation strongly favors the assumption that CRs at these energies are of extra-galactic origin, due to the position of the dipole relative to the Galactic plane (black dashed line). The analysis has further been extended towards lower energies close to the ankle region to examine the expected transition region between Galactic and extra-galactic origins [48].

In parallel, correlation studies of the arrival directions with sources from gamma-ray catalogues are performed, currently favoring a correlation of UHECRs with starburst galaxies [49, 50]. Despite the fact that the theoretical description of the potential acceleration mechanisms of UHECRs in starburst galaxies [51, 52, 53] is discussed controversially, the correlation still seems to be slightly dominant compared to other source candidates. Other investigations of a correlation of the arrival direction of CRs in an on-to-off-plane comparison for the Milky Way are under investigation [54].

2.4.4 Neutral messengers

With the detection of EASs by the Pierre Auger Observatory, predictions and estimations of the arrival rates of other messenger particles besides the charged CRs can be drawn. Thereby, dedicated searches for air-shower events induced by ultra-high energy neutral particles, i.e., photons and neutrinos produced in exotic processes, are performed and upper flux limits of these particle types are obtained. The flux limits provide the opportunity to constrain acceleration processes and propagation effects, as well as open the door for the research of new physics beyond the standard model.

The determination of the arrival rates of photons with energies above 10^{18} eV, which is compatible with a hadron induced background, defines an upper limit to the flux of cosmogenic photons expected from various proposed UHECR models [55, 56]. This can be seen in the diagram in Fig. 2.10. While several top-down and super-massive particle decay
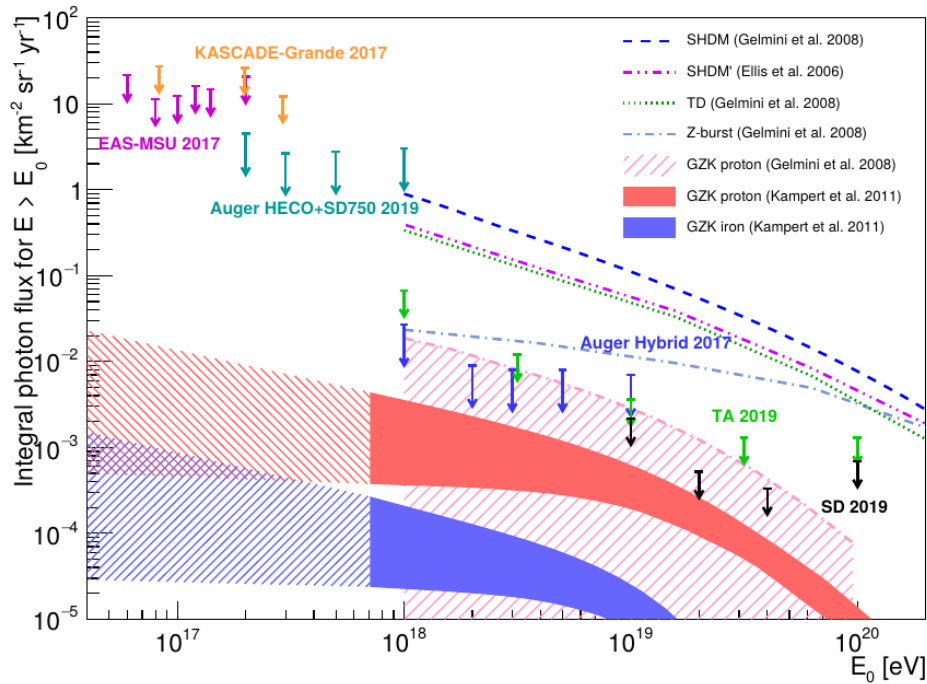
Figure 2.10: Upper flux limits of cosmogenic photons. Several top-down and super-massive decay models are ruled out by the measured data. Taken from Ref. [59].

models (dashed lines) are already ruled out by the measurement data (colored arrows), the potential flux of photons from the decay of neutral pions, which are created by the GZK effect, is limited and thereby strong constraints on the proton fraction in UHECR are obtained. In addition, with the upper photon flux limits, beyond-standard-model phenomena, e.g., Lorentz invariance violation (LIV), can be tested at the highest possible energies [57], and multi-messenger studies of photons form gravitational waves (GW) sources can be carried out [58].

Analogously to the ultra-high energy photons, the upper flux limits of the cosmogenic neutrinos as products from the GZK effect in the CR propagation constrain the expected proton content at the highest energies. With the Pierre Auger Observatory, neutrinos from point-like and transient sources which interact in the atmosphere can be examined by analyzing very inclined EAS events [60, 61]. Additionally, searches for τ-neutrino induced air showers in Earth-skimming or upwards-going shower trajectories are performed [62], enabling comparisons with recent results of the Antarctic Impulsive Transient Antenna (ANITA) experiment [63]. With the first observation of GW events from black hole and neutron star mergers, follow-up searches of high-energy neutrinos have been carried out [64, 65, 66]. The overall upper neutrino fluxes defined by the Pierre Auger Observatory are displayed by the solid and dashed red lines in Fig. 2.11.

With the upgrade of the Observatory, the discrimination of the primary particles of EASs will be significantly enhanced, offering an improved separation of hadron or photon induced events. Thereby the probing effects of physics beyond the standard model, e.g., LIV, will be possible.
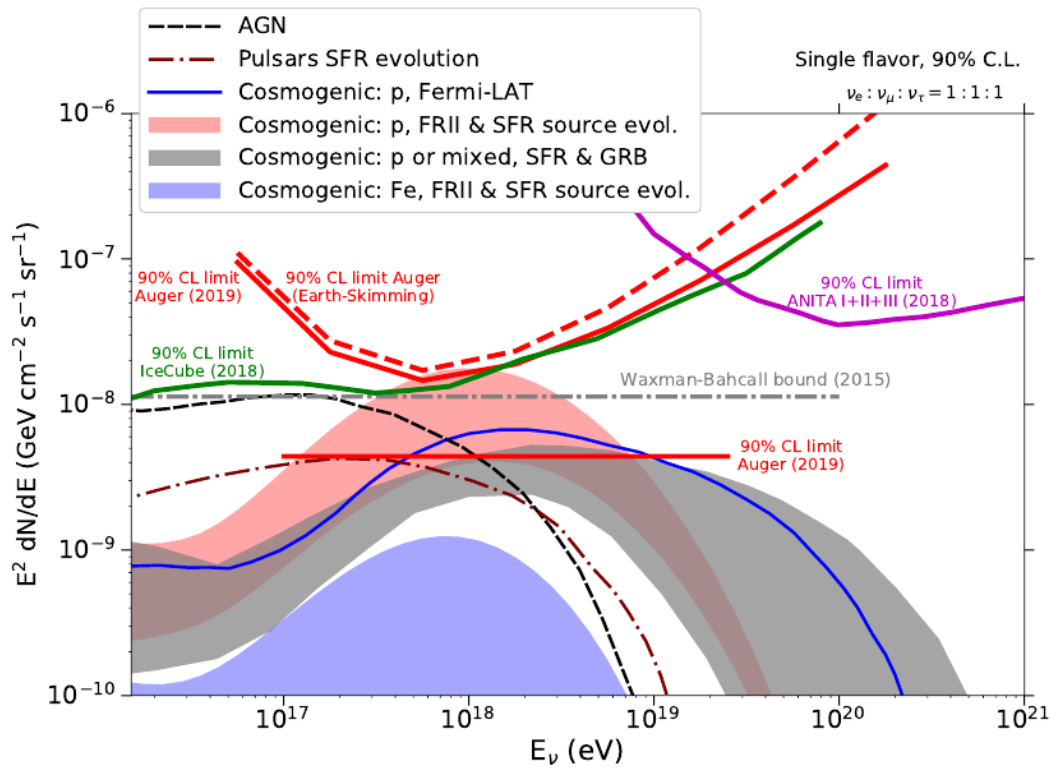
Figure 2.11: Upper flux limits of cosmogenic neutrinos observed with the Pierre Auger Observatory highlighted by the solid and dashed red lines. Taken from Ref. [59].

Chapter

3

The Pierre Auger Observatory

The discoveries and observations during the last two decades in the cosmic ray (CR) research, especially for the ultra-high energy cosmic rays (UHECRs), introduced in the previous Chapter, would not have been achieved without the Pierre Auger Observatory, which holds the status of the world's largest extensive air shower (EAS) experiment up to today. The Observatory was designed to measure CRs at the highest energies above 10^{18} eV by utilizing a hybrid detection method combining the two major detection techniques, which only have been used separately in predecessor experiments. With the observation of the air-shower development in the atmosphere using fluorescence telescopes and the determination of the shower footprint on the Earth's surface with particle sampling detectors, a precise reconstruction of the air showers can be achieved. The experiment has been designed in the late 1990s and started its prototyping and engineering phase in the early 2000s. The measurement stage "Phase I" was launched with the official start of data acquisition in January 2004 with a continuously increasing number of deployed particle detector stations until the final dimension of the Observatory was reached in 2008. Eight years later, the transition to the next measurement period has been commenced with the installation of the first prototype components of the Observatory upgrade with the fitting name "AugerPrime". The official end of "Phase I", which simultaneously marks the start of "Phase II", will take place in 2023 when the majority of particle detector stations will be equipped with upgraded electronics and additional sub-detectors, defining the next decade of UHECR research at the Pierre Auger Observatory.

Matching the two measurement stages, this Chapter is split into two major parts. The first part describes the general detector configuration of the Observatory in its current status of "Phase I". This includes the current set-up of the two main detectors, the Fluorescence Detector (FD) and the Surface Detector (SD), with enhanced focus on the latter due to the high relevance for the following chapters of this Dissertation. In addition, we present the various detector extensions, the benefits of the hybrid method, and an overview of the additional sub-detectors and facilities that have been installed in the Observatory over the last 20 years. In the second major part of this Chapter we introduce hardware changes and modifications in the context of the AugerPrime upgrade. This includes the addition of new types of detectors with different responses to entering air-shower particles, as well as upgrades of the currently deployed devices and electronics.
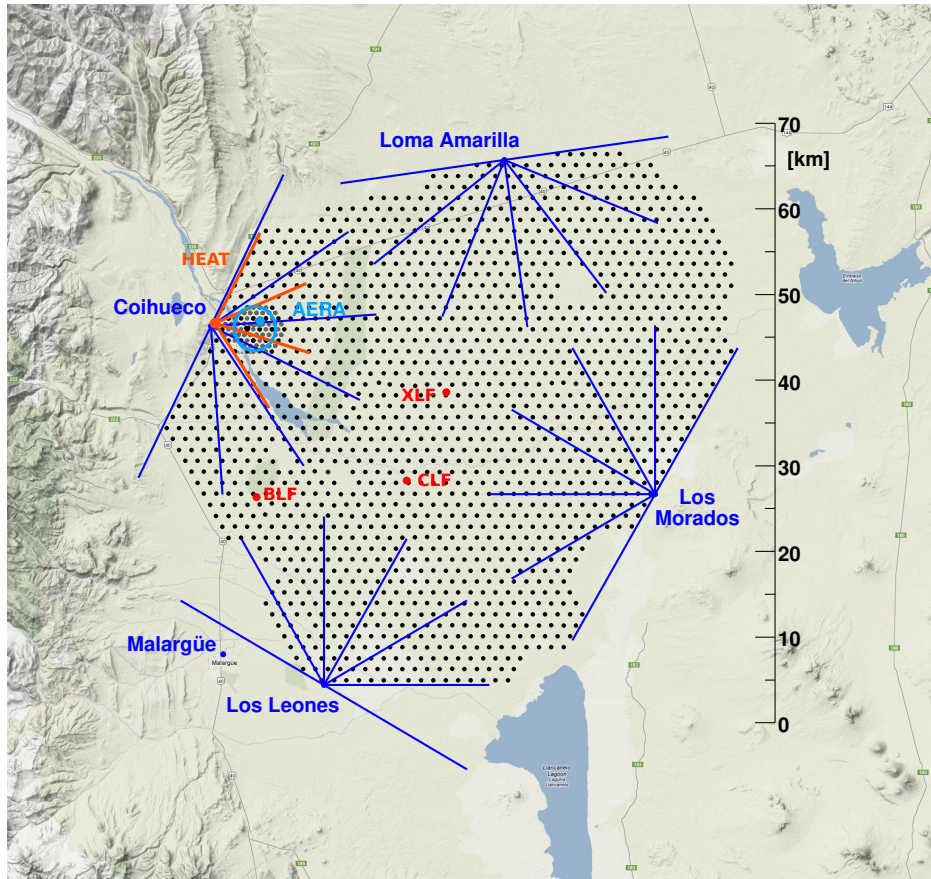
Figure 3.1: Map of the Observatory containing the major detectors and facilities. The four buildings of the FD are located at the borders the Observatory and house the 24 fluorescence telescopes with their FoVs indicated by the blue lines. The red lines display the FoVs of the three telescopes of the HEAT enhancement. The stations of the SD and their distribution in the Observatory are shown by the black dots, with each dot representing one WCD. In addition, the gray dots show the SD stations with a denser grid as part of the enhancement upgrade of the SD. Besides the two main detectors, the location of the AERA is shown by the blue circle, and the facilities for the atmospheric monitoring, i.e., the BLF, the CLF, and the XLF are displayed with red dots. Taken from Ref. [67].

3.1 Current status

The world's largest experiment for the detection of EASs initiated by UHECRs, the Pierre Auger Observatory, is located in the proximity of the city Malargüe in the province Mendoza, Argentina, east of the Andes on an extended plain with an average altitude of ~1450 m a.s.l.. Within the Observatory, extensively described in Ref. [2], the measurement of EASs is realized with two main detectors, the FD which provides 27 fluorescence telescopes located at four sites at the borders of the experiment, and the SD consisting of more than 1600 particle detector stations distributed over an enormous area of ~3000 km^2. A first overview of the detectors and facilities of the Pierre Auger Observatory is shown in Fig. 3.1. In the following sections, the configuration and set-up of these detectors are presented in detail including the extensions they received since the start of their data acquisition to enhance the sensitivity to a lower range of the CR energy spectrum. Additionally, a third detector is introduced which utilizes the third major detection technique to measure EASs, the antennas of the Auger Engineering Radio Array (AERA) detecting the radio signals produced by the propagating

air-shower particles.

The transmission of the data obtained with the main detectors is realized with a radio-frequency telecommunication system which provides two main stages. For the communication with individual SD stations, a wireless local area network is in place. Due to the limited transmission rates of ~1200 bits per second per station, the SD array is divided into multiple sectors which are then connected to one of the four communication towers, one installed at each FD site. The event data of both detectors, the FD and the SD, is transmitted with powerful microwave links from the FD sites to the Observatory campus building in Malargüe. Inside the building, the Central Data Acquisition System (CDAS) is housed which defines the main server system and heart of the Observatory. The server receives and stores the raw detector data, as well as forms the SD array trigger and sends data-readout requests to the individual detector stations. Additionally, the FD telescopes are monitored and operated from a central server room in the Observatory Campus Building [68]. Subsequently to the collection of the raw data, the files are transferred from the servers in Malargüe to the joint data center hosted at the IN2P3 Computing Center in Lyon, France, at which the event merging of the data from the different detectors is performed resulting in the production of hybrid events. In addition, a substantial database of EAS and detector simulations are available at the computing center, as described in Ref. [69].

The analysis and reconstruction of the air-shower events, and thereby the determination of the properties of the primary CR, is realized with two parallel data-analysis software frameworks. One is the software framework built on top of the data-acquisition software running on the CDAS. This framework provides an interface to read the raw data, as well as defines a signal calibration and an event-reconstruction procedure, resulting in a data production named "Herald". A second software framework called $\overline{\text{Off}}\underline{\text{line}}$ was established with the motivation to combine the raw-data readout and subsequent event reconstruction with an extendable detector-simulation framework not only for the currently installed but also for potential future detectors [70, 71]. The data production realized with the $\overline{\text{Off}}\underline{\text{line}}$ framework carries the name "Observer".

3.1.1 Fluorescence Detector

The Fluorescence Detector (FD) of the Pierre Auger Observatory provides the determination of the CR mass composition and energy spectrum by detecting the fluorescence light produced by air showers developing in the atmosphere, as introduced in Section 2.3. This is realized by precisely measuring the depths of the air-shower maxima and determining longitudinal profiles of EASs. The detector consists of 24 fluorescence telescopes which are installed in four buildings located on elevated locations at the borders of the Observatory overlooking the SD array [2]. Of the four buildings each is named uniquely, "Coihueco" (north-west), "Los Leones" (south-west), "Loma Amarilla" (north-east), and "Los Morados" (south-east), and houses six telescopes in a climate controlled and clean environment. The buildings are constructed with semicircular ground areas resulting in a total horizontal field of view (FoV) of 180° for one building, i.e., 30° for each telescope, as can be seen by the radial blue lines in Fig. 3.1. The vertical FoV of each telescope ranges from 1.5° above the horizon up to ~32° in the elevation and is limited by the altitude of the building and the aperture system of the telescopes. In Fig. 3.2 the left image shows as an example the FD building Los Leones with its six open telescope bays.

Each fluorescence telescope is constructed by following a standard design displayed in the schematic on the right in Fig. 3.2. The opening towards the outside is realized with a filter window to limit the wavelength range of the entering photons, as well as an aperture system based on Schmidt optics to reduce undesirable coma aberration effects. In addition, several protection mechanisms, e.g., a general shutter system, are in place to protect the
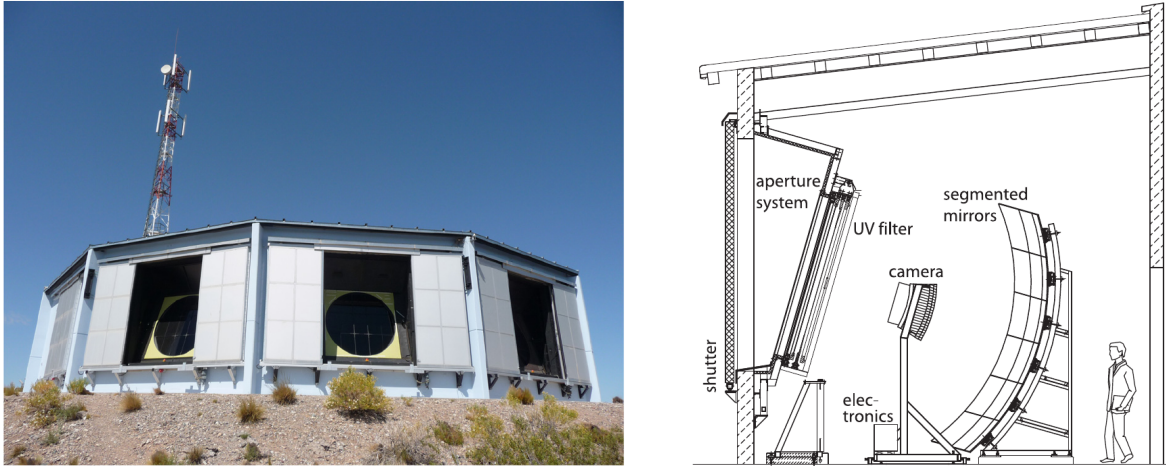
Figure 3.2: *Left:* FD telescope building "Los Leones" with six open telescope bays. *Right:* Schematic of a fluorescence telescope including the main components, the aperture system, the segmented mirror, and the camera. Both images are taken from Ref. [2].

sensitive hardware from sun and moon light, and the whole telescope from weather and climate effects. The focusing of the faint fluorescence light is accomplished with a spherical segmented mirror with a surface dimension of 3.8 m × 3.8 m. The measurement of the light from air showers is realized with a camera unit consisting of 440 hexagonal head-on Photonis XP3062 photomultiplier tubes (PMTs) providing a segmented image of the propagating air shower with an individual pixel size of 1.5° × 1.5°. Each camera unit is produced of a single aluminum block and contains the PMTs arranged in 22 rows and 20 columns.

Due to the design for measuring EASs at the highest energies, the detection sensitivity of the FD telescopes is significantly reduced below CR energies 10^{18} eV. To enhance the sensitivity to lower energies at which the transition between Galactic and extra-galactic CRs is expected, an upgrade was proposed a few years after the start of the official data acquisition [72]. Until 2009 the construction of three addition fluorescence telescopes in the proximity of the original Coihueco building was finished forming the High Elevation Auger Telescopes (HEAT) enhancement [73], highlighted by the three red lines in Fig. 3.1. These telescopes follow an analogous design compared to the standard FD telescopes, with the identical types of mirrors and 440 PMTs inside the camera. Nevertheless, each telescope is installed in a separate small housing which can be mechanically tilted. With this mechanism the vertical FoV can be shifted towards an angle range of 30° to ~60°. In the elevated position, as displayed in Fig. 3.3, the telescopes are able to detect EASs of primary particles with lower energies that develop at a higher altitude in the Earth's atmosphere and would not be detectable with the original FD telescopes. In the downwards position, the observed sky is nearly identical to the FoV of the standard telescopes at Coihueco, thus the possibility of a cross calibration between the telescopes is given. Due to the elevated FoV, the HEAT telescopes are able to observe a significantly increased number of inclined air showers with a shower core pointing directly into the telescopes. For these candidate events, the telescopes are able to measure the non-negligible Cherenkov radiation produced by the air-shower particles.

Before each measurement run of the FD telescopes, a relative calibration procedure is performed by using light-emitting diodes (LEDs), installed at the camera and at the mirror, as stable light sources. With the relative calibration, a functionality check of the telescope hardware is achieved and the long-term behavior of the components is monitored. For the absolute calibration of the telescopes, two different techniques are used. In the original

Figure 3.3: The three telescopes of the HEAT enhancement in upwards position and closed telescope shutters. Taken from Ref. [73].

method, a drum shaped light source with an integrated pulsed LED provides an end-to-end calibration of each pixel of the camera. In the recent years a new absolute calibration method has been developed to replace the original drum calibration. In the new procedure, the so-called "XY-Scanner" is used which provides a small movable light source installed on a grid system to significantly simplifying the handling and operation during the calibration process. A description of the new calibration procedure and results of the first measurement campaigns are shown in Ref. [74].

For the detection and measurement of EASs, a single telescope of a single building of the FD is sufficient. But in the case of an inclined air-shower, i.e., an air shower with a large zenith angle, the light can enter the FoVs of two or more telescopes of the same building, depending on the geometry of the air shower. With the intensity and timing information of all the participating cameras, a plane spanned by the actual air-shower core and the position of the triggered FD building can be reconstructed. This plane is called "shower-detector plane" and constrains the geometry of the air shower, but the pointing within the plane cannot be precisely determined. The majority of observations of air showers with one or more telescopes of the same FD building define the so-called FD "mono events". If the air shower appears at a location close to the center of two or more FD buildings and has a sufficiently high energy, then the air shower can be measured by more than one telescope of different buildings, creating a "stereo event". In these events the air-shower axis can be reconstructed as the line of intersection of the two individual shower-detector planes, but the rate of such events is significantly lower compared to the mono event rate. Generally, the determination of the air-shower geometry can be improved by using the timing information of the SD stations, explained in more detail in Section 3.1.4.

3.1.2 Surface Detector

Detector configuration

The impressive number of more than 1600 independently operating and self-sufficient particle detector stations form the Surface Detector (SD) of the Pierre Auger Observatory [2]. The stations are regularly distributed over a total area of ~3000 km^2 in a triangular grid and provide a standard spacing of 1.5 km between each neighboring station, as shown by the black dots in Fig. 3.1, each marker representing one SD station. An image of a single SD
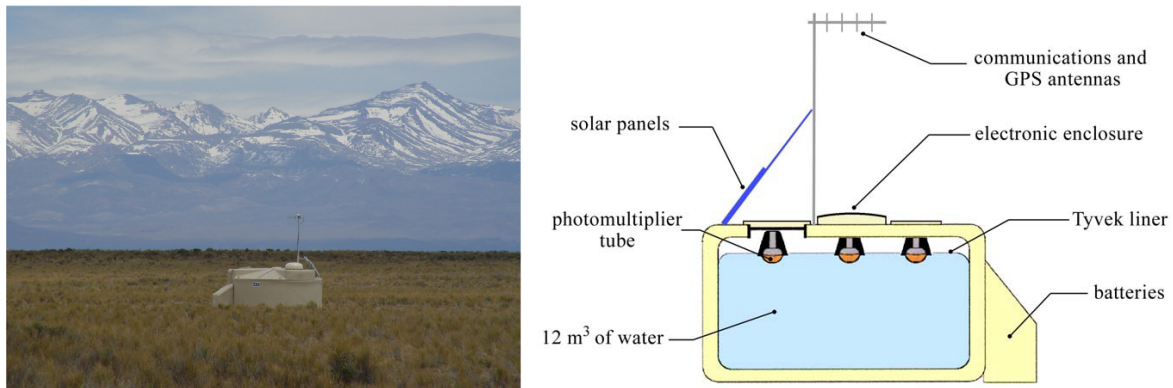
Figure 3.4: *Left:* One of the more than 1600 autonomously operating SD stations of the Pierre Auger Observatory in front of the Andes. Taken from Ref. [2]. *Right:* Schematic of a SD station highlighting the main components: three PMTs detect Cherenkov light produced in $12\,m^3$ pure water which is stored inside a reflective Tyvek liner. The electronics is located on the top of the station and is powered by a solar panel and a battery system. For the data transmission and timing coordination, each station is equipped with communication and GPS devices. Schematic adapted from Ref. [75].

station from the measurement stage Phase I is presented in Fig. 3.4 on the left. To separate the original spacing of the SD stations from the later added enhancement configurations, the standard array configuration is referred to as the "SD-1500 array" in the following sections and chapters. In addition to the single station at each grid position, at certain positions one or more accompanying stations are placed very nearby, i.e., in a distance of only a few tens of meters, resulting in the so-called station multiplets. With these multiplets, measurements of air-shower signal fluctuations and timing resolutions of the station electronics can be realized.

The stations of the SD of the Pierre Auger Observatory detect the air-shower particles arriving at the ground measuring the Cherenkov radiation produced in a dense medium as introduced in Section 2.3. With the so-called water-Cherenkov detectors (WCDs), the light produced by the charged particles propagating through a defined volume of ultra-high purity water is measured, and thereby the total air-shower signal at a certain distance to the core of the air shower is obtained. Finally, when combining the signals of multiple SD stations, the air-shower footprint, i.e., the lateral distribution, can be determined.

The set-up of an SD station follows a robust design with the WCD as the major component. This detector consists of a cylindrical polyethylene tank with a diameter of ~3.6 m. Inside this tank, a sealed Tyvek liner is placed and filled with $12\,m^3$ ultra-high-purity water resulting in a water depth of ~1.2 m. Additionally, the Tyvek liner provides a diffusively reflective inner surface to increase the number of photons detected by the photon-sensitive devices. The measurement of the Cherenkov photons is realized with three Photonis XP1805 head-on PMTs which provide high sensitivity due to a large surface of the photocathode. With a diameter of 9 inch, they are named large photomultiplier tubes (LPMTs). The LPMTs are mounted on the upper side of the detector, facing downwards and looking through transparent windows of the liner. The devices are positioned in a triangle around center of the detector with an identical geographical orientation inside all WCDs to reduce asymmetry effects in the signal calculation depending on the arrival directions of the air showers. The readout of the signals of the LPMTs is realized with the station electronics board installed inside an enclosure on top of the station. The properties of the station electronics, the so-called Unified Board (UB), are described in the electronics comparisons in Section 5.1.1. To power the SD station, a solar panel and a battery system are installed on the outside of the SD station. Moreover, each station
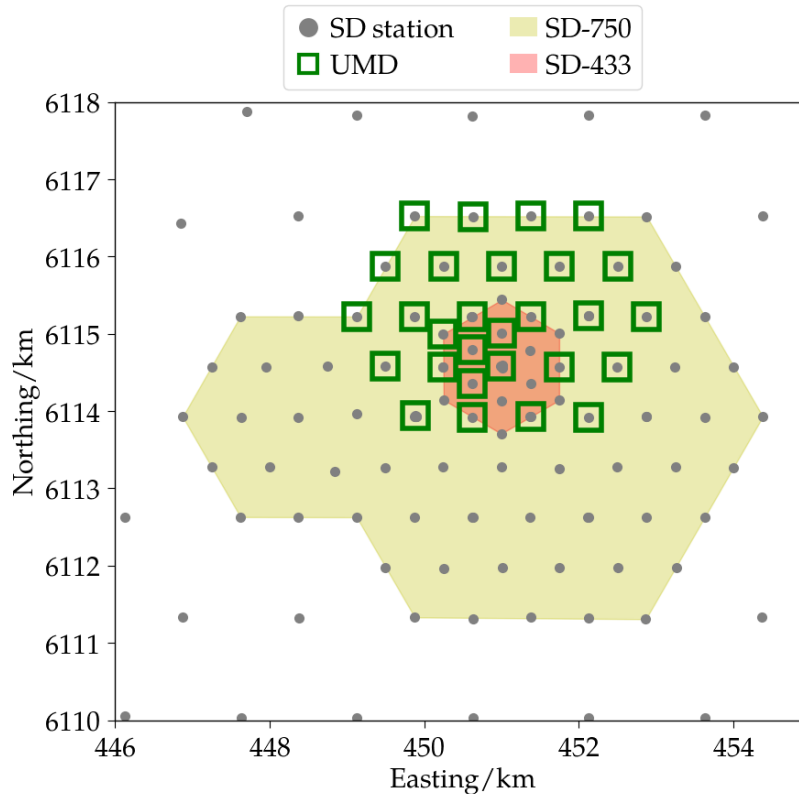
Figure 3.5: Overview map of the SD region with denser grid extensions, the area of the SD-750 array indicated by the yellow background, the SD-433 area by the red background. The green squares display the positions of the already deployed UMD modules (May 2022).

is equipped with a Global Positioning System (GPS) device to receive the necessary timing information. The communication with the CDAS is provided by an additional transceiver utilizing the wireless local area network connection.

Similarly to the telescopes of the FD, the SD array is designed to measure EAS from CRs with the highest energies. For this reason, the detector reaches the full detection efficiency at energies above 3×10^{18} eV. Below this energy threshold, the efficiency falls off with decreasing CR energies. To enhance the sensitivity to lower energies, an extension of the SD as part of the Auger Muon Detectors for the Infill Ground Array (AMIGA) enhancement has been designed accompanying the HEAT enhancement of the FD [72, 76]. This was realized starting in 2008 by deploying 61 additional WCDs in a higher dense grid in the north-west of the Observatory in the FoV of the HEAT telescopes. Each additional station was placed in the center between the original stations leading to a new spacing of 750 m and creating a total area of this configuration of 23.5 km^2. These stations can be seen in Fig. 3.1 by the gray dots between the black dots of the SD-1500 stations. Analogously to the naming of the standard SD configuration, the enhancement is named the "SD-750 array", also internally referred to as "Infill". First results of the SD-750 array performance shortly before and after its completion in 2012 are given in Ref. [77, 78]. In addition to the SD-750 array, another extension of 19 stations with an even smaller spacing of 433 m has been added to the SD, reducing the detectable CR energy even further. The general performance of this station grid, named the "SD-433 array" or internally "AERAlet", is described in Ref. [79]. The areas of both enhancements are shown in the map in Fig. 3.5 by the colored backgrounds, yellow for the SD-750 and red for the SD-433.
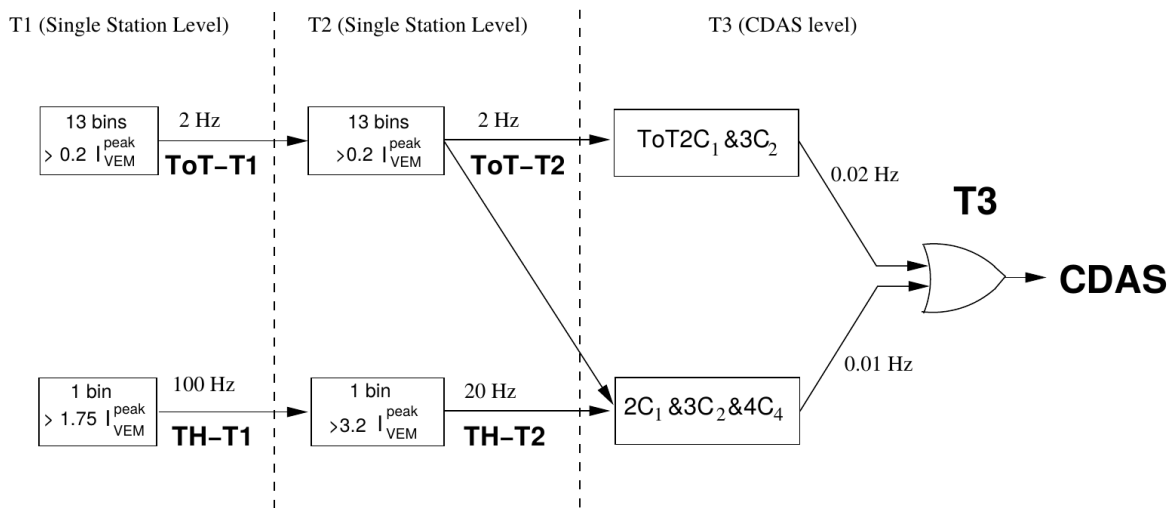
Figure 3.6: Hierarchical system of the SD station trigger. The first two trigger levels T1 and T2 are performed by the individual station electronics. Both levels are composed of two different modes of triggers which are designed to be more sensitive towards different EAS components. With the threshold trigger (TH), a single-bin condition, the station is sensitive to the muonic component of the EAS. And the signals dominated by the electromagnetic particles can be detected with a trigger that assumes a signal above a threshold over a sliding time window (ToT). After the trigger level T2, the rates for candidate events on a single station level is reduced to 20 Hz and ~2 Hz for TH and ToT, respectively. Subsequently to the T2 stage, the array trigger T3 is formed utilizing the time stamps and the T2 trigger types of all participating stations. Two different types of T3 triggers can be created which require different spatial conditions. The T3 events are then sent to subsequent trigger stages. Taken from Ref. [80].

Trigger system

The measured signals of EAS particles arriving at the ground can strongly vary in their detection rate and pulse shape, depending on the distance of the station to the core of the air shower and depending on the amounts of the different types of air-shower particles. Thereby, the majority of signals are created by atmospheric muons arriving at the SD stations with a rate of ~3 kHz and defining the main background for the detection of EASs of UHECRs [80]. Due to the limitation of the station electronics and for the discrimination of the background signals from the "physics" events, the event trigger system of the SD follows a hierarchical structure and can generally be separated into two major parts. A first stage is performed on the level of an individual SD station implemented in the firmware and software of the electronics boards. The second trigger stage is processed in the CDAS, defining the actual air-shower trigger of the SD array utilizing the spatial and temporal information provided by detectors from the previous trigger stage.

As can be seen on the left side in the schematic of the trigger system in Fig. 3.6, the trigger stage of a single SD station, i.e., the local-station trigger, can be divided into two sub-stages, a first trigger level called "T1" and a second trigger level named "T2", which both share an identical structure. For both levels, two different modes of triggers are implemented which are designed to be more sensitive towards different EAS components:

- A threshold trigger mode (TH) with a simple single-bin condition is implemented to detect the muonic EAS component, especially from inclined events and from air showers arriving close to the station.
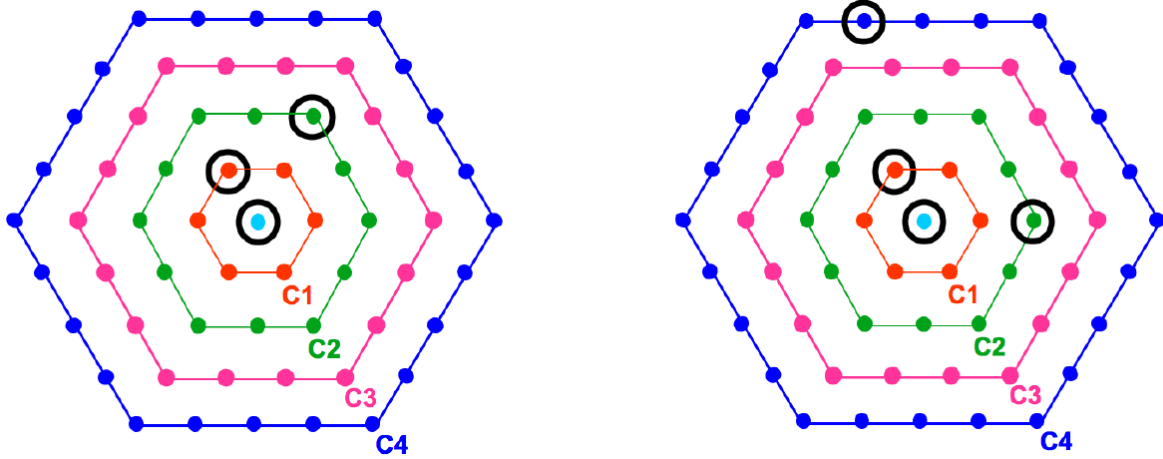
Figure 3.7: Schematic of the two T3 trigger modes of the SD. *Left:* 3-fold T3 condition of at least three ToT-T2 called "ToT $2C_1$ & $3C_2$" with the largest efficiency for vertical events i.e., air showers with zenith angles $\theta < 60°$. *Right:* 4-fold T3 condition of at least four T2 of any type named "$2C_1$ & $3C_2$ & $4C_4$" with an extended geometry for inclined air showers which create large footprints on the ground. Taken from Ref. [80].

- Complementary, a trigger with a time-over-threshold (ToT) condition determines signals for air showers from higher energy CRs that arrive farther away from the station and also from signals dominated by the electromagnetic particles from low-energy CRs with their air-shower core close to the station. This is realized with a sliding time widow requiring the signal to be above a threshold for a certain number of time bins of the window. Thereby, small signals which appear spread in time can be measured.

In case of the first trigger level (TH-T1), the single-bin threshold is applied to reach a trigger rate of 100 Hz in a 3-fold LPMT coincidence with each device surpassing the threshold of $1.75\,I_{VEM}$. To reach this state, the threshold factor I_{VEM} is obtained in an single device calibration procedure which is shortly explained in Section 6.1.2. The time-over-threshold condition of the first trigger level (ToT-T1) is realized by checking if at least two of the three LPMTs provides a signal above $0.2\,I_{VEM}$ for at least 13 time bins in a window of 120. This results in a trigger rate of ~2 Hz.

For the next level of the local-station trigger, the thresholds of the single bin trigger are increased. Thereby the respective trigger rates are decreased, and finally reach the required values for the data transmission. For the single bin trigger (TH-T2) signals from the first level are selected that surpass the increased threshold of $3.2\,I_{VEM}$ in a 3-fold LPMT coincidence resulting in a trigger rate of 20 Hz. In contrast, the thresholds for the time-over-threshold trigger (ToT-T2) are not increased, but all ToT-T1 are passed to the next level as ToT-T2.

Due to their design for the discrimination of background signals from single muons, the original trigger modes show an insensitivity towards signals smaller than the average muon signal, for example for signals of electromagnetic particles. For this reason, two new modes of triggers have been proposed in the late 2000s and have been implemented in the local-station software until 2013, shortly introduced in Ref. [40] and internally in Ref. [81, 82, 83, 84]. One of the new trigger modes is named time-over-threshold deconvolved (ToTd) and is designed to filter background signals from the characteristic exponential decay of the Cherenkov light before the ToT condition is applied. The other addition is the so-called multiplicity-of-positive-steps (MoPS) trigger which is able to detect small but long signals by counting the number of subsequent trace bins with an increasing amplitude inside a sliding time window.

After the local station detected a T2 trigger, the time stamp and the trigger type, i.e., the mode that formed the trigger, are sent to the CDAS for the potential formation of an array trigger T3. This trigger uses the timing and relative location information of multiple stations to create a candidate trigger for an air-shower event. Thereby, two different types of T3 triggers can be created which require different spatial conditions, as displayed in Fig. 3.6 on the right side:

- If at least three local ToT triggers arrive at the CDAS from stations that fulfill a certain position and timing condition, the 3-fold mode "ToT $2C_1$ & $3C_2$" is built. This condition requires at least two stations with valid ToT-T2s in the first crown of stations around a chosen station (C_1) and at least three stations with valid ToT-T2s in the crown (C_2), as highlighted by the left schematic in Fig. 3.7. This mode contains a large number of the desirable physics events due to the low contamination with background events and provides the largest efficiency for vertical air showers, i.e., with zenith angles $\theta < 60°$. Its trigger rate is of ~0.02 Hz or ~1700 events per day.

- The second T3 trigger mode is built by a 4-fold condition using any arriving T2 trigger type, represented by "$2C_1$ & $3C_2$ & $4C_4$". In the right schematic in Fig. 3.7 a candidate of this spatial condition is displayed. Therein, the minimum requirement is two T2 triggered station in the first crown, three stations in the second crown, and four stations in the fourth crown. Due to the extended geometry condition, the 4-fold T3 is designed to detect inclined air showers with $\theta > 60°$ that create footprints with large dimensions on the ground. The rate of this T3 trigger mode is ~0.01 Hz or ~850 events per day.

When a T3 trigger is created, the readout of the signal buffers of all the involved stations with a local T2 trigger is requested. In addition, the stations with a T1 trigger within 30 μs of the T3 are also required to send their buffered data. Furthermore, calibration information from each participating station is sent together with the trigger and trace information and is merged into the raw event data stored at the CDAS. While the T2 information, which is also separately stored in additional files, always holds the highest priority in the data-transmission process to provide a building of a T3 trigger at all times, the additional calibration and monitoring data is prioritized at a lower level.

After the T3 trigger events are stored in the SD raw data files, two subsequent event selection procedures are applied to distinguish vertical EAS events from the still remaining random coincidence triggers. This is realized with the T4 trigger level defining the "physics trigger", and the "fiducial trigger" called T5, both presented in the schematic in Fig. 3.8. Thereby, the T4 trigger uses two criteria to select physics events from the T3 trigger pool:

- For the 3-fold T3 events, the condition of a formation of an isosceles or even equilateral triangle by the three non-aligned neighboring stations each with a ToT-T2 trigger is examined. Additionally, the timing of all stations has to match the propagation of a planar air-shower front. This T4 trigger is then called "3ToT" and provides the majority of high quality events with zenith angles $\theta < 60°$.

- The second criteria, named "4C1" is built on the 4-fold T3 events containing any type of T2 triggers and requiring four neighboring stations matching the planar air-shower front propagation.

Additionally, the so-called "seed" is defined by the three non-aligned neighboring stations with the highest signals forming a triangle. The air-shower front fit is then performed on these three stations, while the timing of the other participating stations is compared to the determined air-shower front. Stations that do not show a matching timing to the air-shower front which propagates with the speed of light, are rejected.
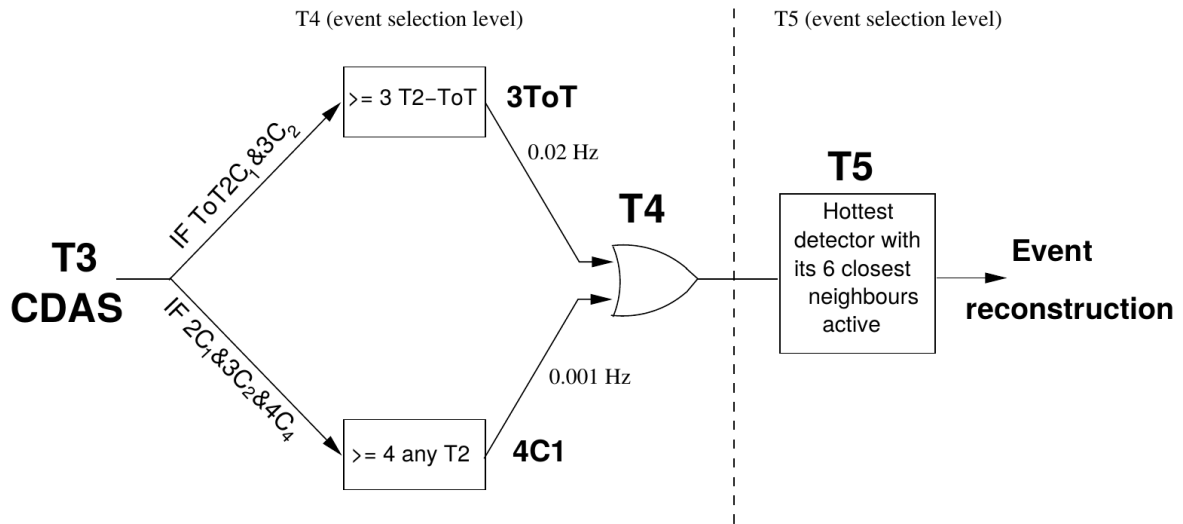
Figure 3.8: Schematic of the physics trigger (T4) and fiducial trigger (T5) system. The T4 trigger level is realized with two criteria to select physics events from the T3 trigger pool. If three ToT-T2 stations form a triangle and match the propagation of a planar air-shower front, a 3ToT event is formed, resulting in the majority of high-quality events. In addition, a 4C1 condition is built on a 4-fold of any type of T2 events. The ultimate trigger stage T5 then examines if the air shower is contained inside the SD array and further quality standards are applied. Takenfrom Ref. [80].

Finally, after the selection of physics events, the last quality check is applied defining the highest trigger level T5. This trigger examines if the air shower is contained inside the SD array. If an air shower reaches the ground too close to the border of the array or if there are malfunctioning stations inside the array, parts of the air shower cannot be detected. This results in an incorrect reconstruction of the air-shower core impact position and arrival direction, and therefore in an incorrect determination of the CR energy. The highest criteria that can be applied prior to the reconstruction of an event is the "6T5" condition which requires six working stations in a hexagon surrounding the "hottest" station of the event, i.e., the station with the largest signal. In addition, a posteriori condition is implemented that checks if the already reconstructed core impact position falls inside an active triangle and if at least four stations are active around the hottest station. For certain analyses, the number of reconstructed events can be increased by relaxing the quality condition to the requirement of 5 or even 4 working surrounding stations.

Calibration and event reconstruction

Besides the trigger system for the event discrimination, the local-station software contains a special trigger condition for the acquisition of additional calibration information shortly described in Section 6.1.3. Due to the fact that each LPMT inside the WCDs has a different response to the same EAS, a calibration process is needed which is performed for each device individually. To compare signals of different WCDs, the values obtained in the integration of the PMT trace pulses in their raw ADC units have to be converted into an unified average reference unit, equivalent to the most probable signal of a vertical central through-going muon, named vertical-equivalent muon (VEM). This unit is related to the deposited energy of a muon passing vertically through the center of the WCD and is comparable to an amount of ∼240 MeV. Generally, an online calibration procedure is implemented on the local-station electronics, as well as an offline calibration algorithm is in place to provide the necessary calibration quantities. Both procedures are introduced and extensively analyzed in Chapter 6.

Subsequently to the calibration process of individual devices, the calculation of the calibrated signals is introduced in the same Chapter. Further on, in the description of the general event reconstruction utilizing the stations of the SD in Chapter 7, the chain of reconstruction processes from the determination of the individual device signals to the final estimation of the energy of the primary particle is presented.

3.1.3   Additional detectors and facilities

Besides the two main detectors for the measurement of the particles produced by the CRs interacting with the Earth's atmosphere, a third type of a detector is installed in the Observatory. With a radio-detector array, the so-called Auger Engineering Radio Array (AERA), a complementary determination of the electromagnetic component of EASs is provided [2]. By detecting the coherent radio emission of EASs arriving at the ground, a third information channel parallel to the fluorescence light and the particle sampling on the ground is in place. The AERA consists of radio antennas distributed with a varying spacing over a total area of $17\,km^2$ in the north of the SD-750 array, as indicated by the blue circle in Fig. 3.1. With the antennas of the AERA, the feasibility of the detection of radio signals in a frequency range from 30 to 80 MHz from EASs on a large scale is tested to develop a competitive detection method for the use in future ground-based UHECR observatories. After the proposal of the design of the new radio-antenna array in the late 2000s, the first 21 antennas have been installed in 2010 providing a first measurement of the EAS radio signals [85]. While for the first antennas the logarithmic periodic dipole antenna (LPDA) type has been chosen, the subsequent deployment of additional antennas was realized with "butterfly antennas", also named "active bowtie antennas", providing an improved noise performance and transient response [86]. In Fig. 3.9, a photo of an LPDA in the AERA is shown. The final configuration of the AERA with 150 antennas has been reached in 2015 and provides two trigger modes [87]. Approximately the half of the antennas utilizes the T1 trigger of the SD as external trigger signal to significantly reduce the selection of noise pulses. The remaining other half is equipped with electronics to internally trigger on radio signals. Due to the measurement of the radio signals majorly produced by the electromagnetic component of the air showers, the antennas of the AERA can be used to obtain an energy estimate of the primary CRs and are suited for a cross calibration with the other detectors of the Observatory.

All detectors of the Pierre Auger Observatory are designed and optimized to measure the signals of EASs under optimal climate and weather conditions utilizing the atmosphere as a calorimeter. Therefore, a precise monitoring of the environmental conditions is necessary to analyze their influences and correct for the effects on the measured signals [2]. This is realized with various devices installed all over the Observatory to monitor the current weather and atmospheric conditions. While ground-based weather stations are installed on top of the telescope buildings to measure the temperature, the pressure, the humidity, and the wind velocity, a Balloon Launching Facility (BLF) was used in the early years of the data acquisition to obtain the atmospheric profiles up to altitudes of 20 or 25 km. The monitoring of the aerosol concentration and the cloud movements above the Observatory is realized with two main laser stations, the Central Laser Facility (CLF) and the Extreme Laser Facility (XLF), both installed inside the SD array. In addition, each FD site is equipped with a Light Detecting And Ranging (LIDAR) station and an infrared cloud camera to determine the current atmospheric condition above each building. These are complemented with additional devices utilizing stars as reference light sources to monitor the atmosphere, e.g., the F/Photometric Robotic Atmospheric Monitor (FRAM) telescope [88]. Furthermore, several star- and background-light cameras, as well as lightning sensors are placed in the Observatory to assure a safe measurement time, especially for the FD telescopes.

Figure 3.9: Photo of a ratio antenna of the type LPDA installed in the AERA. The antenna, receiver, and electronics are powered by a solar panel. Taken from Ref. [86].

3.1.4 Hybrid detection

Although the two main detectors of the Observatory, as well as the antennas of the AERA, are able to serve as individual EAS experiments with distinct air-shower triggers and reconstruction procedures, only the hybrid detection design offers the possibility to recover the weaknesses of these techniques with the advantages of the respective others [2]. When comparing the three detectors, the telescopes of the FD provide the most sensitive determination of the mass composition and energy distribution of the arriving CRs due to the precise measurement of the depth of the air-shower maximum and the longitudinal air-shower profile. But due to the strong dependence on weather conditions and the ambient light, the telescopes can only measure in clear and moonless nights which reduces the duty cycle of the FD to around 10 to 15 % of the total time. This results in a strongly limited detection rate of CR events above $10^{19.5}$ eV where the flux of CRs is suppressed. In contrast, the SD can measure independently of the daytime and local weather condition and reaches nearly ~100 % of the measurement up-time resulting in a significantly higher probability to measure EASs created by UHECRs. Similarly to the SD stations, the radio antennas of the AERA run autonomously over the total time, only depending on the up-time of the SD which provides the trigger of the EAS events.

Besides the overall measurement time difference, the majority of FD events are detected with one or more telescopes of the same building defining the FD mono events, as introduced in Section 3.1.1. In these events, the shower-detector plane, i.e., the plane spanned by the actual air-shower core and the telescope building, can be determined, represented by the projection of the air shower evolving in the telescope camera. But with only the timing information of the individual camera pixels the actual incoming angle of the primary CRs cannot be constrained enough. This issue can be overcome by using the additional timing information of a single SD station in the FoV of the respective FD building. When an FD telescope detects an EAS event, a readout request is sent by the CDAS to the SD stations to search for candidate stations providing a T1 trigger for the time stamp of the event. If a matching SD station is found, the timing information of this station is added in the time-evolution fit of the air shower. This results in the reduction of the two-dimensional shower-detector plane to the one-dimensional

air-shower axis and defines these events as so-called "hybrid events". For EAS events seen by the FD with sufficiently large energies that multiple SD stations are triggered, an additional reconstruction with the SD is possible. These events, which can be successfully reconstructed by both main detectors of the Observatory, are called "golden hybrid events" and represent the events with highest quality criterion in the merged data.

While the telescopes of the FD are limited by their measurement up-time, the SD is able to detect EASs at any time, mainly outside the measurement time of the FD. Therefore, EASs from UHECR measured and reconstructed only with the stations of the SD define the majority of the events detected by the Pierre Auger Observatory. With the precise timing information of the SD stations, the air-shower geometry, including the shower axis and the shower core impact position at the ground, can be reconstructed. But the calorimetric energy and mass composition of the primary CRs are not directly accessible, due to the fact that the SD stations sample only a fraction of the total number of secondary particles reaching the ground. With the determination of the lateral air-shower distribution, a general estimator of the signal depending on the distance to the air-shower core is obtained. By utilizing the data set of golden hybrid events, the signal estimator can be allocated to the energies measured with the FD, and thereby an energy scale for all signals detected with the SD stations is obtained [3]. Similarly, an energy cross-calibration between the SD and the antennas of the AERA has been achieved to validate the determination of the CR energy measuring the coherent radio emission [87].

With the addition of new detectors and sub-detectors, the hybrid detection of EASs has been in the recent years extended to a multi-hybrid measurement and will be even further enhanced by the various components of the AugerPrime upgrade introduced in the following Section.

3.2   AugerPrime upgrade

In the 18 years of data acquisition, the Pierre Auger Observatory has been extensively contributing to the research field of UHECRs leading to numerous breakthrough discoveries and confirmations of the properties of the CRs with the highest energies [89, 5]. With the goal to determine the major characteristics of UHECRs, e.g., their energy spectrum, mass composition, and arrival directions, presented in Section 2.4, significant progress in understanding of the nature of these exceptional messengers has been achieved. Nevertheless, the remaining open questions regarding the origin of the UHECRs and the examination of their acceleration processes require further and more precise studies of EAS events created by ultra-high energy primaries.

Especially the determination of the mass composition of UHECRs plays a key role to distinguish and constrain the various proposed acceleration and source models, as well as the effects of the particle propagation. Since recent observations with the FD depict an indication towards heavier CRs within the available energy range, the mass composition at the highest energies remains unknown due to the limited event statistics of the fluorescence telescopes. At energies above $10^{19.5}$ eV, only the SD stations provide a sufficient EAS detection rate to determine the properties of the primary particles. However, with the current WCDs, the determination of the UHECR masses measuring the muon content of the air shower is strongly limited and suffers large uncertainties.

For this reason, a major upgrade of the individual SD stations has been proposed in 2015 providing a complementary measurement of the air-shower components to the results obtained with the original WCDs, further extending the hybrid detection strategy of the Observatory. With the measurement of air showers with multiple detectors varying in their responses towards electromagnetic and muonic particles, a determination of the CR mass on a shower-by-shower basis becomes possible. This enhancement of the composition sensitivity

of the SD in the energy region of the flux suppression defines the main goal of the so-called "AugerPrime" upgrade. Especially, the estimation of the proton fraction at CR energies above $10^{19.5}$ eV is of high importance for a future introduction of a CR astronomy and the estimation of the general physics potential of current and future CR, gamma-ray, and neutrino detectors. Additionally, the improved mass determination enables studies of composition-dependent anisotropies in the arrival directions of UHECRs.

Besides the mass sensitivity, the AugerPrime upgrade addresses the examination of the muon deficit observed in the air-shower simulations when compared to measurement of EAS signals by the detectors of the Observatory. These simulations utilize the latest Large Hadron Collider (LHC)-tuned hadronic interaction models which require to be further adapted to match the measurements including the search for new physics and exceptional effects, such as Lorentz invariance violation or extra dimensions.

During the design phase of the AugerPrime upgrade, various detector and sub-detectors have been proposed and tested to be installed at the position of each WCD. One candidate design was the Layered Surface Detector (LSD) which can be realized by modifying the WCDs of the SD [90]. For these detectors, the water volume inside the WCDs is divided into two differently deep layers by spanning a reflective sheet inside the water tank. The two layers of the WCD are sensitive to the different air-shower components, the top layer detects the electromagnetic and muonic particles, while the bottom layer measures only the muonic component of the EAS.

In contrast to the LSD, the other proposals for the AugerPrime upgrade included the addition of new types of detectors instead of modifying the original WCDs. Thereby, the position of the additional detectors varied among the candidate proposals. For instance with the Muon Array with RPC for Tagging Air showers (MARTA) detectors, a direct measurement of the muon content in air showers is aimed [91]. The detector is based on resistive plate chambers (RPCs) placed inside a concrete structure underneath each WCD. The WCD provides a shielding of the electromagnetic particles due to the absorption effects and the purely muonic air-shower component can be measured with the RPCs.

Other proposals defined the goal to equip each SD station with plastic scintillation detectors, either on top of the WCD or under a few meters of soil next to the station. While the underground scintillation detectors directly measure the muon content due to the soil shielding against the electromagnetic particles, the scintillators on top of the WCDs provide complementary measurements of both main components of the air showers leading to a composition-sensitive determination of the lateral particle distributions which differ for electromagnetic and muonic particles.

Despite the fact that the LSD, the MARTA detectors, or the underground scintillators are providing a direct access to the muonic air-shower component, the technical realization, cost efficiency, and the interference with the continuous data acquisition disfavored these candidates, resulting in the selection of a plastic scintillation detector on top of each WCD as a main AugerPrime upgrade component. As the baseline design for the new sub-detectors of the SD stations the so-called Surface Scintillator Detectors (SSDs) have been chosen. With the selection of scintillation detectors, installed on each SD station with the standard spacing of 1.5 km, a similar detector design than the SD of the Telescope Array (TA) experiment is realized, enabling more detailed comparisons between the detection methods and reconstruction strategies of both observatories.

With the AugerPrime upgrade, the start of the measurement stage Phase II is launched extending the lifetime of the Observatory until the year 2030 and beyond. Besides the already mentioned addition of SSDs, various new sub-detectors and hardware components will be deployed in the Observatory in the upcoming years to strongly enhance the sensitivity of the current detectors, mainly of the SD [5, 93].

In the case of the FD, no additional hardware will be installed in the context of the

Radio Detector (RD)

Upgraded Unified Board (UUB)

Surface Scintillator Detector (SSD)

Water-Cherenkov Detector (WCD)
containing small photomultiplier tube (SPMT)
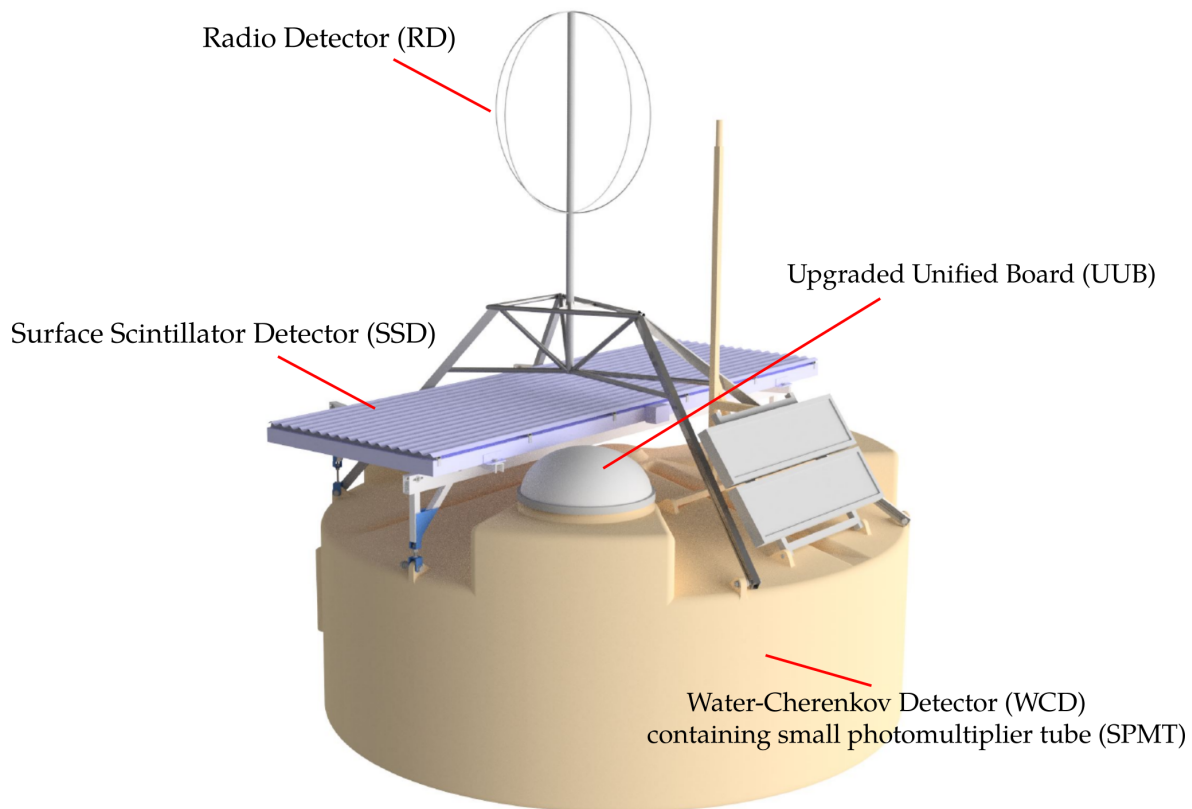
Figure 3.10: Schematic of an AugerPrime station including the main upgrade components: the new electronics board UUB to enhance the processing capabilities of the station, the additional small PMT inside the original WCD which increases the dynamic range of the detector, and the new scintillation detectors SSDs providing a complementary measurement of the electromagnetic and muonic air-shower components. On top of the WCD, a radio antenna for the RD is installed. Adapted from Ref. [92].

AugerPrime upgrade, but a modification of the operation mode is foreseen. With an adjustable decrease of the gain of the PMTs in all telescopes of the FD up to a factor of 10, the measurement time of the FD can be increased at the beginning and the end of each night, due to possibility to detect EASs during periods with higher background light. This enhances the measurement up-time of the FD to approximately 20 %, slightly improving the detection rate of EASs produced by UHECRs.

Nevertheless, the enhancement of the mass sensitivity of the SD will provide a significantly larger impact on the future determination of the properties of UHECRs. In Fig. 3.10, a schematic of an AugerPrime station with the main upgrade components is presented. To increase the general capability of each SD station, a new electronics board with superior resolution, sampling frequency, and timing accuracy, will be installed, representing the new basis of the future AugerPrime stations. With the addition of a small photomultiplier tube (SPMT) inside the WCDs, the dynamic range of the detector is further extended towards higher signals measured with stations close to the air-shower core.

In the SD-750 and SD-433 arrays, the modules of the Underground Muon Detector (UMD), deployed underneath a few meters of soil next to the more than 60 SD stations, will extend the original muon detection modules of the AMIGA enhancement [77]. The UMD will provide a direct measurement of the muonic air-shower component, increasing the mass sensitivity for primary energies around the ankle region of the energy spectrum.

To further enhance the hybrid detection method of EASs, especially in the case of inclined air showers, each SD station will be equipped with a radio antenna defining the future Radio Detector (RD), as can be seen in Fig. 3.10.

Finally, for the analysis of the new detectors with different responses to EAS events, adaptations and optimizations of the current calibration and reconstruction algorithms are needed. With the improved analysis software frameworks, not only the analysis of the Phase II data will be possible, but also the opportunity to reanalyze the Phase I data is given. To provide an overview of the AugerPrime upgrade, the individual components are shortly introduced in the following.

3.2.1 Surface Detector electronics

The installation of new electronics boards named Upgraded Unified Boards (UUBs) with significantly enhanced processing capabilities compared to the original UBs defines the main component of the AugerPrime upgrade [5, 94, 95, 96]. The new UUBs are produced by the company SITAEL [97] in Italy and are the chosen electronics board design to replace the original UB in all SD stations.

To cope with the increased amounts of data from the additional sub-detectors and to increase the overall measurement performance of the stations, the UUB provides a four times higher resolution, i.e., a 12-bit instead of the a 10-bit resolution, and a faster flash analog-to-digital converter (FADC) with a sampling frequency of 120 MHz, i.e., three times faster than the original electronics board. With five main input channels, the signals of the four PMTs of the WCD, the three LPMTs and the new SPMT, are obtained. The last channel is reserved for the single PMT of the new SSD. Each in channel is split on-board to provide a low- and a high-gain channel for each input, resulting in 10 signal channels. In addition, a digital connection to the antennas of the RD is provided.

With the implementation of the local-station software including the event and calibration trigger algorithms, the UUBs trigger system has been adapted to match the original design of the UBs, introduced in Section 3.1.2. While the UB samples the PMT signals with a frequency of 40 MHz defining the TH-T1 traces, the new UUB provides two types of traces stored in the memory buffers for each threshold trigger. With the increased sampling frequency, a new full bandwidth single-bin trigger with 120 MHz is implemented for the TH-T1 condition to utilize the full potential of the new electronics boards.

In addition, a so-called "compatibility mode" is available emulating the 40 MHz single-bin trigger of the original UB by using a filter algorithm on the full-bandwidth traces followed by a down-sampling procedure. The compatibility mode enables trigger comparisons between the two electronics generations necessary to finalize the software adaptations for the AugerPrime stations in the near future. During the deployment phase of the AugerPrime components, the UUB event data acquisition will be performed on the compatibility threshold triggers to guarantee a smooth transition from the Phase I to the Phase II. The other local-station triggers, the ToT, ToTd, and the MoPS conditions are implemented only on the compatibility mode traces of the UUB.

Since the deployment of the first prototype version of UUBs in 2016, extensive studies of the performance of the different UUB versions in the Observatory have been carried out. The results of the performance analyses together with a more detailed description of the properties of the UUBs and comparisons with the original electronics boards are presented in Section 5.1, including photos of the different UUB versions in Figs. 5.27 and 5.28.

3.2.2 Small photomultiplier tube

Since the engineering phase of the Pierre Auger Surface Observatory, the WCDs are providing a precise measurement of the air-shower particles arriving at the ground by determining the

lateral shower distribution. The high sensitivity of the detectors on entering particles offer the detection of the very low flux of air-shower particles in a distance of multiple kilometers to the air-shower core. Contrarily, the measurement of the EAS signal a few hundreds of meters from the core is strongly limited by the dynamic range of the three LPMTs in the WCDs. The high particle flux results in the production of a large amount of Cherenkov light inside the WCD which causes the devices to saturate. The saturation limit of an WCD has been determined in preceding measurements in the early phase of the SD and is expected to appear when the signal exceeds approximately 650 VEM, i.e., 650 times the signal of a vertical central through-going muon [2]. This limit would be reached when the WCD is a distance of ~500 m to the air-shower core of an EAS from an UHECR with 10^{20} eV. Due to the saturation, the total signal is underestimated resulting in a different treatment of the saturated WCD in the determination of the lateral air-shower distribution.

With the AugerPrime upgrade, the properties of EASs produced by UHECRs with energies in the flux suppression region above 5×10^{19} eV will be investigated. To increase the dynamic range of the WCDs to measure unsaturated signals closer as 250 m from the air-shower core, a new small photomultiplier tube (SPMT) will be installed inside each WCD [5, 98]. Similarly to the original three LPMTs, the SPMT is mounted on the upper side of the detector above the Tyvek liner facing downwards through a window into the liner. Thereby, the SPMT is located near the center of the WCD between the three LPMTs.

After testing various types of devices, the head-on Hamamatsu R8619 PMT [99] has been chosen to be deployed in each SD station. The PMT offers a significantly smaller photocathode of 1 inch diameter compared to the LPMTs and is equipped with a passive-base electronics connected to a power supply of the type A7501PB produced by CAEN [100]. Due to the small active area and the use of a non-amplified input channel on the UUB, the SPMT extends the dynamic range of the WCD by a factor of 30. Thus, large signals close to the shower core with values up to ~20 000 VEM can be measured without the saturation of the detector matching the dynamic range of the new SSDs. First results of the performance of the installed SPMTs in the AugerPrime test arrays in the Observatory, together with simulation studies, are presented in the Refs. [98, 101, 96].

3.2.3   Underground Muon Detector

Besides the upgrade of the SD station electronics and the dynamic range enhancement of the WCD, a new type of detector named Underground Muon Detector (UMD) will be deployed in the SD-750 and SD-433 arrays to increase the mass sensitivity of the SD for CRs with energies around the ankle feature of the spectrum [5]. The UMD is designed to extend the original muon detectors of the of the AMIGA enhancement [76, 77] to all the SD stations in the denser grid arrays. By the direct measurement of the pure air-shower muon component, as well as the average muon time structure, the modules of the UMD provide a determination of the lateral muon density distribution [46]. Additionally, in combination with the WCDs and the new AugerPrime detectors, a disentanglement of the electromagnetic and muonic component on a event-to-event basis will be provided, enforcing the future cross-calibration and multi-hybrid detection concepts.

For the UMD, three planar scintillation modules with a total surface area of ~30 m^2 are buried at a depth of 2.3 m next to each of the SD stations in the sub-arrays. The positioning of the modules relative to the SD station is shown in the schematic in Fig. 3.11. Each detector module is equipped with 64 plastic scintillator bars, each with a length of 4 m, and a width and thickness of 40 mm and 10 mm, respectively [102]. The bars are arranged in two symmetric wings with 32 bars and are coupled with wavelength-shifting (WLS) optical fibers to an silicon photomultiplier (SiPM) array placed between the scintillator wings which offers a counting strategy of single muons reading out the signals produced in individual scintillator bars.
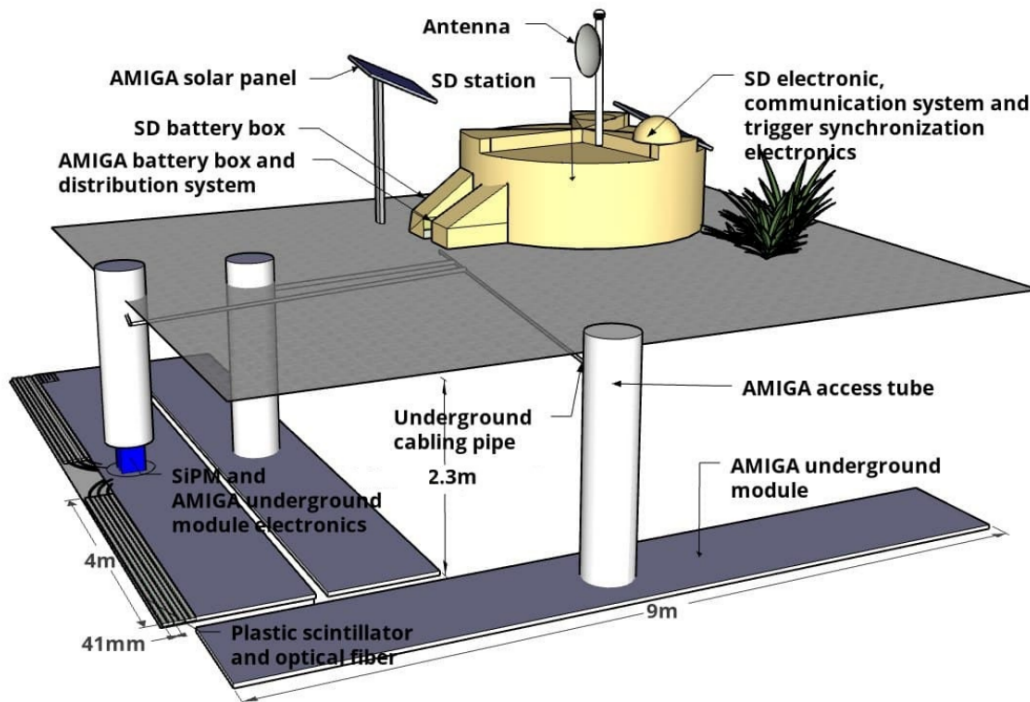
Figure 3.11: Schematic of the positioning of the three muon counter modules next to an SD station. Each module is equipped with 64 plastic scintillator bars connected to an SiPM array using optical fibers. The module and its electronics are placed at a depth of 2.3 m and are accessible through a plastic tube. All modules are connected to the SD station at the respective location and define the UMD in the SD-750 array. Taken from Ref. [103].

Due to the soil shielding, the electromagnetic air-shower component is strongly suppressed and a lower energy threshold for vertically arriving muons is set to ~1 GeV. For the readout and calibration of the UMD modules, the T1 trigger of the neighboring WCD is used as an external trigger input [103]. The general calibration strategy, as well as recent performance results of the UMD modules are presented in Ref. [104]. The installation of the UMD is expected to be finalized in the upcoming two years to commence its data acquisition in coincidence with the fully upgraded SD array. To visualize the current status of the UMD deployment at the submission date of this Dissertation, the detector positions are depicted in Fig. 3.5 by the green rectangles.

3.2.4 Radio Detector

The addition of planar scintillation detectors above the WCDs and next to the stations under a few meters of soil significantly enhances the hybrid detection of EAS events, and therefore increases the mass sensitivity of the SD. While this statement is valid for vertical air showers, for air showers with an inclined axis, i.e., $\theta > 60°$, the active area of the scintillators significantly reduces due to projection effects. This strongly affects the detection efficiency and results in a reduction of the number of hybrid measurements.

To compensate for the detection inefficiency of the AugerPrime stations for horizontal air showers, each station will be equipped with a radio antenna for the future Radio Detector (RD) of the Pierre Auger Observatory [105]. With the antennas of the RD, the electromagnetic energy of inclined EAS can be measured and in combination with the detection of the muonic component by the WCDs, the hybrid analysis of these air showers is provided. By precisely determining the ratio between electromagnetic and muonic particles for inclined geometries,

the hadronic interactions models, as well as the CR mass composition can be further examined. In addition, the measurement of the coherent radio emission of air showers offers a second method to determine the CR energy scale, besides the FD energy determination, as has been shown for the AERA [87].

Similarly to the antenna designs of the AERA, the RD upgrade will be realized with radio antennas sensitive in a frequency range from 30 to 80 MHz. But instead of LPDA or butterfly antennas, the short aperiodic loaded loop antenna (SALLA) type with a diameter of 1.2 m has been chosen as a standard design for the RD. This antenna type offers a robust and cost efficient structure combined with a sufficiently high ultra-wideband sensitivity, and therefore defines the optimal choice for the installation on a large scale. The antenna will be mounted on top of each SD station and the local-station trigger defined by the WCD is utilized to trigger the SALLA readout. In the schematic in Fig. 3.10, the installation radio antenna for the future RD on top of the original WCD is displayed.

To predict the performance and detector behavior of the future RD, extensive simulation studies have been performed [106]. Additionally, several prototype antennas have been installed in the AugerPrime test array in the Observatory in 2019. With these test antennas, the mechanical stability, as well as signal detection and calibration procedures are tested. First results from the RD prototype antennas are presented in Ref. [107].

3.2.5 Surface Scintillator Detector

One of the largest projects in the AugerPrime upgrade process is the production, deployment, and final implementation of the Surface Scintillator Detectors (SSDs) [5]. With the installation of a planar scintillation detector on top of the WCD, a complementary measurement of the electromagnetic and muonic air-shower components can be achieved, utilizing the different responses of the two detectors towards different types of through-going particles. By parametrizing the measured signals from both detectors for the same vertical air shower, the muon content of an EAS can be obtained on an event-by-event level, finally leading to an estimation of the mass of the primary CR.

Various approaches to determine the primary mass have been developed and tested on simulated data, as well as on data obtained with the prototype AugerPrime components installed in the Observatory [108, 109, 110]. With the completion of the AugerPrime upgrade in the upcoming years, these mass-determination techniques will be further optimized and adapted to the data from the final SD configuration. In this Dissertation, we also use the general term "scintillation detector" as a synonym for the SSD.

Similarly to the modules of the UMD, each SSD provides a simple and robust design with a planar structure and is separated in two symmetric wings. Each has an active area of $\sim 2\,\text{m}^2$ forming a total active detection area of $\sim 4\,\text{m}^2$ [5, 111]. In the photo in Fig. 3.12, a top view of an SSD wing containing all the relevant components is shown. Each wing is defined by 24 plastic scintillator bars coupled to WLS fibers which path the photons produced by the through-going charged particles to a centrally placed PMT to readout the signal. In contrast to the UMD modules, the readout with a single device provides a determination of the total signal deposited in all 48 scintillator bars, but no information about the individually hit bars is obtained.

Due to the installation on top of the numerous WCDs over the total SD array, the SSD is designed to be cost efficient and to require low maintenance. To avoid damaging of the polyethylene tank of the station, the weight of the SSD is limited to 120 kg, thus the enclosure frame of the detector, as well as the support structure to mount the SSD are built with aluminum. A robust aluminum frame with a length of 3.80 m and a width of 1.28 m consisting of hollow L-shaped beams defines the basis of the rectangular enclosure. The bottom is realized with a composite panel consisting of two layers of aluminum with a thickness of 1 mm and an extruded polystyrene (XPS) layer of 22 mm in-between.

Figure 3.12: Top view of a completed wing of an SSD, including the 24 narrowly arranged scintillator bars, the WLS fibers inserted in the bars and routed by the XPS forms towards the readout device. Taken from Ref. [108].

For the top of the SSD, a 1-mm-thin aluminum layer is used covering the vulnerable inner components and providing a protection against the harsh weather conditions in the Observatory, e.g., rain, snow, or strong winds. To reduce the mechanical stress on the aluminum frame from expanding and compressing air volumes due to the alternation of the environmental temperature, the SSD is filled with expanded polystyrene (EPS) to limit the inner air volume to less than 10 L. Additionally, each detector is equipped with a sun roof assembled of corrugated aluminum plates to protect the detector from direct sunlight. A detailed description of the SSD enclosure including the various minor modifications tested during the engineering phase and the overall construction procedure are presented in Ref. [112].

The detection of air-shower particles with the SSDs utilizes the scintillation light created by the through-going charged particles like electrons and muons, depositing their kinetic energy inside the scintillator, and thereby exciting and ionizing atoms in the plastic material [5]. In the de-excitation process, a cloud of photons is produced whose size is proportional to the deposited energy. These photons can be absorbed by WLS fibers coupled to the scintillator and further propagated through the fiber by total reflection from the point of interaction towards the signal readout device, in the case of the SSD an PMT. One example coupling method is depicted in the schematic in Fig. 3.13, presenting the two main active components of the scintillation detector, the scintillator bar in light blue with a U-shaped groove on the top, and the connected WLS optical fiber in green. After extensive studies of various combinations of scintillator bars and optical fibers with different dimensions and brands have been carried out in 2016 [114], the best fitting type of scintillator has been chosen for the SSDs.

The scintillator bars are produced at the Fermi National Accelerator Laboratory (FNAL) in the USA in an extrusion process using liquid polystyrene (Polystyrene Dow Styron 663 W) pressed through a variable machine head to create scintillator bars with the desired cross section shape [115, 116, 117]. In contrast to the bar shown in the schematic, the scintillator bars for the SSD provide two kidney-shaped holes inside the plastic material, extruded along the total length of the bar, as shown by the cross section in the left photo in Fig. 3.14. With this specific shape of the scintillator, the fibers can be inserted into the holes without the use
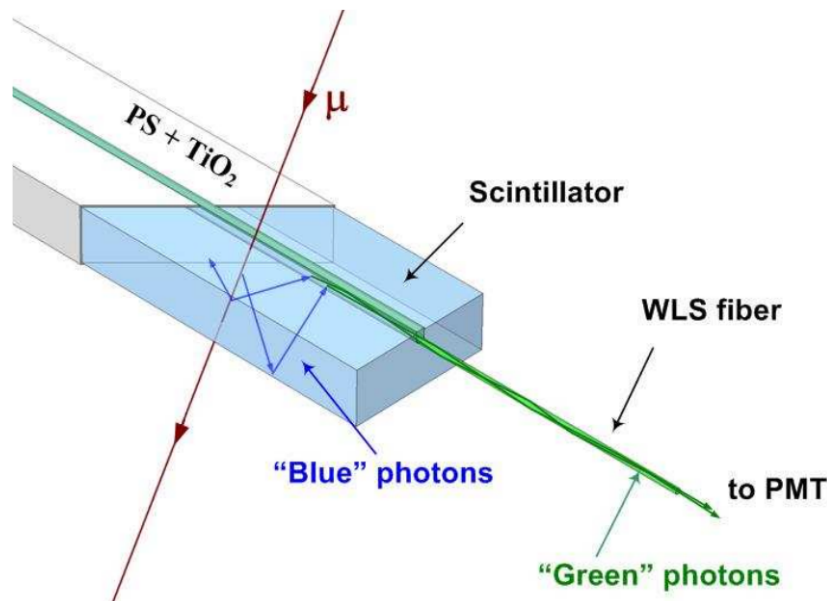
Figure 3.13: Schematic of the detection process of a muon utilizing a plastic scintillator bar (light blue) coupled to a WLS fiber (green). The muon (red arrow) deposits energy in the scintillator bar producing blue scintillation photons. These photons enter the optical fiber and are wavelength-shifted to the green region. The green photons with a significantly increased attenuation length propagate inside the fiber through the total reflection effect towards the signal detection device (PMT). Taken from Ref. [113].

of an optical glue to couple the fibers to the scintillator, as is necessary in the case of the bar with a groove on the top. Thereby, the assembly process is simplified and its duration can be significantly decreased.

Each scintillator bar of the SSD provides a length of 1.6 m, a width of 50 mm, and a thickness of 10 mm. The scintillation photons, created by passing charged particles, are in the ultraviolet (UV) wavelength with an average attenuation length of a few centimeters. To increase the photon propagation length in the scintillator, different dopants with WLS properties are added to the liquid polystyrene before the extrusion. These dopants absorb photons with a certain wavelength and emit photons with a larger wavelength, i.e., with a lower energy, resulting in an increase of their attenuation length. In the case of the FNAL scintillator bars, two fluorescent dyes are added, 1 % of PPO (2,5-diphenyloxazole) with an emission peak at ~365 nm and 0.03 % of POPOP (1,4-bis (5-phenyloxazol-2-yl) benzene) with an emission peak around 420 nm. With these dyes, the final photon wavelength is shifted into the blue region of the visible spectrum.

Additionally, during the production process, the scintillator bars are co-extruded with an outer film of polystyrene mixed with 15 % of a titanium dioxide (TiO_2) pigment. This thin outer TiO_2 layer with a thickness of ~0.25 mm can also be observed in the left photo in Fig. 3.14. With the co-extruded film on the outside of the bar, the inner surface of the scintillator appears diffusively reflective, increasing the photon density at the connection with the WLS fiber. Furthermore, the dense layer offers protection against mechanical damage and prevents external photons from entering the scintillator bar.

Accompanying the scintillator-bar production at the FNAL, a selection of the type of WLS fibers has been performed during extensive scintillator-sample tests presented in Ref. [114]. For the SSDs of the AugerPrime upgrade, the WLS optical fibers of the type Y-11 (300) MSJ with a diameter of 1 mm produced by Kuraray in Japan were chosen [118]. This type of fibers offers a multi-cladding structure with a polystyrene core resulting in multiple surfaces of
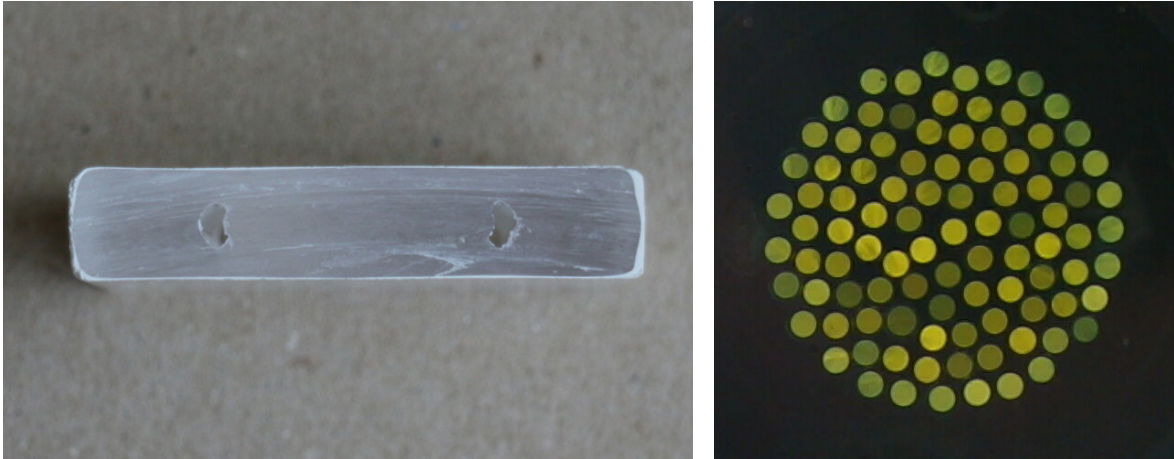
Figure 3.14: *Left:* Cross section of the SSD scintillator bar providing two kidney-shaped holes for the insertion of the WLS fibers. In addition, the thickness of the outer (TiO$_2$) film can be observed. Taken from Ref. [112]. *Right:* Photo of the 96 fiber ends glued into the so-called cookie.

materials with different refractive indices [119]. With this structure, the photons entering the fiber are trapped due to the total reflection effects at the various material surfaces and the total light yield inside the fiber is increased.

Similarly to the scintillator bars, the optical fibers contain a dopant to shift the wavelength of the photons towards larger values. In the case of the fibers for the SSD, the fluorescent dye K-27 in a concentration of 300 ppm is added to the polystyrene core. This dye provides a photon absorption below 450 nm with a coupled emission above ~490 nm. The entering photons are wavelength-shifted from the blue towards the green region of the visible spectrum. This increases the attenuation length above values of 3.5 m which are necessary when the dimensions of the SSD are accounted for. To detect photons with the central PMT at the farther end of the scintillator bar, a minimum photon travel length of ~2.5 m is needed, and due to the fiber routing in a U-turn, even larger photon travel lengths are possible.

During the SSD assembly, in total 48 WLS optical fibers are inserted by hand into the holes of the scintillator bars directly from the transport roles. Each fiber is cut to a length of 5.85 m resulting in a total length of ~280 m of WLS fiber inside one SSD. At the edges of the SSD, the fibers are routed in a U-turn when exiting the scintillator bars to provide two travel paths for the photons, and thereby increasing the number of arriving photons at the detection device. This design significantly improves the detection homogeneity along the scintillator bars when compared to scintillator-fiber combinations which contain fibers cut at the end of the bars [108]. To realize the bending of the fibers and connecting the narrowly packed scintillator bars, the type of fiber with an enhanced mechanical strength against damage and a higher flexibility is chosen. Nevertheless, a minimum bending diameter of 100 mm has to be maintained to prevent photon loss on the fiber surfaces. To assure the U-turn bending with the minimum diameter and to protect the fiber surfaces, diffusive-reflective XPS forms are used to guide the fibers outside the scintillator bars. Besides the routings at the edges of the SSD, XPS forms between the two active wings are installed to guide the fibers and assure an identical fiber path length from the scintillator bar to the readout device.

The insertion of the fibers is followed by a melting process of all 96 fiber ends to remove scratches on the surfaces [111]. The fiber ends are glued with an optical cement into a transparent poly(methyl methacrylate) (PMMA) cylinder, the so-called "cookie", which provides the connection of all fiber ends to the same readout device. A cookie with the 96 glued fiber ends is displayed in the right photo in Fig. 3.14. The arriving photons are measured with a 1.5 inch head-on PMT Hamamatsu R9420 with a photocathode sensitive in the blue and green
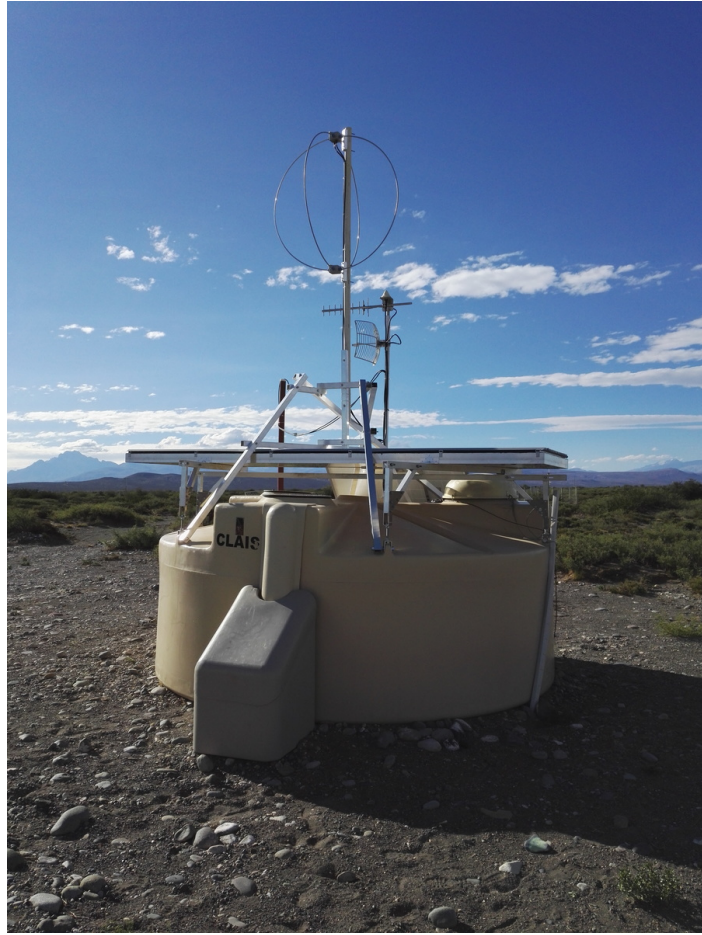
Figure 3.15: Photo of an AugerPrime station in the test array in the Observatory. Two main components of the upgrade can be observed, the SSD and the antenna for the RD.

region of the visible spectrum [120]. The PMT is equipped with an active base produced by Iseg which provides the necessary voltage for the base electronics [121]. The PMTs and their accompanying base electronics have been tested and characterized in advanced laboratory measurements described in Ref. [122]. Finally, after the assembly of the active components, the SSD is sealed and tested before the transport to the Pierre Auger Observatory. At the Observatory workshop in Malargüe, the sun roof and further protection components are added, before the SSDs are deployed on top of the WCDs, as shown in the schematic in Fig. 3.10.

In the current configuration of the SD trigger system, the SSD PMT is not included in the local-station trigger condition, but the data is read out when a T1 trigger request is required from the CDAS. In the future, a self-trigger mode of the SSDs will be implemented in the SD station software to provide a fully independent measurement of the EAS particles by the two main sub-detectors. Analogously to the calibration of the WCD, a calibration procedure is implemented utilizing a unified reference unit to convert the raw ADC values obtained with the FADC. In the case of the SSD PMT signals, the unit is defined as the most probable signal produced by a vertical through-going charged particle with the energy of a minimum ionizing particle (MIP), and therefore the relative unit is named "MIP", further described in Chapter 6. The aimed dynamic range of the SSD is approximately 20 000 MIP which matches the increase of the dynamic range of the WCD by the installation of the SPMT [5].

In 2016, the first 14 prototype SSDs have been assembled and installed in the AugerPrime

test array to analyze their performance under the rough environmental conditions in the Observatory. In the photo in Fig. 3.15, a station equipped with the prototype AugerPrime components can be seen. First results of the data acquisition with these scintillation detectors have been presented in the Refs. [123, 101]. Before the transport to the Observatory, additional quality and validation tests under laboratory conditions of the first generation of SSDs have been performed [124, 112]. Approximately one year later, the main production phase of the SSDs with a slightly optimized enclosure design has been commenced at various production sites in the Auger Collaboration, presented in Ref. [125]. Therein, the general description of the assembly procedure and of the validation measurement principles is given. Furthermore, in Section 4.2 the extensive validation measurements of the main production SSDs at the Institute for Astroparticle Physics at the Karlsruhe Institute of Technology (KIT) are presented. Until 2020, more than 1500 SSDs have been assembled to be deployed in SD array on top of each WCD except the most outer rows of stations. The status of the deployment of the AugerPrime components at the submission date of this Dissertation is presented in Section 5.5.

Chapter

4

Laboratory Measurements of Scintillation Detectors

Since the first Surface Scintillator Detectors (SSDs) have been assembled at the beginning of the AugerPrime engineering phase in 2016, the in-depth studies of their performance have been a major criterion for the validation of the detector characteristics and quality. The knowledge about the behavior and capabilities of the future Surface Detector (SD) sub-detectors in the Observatory is of high importance for a successful outcome of the Upgrade. With the launch of the main production and assembly process at the end of 2017, the test measurements have been established as the standard procedure for the necessary quality assurance stage and have been continuously performed over the total production period of more than two and a half years.

While the main production of the SSDs was carried out at various production sites in the Auger Collaboration using slightly varying methods to analyze the detector performance, in this Dissertation, we present the results of the SSD performance tests at the Institute for Astroparticle Physics at the Karlsruhe Institute of Technology (KIT). From 2017 to 2020, 661 of the more than 1500 SSDs have been assembled and subsequently probed to detect potential malfunctioning components before their shipment to Argentina has been initiated. For all detectors, the measurement of the SSD performance has been performed using the "muon tower" set-up. This device is capable to detect and reconstruct tracks of single through-going charged particles from extensive air showers (EASs), mostly muons, which then can be used to determine the signal uniformity and detection efficiency of any thin planar probe detector.

In the first part of this Chapter, we introduce the SSD test set-up, including the general design of the muon tower, as well as the configuration of the test detector data readout. In addition, a data-driven method is presented that provides the possibility to obtain the height position of the probe detector inside the muon tower. The precise knowledge of the actual height position is crucial in the proper determination of the detection efficiency and spatial homogeneity of the probe detector. Subsequently, we describe the results of the extensive validation measurements of the SSDs obtained during the main production phase. In these laboratory tests, we have determined the light yield of each individual detector which defines their overall performance. Furthermore, the measurement data of the signal uniformity and the spatial homogeneity of each of the SSDs is available. For the analysis of the quality of the aluminum enclosure, a light tightness check has been performed utilizing the intrinsic dark

Figure 4.1: Photo of the muon tower during the SSD validation tests. The set-up shows the three planes of LST chambers. An SSD is inserted between the center and the bottom plane on top of the movable support structure.

pulse rate of the installed detection device.

Finally, in the third part of this Chapter, comparisons between the laboratory measurements of the SSDs and detector simulations obtained with the $\overline{\text{Off}}\underline{\text{line}}$ analysis software framework are carried out. These comparisons focus on the light output of the detectors, as well as on the general shape of the pulses from passing particles.

4.1   The Muon Tower

For the measurement of the performance of the SSDs of the AugerPrime upgrade, a test set-up with the name "muon tower" has been used. The muon tower consists of one module of the large area muon tracking detector (MTD), originally used at the Karlsruhe Shower Core and Array Detector (KASCADE) experiment and its successor the KASCADE-Grande experiment [126, 35, 36]. The MTD was designed as an underground position-resolving detector to measure and identify charged particles regarding their incoming direction by reconstructing their trajectories when passing through the detector. The 16 modules of the MTD were placed in the north of the KASCADE central detector inside a ~50 m long tunnel under the scintillator station array. The detection of single charged particles was realized with three horizontal planes of limited-streamer tube (LST) chambers placed at constant heights that determine the line of propagation by measuring the intersection points of particles with all three planes. In addition, each module was equipped with a fourth LST plane installed vertically on the side of the module to enhance the geometrical detection efficiency and to measure particles with very inclined trajectories. With a total detection area of ~128 m^2, the total detection acceptance of the MTD has been limited by the geometry of the individual modules and resulted in approximately 500 m^2 sr. The tunnel was designed to provide a shielding depth of 18 radiation length to suppress the measurement of electromagnetic particles and to set the detection energy threshold of the remaining atmospheric muons to

~0.8 GeV.

After the disassembly of the KASCADE detectors, several modules of the MTD have been conserved of which one was recovered and installed inside the production hall of the Institute in proximity to the SSD production. With this module containing the three horizontal planes, but not the single vertical plane, a test stand to analyze the newly assembled SSDs has been set up, the so-called "muon tower", which is shown in Fig. 4.1. In the following, the technical design and data acquisition system of the muon tower is presented. Additionally, the signal readout set-up of the probe SSDs is described, especially focusing on the devices and configurations for the test measurements of the main production detectors. During the performance measurements, the knowledge of the position of the SSD inside the muon tower is required to properly estimate the intersection densities and to provide sharp images of the respective quantity diagrams. For this reason, the technique is described to determine the relative height position of the probe detector utilizing the sharpness information of the obtained data.

4.1.1 Technical design and data acquisition

The muon tower as module of the MTD was designed to measure single charged particles from EASs passing through the detector and reconstruct their trajectories. This information was then used to constrain the determination of the arrival direction of the primary cosmic ray (CR) particles. In general, charged particles can be detected through their interaction with matter [8]. This process depends on different characteristics of the examined particles, e.g., their energy and charge, as well as on the properties of the target material. For GeV muons which are produced in EASs, the leading process is the energy deposit inside the detector through the ionization of the surrounding matter. For this reason, thin detectors filled with an ionizable gas can be used to measure the discharge locations of individual charged particles, and thereby determining the intersection positions.

In the adapted set-up, the penetrating single charged particles are used to analyze the performance of thin and plane particle detectors which can be measured and imaged utilizing the geometrical information of the muon tower. The only necessity for the probe detector is the requirement of being sensitive to the same particles that can be reconstructed with the muon tower. With the coincidence trigger of the three planes of the muon tower, the intersection position of the particle track with the probe detector plane can be assigned to a signal in the probe detector which does not provide a spatial resolution by itself. With the knowledge of the exact position of the probe detector inside the muon tower, in particular the height difference relative to the center plane, various two-dimensional detector characteristics can be determined, e.g., the spacial signal uniformity or the general detection efficiency. The muon tower is approximately 4.3 m long, 2.1 m wide and has a total height of 2.3 m. The three LST planes, displayed in the schematic in Fig. 4.2 by the white horizontal rectangles, are installed at an equal distance of 0.82 m between each other. The active area of each plane is limited to approximately 4.0 m × 2.0 m.

Each plane of the muon tower consists of 12 LST chambers with a length of 4.0 m [126]. These LST chambers are constructed of two high-resistivity polyvinyl chloride (PVC) comb structured profiles providing in total 16 cells each with a dimension of 9 mm × 9 mm and serving as the cathode of the tube. In addition, each cell contains a copper-beryllium wire of 0.1 mm diameter which defines the anode of the cell. This results in 16 wires inside one LST, and in total 192 wires per plane.

To supply the LST chambers with an ionization medium, the muon tower was originally continuously flushed with argon as ionization gas together with isobutane serving as quenching gas. This quenching gas had the purpose of restricting the propagation of the discharges, and thereby limiting them to a defined location. To simplify the operation of the muon tower during the SSD test measurements, the gas system is filled with pure carbon dioxide as
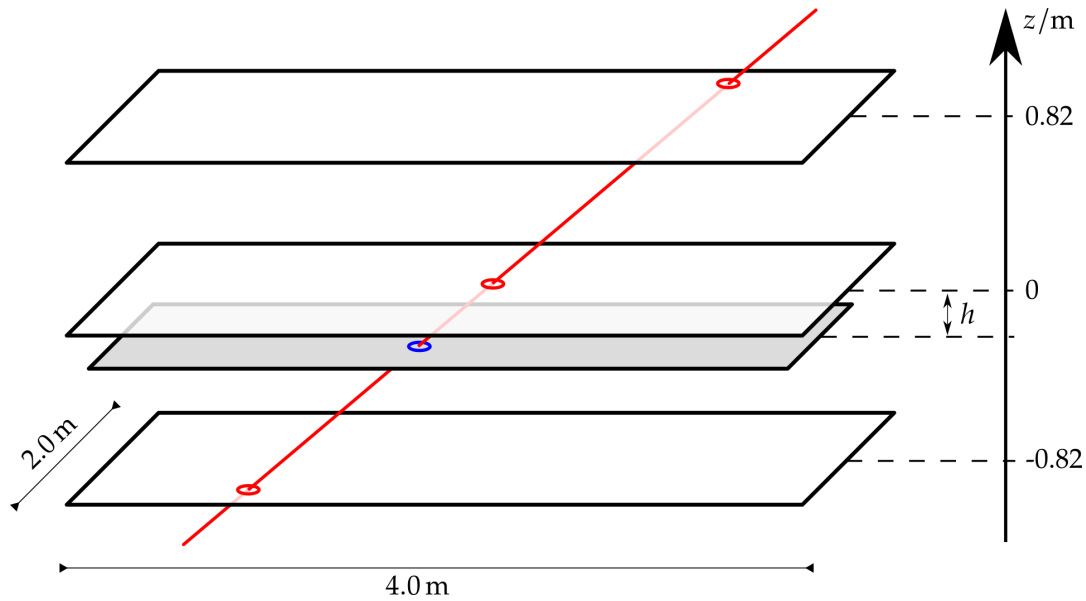
Figure 4.2: Schematic of the set-up for the SSD validation tests. The three active LST planes are displayed by the white rectangles, the inserted probe detector is shown by the gray rectangle. The red line displays a through-going charged particle which intersects all four planes. The center plane of the muon tower defines the zero point for the z coordinate, the relative distance between the center plane and the SSD is given by the height h.

ionization gas and no quenching gas is added. The ionization of the gas inside the LSTs requires a large electric potential to measure the discharges and prevent the recombination of the ions and electrons. This is realized with a supply voltage of 5000 V which is applied to the anode wires. Through-going charged particles ionize the gas and produce transient clouds of discharge streamers, i.e., electron avalanches, which are accelerated towards the anode wires where they create currents of the order of 100 mV.

On top of the LSTs, a thin polyester foil is mounted which contains 192 evaporated aluminum strips that are able to measure induced currents produced by the electric fields of the moving positive ions inside the LSTs. These pick-up strips are oriented perpendicular to the tubes and have a length of 2.0 m each. In addition, a second layer with the identical amount of pick-up strips, but now diagonally orientated by 30° to the wires, is installed below the plane of LST chambers.

With the signals of the anode wires, the x-coordinate of the particle-plane intersection points are defined. Thereby, each wire covers a width of 1 cm. Analogously, the pick-up strips provide information about the y-coordinate of the intersection points with a coverage of 2 cm by the perpendicular strips and 4 cm by the diagonal strips. When combining the signals obtained by the three different detection components, the particle intersection point can be precisely determined by triangulation, resulting in a spatial resolution of ~1 cm. In general, the here described method requires the assumption that each LST plane is represented by a infinitesimal thin interaction plane.

For the case that the three intersection points of the LST planes match the coincidence trigger condition, the best fitting trajectory for each single particle can be reconstructed offline with a 3-point resolution of less than 1 cm. This is highlighted by the red line in the schematic in Fig. 4.2. If the reconstructed trajectory line differs from the measured intersection points by a distance larger than 3 cm, the single particle event is rejected. In the reconstruction process, the signals of single muons can be selected by their sharp and narrow pulses, contrarily to the wide signals of particle showers containing multiple particles. Similarly to the rejection

of the trajectories with large uncertainties, every event with two or more intersection points on one plane are not reconstructed due to the lack of a well defined particle trace.

Each LST plane contains 15 front-end electronics boards in a daisy chain to read out the respective signals [127]. Six of these boards are dedicated for the anode wires, and an equal number is connected to the perpendicular strips. The diagonal pick-up strips are read out in pairs, hence only three boards are necessary for the readout. With the potentiometers on the front-end electronics boards, a digitization threshold is set at which the analog currents are converted into digital signals. The electronics boards of the wires additionally provide a digital OR condition on each individual wire which is used as the trigger condition for the respective plane. When the condition is fulfilled, the signals in the registers of all 15 electronics boards of each LST plane are transmitted in a serial chain utilizing a bitwise shifting process.

After the search for a coincidence signal between all three planes, the signals of all front-end electronics boards are sent to the streamer tube acquisition system (STAS) controller board which serves as an interface to the subsequent trajectory reconstruction software on the operating computer. A more detailed description of the readout electronics chain, as well as performance tests and optimizations to the trigger logic are presented in Ref. [112]. During the period of the SSD production and validation measurements, several components of the electronics chain for the signal readout have been exchanged. The STAS controller and accompanying logic boards were replaced by a Raspberry Pi [128] system which optimizes and parallelizes parts of the muon tower plane readout.

With the muon tower set-up, the performance of any particle-detection device can be analyzed when certain requirements are fulfilled. For instance the maximum size of the probe detector is limited to the dimensions of the muon tower, i.e., the probe detector cannot exceed a length of 4.0 m and a width of 2.0 m. Despite the fact that the height of the probe detector can reach up to 0.6 m, for the particle interaction area, the same requirements of a thin and plane approximation have to be fulfilled. This is the case for the SSDs of the AugerPrime upgrade for the Pierre Auger Observatory due to the use of plastic scintillator bars with a thickness of 1 cm. Besides the main purpose of measuring the SSD performance, the muon tower is also used to analyze similar types of detectors, for example the new scintillation detectors for the surface detector of the IceCube-Gen2 experiment [129, 130] or the Aachen Muon Detector [131]

The position of the probe detector inside the muon tower is represented by the gray rectangle in Fig. 4.2. For the proper determination of the detector quantities which are sensitive to the actual intersection position, the probe detector has to be placed at a constant height, i.e., at a constant z-coordinate. This is guaranteed by a support structure providing a movable top for a simple inserting and removing process, as can be seen in Fig. 4.1.

4.1.2 Probe detector data readout

For the readout of the probe detector signals, the coincidence trigger of the muon tower is used as an external trigger condition applied to the sampling device of the readout electronics chain. Depending on the type of the inserted probe detector, the electronics settings slightly differ. The procedure and settings that we present in this Dissertation describe the data acquisition and handling process for the validation measurements of the newly assembled SSDs starting at the end of 2017. In these performance tests, the SSD is equipped with a photomultiplier tube (PMT) to detect the photons produced in the scintillator bars. The PMT is equipped with a passive base electronics, and therefore an external power supply is connected. In contrast to the measurement conditions of the SSDs in the Observatory, the PMT is operated at a significantly higher voltage value, at the maximum supported value specified by the producer. These settings are necessary to avoid the use of pre-amplifiers, but still allow to distinguish the small pulses produced by single photoelectrons (SPEs) at the

same time than the larger pulses of ionizing particles passing through the scintillator. As an undesirable result, noise pulses and background signals are also amplified.

To enable comparisons of the detector performance, the measurement of all 661 SSDs was originally planned to be carried out with one single PMT of the type Hamamatsu R9420 [120] which is the chosen model for the use in the SSDs in the Observatory. At the beginning of the validation tests, the PMT Hamamatsu R9420 with the serial number #DE2779, in this Chapter named "PMT 1", was operated at a voltage of (1500±2) V and a current of ~51 µA. Due to the continuous operation at the maximum supply voltage, intrinsic noise effects of the amplification system of the PMT became visible. Additionally, the material aging of the device was significantly enhanced, finally resulting in the partial malfunction of the PMT after approximately six months of SSD tests. The PMT was exchanged by a device of the same type with the serial number #DE2758, in the following called "PMT 2" . Analogously, the second PMT was operated at a voltage of (1500±2) V and a current of ~52 µA. This device was used during the validation tests until the beginning of 2019. After experiencing increased internal noise, the detection device was substituted once again. This time, a different PMT model was chosen which provides a similar size and shape than the regular SSD PMT, but can be operated at a lower voltage while still retaining the high sensitivity towards small signal pulses. The "PMT 3" was of the type Hamamatsu R11102 [132] with the serial number #A79233 and was operated at (980±2) V and ~247 µA. This PMT was then used until the end of the SSD production at the end of 2020.

For all three PMTs, the analog signal output of the base electronics was connected to one of the input channels of a mixed-signal PicoScope 6403A [133] which digitized and buffered the signal traces. The PicoScope offers a vertical 8-bit resolution and an analog bandwidth of 350 MHz. The voltage range of the input channels is limited to −50 to 50 mV and a maximum sampling rate of 5 Giga samples per second is provided. During all standard measurements of the validation tests of the SSDs production, we chose a sampling interval, i.e., the size of a time bin, of 1.6 ns.

When a trigger signal of the muon tower arrives at the PicoScope, a PMT time trace of a total length of 4 µs is stored. Thereby, the time window is chosen relative to the external trigger which defines the reference time stamp $t = 0$. Due to the delay of the electronics readout chain, the PMT pulse of the single particle which triggered all three planes of the muon tower is expected to appear before the external trigger reaches the PicoScope. For this reason, the stored PMT trace contains all the signals 3.2 µs before $t = 0$ and 0.8 µs after the zero time stamp.

After storing the time traces on the operating computer, an offline baseline and pulse finding algorithm is applied to each PMT trace. This algorithm is designed to search for one or more pulses in the traces independently of the origin of the pulses. For the determination of the baseline of each trace, the most probable value of the time bin entries is determined. Thereby, the amplitude values range from −127 to 126 ADC due to the 8-bit resolution of the PicoScope. The distribution of time bin entries is then truncated by rejecting all bins with entries that are at least 4 ADC above or below the most probable value. Finally, the mean $\bar{b}$ and the standard deviation σ_b of the remaining distribution is calculated defining the trace baseline.

The signal pulses are determined utilizing a pulse trigger threshold of $4\,\sigma_b$. If the trigger condition is fulfilled, the pulse is then defined by the time bins before and after the trigger bin which surpass an entry threshold of $1.5\,\sigma_b$. To even further extend the pulse definition, seven bins before and seven bins after the first and the last bin surpassing $1.5\,\sigma_b$ are added to the pulse. For each pulse, various quantities are then determined, e.g., the pulse height defined by the bin with the largest amplitude, or the charge of the pulse which represents the area received after the integration of the pulse bins. Furthermore, several of these quantities are used to apply an additional filter to the ensemble of pulses due to the effects of the intrinsic noise
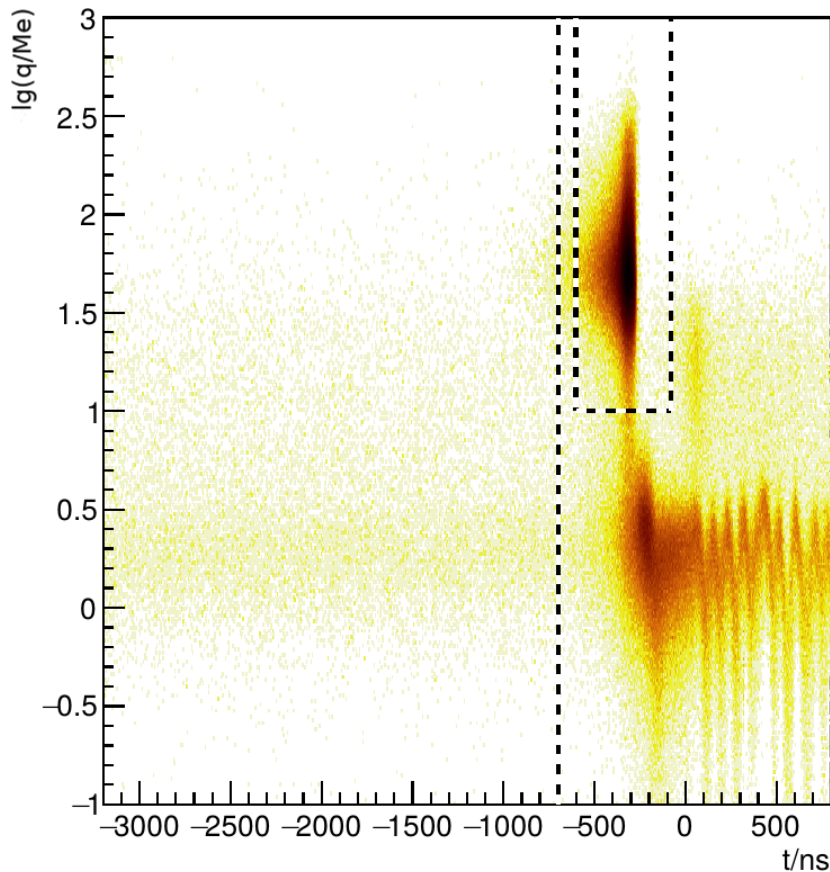
Figure 4.3: Distribution of pulses of the measurement of the detector SSD-02-KA-0341 depending on the relative appearance time and the logarithmic pulse charge. The reference time stamp $t = 0$ is defined by the trigger-timing signal of the muon tower. The rectangle formed by the dashed lines close to the time stamp $t = 0$ represents the selection window of the MIP pulses. The vertical dashed line at -700 ns indicates the closest possible timing to the MIP window in the selection of random pulses.

of the first two PMTs. Especially for the determination of the average SPE pulse properties, the filter significantly reduces the contamination with electronics noise pulses. The filtering is realized by selecting only pulses which provide a Shannon's information entropy value inside a well defined range, as well as requiring a minimum pulse height and a minimum ratio of the integrated area of the pulse to the pulse height.

In general, the detected pulses can be separated into different types. This can be expressed with the two-dimensional distributions of the appearing time stamp of the pulse relative to $t = 0$ and the charge value of the pulse. The resulting pulses of the measurement of the detector SSD-02-KA-0341 is shown in the diagram in Fig. 4.3. Therein, the logarithmic charge distribution of the observed pulses in dependence of the relative appearance time is presented. For the analysis of the probe detector performance, two main types of detected pulses are relevant which can be selected from certain areas of the two-dimensional distributions. The pulses with the highest importance are the signals created by the single ionizing particles that triggered the muon tower, and therefore offer a reconstructed trajectory. Due to the energy-dependent distribution of the arriving charged particles particles, the highest density can be observed for the average energy of a minimum ionizing particle (MIP). The pulses are expected to be large, i.e., to show a large charge value, and appear very close the trigger time stamp $t = 0$. For this reason, a selection time window of -600 ns to -80 ns is chosen.
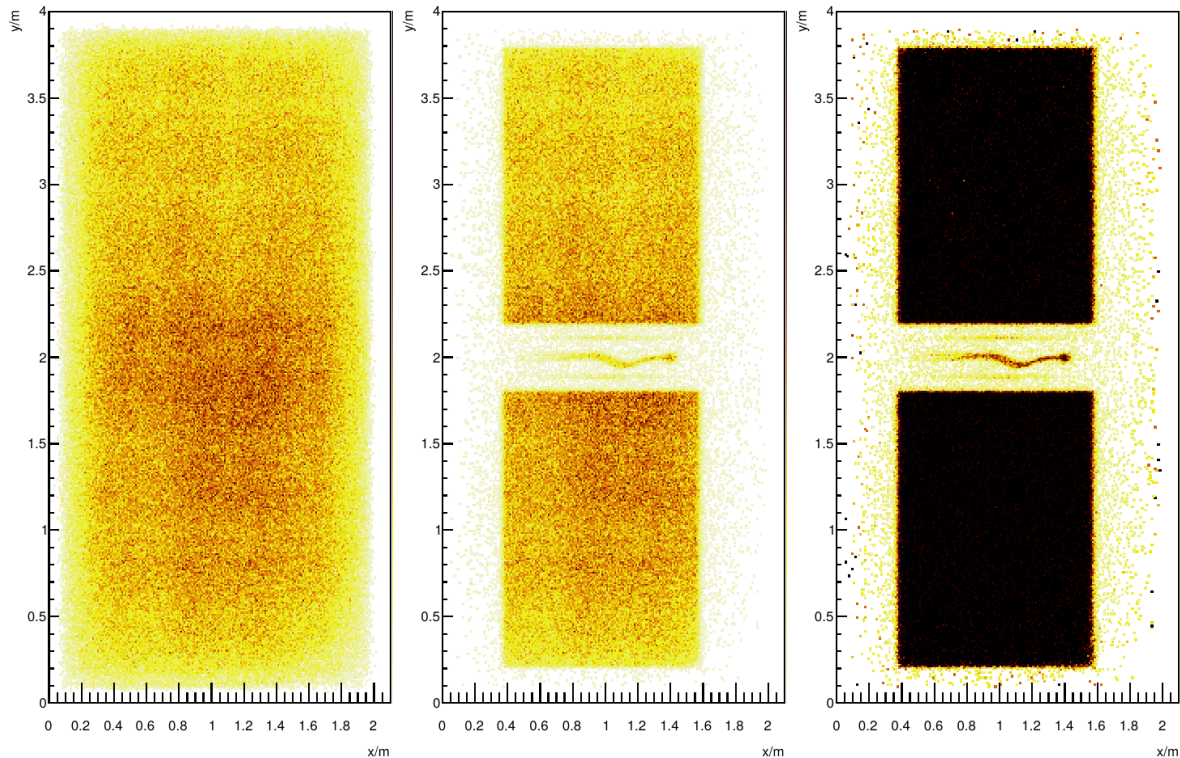
Figure 4.4: *Left:* Distribution N of intersection points of all reconstructed particle trajectories evaluated at the height position at which the probe detector would be placed. *Center:* Distribution M of a subset of intersection points which offer an additional MIP pulse signal in the detector SSD-02-KA-0341. *Right:* The ratio of the center and left distributions $\varepsilon_i = M_i/N_i$ defines a measure for the spatial detection efficiency of the SSDs.

In addition, only pulses above the charge threshold of 10 Me are included into this pulse category. The selection area is highlighted in the diagram in Fig. 4.3 by the dashed lines forming a rectangle. Due to the change to a different PMT type for the last period of validation measurements, the selection criteria have been adjusted to a appearance time window of $-700\,\text{ns}$ to $-200\,\text{ns}$ and a minimum charge threshold of 25 Me. In the following, the pulses are used to measure the light yield of the probe detector and are often referred to as "MIP pulses", corresponding to their origin. The average pulse length of the MIP pulses usually ranges from 10 to 30 ns.

Besides the MIP pulse selection, we define a second main pulse category which is only selected by their appearance time. These random pulses are not correlated with single particle trajectories, but mostly contain the SPE pulses which describe the intrinsic detection properties of the PMT. With the random pulses, the dark currents and baseline fluctuations can be analyzed which offers the opportunity to search for noise sources and potential issues of the light tightness of the detector enclosure. In the case of the first two PMTs of the validation measurements, the random pulses contain all pulses which appear in-between the time stamps $-3200\,\text{ns}$ and $-700\,\text{ns}$, i.e., with a sufficient time distance to the MIP pulses, as shown by the vertical dashed line in the diagram in Fig. 4.3. This time window was then slightly decreased for the third PMT, ranging from -3200 to $-800\,\text{ns}$. Contrarily to the MIP pulses, the "SPE pulses" do not provide a counterpart event from the muon tower. Therefore, a clear separation in the MIP pulse an SPE pulse selection is necessary.

Finally, additional populations of pulses are visible in the timing and charge distributions in Fig. 4.3 which are not included in one of the two main pulse categories. These pulses are

either produced by accompanying air-shower particles with lower energies or can be the results of signal oscillations and reflections in the long readout cables. All pulses outside the time windows that define the MIP or SPE pulses are not further analyzed in this Dissertation.

With the definition of the MIP pulses which provide a corresponding particle trajectory and the knowledge of the precise height position of the probe detector inside the muon tower, the fraction of single particle events that also produce a defined pulse in the SSDs can be determined. This fraction represents the overall detection efficiency of the SSDs and provides a first check of malfunctioning parts, e.g., broken fibers. The fraction is calculated from two two-dimensional distributions of particle intersection points. The first distribution are the intersection points of all reconstructed particle trajectories which have been reconstructed with the muon tower. Thereby, the two-dimensional distribution N is evaluated at the height position at which the probe detector would be placed and is the result of the convolution of muon tower geometry and the natural zenith-angle distribution of the incoming particles. This is shown in the left diagram in Fig. 4.4 for the measurement of the detector SSD-02-KA-0341. The darker the color of the bin, the higher is the density of intersection positions. The second distribution contains a subset of the same trajectories which fulfill also the additional condition that a matching MIP pulse in the SSD was measured. The intersection-position distribution M at the height of the SSD is displayed in the center diagram in Fig. 4.4. Therein, even the matching signals produced by the fiber bundle and the cookie outside the scintillator bars can be seen. Finally, the ratio of these distributions describes the spatial detection efficiency ε of the SSD. For each bin i the efficiency is calculated by

$$\varepsilon_i = M_i/N_i. \tag{4.1}$$

The resulting detection efficiency at the height of the SSD is shown in the right diagram in Fig. 4.4. Therein, we can observe that basically all through-going single particles produce a sufficiently large pulse in the SSD indicating a proper functioning of all active components of the scintillation detector.

4.1.3 Position determination of probe detector

For the determination of the proper intersection distributions, the precise position of the probe detector inside the muon tower has to be known, especially the height position relative to the three LST planes. This information was originally obtained manually with tools like a measuring tape. Thereby, the actual height position of the scintillator bar plane has to be calculated with the cross section of the SSD. To optimize the determination of the height position, we developed a data-driven method which utilizes the "sharpness" of the images of the intersection point distributions to derive the real height. Thereby, only data obtained during the SSD validation measurements is used, more precisely the detection efficiency ε. The development of the height determination method was carried out using the data of the scintillation detector SSD-02-KA-0251 which offers a long measurement period, from 25 September to 8 October 2018.

To visualize the height dependence of the reconstruction of the efficiency, in Fig. 4.5 the efficiency distributions determined for three assumed height positions $h = 0.4\,\mathrm{m}, -0.4\,\mathrm{m}, -0.7\,\mathrm{m}$ are shown. In the schematics on the left, the position of the SSD relative to the LST planes is displayed. On the right, the corresponding efficiency distributions determined at the assumed heights are shown. When comparing the efficiency distributions for the three heights, a clear difference in the image sharpness is visible. While for the lower two heights, $h = -0.7\,\mathrm{m}$ and $h = -0.4\,\mathrm{m}$, both active areas of the SSD are still distinguishable, but slightly blurry at the edges, the efficiency distribution for $0.4\,\mathrm{m}$, i.e., above the center LST plane, barely depicts the shape of the SSD. This indicates that the true height position of the SSD is closer to the lower assumed heights than to the upper height, actually lying in-between the two lower heights. If
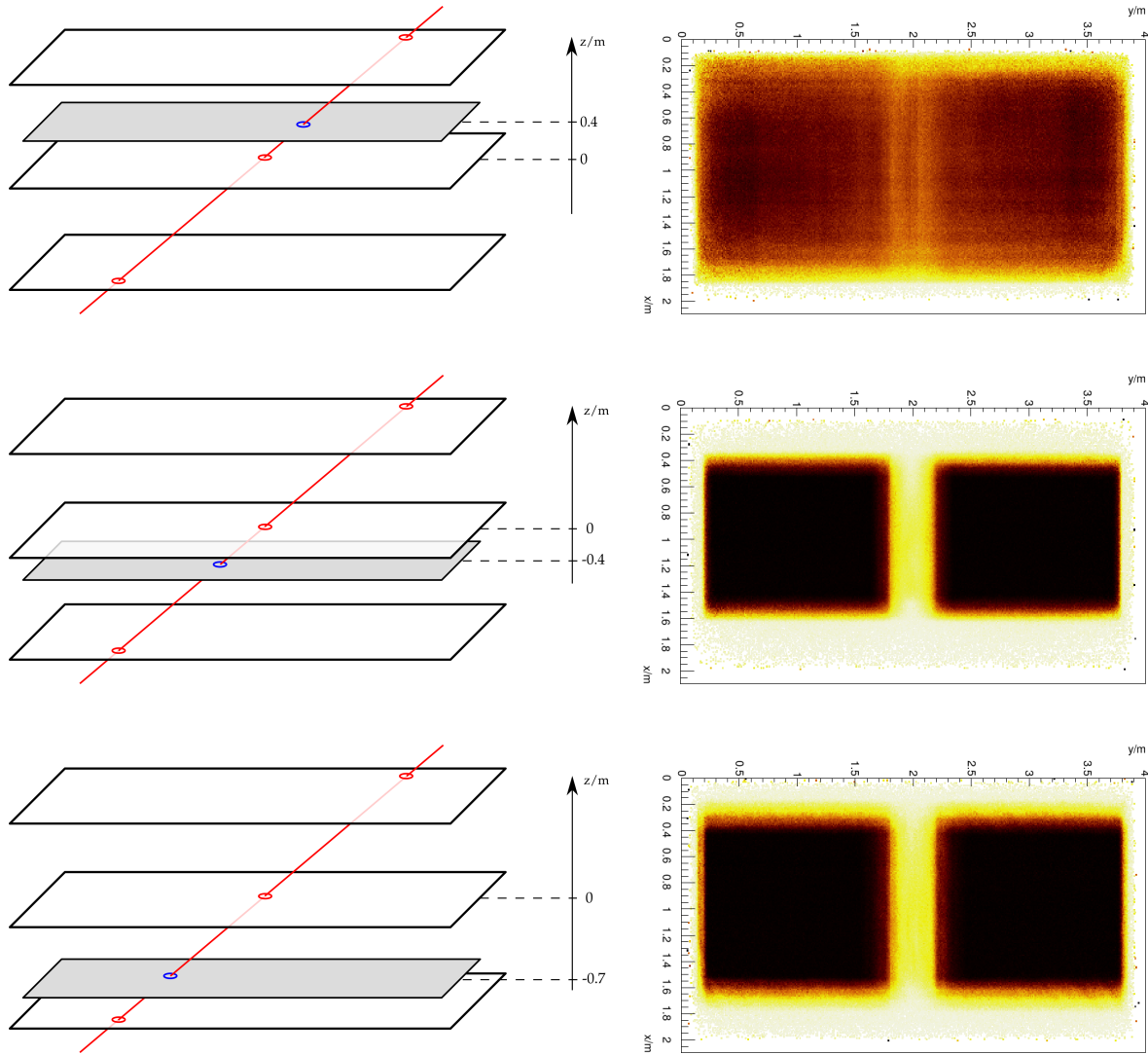
Figure 4.5: *Left:* Schematic of the assumed height of the inserted SSD, at three selected height values: $0.4\,\mathrm{m}$ (top), $-0.4\,\mathrm{m}$ (center), and $-0.7\,\mathrm{m}$ (bottom). *Right:* Corresponding distributions of the efficiency function with varying image sharpness. The data was acquired with the detector SSD-02-KA-0251.

the efficiency distribution at the true height position is determined, we assume a maximum in the sharpness of the image.

The image sharpness can be quantified by using the Shannon's information entropy S which is defined as

$$S = - \sum_i p_i \ln p_i \tag{4.2}$$

with p_i representing probabilities. Here, the probabilities p_i are defined by the efficiency bin entries normalized by the sum of the efficiency bin entries

$$p_i = \frac{\varepsilon_i}{\sum \varepsilon_j}. \tag{4.3}$$

The entropy does not provide a high sensitivity on very small structures, but offers the possibility to distinguish the sharpness differences for varying height positions. With this entropy definition, the sharpest image is expected to be obtained when the minimum of the entropy function is reached. Under this assumption, the true height position of the SSD can
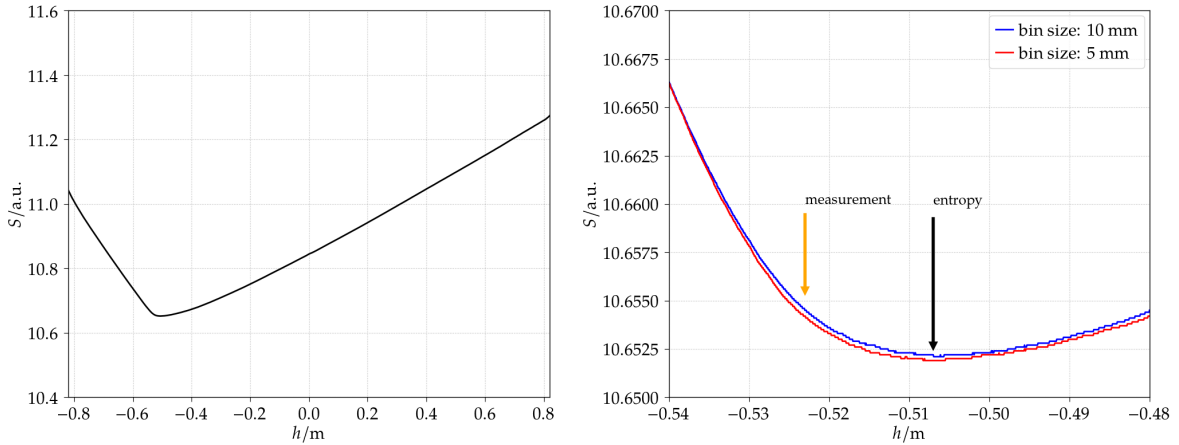
Figure 4.6: *Left:* Entropy values for 1000 equally distributed heights h in the range of $-0.82\,\text{m} < h < 0.82\,\text{m}$. The entropy depicts a minimum at the true height position of the SSD. *Right:* Zoom onto the entropy values in the proximity of the minimum. The entropy is determined for two bin sizes of the distributions, $10\,\text{mm} \times 10\,\text{mm}$ (blue) and $5\,\text{mm} \times 5\,\text{mm}$ (red).

be determined by scanning the height h over a range of possible values between the heights of the upper and lower LST plane.

For the analysis of the height dependence, we define a set of 1000 equally distributed heights in the range of $-0.82\,\text{m} < h < 0.82\,\text{m}$ and calculate the entropy for each h value. The resulting entropy function is displayed in the left diagram in Fig. 4.6. Therein, the decrease of the entropy, i.e., the increase of the image sharpness, is visible when the assumed height values converges to the true height position, ultimately resulting in an entropy minimum. To enhance the precision of the analysis, the height-dependent determination of the entropy was repeated by selecting a shorter range of height values centered around the entropy minimum and applying small height steps. In addition, we analyze the potential effects of the granularity by performing the scanning for two different two-dimensional bin sizes, the default size of $10\,\text{mm} \times 10\,\text{mm}$ and for a bin size of $5\,\text{mm} \times 5\,\text{mm}$. The results of the height scans around the entropy minimum are shown in the right diagram in Fig. 4.6, containing the curve of the scan with the default bin size in blue, and the determination of the entropy with the reduced bin size in red. In the diagram, we can observe that no binning effect is prominent and both curves return an entropy minimum for a height position of $h_{\text{min}} = -0.507\,\text{m}$. This position is highlighted by the black arrow named "entropy". To further compare the height position determined by the data-driven approach with the measuring tape method, the manually obtained height value is added by the orange arrow named "measurement", pointing at $h_{\text{meas}} = -0.523\,\text{m}$. The difference of the two height estimates of $16\,\text{mm}$ can be attributed to various sources of uncertainties, for example the accuracy of the manual measuring tools, the tolerances in the structure of the muon tower, as well as systematic uncertainties in the calculation of the entropy on the efficiency distributions. Overall, we can conclude that the information entropy can be used as a measure of the sharpness of a two-dimensional image and a valid estimate of the intersection plane position can be derived.

4.2 Validation measurements

With the start of the main production of the SSDs at the end 2017, the regular test measurements of each scintillation detector became essential for the assurance of a constantly high level of quality. Already in 2016, the first 14 prototype SSDs for the AugerPrime engineering phase

Figure 4.7: Construction area for the assembly of the 661 SSDs at the Institute for Astroparticle Physics at the KIT. The two assembly tables can be tilted up to ~80° to avoid a bending of the fibers during the gluing process. The surrounding curtains provide a protection of the sensitive scintillator bars and fibers against UV radiation. Taken from Ref. [125].

were assembled at the Institute for Astroparticle Physics at the KIT. Before these detectors were shipped to Argentina, the first SSD performance tests inside the muon tower were carried out. A summary of the results of these test measurements is internally presented in Ref. [124]. In the transition from the engineering to the main production phase, minor changes in the final detector design were applied, and a small number of adaptations and optimizations of the test measurement procedure have been implemented. One example of the changes is the use of a silicone pad. At the time of the engineering phase, an additional transparent silicone rubber pad with a thickness of 2 mm was foreseen as the optical coupling between the ends of the wavelength-shifting (WLS) fibers glued in the cookie and the entrance window of the PMT to enhance the photon transmission. After several measurements with and without a silicone pad, the use of the pad was rejected due to the fact that the light yield enhancement by the silicone pad was only marginal. With this decision the general detector design and measurement process including regularly entering and removing the PMT into the SSDs was simplified.

The SSD main production at the KIT lasted approximately three years, starting in November 2017, and was completed in August 2020. In total, 661 SSDs have been assembled and tested, following a uniform production and measurement procedure. The production was carried out with a maximum assembly rate of six SSDs per week. This rate was limited by the availability of only two tables for the parallel assembly of the detectors and the minimum curing time of the optical cement of 24 h which prohibited a movement of the detector. A photo of the assembly set-up for the active detector components including the tiltable tables can be seen in Fig. 4.7. A summary of the SSD main production process in the Pierre Auger Collaboration, as well as a description of the detector assembly and test procedure is given in Ref. [125].

The daily laboratory measurements of the SSDs inside the muon tower defined the last
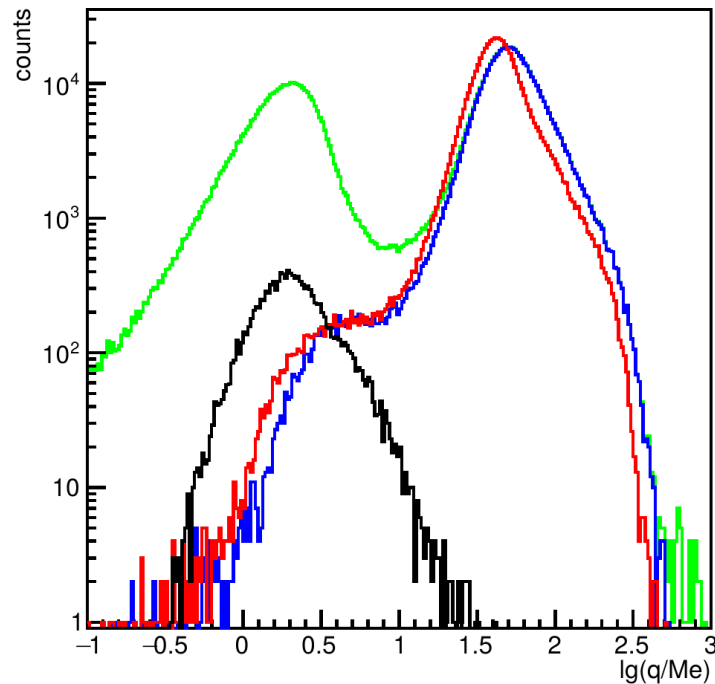
Figure 4.8: Histograms of the pulse charges of different pulse categories for the measurement of the detector SSD-02-KA-0341. The green curve displays the charges of all detected pulses, the black histogram contains all pulses of the SPE pulse category, and the blue histogram shows the charges of the MIP pulses. The red distribution contains the charges of the vertically equivalent MIP pulses which have been corrected by the zenith angle of the trajectory.

step in the detector production process and were performed immediately after the closing of the detector, before the preparation for the shipment to Argentina. By obtaining various quantities, the general performance of the SSDs can be tested and major criteria for the validation of the detector characteristics can be defined. In these test measurements, the SSDs were checked if they fulfill the minimum requirements formulated in Ref. [5], and at the same time if a high production quality over the long time period can be assured. Thereby, the duration of the measurements varied from SSD to SSD. While the majority of the detectors were measured for several hours inside the muon tower, a few SSDs have been studied in measurements that prolonged more than 14 days. In total, nearly 20 thousand measurement hours of SSDs with the muon tower have been acquired. Additionally, the detector placed inside the muon tower had to be exchanged between the measurements, requiring an average exchange time of 30 min for each SSD. In general, a test measurement of a few hours inside the muon tower is sufficient to determine the performance quantities with an acceptable precision.

Due to the high resolution of the muon tower set-up, we have the possibility to discover potential malfunctioning parts, e.g., broken fibers or damaged scintillator bars, which would negatively influence the detection efficiency and light output. In the following, the results of the SSD validation measurements are presented, focusing on the light yield of each of the SSDs, their spatial homogeneity and signal uniformity, as well as the analysis of the light tightness of the detector enclosure. The results of the measurements carried out at the KIT are stored together with the test measurements of all other production sites in a joint database [134].
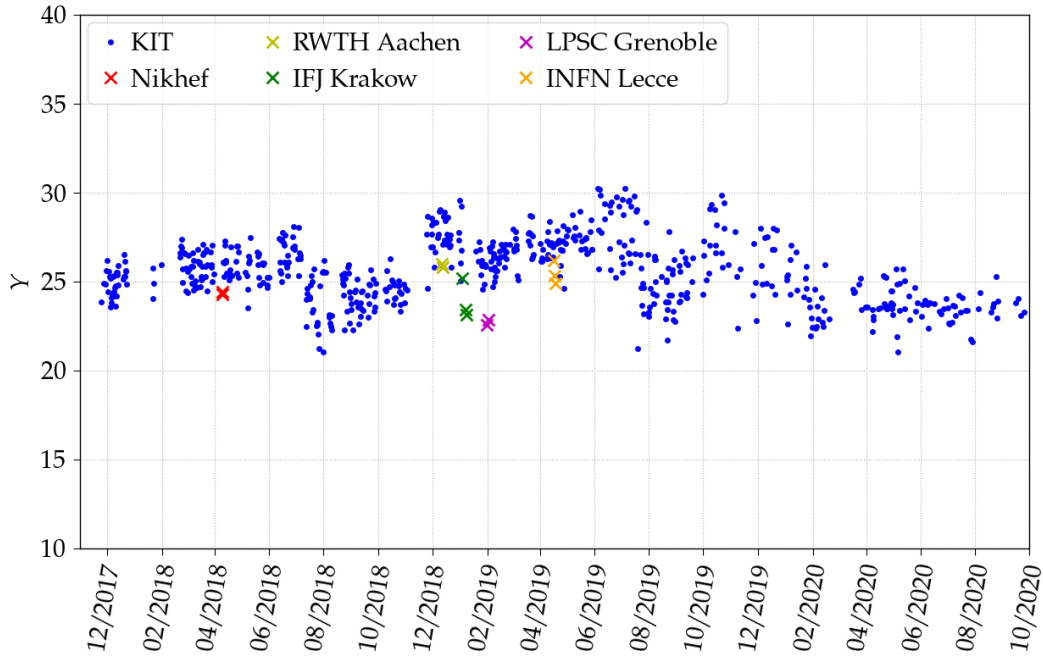
Figure 4.9: Light yield values of all SSDs depending on the date of the measurement. The results for the 661 SSDs produced and tested at the KIT are shown in blue. Additionally, the results of the SSDs assembled by the other production sites of the Pierre Auger Collaboration are included.

4.2.1   Light yield and production uniformity

In the muon tower measurements, all signal pulses detected with the SSDs in the time window around the coincidence trigger time stamp are stored. From these time traces, several quantities are derived of which the pulse charge represents one of the most important observables to describe the detector performance. Thereby, the pulse charges are obtained by integrating the time bin entries after the subtraction of the baseline. With the separation of the pulses into different categories, we can then determine the respective charge distributions. The diagram in Fig. 4.8 displays the various distributions of charges from the validation measurement of the detector SSD-02-KA-0341. Therein, the green histogram contains the charge values of all detected pulses in the data set, and the charge distribution of the selected SPE pulses is shown by the black histogram. The blue and red histograms represent the charge distributions of the MIP pulses and the vertically equivalent MIP pulses, respectively. Thereby, the vertical MIP pulse charges are calculated from the omnidirectional MIP pulses by multiplying them by the factor $\cos\theta$.

For the determination of the most probable SPE pulse charge Q_{SPE}, as well as the most probable MIP pulse charge Q_{MIP}, both distributions are separately fit with a Gaussian function at the position of their respective maximum. With these charge values, the light yield Y of each SSD, i.e., the average light output for through-going single particles in numbers of produced photoelectrons, can be determined by calculating the ratio of the most probable MIP pulse charge and the most probable SPE pulse charge

$$Y = \frac{Q_{\mathrm{MIP}}}{Q_{\mathrm{SPE}}}.\tag{4.4}$$

This light yield then serves as an unified quantity to generally describe the detection quality of the SSDs.

After the measurement of the 661 SSDs, the average light yield of each individual SSD over the total production and test period are shown in the diagram in Fig. 4.9. Therein, the
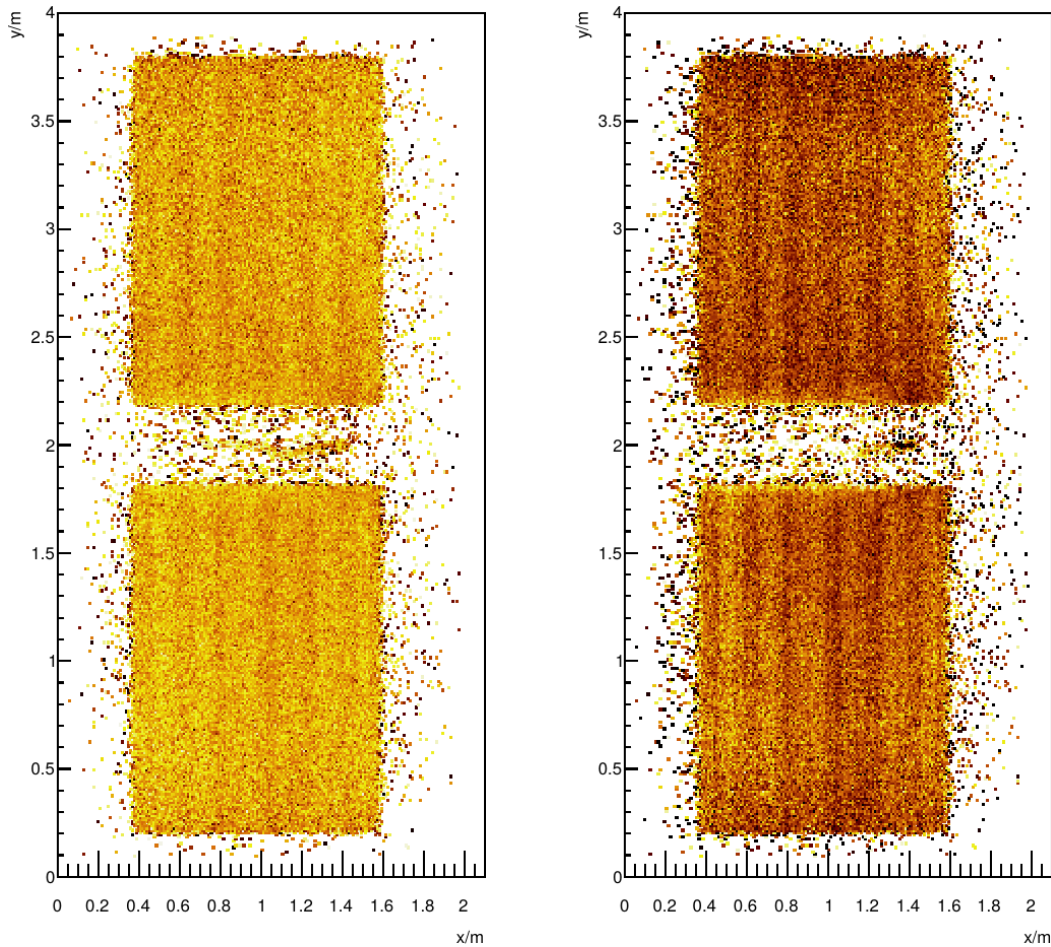
Figure 4.10: Two-dimensional average charge distributions from the measurement the detector SSD-02-KA-0341. *Left:* Averages of the linear charges. *Right:* Average of the logarithmic charges.

results for the 661 SSDs assembled at the KIT are displayed by the blue markers, including the measurements with all three different PMTs introduced in Section 4.1.2. When analyzing the measurements of all the SSDs, we can observe that no SSD was found which strongly diverges from the average light yield. The variances of the light yields are rather small, i.e., for the majority of detectors below 10 % and all measured SSDs surpass the minimum light yield requirements formulated in Ref. [5]. For a comparison of the scintillation detectors assembled by the other production sites, several SSDs of each site were transported to the KIT and measured inside the muon tower with the respective PMT at that time. The light yield results of these detectors then have been added in Fig. 4.9, indicated by the colored crosses. When comparing to the average light yields of the SSDs produced at the KIT, all externally assembled SSDs provide values well inside the range of the regular fluctuations between individual SSDs. This implies that the detectors of all the production sites fulfill the necessary quality standards and minimum requirements which are crucial for a successful outcome of the AugerPrime upgrade.

4.2.2 Spatial homogeneity and signal uniformity

Besides the light yield, the spatial homogeneity and general signal uniformity over the surface area of the newly assembled SSDs is of high importance for the later performance as a sub-detector of the SD of the Pierre Auger Observatory. For this reason, we analyze the average MIP pulse charges measured with the PMTs inside the SSDs in dependence of the intersection
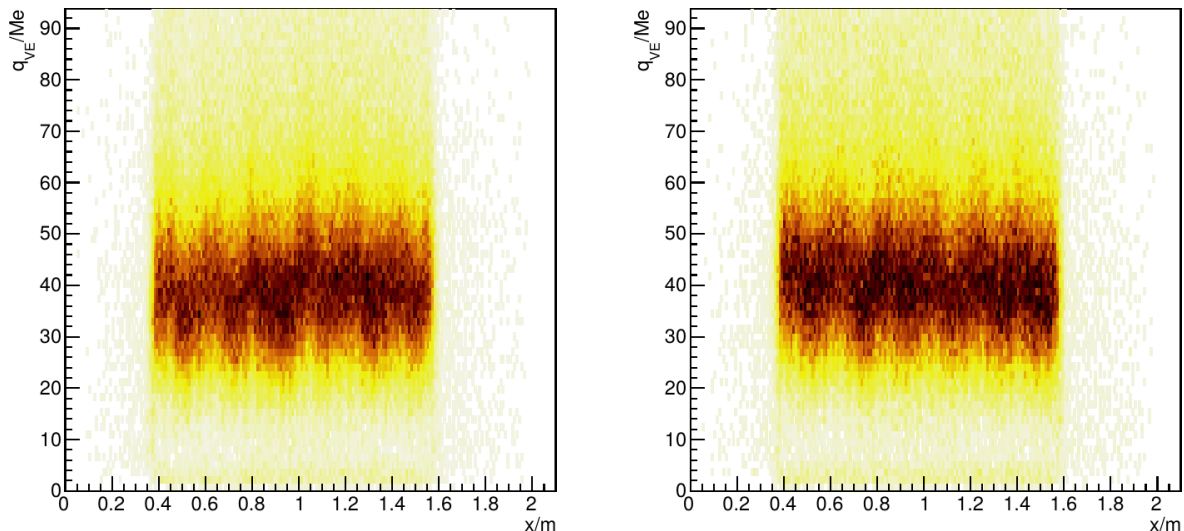
Figure 4.11: Projections of the MIP pulse charges onto the x-coordinate separated for the two active modules of the SSD. The color scale indicates the particle intersection density. *Left:* Projection of the SSD wing spanning $0\,\mathrm{m} < y < 1.9\,\mathrm{m}$. *Right:* Projection of the SSD wing spanning $2.1\,\mathrm{m} < y < 4\,\mathrm{m}$.

position from the reconstruction of the through-going particle trajectories. Thereby, the high resolution of the trajectory reconstruction of the muon tower offers the possibility to analyze the pulse charges with a resolution of $1\,\mathrm{cm} \times 1\,\mathrm{cm}$. In the two diagrams in Fig. 4.10, the two-dimensional distributions of the average charge values from the measurement of the detector SSD-02-KA-0341 are presented. In both diagrams, the color scale describes the average pulse charge in each spatial bin, i.e., the darker the color of a charge bin, the higher is the average signal at this position. While in the diagram on the left, the average pulse charges are displayed in a linear scale, the diagram on the right contains the identical set of pulses, but the average of the logarithmic charges is highlighted by the color.

In both diagrams, we can observe that variances in the average pulse charges appear along the x-coordinate which seem to match the positions of individual scintillator bars. Especially in the right diagram, the average charge values resolve single scintillator bars due to the enhanced contrast, and even the response differences of single fibers can be assumed. With these average charge distributions, a measure is provided to search for potentially damaged scintillator bars or broken fibers which would visibly reduce the measured signals in a defined region on the detector surface. During the total SSD production phase, no detector has been found with a visible malfunctioning component. Nevertheless, in the signal uniformity diagrams, the limitations of the test set-up can be observed. Despite the fact that the muon tower and the probe detector readout chain provide a robust method to assign the signals from the SSD to the intersection points of the precisely reconstructed particle trajectories, a small amount of pulses from particles that missed the SSD appear in the data. These events are the consequence of random coincidences of the signal in the SSD with a different particle reconstructed by the muon tower.

To further analyze the signal uniformity of the SSDs, the projections of the MIP pulse charges across and along the scintillator bars and fibers are determined. For the analysis of the individual scintillator bar variances which can be observed in the two-dimensional average charge distributions, the projection of the charge values onto the x-coordinate are calculated. Thereby, the projections are separately calculated for the two active modules of the SSD. In the diagrams in Fig. 4.11, the charge projections are shown. The diagram on the left displays the projection of the charges for the SSD wing which spans from 0 to $1.9\,\mathrm{m}$ on the y-coordinate. The diagram on the right contains the values of the other wing
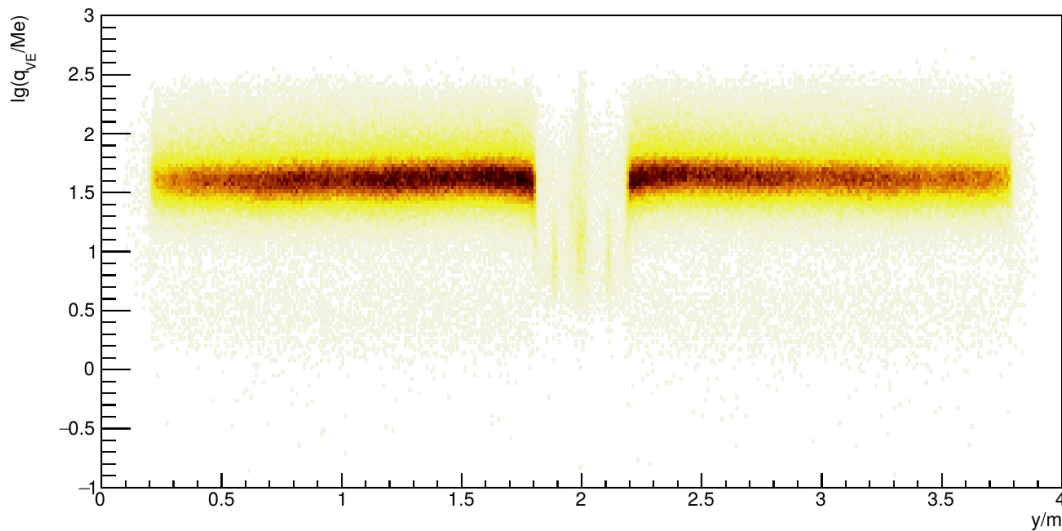
Figure 4.12: Projections of the MIP pulse charges onto the y-coordinate. An increased detection efficiency of particles passing close to the center of the SSD can be observed related to attenuation effects on the photons with different travel-path lengths.

which is placed inside the muon tower from 2.1 to 4 m in y-direction. In both diagrams the shapes of individual scintialltor bars can be observed due to the small differences in their signal response. Here, the color scale indicates the density of particle intersections at the respective x-coordinate. This density appears to be stable over the total width of the SSD indicating a homogeneous detection efficiency across the scintilator bars. For the comparison of the responses of individual scintillator bars, the MIP pulse charges are displayed in a linear scale in both diagrams. Overall, a maximum difference between bars of ~10 % can be observed which matches the results obtained in similar measurements of the engineering-design SSDs. As an explanation for the periodically alternating responses of the scintillator bars, the routing of the fibers through multiple scintillator bars can be mentioned. The optical fibers represent the mechanically weakest part in the detector assembly, and therefore have the highest probability of being damaged.

Additionally to the projections across the scintillator bars, the charge projection onto the y-coordinate, i.e., along the scintillator bars, provide valuable information about the general performance and spatial homogeneity of the SSDs. The resulting projection for the measurement of detector SSD-02-KA-0341 is shown in the diagram in Fig. 4.12. Analogously to the other projections, the color scale represents the density of particle intersections, which indicates an increased detection efficiency in the center of the SSD, i.e, close to the PMT. This can be explained by attenuation effects on signals from particles passing at the edges of the SSD due to the long travel paths of the photons. Despite the fact that the detection efficiency is significantly increased by routing the WLS fibers in a U-turn when compared to cutting the fiber at the end of the scintillator bars, the differences of the photon travel lengths impact the number of detected pulses. In addition, we can observe a decrease of the charge values of approximately 5 % along the scintillator bars from the center towards the edges.

In general, we can conclude that the SSDs from the main production display a high level of signal uniformity over the total active surface area. In the validation measurements, the expected detector behavior was reproduced, and no SSD with large spatial inhomogeneity was found.
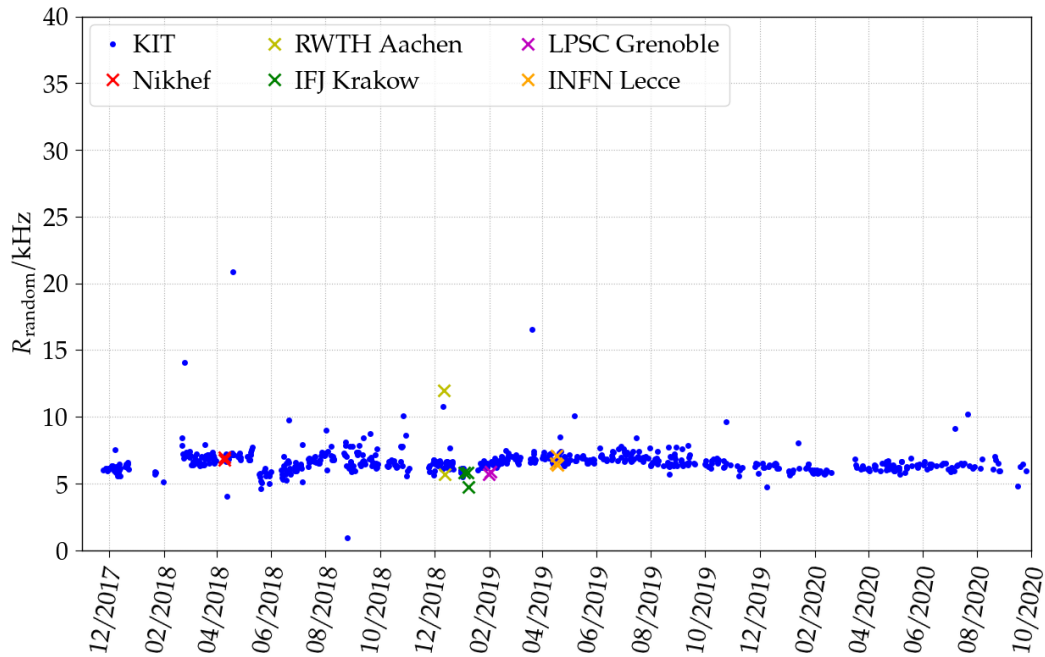
Figure 4.13: Appearance rate of random pulses of all SSDs depending on the date of the measurement. The results for the 661 SSDs produced and tested at the KIT are shown in blue. Additionally, the results of SSDs assembled by the other production sites of the Pierre Auger Collaboration are included.

4.2.3   Light tightness

During the process of the SSD main production, all assembly sites in the Pierre Auger Collaboration encountered issues with the light tightness of the detector enclosure. This was tested in laboratory measurements which included comparisons of the detector responses obtained during daytime and nighttime, as well as in tests using strong light sources. The leakage of external photons into the SSD strongly increases the appearance of noise signals measured with the PMT, and therefore reduces the performance of the detector and accelerates mechanical aging. In the SSD test measurements at the KIT, due to the simultaneous detection of small randomly appearing pulses together with the pulses from through-going particles in the same time traces, an analysis of the general pulse-appearance rate can be carried out. In the case of a light leakage, the number of small pulses sorted into the random pulse category is significantly increased.

In the diagram in Fig. 4.13, the appearance rate of the random pulses of all SSDs from the main production period are presented depending on the measurement date. Identically to the light yield diagram, the results for the 661 SSDs assembled at the KIT are displayed by the blue markers. In this diagram, we can observe that the large majority of scintillation detectors show a stable pulse rate between 5 and 10 kHz. Only a few SSDs indicate an increased rate of random pulses by a factor of 2 to 3. These individual SSDs have been then further investigated by analyzing various performance-sensitive quantities which have been obtained in the validation measurements. When investigating their pulse-appearance time and charge distributions, an additional noise pattern became visible. This noise was related to an external noise signal which was picked up by the PMT readout electronics chain of the SSD, i.e., no light tightness issue of the detector enclosure was found.

Similarly to the light yield comparisons, the pulse appearance rates of the SSDs assembled by the other production sites are depicted in the diagram. The results of these detectors match the average values for the respective PMTs and exclude a potential light leakage issue

for these individual detectors.

4.3   Detector simulation comparisons

In the context of the AugerPrime upgrade, the installation and implementation of the new detector components currently define the major task for the Pierre Auger Collaboration. This includes not only the hardware parts and the data acquisition software for the new configuration of detectors, but also the detailed detector simulations which are implemented in the $\overline{\text{Off}}\underline{\text{line}}$ software framework [70, 71]. These simulations are of high importance to interpret the acquired real air-shower observations, as well as for the development of algorithms and parametrizations to reconstruct the primary CR properties, e.g., the particle masses [135]. In the case of the SSDs, the simulations are based on the detector design and have been developed during the engineering phase of the AugerPrime upgrade. For other sub-detectors, for example the Underground Muon Detector (UMD) modules and the Radio Detector (RD) antennas, the simulations utilize the implementations of the predecessor projects, the Auger Muon Detectors for the Infill Ground Array (AMIGA) and the Auger Engineering Radio Array (AERA). In general, for the simulations of the future AugerPrime SD stations, the relative positions between the individual sub-detectors are very important, especially for the particles which pass through multiple sub-detectors.

In the case of the SSDs, the detector simulations were implemented utilizing data obtained with the first prototype SSDs in the muon tower. To validate the performance and detector properties of the latest SSDs design, the laboratory measurements presented in the previous Section can be used to enable comparisons. The simulation process is based on the Geant4 framework [136] and models the energy deposition in the detectors. With the deposited energy from the through-going particles, the expected effective number of photoelectrons produced at the photocathode of the PMT is determined. Thereby, this number depends on the attenuation of the photons inside the detector which is strongly related to the particle intersection position. In addition to the energy deposit inside the detector, the timing information of the particle intersection, as well as of the production of the photoelectrons, i.e., the arrival of the photons at the photocathode, are simulated. This is realized by a random sampling process of two exponential decay functions for each photoelectron and the addition of the photon travel timing from the particle intersection point to the surface of the WLS fibers.

Despite the fact that several important quantities for the development of the detector simulations had been already determined using the data from the studies of the engineering SSDs inside the muon tower, certain measurements and analyses were repeated using SSDs from the main production. In the following comparisons, a simulation data set of approximately 1.3 million pulses from muon events with a defined average energy of 2.7 GeV have been used. Each of these MIP pulse traces consists of the fixed number of 76 time bins with a bin size of 8.33 ns to match the sampling frequency of the new Upgraded Unified Boards (UUBs) of 120 MHz.

The data obtained with the muon tower was acquired with a measurement of the detector named SSD-02-KA-0127 in April 2018 during the main production validation measurements. At that time, the PMT 1, i.e., the PMT Hamamatsu R9420 with the serial number #DE2779, was in use. In contrast to the regular SSD tests, the sampling interval was decreased from 1.6 to 0.8 ns for this measurement. Thereby, the resolution is improved and the individual signal pulses are better resolved, especially the small SPE pulses. Two data sets from the muon tower measurements for both of the relevant pulse categories have been obtained. The MIP pulse data set contains ~1.4 million particle induced pulses, each with a pulse-trace length of 220 time bins. In these time traces, the first bin surpassing the trigger condition is set to bin number 21. The second data sets consists of ~1.5 million SPE pulses with a fixed number of 170 time bins. Analogously to the MIP pulses, the SPE pulse time traces contain 20 bins
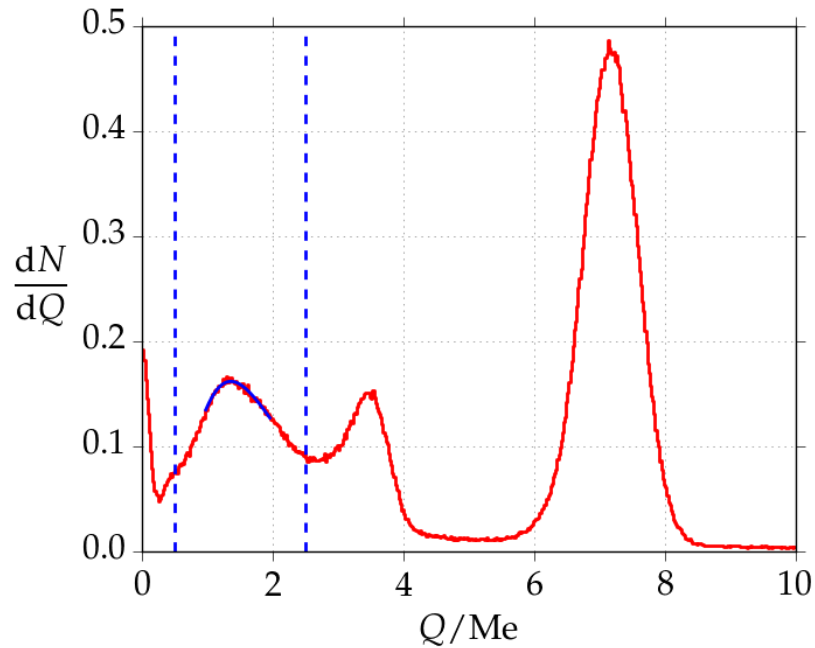
Figure 4.14: Normalized distribution of the SPE pulse charges of the muon tower measurement.Besides the expected charge maximum for the SPEs, two additional peaks produced by external noise are visible. The determination of the average SPE charge value is limited to the pulses in-between the two blue vertical dashed lines. The Gaussian fit is shown by the blue solid curve.

before the trigger bin appears.

To separate the simulated data from the muon tower data in the following sections, the results for the simulations are presented by the color black and the muon tower measurements are depicted by the color red.

4.3.1   Light yield

In the characterization of the SSD signals, the analysis of the deposited energy of the charged particles passing through the scintillator bars plays a major role. Especially, the charge distributions of the MIP pulses and SPE pulses, and the resulting light yield Y values describe the general performance of the detectors in the muon tower measurements, as well as in the simulations. To further study these sensitive quantities, we additionally analyze their dependence on the zenith angle of the through-going particle.

Identically to the light yield analysis in the SSD validation measurements in Section 4.2.1, Y is defined as the ratio of average MIP pulse charge and the average SPE pulse charge, both determined for the measurement data from the most probable signals of the respective distributions. The SPE pulse charge distribution for the muon tower data is shown in the diagram in Fig. 4.14. Therein, three peaks are visible of which only one defines the actual average SPE charge. For this measurement, the pulse filter to suppress the effects of the intrinsic PMT noise and the external noise pick-up was not enabled, and therefore two additional noise peaks detected by the PMT at that time can be seen. Therefore, to determine the average charge of an SPE pulse, the data is reduced to pulses in-between the two blue vertical dashed lines. A Gaussian fit is applied to the maximum of the pulse charge distribution, at ~1.4 Me, which is highlighted in the diagram by the blue solid curve.

Together with the determination of the SPE pulse charges, the charge distributions of the MIP pulses were analyzed. In general, the SSD response mainly depends on two variables,
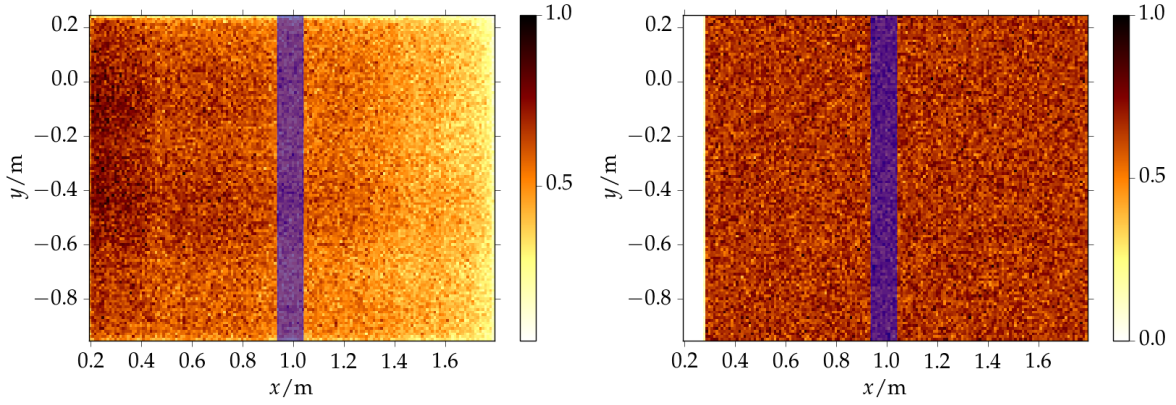
Figure 4.15: Density maps of particle intersection positions with the SSD. For the analysis of the zenith angle dependence, the pulse selection around the optimal distance of $x_{opt} = 0.986$ m is highlighted by the blue area. *Left:* Density map of the muon tower data. *Right:* Density map of the simulation data.

the track length of the particle inside the detector which is defined by the zenith angle of its trajectory, and the intersection position coordinates of the particle with the plane of scintillator bars inside the SSD. To enable comparisons of the muon tower measurement with the simulation results, the original intersection position coordinates of the muon tower are converted to the SD station coordinate system which originates in the center of the water-Cherenkov detector (WCD). In addition, the intersection area, defined by the coordinates x and y, is restricted to the dimensions of a single active wing of an SSD, i.e., all intersections of one SSD wing are projected and stacked onto the other wing by using the absolute values for the x-coordinates. The resulting density map of intersections for the muon tower measurement is shown in the left diagram of Fig. 4.15. For the comparison with the simulated pulses, we display the intersection density map obtained with the simulation data in the diagram on the right. Both density maps are generated with a resolution of 1 cm × 1 cm and contain particle trajectories with zenith angles of $0° < \theta < 90°$. While the simulated MIP pulses are generated uniformly over the whole module, the intersection position density of the measured data reflects the spatial efficiency of the muon tower as already introduced in Section 4.1.2. This results in a higher intersection density close to the center of the SSD, i.e., at smaller x values.

Before applying any constraints on the interaction position or on the zenith angle distribution, we obtained the MIP pulse charge distributions of both data sets. The results are shown in Fig. 4.16, in the left diagram for the measurement data and in the right diagram for the simulations. The MIP pulse charge distribution of the simulated data was thereby determined from the original distribution of the effective number of photoelectrons and assuming a constant SPE pulse charge. Both distributions are then individually fit by using Landau distributions, indicated by the blue curves. With the most probable charge values of the MIP pulses and SPE pulses, the light yield of the SSD for the measurement data can be calculated.

For the further analysis of the zenith angle dependence, only MIP pulses inside a defined small intersection area were selected. If we assume a homogeneous response between individual scintillator bars, then only the x-coordinate, i.e., the coordinate along the scintillator bars, influences the measured signal. This position dependence of the signal can be described by the attenuation function which depicts its average value in the center of the scintillator bar at an optimal value of $x_{opt} = 0.986$ m. Therefore, the MIP pulses are selected within a range of -0.05 m $< x_{opt} < 0.05$ m. In both intersection density maps in Fig. 4.15 these constraints are highlighted by the blue area. After the restrictions on the intersection coordinates, the reduced data sets contain approximately 85 thousand MIP pulses each.
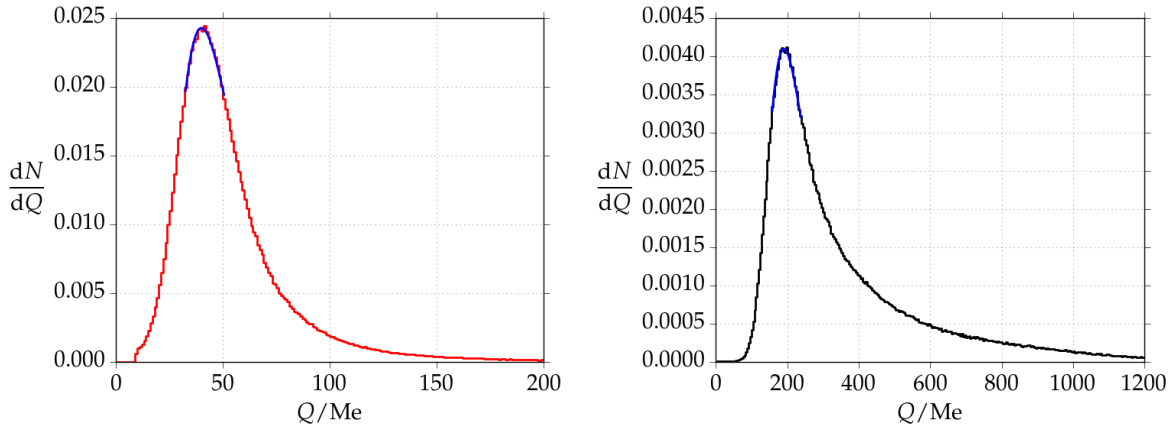
Figure 4.16: Normalized distributions of the MIP pulse charges. The resulting fit curves at the maxima of the distributions are shown by the blue solid lines. *Left:* Distribution of the muon tower data. *Right:* Distribution of the simulation data.
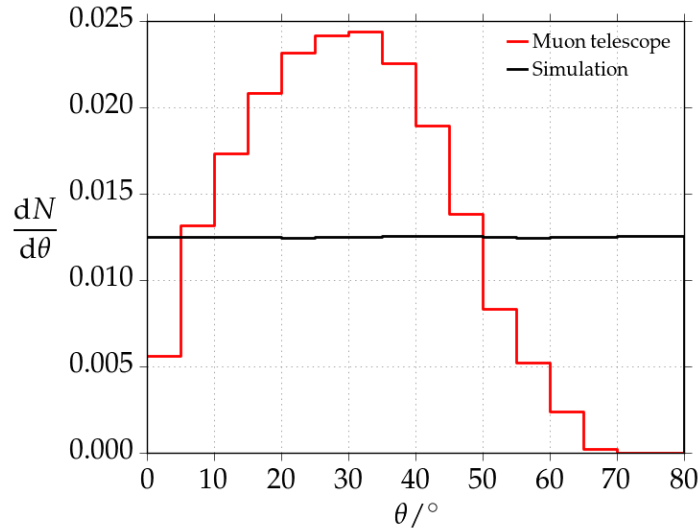
Figure 4.17: Zenith-angle distributions for the muon tower data set in red and the simulation data set in black. While the muon tower is unable to measure trajectories of particles with zenith angles $\theta > {\sim}60°$, the simulated data is generated with a flat zenith-angle distribution.

The determination of the zenith angle dependence was then performed by binning the data sets in intervals of $\Delta\theta = 5°$ over the whole range of $0° < \theta < 90°$. The resulting zenith angle distributions of both distributions are shown in Fig. 4.17. The simulation data is generated with an equally distributed number of pulses per bin over the total zenith angle range. In contrast, similarly to the intersection plots, the zenith angle distribution of the muon tower data displays the spatial efficiency of the measurement set-up with a defined maximum up to intermediate zenith angles of ${\sim}60°$.

Subsequently, the MIP pulse charge distributions for each zenith angle bin were determined and the average MIP charge value Q_{peak} is determined by fitting Landau functions to the distributions. The resulting charge peak values are presented in the diagrams in Fig. 4.18. Therein, the determined charges of both data sets show a similar functional behavior and can generally be described with the function

$$Q_{\mathrm{peak}}(\theta) = A \sec \theta = \frac{A}{\cos \theta}. \tag{4.5}$$
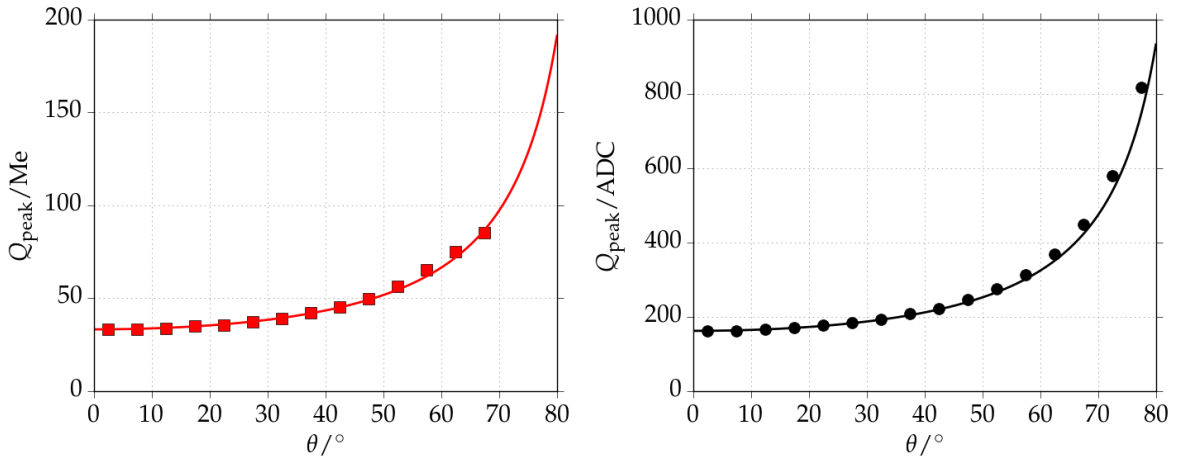
Figure 4.18: Zenith angle dependence of the MIP pulse charges for both data sets. *Left:* For the muon tower data. *Right:* For the simulation data.
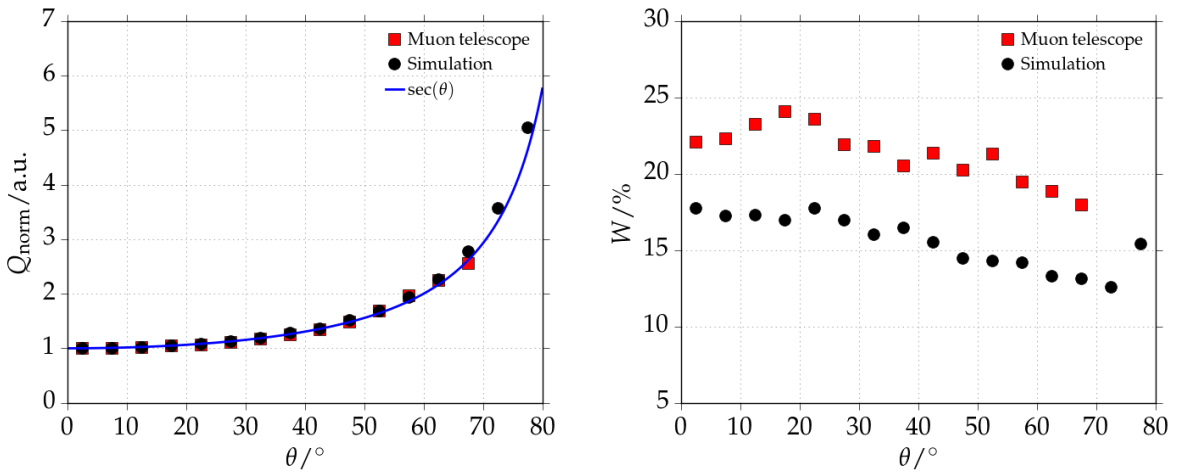
Figure 4.19: *Left:* Zenith-angle dependence of the normalized charge values for both data sets. The blue curve represents a general secant function. *Right:* Zenith-angle dependence of the relative width of the peaks of the respective charge distributions.

Here, A defines a constant amplitude. To compare the functional shape of the muon tower data and the simulations, the charge values are normalized by applying individual fits using the functional behavior and then dividing by the amplitude A. The results for both data sets can be seen in the left diagram in Fig. 4.19. Therein, the blue curve highlights the secant function of the zenith angle. We can observe that the behavior of the simulated pulses perfectly matches the measurement from the SSD in the muon tower. Furthermore, the quality of the fits can be described with the relative width of the peaks of the respective charge distributions which is defined as

$$W = \frac{\delta Q}{Q_{\text{peak}}}. \tag{4.6}$$

The results for the analysis of the peak width are presented in the right diagram in Fig. 4.19. In general, the relative peak width decreases with an increasing zenith angle which can be explained with faster scaling of the charge value than the width of the peak. When comparing the muon tower measurements with the simulations, the distributions from the simulations appear narrower. This fact might indicate that the simulations are slightly overestimating the absolute light yield of the SSD.
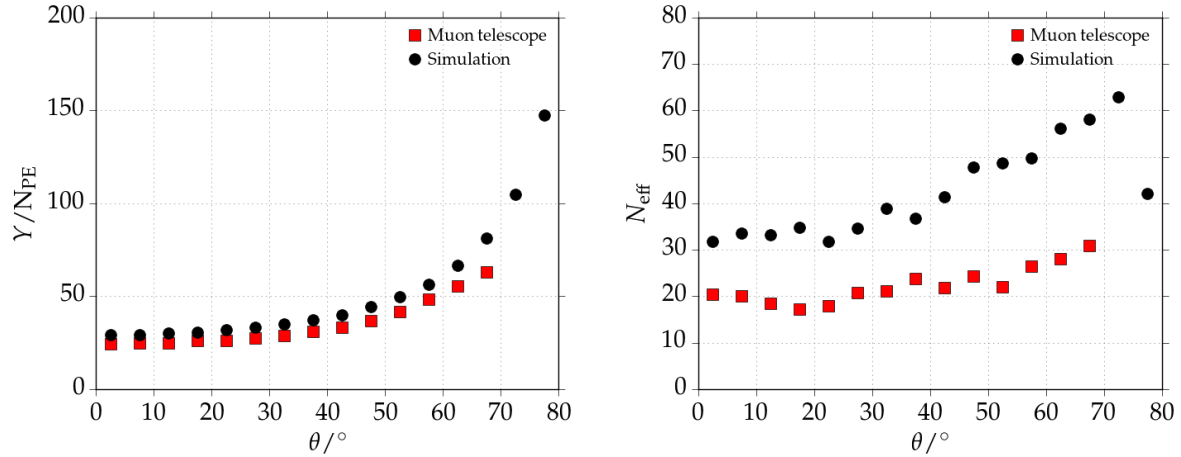
Figure 4.20: *Left:* Zenith-angle dependence of the light yields for both data sets. *Right:* Zenith-angle dependence of the effective number of photoelectrons.

To further analyze this potential behavior, the light yield values Y, i.e., the ratio of the MIP pulse and SPE pulse charges, for each zenith angle bin have been compared. The resulting values for both data sets are displayed in the left diagram in Fig. 4.20. In the diagram, we can observe that while the functional shapes of both data sets match each other, the light yields determined with the simulation data appears to be larger than the measurement data by a zenith dependent offset. This is an additional indication that the initial light-yield estimate obtained in the measurements of the engineering SSDs are at a higher level compared to the SSD from the main production. Nevertheless, we have to state that the absolute light yield strongly depends on the used PMT and fluctuates between individual detectors.

Finally, an approach to determine the light yield was tested only using the MIP pulse information, i.e., without the normalization to the PMT dependent SPE response. If we assume that the effective number of photoelectrons created at the photocathode follows a pure Poisson distribution, i.e., $\delta N_{\text{eff}} = \sqrt{N_{\text{eff}}}$, and is proportional to the deposited charge, the effective number can be calculated as

$$N_{\text{eff}} = \left(\frac{Q_{\text{peak}}}{\delta Q}\right)^2 . \tag{4.7}$$

In this equation, Q_{peak} represents the charge peak value, and δQ the uncertainty of the distribution, i.e., a measure of the peak width. The resulting curves for both data sets are displayed in the right diagram in Fig. 4.20. The calculated N_{eff} values for both data sets indicate the expected increase with an increasing zenith angle. Similarly to the previous comparison of the widths of the charge distributions, the simulated data shows a narrower charge distributions for the same amount of deposited charge compared to the muon tower measurement data which can be related to unknown scaling factors when using different detection devices.

4.3.2   Pulse shape

Besides the light-yield and pulse-charge analyses of the SSD signals, the shape of the pulse traces for SPE and MIP pulses were studied. Due to the appearance of noise fluctuations on the PMT signal, the pulse traces of the muon tower data set are filtered with an upper bandwidth filter resulting in smoother shapes of the traces. Thereby, the applied filter is a 5th order Butterworth low-pass filter with an upper bandwidth limit of 65 MHz which is similar to the Bessel filter implemented on the AugerPrime electronics boards which are sampling
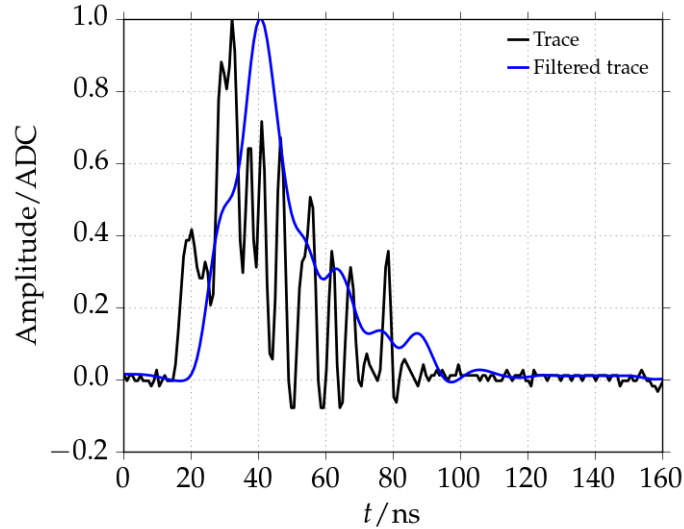
Figure 4.21: Example MIP pulse trace of the muon tower measurement data. The unfiltered trace with bin-to-bin fluctuations is shown in black, whereas the blue curve depicts the same trace after the filtering process.
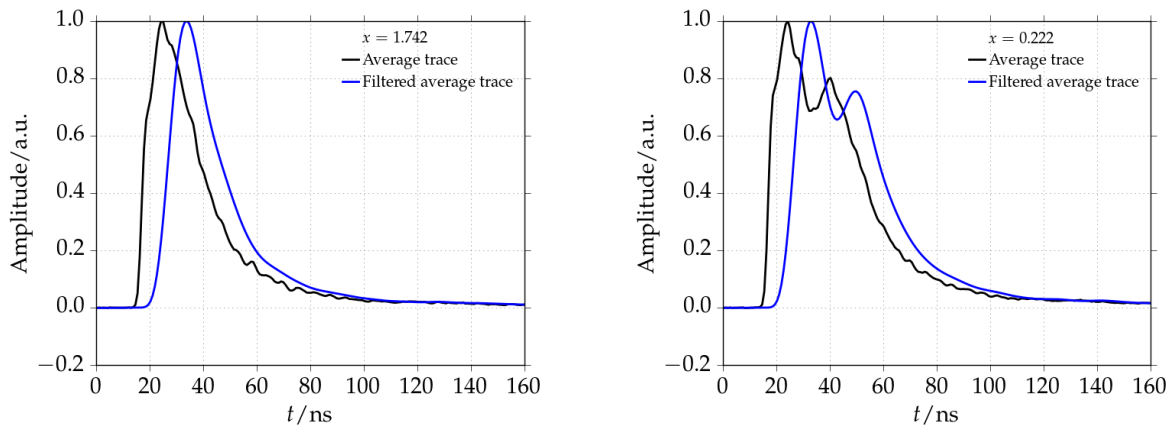
Figure 4.22: Average MIP pulse traces from the muon tower measurement. *Left:* Averages for an intersection area close to the edges of the SSD, i.e., for large x values. *Right:* Averages for an intersection area close to the center of the SSD, i.e., for small x values.

the signals of all PMTs of an SD station at a frequency of 120 MHz. The sampling frequency of the PicoScope used in the muon tower measurements is set to 1.25 GHz and the analog bandwidth is 350 MHz. An example MIP pulse time trace from the measurement in the muon tower is presented in the diagram in Fig. 4.21. Therein, the black curve displays the unfiltered trace with a large number of fluctuations, while the filtered trace in blue appears smoothed.

When analyzing the MIP pulse time traces, the SSD design containing the WLS fibers in a U-turn routing and thereby providing two paths for the photons to travel, results in a variation in the shape of the MIP pulse traces depending on the point of intersection. Therefore, we divided the active wings of the SSD into small slices along the scintillator bars, i.e., along the x-coordinate, with a slice width of 2 cm. For each slice, an average pulse trace is calculated for both types of traces, the filtered and unfiltered. If the particle passes through the detector close to the edges of the SSD, i.e., for a large x-value, a single peak in the trace is visible, as can be seen in the left diagram in Fig. 4.22. In this case, the lengths of the two
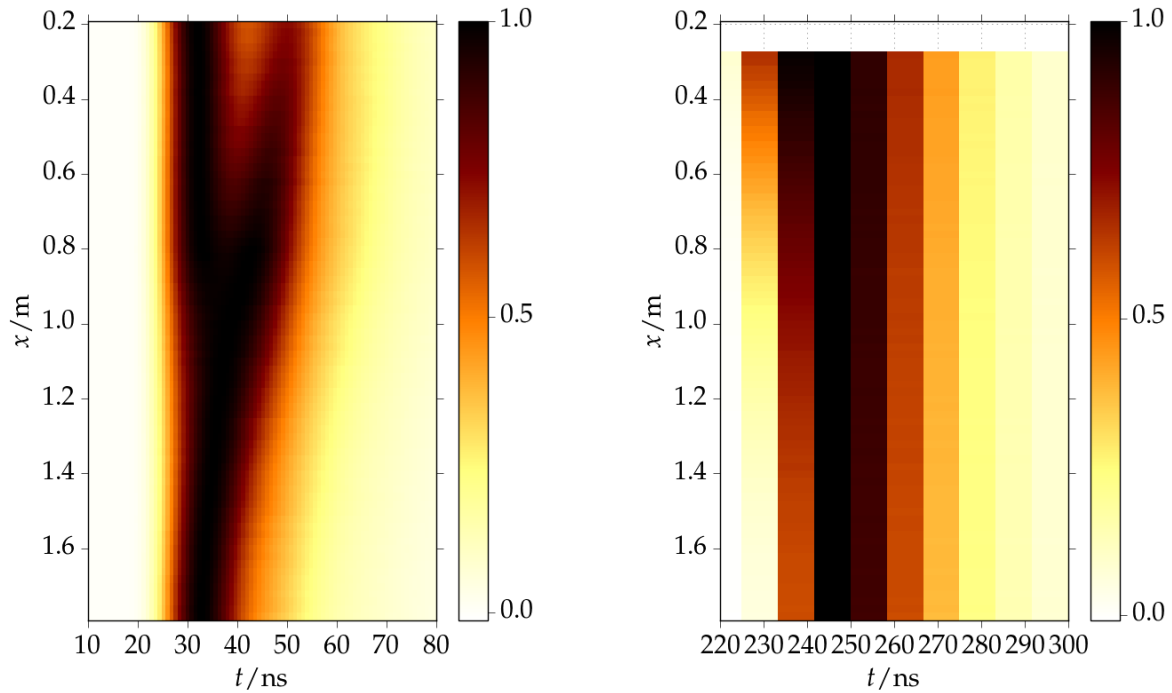
Figure 4.23: Two-dimensional distributions of the average pulse amplitudes. *Left:* Distribution of the muon tower data. *Right:* Distribution of the simulation data.

photon travel paths are nearly identical, resulting in the photons arriving at the same time at the PMT. Thereby we can note that by calculating the average traces, the impact of the single time bin fluctuations is significantly reduced and the general shape can be determined with the unfiltered traces. In contrast, if the particle deposits its energy close to the center of the SSD, i.e., for a small x-value, a clear double peak structure can be observed in the average trace which is shown in the right diagram in Fig. 4.22. This shape can be explained with the differences in the lengths of the photon travel paths, and therefore, the different photon arrival times at the PMT.

To show the dependence of the pulse trace shapes with the x-coordinate of the intersection position, i.e., the development along the scintillator bars, the average trace of each x-slice of the measurement data are displayed in the two-dimensional distribution in the left diagram in Fig. 4.23. Therein, the color scale represents the normalized trace amplitude, with the darkest color for the maximum value. In the distribution, the change of the shape along the scintillator bars is clearly visible, from a single peak appearing in traces with large x-values to a double-peak structure for pulses from particles passing close to the center of the SSD. This result matches the observations with the prototype SSDs and confirms the time trace parametrization. In addition, the analogous amplitude distribution for the simulated data is shown in the right diagram in Fig. 4.23. Similarly to the measurement data, the increase of the width of the pulses for smaller x values can be seen. But due to the limited time resolution, the detailed pulse shape cannot be resolved.

4.4   Summary and conclusions

The laboratory measurements of the performance of the newly assembled SSDs not only serve as a quality assurance in the detector production process, but also define a crucial step in the validation of one of the most important hardware components for the AugerPrime upgrade of the Pierre Auger Observatory. For this reason, the analyses presented in this Chapter

address several major questions: Can the SSDs in their final version reach the requirements which have been defined during the planning and designing phase of the upgrade? Is a stable and continuous detector assembly on a large scale in combination with a high level of production quality achievable? And furthermore, can the detector simulations be validated and potentially further optimized to match the measured data?

To answer all three questions, a measurement set-up is required which needs to fulfill various criteria. For a precise measurement of the most important quantities to describe the performance of the SSDs, a reliable and large set-up is required. This is realized with the "muon tower" test stand which is introduced in detail at the beginning of this Chapter. The moun tower is equipped with a coincidence trigger of three LST planes in which are able to precisely reconstruct the trajectories of single charged particles. By utilizing the charged particles of air showers constantly arriving at the ground, the SSDs can be analyzed concerning their signal response to these particles, and thereby conclusions on their future behavior in the Observatory can be drawn. Due to the large size of the muon tower, one complete SSD can be measured at the same time. And with the knowledge of the height position of the SSD inside the set-up which is obtained with a data-driven method developed in this Dissertation, the performance of the SSDs can be analyzed in detail.

The performance analysis of the SSDs produced at the KIT defines the second part of this Chapter and relates to the first two questions formulated above. Thereby, we focused on the determination of three major quantities to describe the detector characteristics by analyzing the nearly 20 thousand hours of measurements. One of these quantities is the light yield of the SSDs which represents a measure for the average light output when a single particle passes through the detector. In the analysis of the validation measurements, we presented that all SSDs provide a stable performance and a comparable light yield with variations below 10 % between the individual detectors.

Besides the light yield, the spatial homogeneity of the newly assembled scintillation detectors was analyzed in detail. To realize this, the spatial distributions of the pulse charges have been obtained. With these distributions, as well as with the projections of the pulse charges onto the two sides of the SSDs, the response variations of individual scintillator bars and the inserted fibers can be resolved. This resolution offers the possibility to search for malfunctioning detector components, e.g., broken fibers, which would reduce the signal uniformity. During the studies of the SSD production we did not find a detector with spatial inhomogeneities above the expected fluctuations of ~10 % from statistical and systematic uncertainties.

To further analyze the hardware components of the SSDs, the light tightness of the aluminum enclosure has been studied. For this check, the total number of pulses obtained in the measurements of the SSDs have been used to derive a measure of the appearance of small pulses. If external photons enter the SSD, a strong increase in the detection of noise pulses is expected. By analyzing the appearance rate of these pulses, we determined the general detector behavior concerning light leakage. A few potential candidates for a light leakage have been found and individually checked. For these SSDs, external noise pulses related to the readout electronics chain have been found. After removing the identified noise pulses, no further light leakage pulses have been observed.

Conclusively, no decrease in the quality or the uniformity of the SSDs was observed over the total production period, and we were able to show that a stable production of more than 660 detector units over a duration of nearly three years was achievable. This number represents nearly 44 % of the total number of SSDs produced by the Pierre Auger Collaboration. Furthermore, we can conclude that the requirements on the new scintillation detectors have been fulfilled.

Finally, together with the muon tower measurement data obtained for the SSDs, comparisons with the detector simulations implemented in the Offline software framework have been

presented. In these comparisons, we showed that the light yield values in the measurement of a main production SSD indicate the expected geometrical behavior. Under the assumption of a constant scaling factor, these light yield values are comparable with the data from the detector simulations which had been tuned with measurement results from the engineering phase. This further indicates that the differences in the absolute light yields are induced by the properties of the different PMTs used in the measurements. When analyzing the average pulse shapes in the latest laboratory measurements, the distributions strongly match the previously determined detector measurements, as well as the simulation results, and therefore a successful validation of the required signal response can be attested. To further proof this statement for the SSDs and other components of the AugerPrime upgrade, the following Chapter extends the performance analysis to measurements under field conditions in the Observatory.

Chapter

5

AugerPrime Detectors in the Observatory

Simultaneously to the production and validation measurements of the new Surface Detector (SD) sub-detectors presented in the previous Chapter, the AugerPrime upgrade entered the testing phase of the first prototype components under field conditions in the Observatory. Starting in the second half of 2016, the first test array has been selected and prepared by transporting SD stations at predefined positions together with the installation of the first new Surface Scintillator Detectors (SSDs), and electronic boards. The field performance studies of these newly introduced hardware are crucial in the finalization of the design decisions of the individual upgrade components and define the main content of this Chapter. Herein, we analyze the data acquired with the new electronics and detectors in the field regarding different aspects of data quality, for example the noise levels, the dynamic range capabilities, and the general signal stability under changing environmental conditions. This is realized by analyzing time traces detected with the different detectors and devices, together with monitoring data, while the information from the calibration data stream is studied in the subsequent Chapter. Additionally, an overview of the various deployments and configurations of different upgrade parts is given.

In detail, this Chapter is divided in four major parts, starting with the analyses of the station electronics performance by focusing on the comparison of the different versions of the new electronics boards, named Upgraded Unified Boards (UUBs), which have been installed and exchanged over the test phase of more than four years, including comparisons with the original electronics boards, the so-called Unified Boards (UBs). The performance studies are followed by the detailed description of the two AugerPrime test arrays containing stations equipped with the new electronics and detector components, the AugerPrime Engineering Array (EA) acquiring data from 2016 until 2021, and the follow-up array, the Upgraded Unified Board pre-production array (UUB PPA), launched in 2020. This additionally includes an overview of the operation status over their respective lifetimes. Subsequently, we introduce the Surface Scintillator Detector pre-production array (SSD PPA) which was in operation from 2019 until 2021, and served as an intermediate test configuration for in-depth studies of the scintillation detectors under field conditions before a sufficient amount of new electronics boards have been available. In the last part of the Chapter, we show the effects of changes of

environmental conditions on the signals observed with the upgraded detectors. This includes the analysis of thunderstorm events with data from both, AugerPrime and non-upgraded stations, as well as dependence checks from temperature fluctuations and their effects on the signal stability. As the main sources for the information about the installed hardware, the locations of individual detector stations, and measurement periods, we use three databases and work logbooks, the Auger electronic logbook (Elog) [137], the Auger Parts Management System (PMS) [138], and the Auger monitoring database [139].

5.1   Upgraded Surface Detector electronics

With the AugerPrime upgrade, a new version of electronics boards, the UUBs, will be installed in all of the SD stations (approximately 1660) and will replace the currently used UBs. The new electronics was designed and developed within the Pierre Auger Collaboration and passed through multiple design changes and test phases since the first prototype was produced in 2016. Four different versions of UUBs have been developed, produced and tested, until in 2021, the final design was chosen and the mass production at the company SITAEL [97] was launched. In the following sections, we present multiple studies and tests of the performance of each UUB version, the three prototype versions V1, V2, and V3, as well as the pre-production version. These checks and analyses have been performed continuously over total test period and for each version to provide regular feedback to the design and construction team, ultimately leading to electronics board layout changes and improvements during the transition to the next electronics version.

As an introduction to the electronics comparisons, a general overview of the characteristics of both, the originally used UB and the new UUB with all its different versions is given. Then, we present the analysis of the electronics behavior and noise levels for all electronics versions, as well as a data-driven determination of the gain amplification of the input channels of the boards.

5.1.1   Electronics board generations

Unified Board (UB)

In the SD array, two different generations of electronics boards are used at the moment. Up to the submission date of this Dissertation, the majority of the SD stations contain a Unified Board (UB) which was designed in the early 2000s and intensively tested and used in the Observatory dating back to the start of the SD engineering phase.

The UB contains six input channels with one flash analog-to-digital converter (FADC) each that provide a sampling frequency of 40 MHz and a 10-bit resolution [2]. The resolution results in a dynamic range of 2^{10} = 1024 FADC channels, also often called FADC counts or short just "ADC".

To further increase the dynamic range of the detection devices (photomultiplier tubes (PMTs)), the signals are additionally split on the device electronics and partially amplified providing two different gains. The six identical main input channels are connected to the three large photomultiplier tubes (LPMTs) of the water-Cherenkov detector (WCD) using two cables per PMT, one cable for each signal gain. The electronics of the LPMTs provides two outputs with a different amplification status. A low-gain channel returns the signal from the PMT anode, while a high-gain channel is connected to the last dynode of the PMT and provides a signal with an amplification factor of 32. For this reason, the ratio between the two gains is also often called dynode-to-anode ratio (D/A). In addition, to control the power settings of the connected LPMTs, more precisely the integrated high voltage module on the base electronics, and to receive monitoring information from sensors on the PMT electronics, a third cable besides the two signal cables is installed for each of the PMTs. One exception

can be found for the SSD PMTs which are connected to the UB in the stations of the SSD PPA. Due to the design of the SSD PMT base electronics only providing a single signal from the anode, an interconnection device is installed to split the signal in a low and a high gain for the two UB input channels. More details about this set-up and the connection device is shown in Section 5.3.

When an event trigger occurs, the electronics memory buffers are read out and the traces of the PMTs are created. Each FADC trace contains 768 time bins, arranged from 0 to 767, and therefore, a single bin size of 25 ns is provided.

Additionally, the UB contains various attachments and connectors, e.g., light-emitting diode (LED) flasher electronics that can be used for linearity checks of the PMT responses or trigger signal generators. For the event and communication synchronization, a Motorola Oncore UT+ Global Positioning System (GPS) receiver is mounted on the boards.

Upgraded Unified Board (UUB)

To compensate for the amount of additional data of the new detector components and to increase the sensitivity of the existing detectors, a new electronics board was designed to replace the UB. The board with the suitable name Upgraded Unified Board (UUB) provides a three times faster FADC sampling frequency with 120 MHz and a four times higher resolution with 12-bit [5, 94, 95, 96] when compared to the older generation. Here, the resulting dynamic range is 2^{12} = 4096 FADC counts, arranged from 0 to 4095.

The UUB offers five main input channels, three for the LPMTs, one for the new small photomultiplier tube (SPMT) placed inside the WCD, and one for the SSD PMT. In contrast to the UB, only a single cable connection to the individual PMT anodes is used. This is due to the fact that the split and the amplification of the signals is handled on-board by the front-end components of the UUBs, instead of splitting the signal already at the detection device, and varies for the different types of PMTs. In detail, for the LPMTs, one of the signal paths is amplified by a factor of 32 after the splitting (high gain) compared to the second path which remains non-amplified (low gain). In case of the SSD PMT, one of the splits has the same amplification factor of 32 than the LPMT input channels (high gain), but the other path contains an attenuator with a factor of 4 (low gain). Due to this set-up, the total ratio between the two gains of the SSD PMT signals is 128. For the SPMT, the signal is not split or amplified resulting in a single low-gain channel. At last, an empty and non-amplified input channel remains available.

Equivalent to the case of the UB, the control of the PMT power settings and the readout of monitoring data is realized with an additional multipolar cable, if the PMT base is active, i.e., for the three LPMTs and the SSD PMT. In the case of the SPMT equipped with a passive base, and for a short duration in the test phase of different SSD PMT electronics, supplementary power supplies are installed in-between the UUB and the respective PMT.

Compared to the UB, the FADC traces of the new electronics consist of 2048 time bins, here from 0 to 2047, with a single bin size of 8.33 ns. This results in a similar total length of the FADC traces, 19.2 µs for the UB compared to 17.1 µs for the UUB, enabling comparisons of the electronics generations and providing the necessary backwards compatibility to the currently acquired data.

In addition, the UUBs trigger implementation supports a digital filter and downsampling method to reach the sampling frequency of the UB, assuring a smooth transition phase from the original to the new electronics without dividing the data sets by non-upgraded and upgraded stations.

Similarly to the UBs, the new electronics boards provide an additional signal generator for the LED flashers and further connection possibilities, e.g., for the signal cable of the new Radio Detector (RD) electronics. In the first prototypes of UUBs, the chosen GPS receiver for the data synchronization was the type M12M produced by I-Lotus [140]. For the latest version

Table 5.1: Calibration-software versions of UUB stations with their respective implementation dates and accompanying specifications and modifications.

Ver	Date	Specifications and Modifications
256	05 Oct 2016	First UUB release, no calibration information
257	25 Oct 2016	Various calibration histograms for WCD and SSD, no offsets
258	28 Apr 2017	GPS clock sawtooth information (timing)
259	11 Sep 2017	All calibration histograms and offsets
260	14 Aug 2018	"Extra" field for station electronics online information
261	24 Mai 2019	RD software interface
262	27 Oct 2020	Online calibration values, trigger information
263	08 Nov 2021	Additional calibration information (histogram binning)

of upgraded electronics boards, the Synergy Systems SSR-6TF GPS receiver is used [141]. Besides the already mentioned electronics upgrades, the UUB also provides faster processors, as well as an improved monitoring and calibration system compared to the UB.

The field studies of the new electronics boards started in October 2016 when the first UUB version (prototype V1) was installed in the Observatory. Since then, three additional versions have been deployed and studied in the AugerPrime test arrays. For the different versions of the UUB, the main hardware components for the signal manipulation remained unchanged, including their specifications, e.g., the FADCs with the desired sampling frequency and resolution, or the signal amplification chains.

But several parts of the circuit boards, for instance the components for the power handling have been exchanged or modified over the long testing period. The largest modification was made in the transition from the prototype V1 (top photo in Fig. 5.27) to the prototype V2 (bottom photo in Fig. 5.27), when the board layout had to be completely rearranged due to an unstable power management in critical parts of the board. In later UUB versions, i.e., since the prototype V3 (top photo in Fig. 5.28), and after the confirmation of the upcoming RD extension, a low-noise connector for the signal cable to the future radio antennas was added. Since the latest UUB pre-production version, the electronics boards are additionally equipped with Faraday shields[1] for the power converters, i.e., metal housings, to reduce the radio-frequency interference (RFI) created by the electronics components, and thereby improving the sensitivity of the nearby installed radio antennas. The shielding on a pre-production UUB can be seen in the bottom photo in Fig. 5.28.

In parallel to the changes in the hardware, multiple versions of calibration- and data-acquisition software versions have been in use over the more than four years of UUB data acquisition within the test arrays. While in the first days or months after the launch of the AugerPrime tests basically no online calibration or event timing information was available in the software version 256, more and more of these crucial information have been added with each iteration of the calibration-software version. The latest version with the number 263 was implemented in April 2021 and provides almost all necessary information to perform an PMT signal calibration and event reconstruction. Tab. 5.1 displays an overview of the different calibration-software versions with their respective implementation date and the major modifications between the versions.

For an optimal and direct comparison of the performance improvements with each board iteration, we searched for candidate stations that had all versions of UUBs installed since the first day of data acquisition in 2016. From the original 12 stations, only two stations inside

---

[1]Faraday shields, also called Faraday cages, are constructions of conducting materials which prevent external electromagnetic fields from passing through the interior by creating an internal electromagnetic field that cancels the external field. Equally, internal fields cannot pass to the outside.
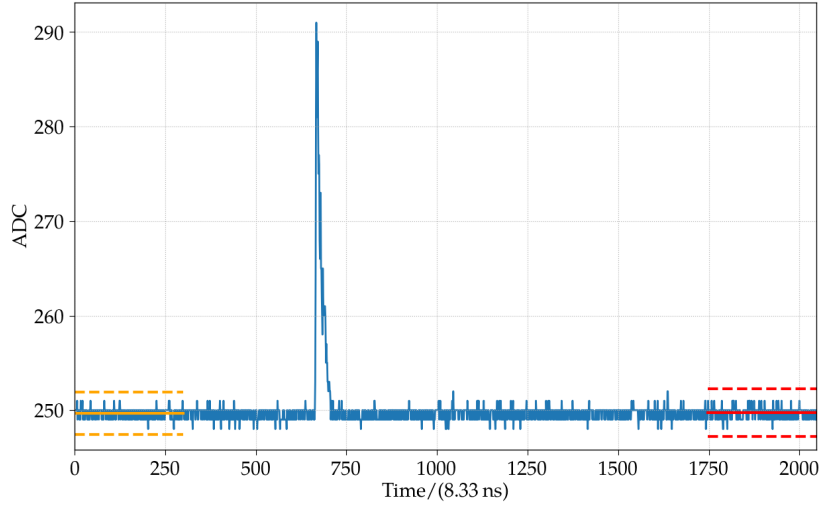
Figure 5.1: Example of a low-gain trace of an LPMT of the station LS20 equipped with an UUB. The orange and red solid lines define the mean values of the bin-count distributions for the first and the last bins of the trace.

the SD-433 array region fulfill this condition, the station LS20, internally named "Trak Jr.", and the station LS22, with the name "Clais Jr.". To analyze the properties of their electronics, we selected for each version a defined time period during which the measure conditions were mostly stable, i.e., non or only a few indications for changes in the power settings of all PMTs or any exchanges of detector components are traceable in the log books. If multiple electronics boards of the same version have been installed, the time period of the board with the largest and most stable test period was chosen. Additionally, the time periods have been further restricted by analyzing the PMT event traces and defining baseline trace segments which are introduced in the next paragraph.

5.1.2 Baselines of photomultiplier tube traces

For the selection of stable measurement periods and for the analysis of the general electronics performance that follows in the upcoming sections, we intensively use the information which are provided by the event traces of the five SD PMTs. Thereby, we analyze the traces of both amplification paths, the low and the high gain, resulting in the maximum number of 10 traces per SD station per event. An example of a low-gain trace of an LPMT of the station LS20 is shown by the blue curve in Fig. 5.1.

Especially, the bins of the trace that do not contain the signal information of the particles passing through the detectors can be used to draw conclusions on the operation stability of the electronics boards and their overall noise level. Due to the fact that the station software usually sets the signal bins close to the center of the time traces when reading out the memory buffer, we focus mainly on bins at the beginning or the end of the traces. In these time bins, basically no pulses are expected and usually only the small fluctuations produced by the electronics components are visible generating the so-called "baseline traces" or in short terms "baselines". Furthermore, we define two baseline ranges in each trace whose lengths vary depending on the type of electronics:

- The first 300 or first 100 trace bins for the UUB or UB, respectively:

$$\text{UUB:} \quad b_{\text{first}}(t), t \in [0, 300) \quad \text{or} \quad \text{UB:} \quad b_{\text{first}}(t), t \in [0, 100) \tag{5.1}$$

- The last 300 or last 100 trace bins for the UUB or UB, respectively:

$$\text{UUB:} \quad b_{\text{last}}(t), t \in (1747, 2047] \quad \text{or} \quad \text{UB:} \quad b_{\text{last}}(t), t \in (667, 767] \tag{5.2}$$
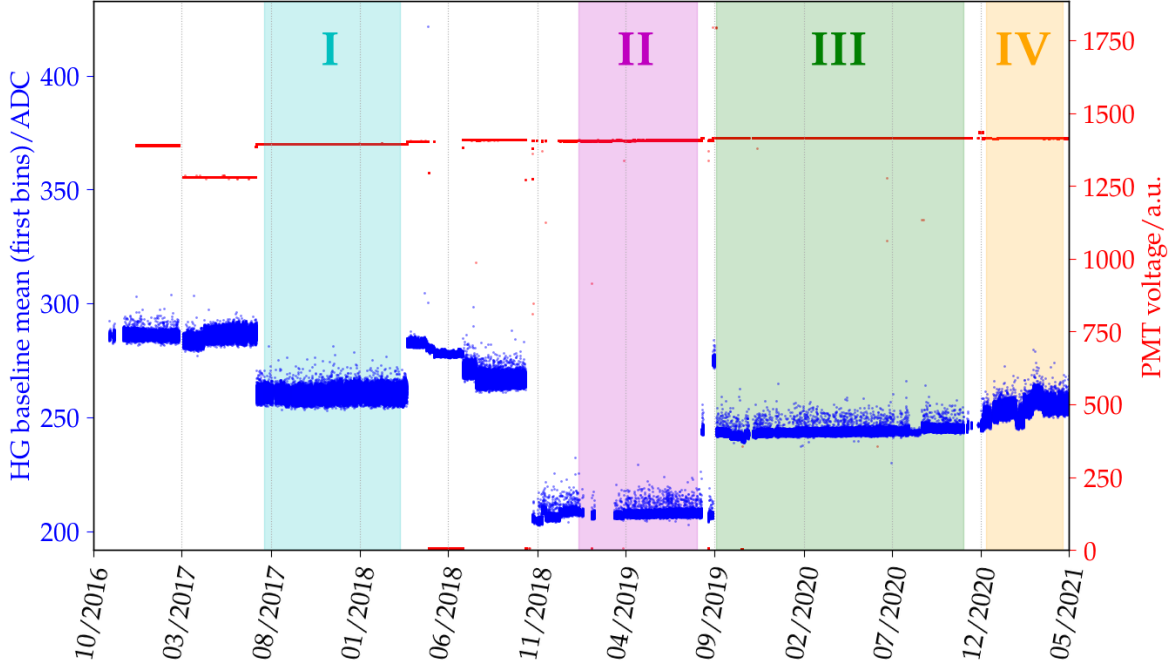
Figure 5.2: Mean of baseline distribution for individual events for an LPMT of station LS20 (blue markers). The read markers indicate the PMT power settings. The colored background intervals show the chosen time periods of different electronics boards versions.

Using these two simple baseline-trace definitions, we can calculate several quantities to describe the properties of the individual events trace, and finally of the electronics. One quantity to describe the general stability of the baseline trace are the mean values $\overline{b}_{\text{first}}$ and $\overline{b}_{\text{last}}$ of the bin-count distributions which can be seen for the trace in Fig. 5.1 indicated by the orange and red solid lines. The definition of the baseline sample means is identical for all PMTs and gains, and is given by

$$\overline{b}_{\text{first}} = \frac{1}{N} \sum_t b_{\text{first}}(t) \quad \text{and} \quad \overline{b}_{\text{last}} = \frac{1}{N} \sum_t b_{\text{last}}(t) \tag{5.3}$$

with N representing the number of bins that define the baseline, i.e., 300 or 100 for the UUB or UB, respectively. In addition, the unbiased estimates for the standard deviations σ_b^{first} and σ_b^{last} of the baseline bin-count distributions are calculated assuming that the bin counts follow a normal distribution:

$$\sigma_b^{\text{first}} = \sqrt{\frac{1}{N-1} \sum_t \left(b_{\text{first}}(t) - \overline{b}_{\text{first}}\right)^2} \quad \text{and} \quad \sigma_b^{\text{last}} = \sqrt{\frac{1}{N-1} \sum_t \left(b_{\text{last}}(t) - \overline{b}_{\text{last}}\right)^2} \tag{5.4}$$

The standard deviations define a measure of the widths of the baseline distributions and can be used together with the baseline means to describe the stability of the electronics signals. These quantities are used in the following sections to define criteria to search for bin-count fluctuations and to infer the electronics noise levels on the individual time traces.

By using the baseline-trace information of the five SD PMTs we can also further restrict the time periods for the electronics analyses to intervals during which most of the PMTs of the station show a stable performance. In Fig. 5.2 the $\overline{b}_{\text{first}}$ of the high-gain channel of one of the LPMTs of station LS20 is shown, indicated by the blue markers. In addition, the power supply settings for this PMT are displayed (red markers). The voltage information is

Table 5.2: Selected test periods of different UUB versions for LS20 and LS22.

Version	Period	LS20 (Trak Jr.)		LS22 (Clais Jr.)	
		Begin	**End**	**Begin**	**End**
Prototype V1	I	Jul 2017	Mar 2018	Mar 2017	Jul 2017
Prototype V2	II	Jan 2019	Aug 2019	Feb 2019	Aug 2019
Prototype V3	III	Sep 2019	Nov 2020	Sep 2019	Nov 2019
Pre-prod.	IV	Dec 2020	Apr 2021	Dec 2020	Apr 2021

extracted from the monitoring data which is streamed from the stations simultaneously to the event and calibration data. The displayed voltage values are given in the raw units directly provided by the power supply component installed on the electronics boards or in the case of Fig. 5.2, by the power supply on the base electronics of the PMT. The discontinuities in the voltage values indicate changes in the power supply settings or exchanges of hardware parts like PMTs or electronics boards.

Applying this procedure to all PMTs of station LS20, the resulting time periods for the data selection have been chosen. In Tab. 5.2 the four time periods for the different types of electronics boards are listed, named from "I" to "IV" in chronological order. These periods can also been seen in Fig. 5.2 as colored background time intervals, cyan for the prototype V1 (I), magenta for the prototype V2 (II), green for the prototype V3 (III), and finally, orange for the pre-production UUB (IV). The same selection and naming procedure was then applied to the second station which was chosen for the upcoming analyses, the station LS22.

5.1.3 Electrical transients

During early laboratory tests of the first versions of UUBs, transient noise peaks and fluctuations in the FADC traces of all input channels, have been observed. These peaks, in the following sections also referred to as "spikes", often appear with an uniform pattern in the traces of multiple input channels at the same time indicating leaking currents or electronics oscillations as sources for the noise. To further investigate this unwanted behavior, we extended the search for transient events to the traces recorded with the PMTs and electronics boards installed in the Observatory. The noise spikes generated by the electronics are usually only distinguishable from the trigger pulses, or in the case of the SD PMT traces, from the signal pulses, when they appear at trace bins distant to the induced pulses, i.e., with a certain time difference to the signal bins. For this reason, we set the focus of our search for electronics spikes to the beginning and end of the PMT traces using the baseline-trace definitions from above.

With the mean and the standard deviation of the baseline bin-count distributions, we can define a trigger condition to search for spikes in the bin ranges of both baseline traces, b_{first} and b_{last}. When a bin count surpasses an upper threshold above the mean of the baseline trace or falls short under a lower threshold below the baseline-trace mean, the trace is classified as "containing a spike". This condition is fulfilled when either the maximum single bin count b_{max} or the minimum single bin count b_{min} of the baseline traces reaches one of the predefined thresholds. For this analysis, we chose the thresholds to be $4\sigma_b$ as a trade-off, small enough to detect peaks with very low amplitudes, but still able to reject bin-to-bin fluctuations. Then, the applied trigger condition can be noted as

$$b_{\text{max}} > \overline{b} + 4\sigma_b \quad \text{or} \quad b_{\text{min}} < \overline{b} - 4\sigma_b \tag{5.5}$$

To visualize this spike search criterion, the upper and lower thresholds are displayed by the orange and red horizontal dashed lines in Fig. 5.3.
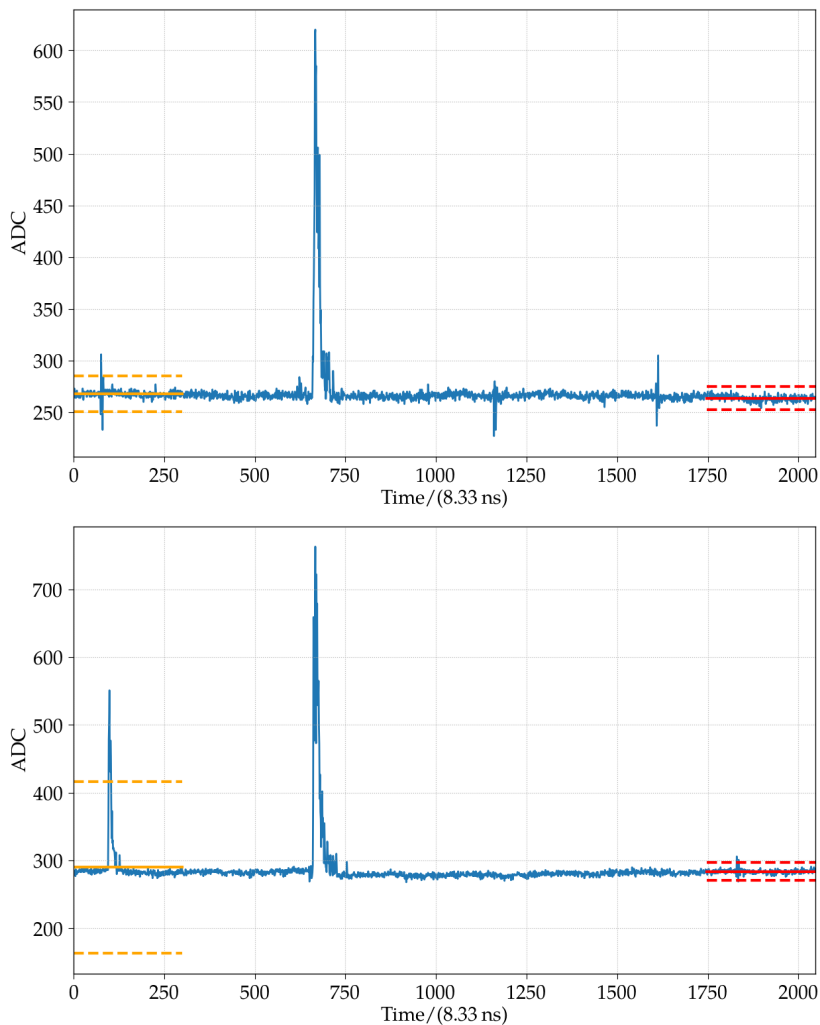
Figure 5.3: *Top:* Example of an UUB trace with symmetric spikes inside the baseline windows, i.e., alternating bins around the baseline mean indicating potential electronics issues. *Bottom:* Example of an UUB trace with additional asymmetric spikes created by air-shower particles.

When analyzing the traces of the SD PMTs, we have to carefully differentiate several types of peaks, or spikes, that can appear in the baseline traces. Hereby, the shape and the symmetry of the peaks play important roles and serve as the main classifiers for the separation of the different spike types.

The peaks that we are searching for, are generated by misbehaving electronics components and will classify the traces as noisy when they appear. These transients have a rather symmetric pulse shape around the baseline mean, similar to a up-and-down ringing of a few consecutive bins, i.e., alternating bin counts above and below the mean. Due to this characteristic, they can be selected by searching for traces which likely trigger both baseline threshold conditions, the upper and the lower bound. An example of such an electronics spike can be seen in the top diagram in Fig. 5.3. A small fraction of these spikes contain a significantly large part of the peak below the mean value which can result in the reaching of only the lower threshold, not the upper. For this reason we include transients that only suffice the lower search condition in the counting of noisy traces.

In contrast, another type of peak with an asymmetric shape around the baseline trace can be observed in the PMT traces as it is shown in the trace in the bottom diagram of Fig. 5.3. These peaks seem to be similar to the signal peaks and can be assigned to real air-shower

events which are not generating an own trigger due to the conceptional design of the trigger algorithm and data readout of the SD station. When a trigger for an PMT is built, a certain amount of time bins before the trigger are read from a memory ring buffer on the electronics boards and is further added to the beginning of the PMT event trace. During this readout process, the PMT cannot form a new trigger if another particle shower is arriving. Nonetheless, the air-shower particles would create a signal in the PMT which is stored in the ring buffer. If by chance the following trigger appears in the time window of the length of the memory, the buffer content containing the peak is read out and added to the event trace of this following trigger. Similarly, the additional signal peaks can appear in the last bins of an event trace due to the fact that no additional trigger was formed.

Besides these peaks created by nearly simultaneously appearing air showers, another type of spikes with asymmetric shapes can be found in the PMT trace, especially in the last bins. These peaks are created by particles of the same air shower which defines the triggered event, but arrive with a large time difference to the bulk of the air-shower particles due to scattering effects in the atmosphere that delay their propagation.

A third type of asymmetric peaks with rather small amplitudes may be found in the event traces. These peaks are created by photons that enter the detector from the outside indicating a problem with the light tightness of the detector enclosure, and thereby providing a measure of the mechanical stability. The studies of these light leakage effects, especially for the newly produced and deployed SSDs, are very important to predict and describe their future behavior and rate of deficiency. While in Section 4.2.3 the results of the light tightness checks during the validation measurements of the main production SSDs at the Karlsruhe Institute of Technology (KIT) has been shown, we present in Section 5.3.2 a study of possible light tightness problems by analyzing the data acquired with the SSD PMTs of the stations of the SSD PPA in the Observatory.

Finally, afterpulsing[2] and intrinsic noise from the amplification stages of the used PMTs cannot be excluded as a source for small asymmetric peaks appearing in the traces. A short discussion about the intrinsic noise behavior of the standard PMT type foreseen to be used inside SSDs has been already presented in Section 4.1.2.

Independently of the origin, we can distinguish the peaks with asymmetric shape from electronics spikes, due to the fact that these peaks only surpass the upper threshold of our spike search algorithm, but not the lower one. Due to the fact that the implementation of the station software, especially the definition of the event trigger algorithm, strongly influences the number of additional peaks induced by arriving particle in both baseline-trace ranges, we do not focus in our analysis on these peaks, but only on the search for the electronics spikes in the event data.

When searching for symmetric peaks in the baseline traces we also have to consider lightning induced noise pulses which show a very distinct shape, similar to the electronics noise, and also usually appear in multiple PMTs of the same station at the same time. By using the above defined search condition with an upper and lower threshold criterion around the baseline mean, it is nearly impossible to distinguish the lightning induced ringing from electronics spikes. For this reason, we intended to select measurement periods for the different versions of electronics boards which show a small number thunderstorm and lightning events observed with various sensors distributed over the SD array. The event rejection is thereby performed using a provided list from the monitoring database which contains events classified as "bad", i.e., events that should be excluded in analyses to avoid biases. In addition, a more detailed investigation of the effects of thunderstorms and lightning on the PMT traces obtained with the original and the new electronics boards is provided in

---

[2]Afterpulsing of photomultiplier tubes describes the appearance of small noise pulses which follow the main signal pulse in a time range of a few nanoseconds up to several microseconds. They are created by elastic scattering of electrons on the first dynode (ns delay) or positive ions reaching the photocathode (ms delay) creating pulses with rather small amplitudes but similar shapes compared to the main pulse [142].

Table 5.3: Appearance of electrical transients for different UUB versions (I to IV) for the high-gain (HG) channels of all PMTs of station LS20 including the values for both baseline-trace definitions and average values for the UB.

Bins	PMT	I %	II %	III %	IV %	UB %
first	LPMT 1	31.67	0.77	0.89	1.05	0.19
	LPMT 2	32.01	0.41	1.50	0.76	0.30
	LPMT 3	30.94	0.75	0.90	0.90	0.27
	Empty	0.60	8.22	0.38	0.39	-
	SSD	2.99	1.28	0.94	0.67	0.22
last	LPMT 1	30.71	0.80	0.74	0.78	0.16
	LPMT 2	31.50	0.49	1.33	0.57	0.28
	LPMT 3	30.35	0.84	0.78	0.80	0.22
	Empty	0.63	8.86	0.39	0.41	-
	SSD	2.55	1.24	0.92	1.62	0.20

Table 5.4: Appearance of electrical transients for different UUB versions (I to IV) for the low-gain (LG) channels of all PMTs of station LS20 including the values for both baseline-trace definitions and average values for the UB.

Bins	PMT	I %	II %	III %	IV %	UB %
first	LPMT 1	0.70	0.58	0.41	0.64	0.43
	LPMT 2	0.71	0.49	0.50	0.56	0.31
	LPMT 3	0.77	0.84	0.37	0.58	0.41
	SPMT	0.58	3.05	0.42	0.56	-
	SSD	0.65	21.99	0.79	2.42	0.23
last	LPMT 1	0.73	0.52	0.40	0.62	0.43
	LPMT 2	0.69	0.48	0.39	0.45	0.33
	LPMT 3	0.71	0.79	0.32	0.54	0.41
	SPMT	0.62	3.09	0.41	0.60	-
	SSD	0.65	21.70	0.74	2.42	0.27

Section 5.4.1.

To compare the different UUB versions, we determine the appearance rates of electronics spikes which trigger the search condition in both baseline ranges for both chosen stations LS20 and LS22. Here, we have to note that the rate values depend on the selection of the condition threshold, and therefore relative comparisons rather than absolute are drawn. The development of the rates over all the selected electronics board periods for station LS20 is shown in Tab. 5.3 for all the high-gain channels, and in Tab. 5.4 for all the low-gain channels of the individual PMTs. Analogously, the results of the analysis of the electronics board versions installed in station LS22 for both gains lead to the spike-appearance rates displayed in Tab. 5.5 and Tab. 5.6. In all four tables, the rates of electronics transients are given for both baseline ranges, the baselines determined from the first trace bins, as well as the baselines determined from the last trace bins.

For both stations, we can observe that the number of electronics spikes in both baseline ranges of the LPMT traces was significantly reduced when the UUB prototype V1 was replaced by the prototype V2. This result confirms the performance problems of the prototype V1

Table 5.5: Appearance of electrical transients for different UUB versions (I to IV) for the high-gain (HG) channels of all PMTs of station LS22 including the values for both baseline-trace definitions and average values for the UB.

Bins	PMT	I %	II %	III %	IV %	UB %
	LPMT 1	17.46	0.80	0.90	0.66	0.19
	LPMT 2	19.33	0.71	0.71	0.59	0.30
first	LPMT 3	3.28	1.72	1.04	0.86	0.27
	Empty	0.49	1.58	0.22	0.50	-
	SSD	9.15	2.42	0.77	0.54	0.22
	LPMT 1	16.93	0.82	0.71	0.72	0.16
	LPMT 2	18.19	0.64	0.53	0.52	0.28
last	LPMT 3	3.30	1.32	0.65	0.74	0.22
	Empty	0.37	1.59	0.21	0.47	-
	SSD	8.72	2.55	1.19	0.95	0.20

Table 5.6: Appearance of electrical transients for different UUB versions (I to IV) for the low-gain (LG) channels of all PMTs of station LS22 including the values for both baseline-trace definitions and average values for the UB.

Bins	PMT	I %	II %	III %	IV %	UB %
	LPMT 1	0.51	0.43	0.42	0.47	0.43
	LPMT 2	0.76	0.75	0.39	0.46	0.31
first	LPMT 3	0.56	0.84	0.59	0.44	0.41
	SPMT	0.60	5.37	0.79	3.74	-
	SSD	0.52	24.31	0.34	3.42	0.23
	LPMT 1	0.50	0.51	0.40	0.41	0.43
	LPMT 2	0.78	0.74	0.39	0.41	0.33
last	LPMT 3	0.49	0.84	0.48	0.46	0.41
	SPMT	0.56	5.26	0.77	3.79	-
	SSD	0.56	24.12	0.30	3.54	0.27

boards caused by malfunctioning electronics components which had been already observed in laboratory tests as mentioned previously. After the major changes in the board layout when switching from the prototype versions V1 to V2, the rate of observed electronics spikes, especially in the high-gain channels, strongly decreased and has remained at a lower levels for all following UUB versions, including the latest pre-production UUB version.

Interestingly, the number of electronics spikes in the SPMT and SSD PMT channels rises for prototype V2 compared to V1, with the strongest increase in the low-gain channel of the SSDs PMT. This hardware issue was then corrected with the design and production of the prototype V3 electronics. The latest UUB version, the pre-production version, shows low rates of electronics spikes for the LPMTs in both gains and both baseline ranges equivalent to the last prototype version V3. Only the SPMT and SSD PMT indicate a slightly increased number of spikes compared to former versions. This result is not necessarily related to misbehaving electronics components, but can also be a consequence of the selection of events. During the first months of data acquisition with the pre-production version UUBs, the number of thunderstorms was uncommonly high, and therefore the number of externally induced spikes
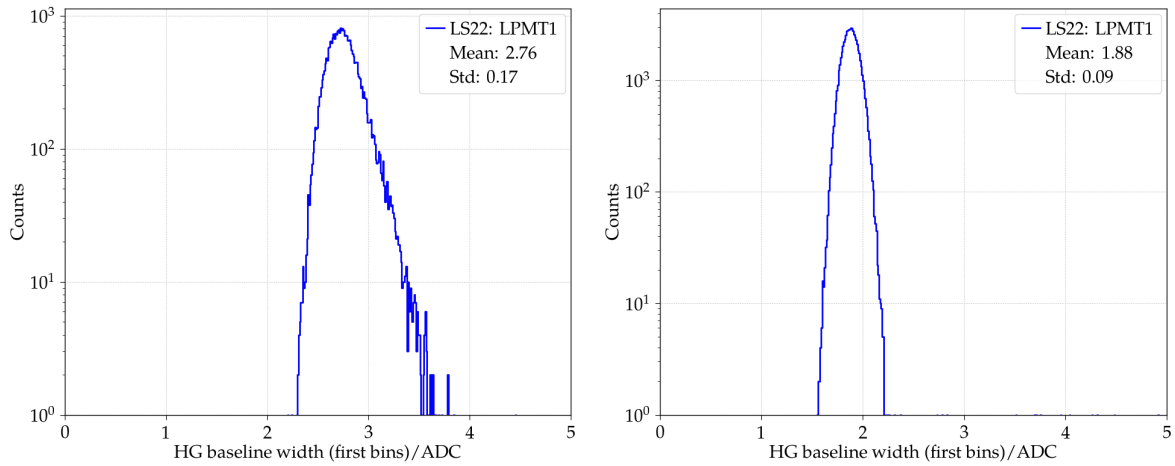
Figure 5.4: Distributions of the baseline standard deviations for the high-gain (HG) channel of an LPMT of station LS22. *Left:* Connected to a prototype V1 UUB (I). *Right:* Connected to a pre-production version UUB (IV).
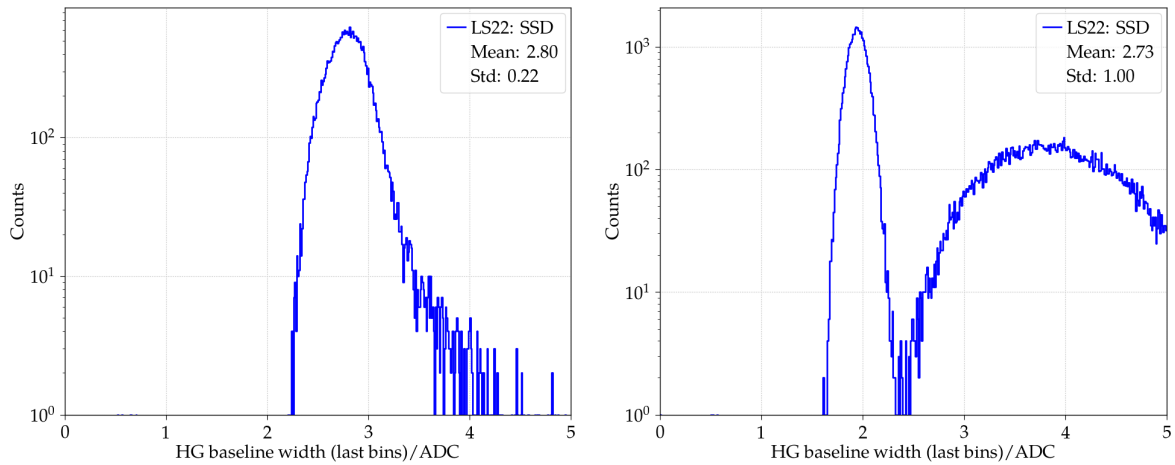
Figure 5.5: Distributions of the baseline standard deviations for the high-gain (HG) channel of the SSD PMT of station LS22. *Left:* Connected to a prototype V1 UUB (I). *Right:* Connected to a pre-production version UUB (IV).

was noticeably increased. Despite the fact that most of the thunderstorm events are filtered from the event data by using the "bad" period list, a fraction of lighting events remains in the data set biasing the count of symmetric spikes. In addition, we can note, that the rate of electronics noise transients is very similar for both baseline definitions, showing the fact that these spikes appear regularly and distributed over the whole PMT trace.

For comparisons between the two electronics generations, all four tables additionally contain the results of the search for electronics spikes in the baseline traces of SD stations equipped with an UB. To guarantee a general comparison between the electronics generations, we used the same threshold condition and calculated for each individual PMT an average value using the data of five stations (LS651, LS656, LS659, LS710, and LS1732). The tables show that for the low-gain channels the values between the two electronics generations are quite similar. Contrarily, for the high-gain channels, the electrical transients seem to appear less frequently for the UB. This might be an effect of the search algorithm not detecting spikes with low amplitudes due to the lower absolute noise level of the old electronics boards (see Section 5.1.4).

5.1.4 Noise level

Besides for the search of transients and spikes produced by electronics malfunctions, the two baseline-trace quantities mean and standard deviation introduced in Section 5.1.2 can also be used to generally describe the noise levels of the embedded hardware components. Especially the widths of the baseline distributions indicate the stability of the electronics signals and provide limits for the resolution and dynamic range of the measurement set-up. Our main focus in this analysis lies on the amplitudes and spreads of the ground level noise of all input channels. Thereby, we have to keep in mind that the standard deviation of the baseline distribution of individual events can be strongly biased when signal peaks or spikes appear in the baseline bin ranges. For this reason, we use the spike search algorithm described in the previous Section to filter out traces with detectable transients. Then, the distributions of the baseline standard deviations of the different electronics board versions are determined.

Similarly to the electrical transient search, the noise level analysis is applied to the baseline traces of the two selected stations, LS20 and LS22, and individually performed for the predefined time periods of the installed electronics board versions. Two examples of distributions of baseline standard deviations are shown in Fig. 5.4, in the left diagram for the high-gain channel of an LPMT of station LS22 equipped with an UUB prototype V1, and on the right side for the same LPMT and channel of station LS22, but now connected to a pre-production version UUB. When comparing both distributions, a difference in the position of the maximum and the spread can be seen. By determining the average values of these distributions for each electronics board version, we can further describe their general noise levels.

To provide an overview and to enable comparisons between the different UUB versions, as well as between the UUBs and the original UBs, the resulting average values for the distributions of baseline standard deviations are given in four tables. In Tab. 5.7 and Tab. 5.8 the high and low-gain channels of the station LS20 are displayed, respectively. Analogously to the spike search analysis, we additionally show the values for both baseline definitions, the first and the last bin baselines. The respective results for the station LS22 for both gains are shown in Tab. 5.9 and Tab. 5.10.

Overall, we can conclude that the noise level of the prototype V1 UUBs show significantly higher values compared to later versions of electronics boards. This observation matches the inferior performance which was already seen in the noise-transient search and the preceding laboratory tests. After the changes of the UUB layout, we determine an average noise level of approximately 2 ADC or slightly below for the high-gain channels of the majority of the PMTs reaching the pre-assigned requirements. This includes the latest UUB version, the pre-production UUB, which represents the nearly final design for the new electronics boards. When comparing the results for the two defined baseline ranges, we can observe that the average values for the first and the last trace bins match for most of the PMTs when considering the measurement uncertainties. Only for the SSD PMT values of the high-gain channel, the values for the last bins seem to be higher. A reason here, might be the contamination with pulses from external effects, e.g., lightning events, PMT afterpulsing, etc., which are not properly filtered by the applied procedure. This can be seen in Fig. 5.5 which displays the distributions of baseline standard deviations for the SSD PMT of station LS22, on the left for the UUB prototype V1, on the right for the UUB pre-production version. For the prototype V1 distribution, the displayed mean value represents the true noise level, i.e., the position of the maximum, while in the distribution of the pre-production version two peaks are visible. Here, the position of the left peak, at lower ADC values, describes the true noise level of the input channel which is in fact on a similar level than for the other PMTs. The second peak is created by the additional pulses that survive the filtering procedure increasing the mean of the total distribution. In case of the low-gain channels, the reduction of the noise level between the different UUB versions is rather faint.

In the result tables we can also observe that the general average values of baseline standard

Table 5.7: Average values of distributions of baseline standard deviations for different UUB versions (I to IV) for the high-gain (HG) channel of all PMTs of station LS20. For the comparison between electronics generations, the higher resolution of the UUB (factor of 4) has to be considered.

Bins	PMT	I ADC	II ADC	III ADC	IV ADC	UB ADC
	LPMT 1	2.74	1.93	2.07	1.96	0.53
	LPMT 2	2.75	1.94	2.20	1.94	0.47
first	LPMT 3	2.82	1.95	2.08	1.94	0.46
	Empty	0.66	0.68	0.57	0.80	-
	SSD	2.75	2.02	2.00	1.98	0.60
	LPMT 1	2.86	1.98	2.14	2.04	0.53
	LPMT 2	2.87	1.96	2.29	2.00	0.48
last	LPMT 3	2.92	1.98	2.11	1.98	0.46
	Empty	0.66	0.71	0.57	0.83	-
	SSD	2.77	2.02	2.22	2.28	0.60

Table 5.8: Average values of distributions of baseline standard deviations for different UUB versions (I to IV) for the low-gain (LG) channel of all PMTs of station LS20. For the comparison between electronics generations, the higher resolution of the UUB (factor of 4) has to be considered.

Bins	PMT	I ADC	II ADC	III ADC	IV ADC	UB ADC
	LPMT 1	0.66	0.57	0.57	0.55	0.52
	LPMT 2	0.62	0.60	0.57	0.56	0.48
first	LPMT 3	0.64	0.60	0.58	0.55	0.47
	SPMT	0.71	0.60	0.57	0.55	-
	SSD	0.76	0.64	0.68	0.64	0.46
	LPMT 1	0.67	0.57	0.57	0.55	0.52
	LPMT 2	0.64	0.60	0.58	0.56	0.47
last	LPMT 3	0.66	0.60	0.61	0.56	0.47
	SPMT	0.71	0.60	0.57	0.55	-
	SSD	0.76	0.64	0.68	0.64	0.47

deviations of the original UB are consistently lower than the values of the UUB versions in absolute ADC units, especially for the high-gain channel signals. This result is slightly misleading due to the fact that the different board generations have different dynamic ranges, i.e., FADC resolutions. Therefore, the absolute average values have to be normalized by the respective FADC resolutions to enable a comparison. The resolution of the UUB (12-bit) is by the factor of 4 higher than for the UB (10-bit). When applying this scaling factor, the noise levels of the latest version of UUB lie on a similar or even slightly lower level compared to the levels of the original UB.

5.1.5 Input channel amplification

The third comparison of the different electronics board versions and generations presented in this Dissertation is the analysis of the amplification chains of the individual input channels.

Table 5.9: Average values of distributions of baseline standard deviations for different UUB versions (I to IV) for the high-gain (HG) channel of all PMTs of station LS22. For the comparison between electronics generations, the higher resolution of the UUB (factor of 4) has to be considered.

Bins	PMT	I ADC	II ADC	III ADC	IV ADC	UB ADC
first	LPMT 1	2.76	1.95	1.92	1.89	0.53
	LPMT 2	2.73	1.99	2.00	1.93	0.47
	LPMT 3	2.11	1.97	1.93	1.92	0.46
	Empty	0.65	0.59	0.57	0.54	-
	SSD	2.79	1.97	1.94	1.99	0.60
last	LPMT 1	2.75	2.00	1.95	1.88	0.53
	LPMT 2	2.73	2.04	2.02	1.93	0.48
	LPMT 3	2.10	2.03	2.00	1.94	0.46
	Empty	0.65	0.59	0.57	0.54	-
	SSD	2.81	2.08	2.19	2.80	0.60

Table 5.10: Average values of distributions of baseline standard deviations for different UUB versions (I to IV) for the low-gain (LG) channel of all PMTs of station LS22. For the comparison between electronics generations, the higher resolution of the UUB (factor of 4) has to be considered.

Bins	PMT	I ADC	II ADC	III ADC	IV ADC	UB ADC
first	LPMT 1	0.59	0.59	0.56	0.56	0.52
	LPMT 2	0.70	0.59	0.57	0.56	0.48
	LPMT 3	0.58	0.59	0.56	0.57	0.47
	SPMT	0.63	0.60	0.55	0.51	-
	SSD	0.64	0.62	0.65	0.62	0.46
last	LPMT 1	0.60	0.59	0.56	0.56	0.52
	LPMT 2	0.70	0.59	0.57	0.56	0.47
	LPMT 3	0.58	0.59	0.56	0.57	0.47
	SPMT	0.63	0.60	0.55	0.51	-
	SSD	0.64	0.62	0.65	0.62	0.47

This study is realized by applying a data-driven determination of the amplification factors between the two gains of each input channel to verify the dynamic range of the electronics design.

As already explained in Section 5.1.1, the splitting and amplification of the input channels of the UUBs is handled by the front-end components of the boards. They are expected to provide the nominal values of 32 for the LPMTs and 128 for the SSD PMTs with only small uncertainties of a few percent due to the production quality of the components. As a reminder, the UBs are connected by two cables to the two different output channels of the PMT base electronics which are providing the expected gain factor of 32.

In this analysis we determine the amplification factors by defining a procedure to calculate the pulse signals for both gains on individual event traces. Subsequently, the signal ratios of each event are determined for the different electronics board versions. Hereby, we have to select traces that fulfill certain quality criteria. On the one hand, only events with a minimum
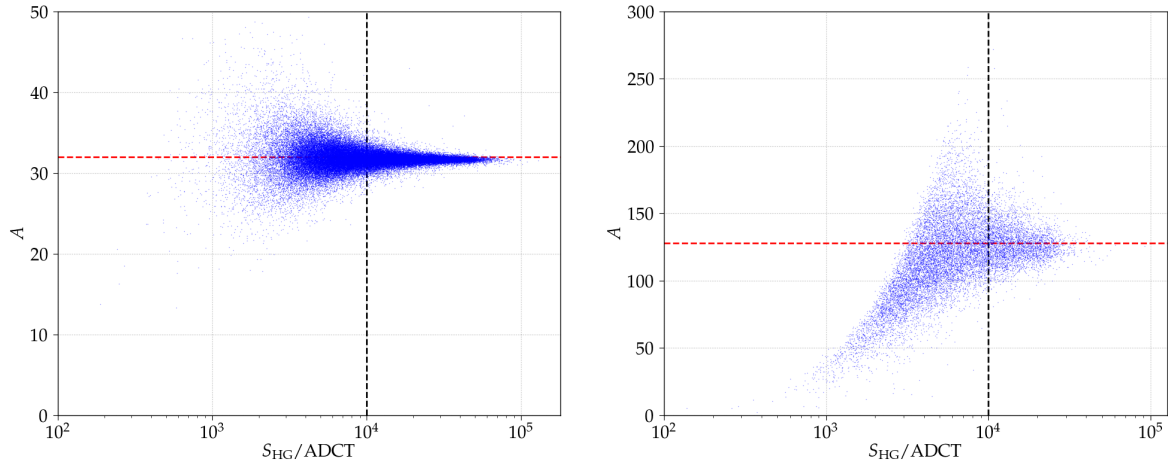
Figure 5.6: Signal ratios after applying the signal-to-noise event selection for two
PMTs of station LS20 equipped with a pre-production UUB. *Left:* Signal ratios of
one of the LPMT. *Right:* Signal ratios of the SSD PMT.

deposited energy to produce signals in both, low and high-gain traces, can be used. On
the other hand, for a proper calculation of the total signal of the pulses, traces which show
saturation, i.e., one or more trace bins reach the maximum possible ADC value (4095 for
the UUB or 1023 for the UB), are rejected. The signals S for both gains are then calculated
by subtracting the baseline-trace mean $\overline{b}$ from each trace bin and summing the bin entries
between the start bin t_{start} and the stop bin t_{stop} which are determined by the signal integration
algorithm in the $\overline{\text{Off}\underline{\text{line}}}$ [70]:

$$S = \sum_{t_{\text{start}}}^{t_{\text{stop}}} \left(s(t) - \overline{b} \right) = \sum_{t_{\text{start}}}^{t_{\text{stop}}} s(t) - N\overline{b} \tag{5.6}$$

with N defining the number of bins from the start to the stop position, including both most
outer bins. This calculation of the individual PMT signals slightly differs from the general
procedure implemented in the $\overline{\text{Off}\underline{\text{line}}}$ which is in introduced in Section 6.4.2, but serves here
as simple signal estimation. The amplification factor A of each event is then given as the ratio
between the high-gain signal S_{HG} and the low-gain signal S_{LG}, i.e.,

$$A = \frac{S_{\text{HG}}}{S_{\text{LG}}}. \tag{5.7}$$

This calculation does not yet include any check if the signal determination returns reliable
values. especially for the low-gain signals which are often very small or even adopt negative
values due to the fact that the low-gain traces often do not contain any signal pulse. In addition,
the simplified calculation of the signals is not accounting for possible under- or overshoots
of the pulses. These uncertainties lead to a large spread in the calculation of signal-ratio
values. To assure minimum signal sizes for a proper calculation of the amplification factors,
we implement an additional condition which filters the events before the ratio is determined.
This condition defines a minimum signal-to-noise threshold that has to be surpassed. The
noise σ_S to the respective signal S can be inferred from the noise values of each trace bin.
These noise values are assumed to be constant for all bins and are given by the baseline
standard deviation σ_b. This result in

$$\sigma_S^2 = \sum_{t_{\text{start}}}^{t_{\text{stop}}} \sigma_b^2 = N\sigma_b^2 \quad \rightarrow \quad \sigma_S = \sigma_b \sqrt{N} \tag{5.8}$$
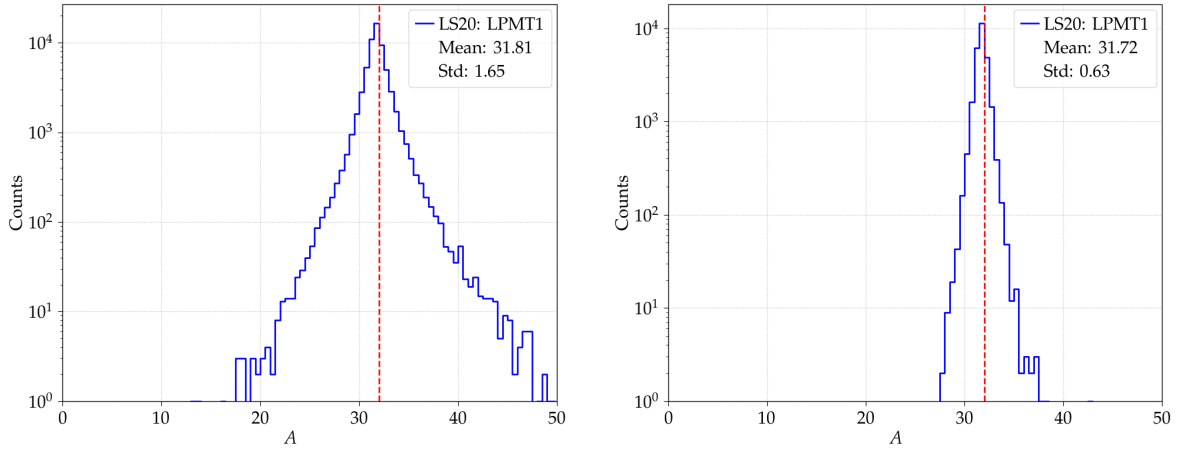
Figure 5.7: Signal-ratio distributions of an LPMT connected to a pre-production UUB in station LS20. *Left:* Before the event selection on the high-gain signals. *Right:* After the high-gain signal cut is applied.
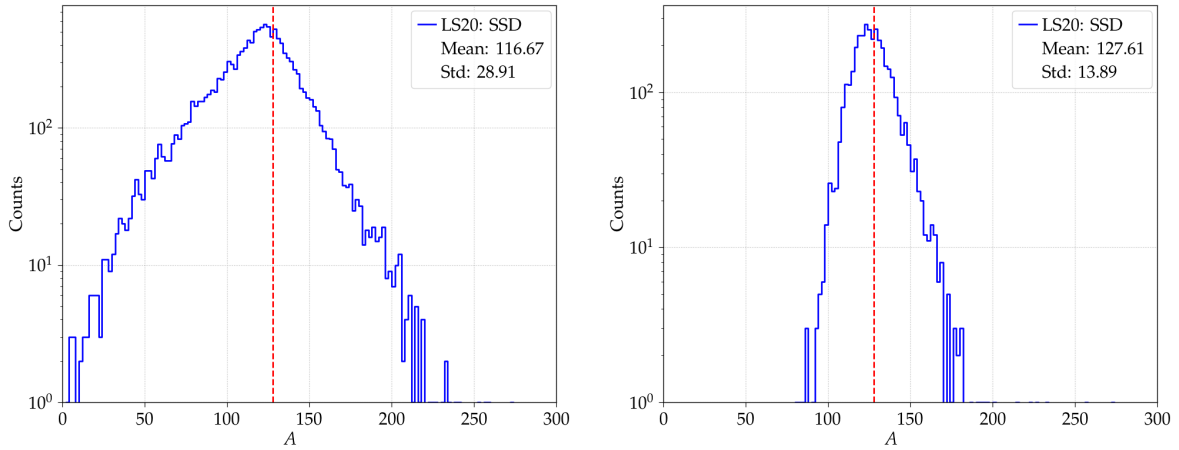
Figure 5.8: Signal-ratio distributions of the SSD PMT connected to a pre-production UUB in station LS20. *Left:* Before the event selection on the high-gain signals. *Right:* After the high-gain signal cut is applied.

The event selection is then performed by requiring a certain signal-to-noise ratio which we chose to be larger than 5 for both signals:

$$S > 5\sigma_S \quad \rightarrow \quad S > 5\sigma_b \sqrt{N} \tag{5.9}$$

The resulting signal ratios after applying the event selection are displayed in the diagrams in Fig. 5.6. Therein, the signal ratios of single events of two PMTs of the station LS20 equipped with a pre-production UUB are shown in dependence of the respective high-gain signal. In the left diagram, the ratios for an LPMT with the nominal amplification factor of 32 can be seen depicted by the red horizontal dashed line. The diagram on the right shows the resulting values for the SSD PMT, with the nominal factor of 128, also highlighted by the red horizontal dashed line.

Despite the fact that the selection criteria removes already a large fraction of events, an increase of the fluctuations in the signal ratios when going towards lower signals is still visible in both diagrams, especially for the SSD PMT. For this reason, we include an additional selection criterion to the amplification factor calculation. By choosing only events with $S_{\mathrm{HG}} > 1{\times}10^4$ ADCT the spread of the signal-ratio distribution can be significantly

Table 5.11: Average values of signal-ratio distributions for different UUB versions (I to IV) of all PMTs of the stations LS20 and LS22. The nominal amplification factors are 32 and 128 for the LPMTs and the SSD PMT, respectively.

Station	PMT	I	II	III	IV
LS20	LPMT 1	31.06±0.76	31.80±0.62	31.31±0.77	31.72±0.61
	LPMT 2	31.55±0.73	31.38±0.65	31.25±0.73	31.40±0.59
	LPMT 3	31.39±0.71	31.70±0.60	32.26±0.79	31.51±0.65
	SSD	122.18±19.18	131.58±18.64	126.05±17.78	127.61±13.88
LS22	LPMT 1	31.34±0.67	31.53±0.64	31.32±0.63	32.70±0.65
	LPMT 2	81.89±5.58	31.76±0.63	32.73±0.75	31.28±0.57
	LPMT 3	9.85±7.05	31.94±0.61	31.35±0.67	31.59±0.59
	SSD	117.36±17.45	143.30±20.41	122.92±16.79	138.08±15.22

reduced and the mean of the remaining ratio values is determined. The applied signal threshold is visualized by the black vertical dashed lines. To show the effect of the signal threshold condition, the signal ratio distributions of an LPMT and of the SSD PMT are presented in the diagrams in Fig. 5.7 and Fig. 5.8, respectively. In the left diagrams of both figures, the respective distributions before applying the high-gain signal cut can be seen, including their mean values and standard deviations. Whereas the distribution of the LPMT is symmetric around the maximum value resulting in an average value very close to the expected factor of 32 (red vertical dashed line), the signal ratios of the SSD PMT form a wider and asymmetric distribution which leads to a mean value below the nominal value and a large standard deviation. After the selections of events which contain only high-gain signals above the selected threshold, the distributions transform to the ones shown in the right diagrams of both figures. The spread is significantly reduced and the average values approach the nominal values provided by the hardware components.

Applying this event-based procedure to all PMTs of the stations LS20 and LS22, and all installed UUB versions, we have the possibility to investigate the embedded hardware components concerning their minimum requirements and production quality. The resulting average amplification factors and standard deviations are displayed in Tab. 5.11. For the station LS20, all UUB versions show a rather stable average signal ratio for all the connected PMTs, even in the case of the prototype V1 UUB. In contrast, the average values for the UUBs in station LS22 changed over the different versions. For prototype V1, the signal ratios for two LPMTs strongly deviate from the expected values which might be related to malfunctioning or incorrectly installed electronics components. After the switch to the prototype V2, the average signal ratios for all PMTs approach the nominal factors considering the statistical uncertainties.

Finally, we have to note that the two-stage filtering significantly reduces the number of events, especially for the SSD PMTs, which can produce the large fluctuations between the average values observed for station LS22. For this reason, the applicability of our data-driven method is limited to stations that are part of the SD-433 or the SD-750 array with denser station spacing, leading to an increased number of detected events.

5.2 AugerPrime array configurations in the Observatory

The studies and field tests of individual AugerPrime components and fully upgraded stations were and are still performed in two main array configurations which are introduced in this Section: the AugerPrime EA and the UUB PPA. We classify both arrays as "AugerPrime
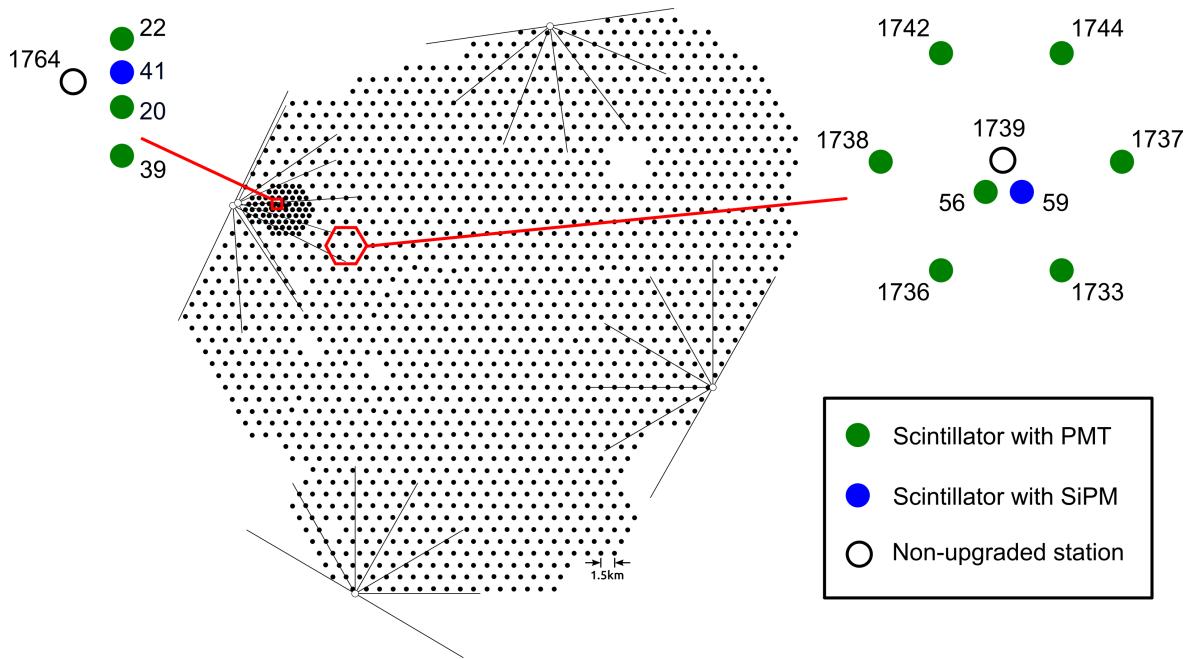
Figure 5.9: Latest configuration of the AugerPrime Engineering Array from September 2018 to April 2021. Four AugerPrime stations are located in the SD-433 array, the remaining eight stations form a hexagon in the standard SD array with a doublet in the hexagon center.

configurations" due to the fact that the original electronics boards UB have been replaced by the new UUBs in all belonging stations. A third array configuration was established with the start of the test phase of the newly installed SSDs in combination with UBs, the so-called SSD PPA which is presented in the subsequent Section. Information about changes in the array configurations and modifications of single stations can be found in Ref. [137] and Ref. [138].

5.2.1 AugerPrime Engineering Array

The AugerPrime Engineering Array (EA) was deployed and launched in October 2016 to test the performance of the four major parts of the experiment upgrade, the UUB as the new station electronics boards, the additional SPMT inside each WCDs, the SSDs on top of the WCDs, as well as the newly designed radio antennas for the upcoming RD. The array was located in the western part of the SD array in the proximity of the SD-750 region and consisted of 12 stations. After the start of the data acquisition, the AugerPrime EA contained nine stations in the standard SD-1500 array, with six stations (LS1733, LS1736, LS1737, LS1738, LS1742, and LS1744) forming a hexagon around a non-upgraded central station. These six stations have been part of the main SD data production before they received the upgraded components by what they dropped out of the production station list which is used for physics analyses in the Pierre Auger Collaboration. The additional three stations (LS56, LS59, and LS60) were placed inside the same hexagon as accompanying stations in so-called multiplets, two at the central station forming a triplet, and one at the south-eastern station in the hexagon forming a doublet.

To acquire significantly more events in a short period of time, and thereby enabling fast tests of new hardware and software, originally three stations (LS20, LS22, and LS39) were placed in the SD-433 array in a quadruplet to the non-upgraded station LS1764. In September 2018, the station LS60 was moved from the hexagon to this multiplet in the SD-433 array and renamed to LS41 forming a station quintuplet. This set-up defines the latest configuration

of the AugerPrime EA shown in the map in Fig. 5.9 wherein we also highlight the location inside the SD array. The end of the AugerPrime EA was defined in April 2021 with the exchange of the prototype electronics boards with the latest pre-production version UUBs. The majority of the former EA stations are now assigned to the newly deployed UUB PPA which is introduced in the following.

As mentioned previously, various prototypes of all of the main AugerPrime upgrade components, described in Section 3.2, have been tested in the AugerPrime EA. The test phase started in 2016 with the UUB prototype V1 and was carried on with two more prototype versions of electronics boards over the period of four years. The performance of the electronics boards has been heavily monitored and tested, and comparisons with the latest pre-production version, as well as with the original UBs are presented above in Section 5.1.

Together with the new electronics, the SPMTs were added inside the WCDs providing an extension of the dynamic range of the detector towards higher energies. These PMTs are mounted above a window on the top side of the Tyvek liner, between the three LPMTs. In the first months, three different types of head-on PMTs with diameters between 1 inch and 1.2 inch have been tested, the Hamamatsu R6094 [143], the ET Enterprise 9107B [144], as well as the Hamamatsu R8619 [99]. Finally, the latter was chosen to be the baseline type of the SPMT. First performance results together with simulation studies of events including SPMT data can be found in Ref. [98].

In the middle of 2018, the first radio antenna of the short aperiodic loaded loop antenna (SALLA) type has been installed on the ground, a few meters next to the AugerPrime station LS22 in the SD-433 array, to test the readout connection between the antenna front-end electronics and the UUB, as well as for studies of the RFI level of the new electronics boards. A few months later, the antenna was mounted at its assigned position on the top of the station above the SSD creating the first complete AugerPrime station in the Observatory. To extend the performance tests, seven additional SALLAs have been deployed in the field, two in the station multiplet in the SD-433 array (LS20 and LS39), and four in the AugerPrime hexagon (LS56, LS1737, LS1742, and LS1744), all connected to UUBs of prototype versions V2 or V3. The results of the data acquisition with the first RD antennas are shown in Ref. [107].

The last upgrade component discussed in this Section are the SSDs which ultimately will be mounted on top of the majority of the SD stations when the upgrade phase will be finished. For the AugerPrime EA, a first series of 13 SSDs has been produced at the KIT, and one additional SSD has been assembled locally in the workshop building on the Observatory campus in Malargüe. Between these detectors, small differences and modification in the design were present which indicate the development and optimization of the assembly procedure over the first months of production. The scintillation detectors for the AugerPrime EA contained additional temperature and humidity sensors, as well as LEDs for potential calibration and functional capability tests. Later, both features, the sensors and the LEDs, have been withdrawn from the final design of the SSD to reduce the complexity of the detector.

Another example of the small design differences among the first SSDs, are the varying types of couplings between the wavelength-shifting (WLS) fibers and the respective detection devices, the so-called cookies, which have been tested in the engineering detectors in the field. For the signal readout with PMTs two different coupling methods have been tested. One SSD contains a cookie that was produced by gluing the fiber ends with into a poly(methyl methacrylate) (PMMA) cylinder followed by a long process of polishing the fiber ends with sandpapers of different roughness to receive a flat and homogeneous surface. Contrarily, in the case of the other SSDs assembled for the operation with PMTs, the fiber ends are melted on a hot glass plate before gluing them into a PMMA cylinder with an additional transparent window to protect the fiber ends from dust and pressure. With this technique, a homogeneous surface condition of the fiber ends is reached, while the preparation time is reduced compared to polishing the fibers. Thus, this method has been chosen for the main
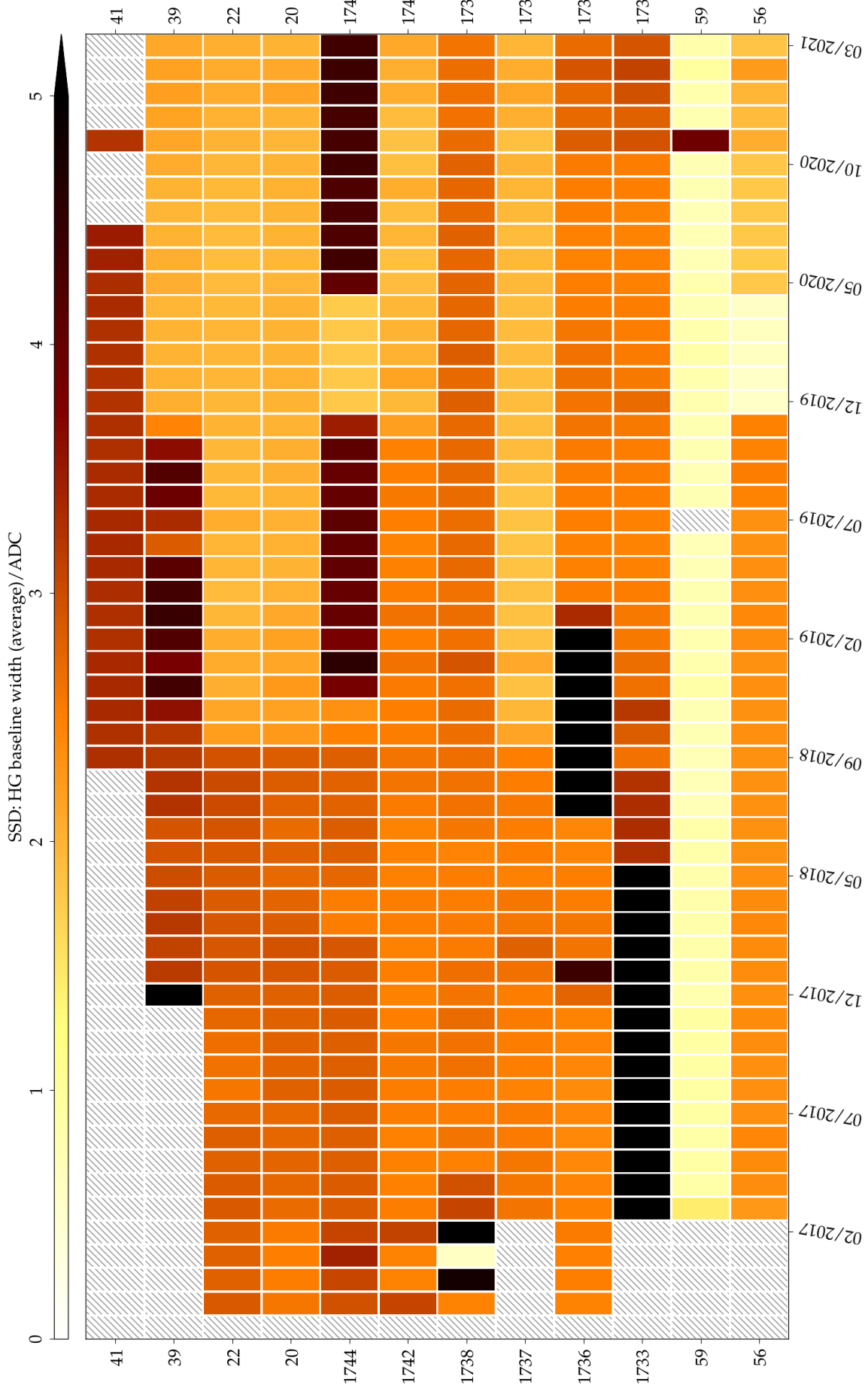
Figure 5.10: Monthly averages of baseline-distribution widths for the SSD PMT high-gain (HG) channels of all AugerPrime EA stations.

production of the SSDs at all assembly sites in the Pierre Auger Collaboration.

In addition, three out of the 13 SSDs contained a particularly shaped cookie with the fiber stack split into two equal bundles and glued into two holes with one window each. These cookies have been designed to couple the fiber ends to silicon photomultipliers (SiPMs) which had been proposed to be used as the default device for the signal readout in all SSDs of the AugerPrime upgrade. A more detailed description of the coupling method, the newly developed SiPM electronics, as well as the results from first studies of their performance in the Observatory are presented in Ref. [145]. From the start in 2016, two station, LS59 and LS1733, were equipped with SiPM SSDs to test the performance with slightly modified UUB prototype versions. With the movement of one station from the hexagon into the SD-433 multiplet, the station LS41 also received an SiPM SSD while the station LS1733 was changed to a PMT SSD station, which can be seen in the map in Fig. 5.9.

For the readout of the standard cookie SSDs, mostly all detectors have been equipped with standard version of the head-on Hamamatsu R9420 PMT with a diameter of 1.5 inch [120]. Only one station received a Hamamatsu R9420-SLE which is an exemplar particularly selected by the manufacturer in order to guarantee a high linearity at very high-gain values. Due to the fact that first results of the SSD performance had shown that with the standard PMT version the maximum dynamic range of the detectors can be reached, the significantly more expensive SLE version was rejected as default device for the Upgrade.

Besides the PMTs, also different types of their base electronics were tested over the whole time period, starting with nearly all PMTs equipped with a passive base connected to a power supply of the type A7501PB produced by CAEN [100]. Later on, most of the passive bases have been substituted by active bases provided by ISEG [121] of which three different generations were tested in the AugerPrime EA. The advantage of avoiding an additional power supply and a second connection cable lead to the selection of the active base as default for the SSD PMTs. More detailed information about the particularities of certain SSDs can also be found in Ref. [112] and internally in Ref. [124].

The studies of the performance of the AugerPrime EA have been crucial for the development of the AugerPrime upgrade and the design optimizations of its main components. A first presentation of the early test results half a year after start of the engineering phase is given in Ref. [123]. In 2019, an update on the upgrade performance was shown in Ref. [101], also including events acquired with the SSD PPA which is introduced in Section 5.3. In this Dissertation, we present the performance of the AugerPrime EA in the four years of data acquisition mainly focusing on the data of the three LPMTs inside the WCD, as well as of the SSD PMTs. As already mentioned, the numerous modifications of hardware, i.e., electronics, detectors or even whole stations, as well as various changes of PMT power settings and constant updates of the local-station and data-acquisition software complicated the analysis of the performance. These effects can be seen for instance in the time evolution of the baseline-trace mean values of one LPMT of station LS20 displayed in Fig. 5.2. Herein, the blue markers are distributed in multiple populations with different average values depending on the version of electronics board or connected readout devices.

Additionally, we can use the widths of the baseline distributions, i.e., the standard deviations introduced in Section 5.1.2 to describe the overall performance of not only the stations in the AugerPrime EA, but also of the other array configurations introduced in the following sections. The diagram in Fig. 5.10 summarizes the performance of the first 12 AugerPrime stations by showing the monthly averaged baseline widths of the high-gain channel of the SSD PMTs of all stations over the total time period, from the start in October 2016 until the end in March 2021. By analyzing this data, we can draw various observations and conclusions:

- Although the first SSDs have been deployed and connected in October 2016 (first time bin) the first events in this diagram start one month later due to the fact that the necessary software update was rolled out at the end of October 2016 (see calibration
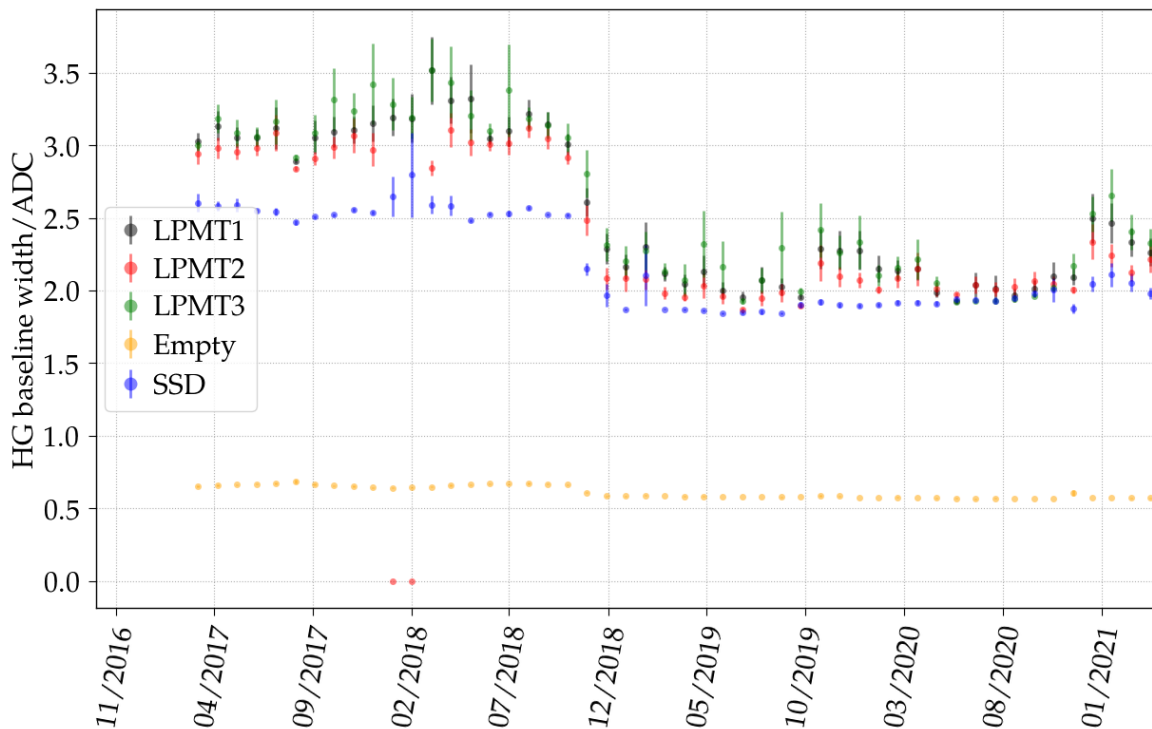
Figure 5.11: Monthly averages of baseline-distribution widths for the high-gain (HG) channels of the station LS1737.

version 257 in Tab. 5.1).

- The stations LS39 and LS41 have been placed and equipped later than the other stations and started their data acquisition at the beginning and the end of 2018, respectively. We can also observe in the diagram that the station LS41 was not sending data for the last months which might indicate a malfunction of its prototype V1 UUB containing modifications for the readout of SiPMs.

- The second SiPM SSD in the data was mounted on top of station LS59 and shows a significantly lower baseline width compared to the other detectors which can be also related with the adapted electronics for the different detection device.

- To search for potential differences between stations in the standard SD-1500 grid compared to stations in the SD-433 array with approximately 10 times more events, we display the group of stations from the hexagon on the bottom, while the four stations of the quintuplet are shown on the top. Selecting two example stations, LS1737 for the first group and LS20 for the latter, no significant differences in the average behavior between these stations can be observed. Merely, the station LS1737 shows a delay in the start of the data acquisition which is the result of the belated installation of the SSD and the first UUB.

- Finally, we can see for certain stations, e.g., LS20, LS22, or LS1737, that their average baseline widths dropped at defined months which contain the dates of the transition from the prototype V1 UUBs to the prototype V2 boards.

The downwards trend in the noise levels mentioned in the last item was already analyzed in the UUB version comparisons in Section 5.1.4 and can also be observed in the diagram in Fig. 5.11. Therein, the monthly average baseline-width values for all the five high-gain channels of station LS1737 are displayed as profiles including the mean value and its standard
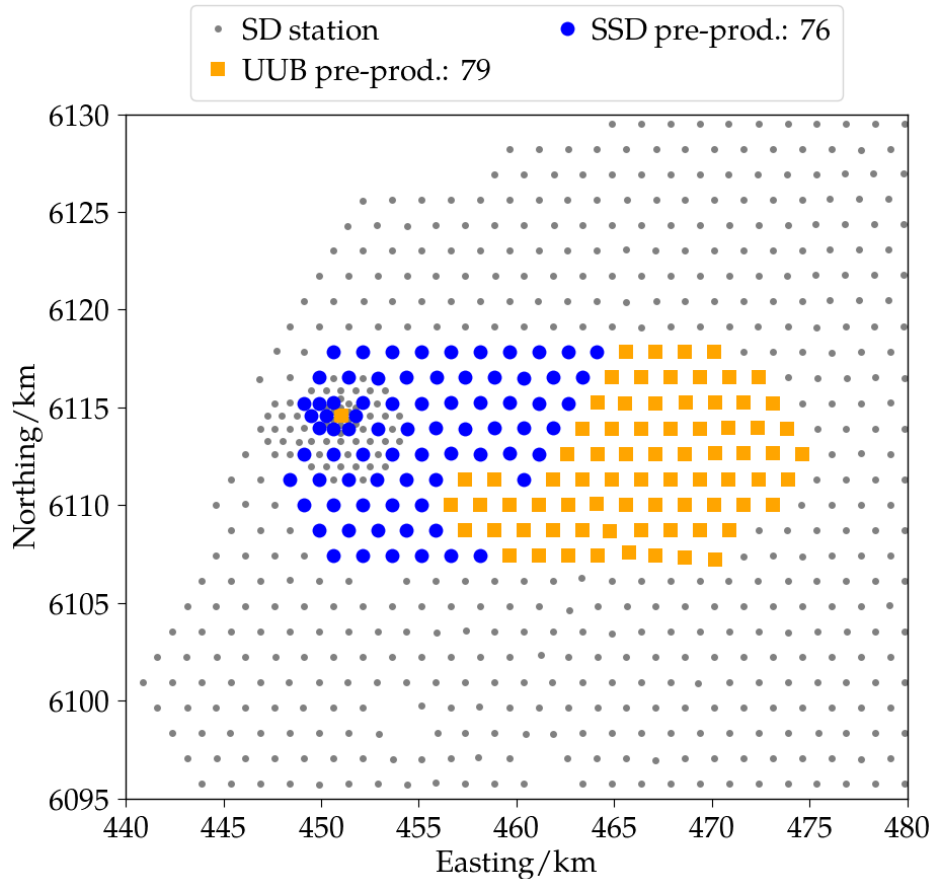
Figure 5.12: Surface detector station map with the two sub-arrays containing Auger-Prime upgrade components from June 2021. The stations of the UUB PPA are highlighted by the orange squares, while the blue circles represent the station positions of the SSD PPA.

error as uncertainties. For all input channels connected to an PMT, a discontinuity in the monthly averages can be seen in the last months of 2018 indicating the decrease of the noise levels due to the change of the UUB. Additionally, the differences in the uncertainty values of the respective PMTs can be explained with the individual intrinsic noise levels of the devices and their base electronics.

Despite the fact that several studies of upgraded components have been carried out, we have to conclude that the number of stations in the AugerPrime EA was to low to test the future SD performance on a larger scale, i.e., the reconstruction of air showers with an array area of ~6 km² is rather limited. In addition, the number of frequent modifications in the engineering phase was too large to draw conclusions on long-term stability of the new detectors and devices. For this reason, the UUB PPA was launched at the end of 2020.

5.2.2 Upgraded Unified Board pre-production array

With the production and the deployment of the first pre-production UUBs, the latest extension of the AugerPrime test phase with the fitting name Upgraded Unified Board pre-production array (UUB PPA) was introduced in the SD array of the Pierre Auger Observatory. This configuration started as a test array for the final UUB version, but will continue as the official upgraded SD array when all UUBs will be deployed in 2023.

In general, the upgrade of the SD stations can be realized rather fast, due to the fact that the SSDs have been already installed in a separate deployment campaign, but just have not

been equipped with an PMT, i.e., have not been added in the data acquisition process yet. For this reason, only the SPMTs inside the WCDs and the SSD PMTs have to be installed, together with the new UUBs. The UUB deployment is usually carried out in batches due to the prior testing and transport scheduling in Europe. The first 31 pre-production UUBs have been deployed in December 2020, marking the start of data acquisition of the new UUB PPA. These first stations are located in the standard SD-1500 grid at the border of the former AugerPrime EA location towards the east. Additionally, this deployment stage included the upgrade of two stations in the SD-433 array, the stations LS20 and LS22, which have been already intensively studied and described in this Chapter.

With the installation of the second batch of 48 UUBs in March and April 2021, the majority of former AugerPrime EA (LS56, LS1733, LS1736, LS1737, LS1738, LS1742, and LS1744) stations received a new UUB, as well as an SSD from the main production series which have been introduced and validated in Section 4.2. This marked the end of the AugerPrime EA test phase. In the case of the former engineering station LS59, located in the multiplet in the center of the EA hexagon, the already installed outdated SSD was removed and a pre-production UUB was installed. Together with the other two fully upgraded stations in this triplet, the effects of the mounted SSDs on the total station response can be studied.

After the deployment campaigns of the first two UUB batches with 79 stations, the UUB PPA reached a sufficient size to start analyzing the performance of the air-shower reconstruction using data acquired with the detectors of the AugerPrime upgrade. In this configuration, the UUB PPA spans an area of ~120 km^2 and the locations of the stations are indicated by the orange squares in Fig. 5.12. This configuration of SD stations containing pre-production UUBs is used in the reconstruction comparisons of the different array configurations in Section 7.3.

In October 2021, the deployment of UUBs continued, and since then, is regularly carried out. Up to the submission date of this Dissertation, already the large number of more than 250 UUBs have been installed in the Observatory. The latest status of the AugerPrime upgrade is displayed in the map in Fig. 5.26.

Analogously to the analysis of the AugerPrime EA data, we use the baseline-trace information to describe the performance of the UUB PPA. By calculating the baseline-distribution width, the quality of the electronics components, as well as of the installed detection devices can be analyzed. In the diagram in Fig. 5.13 the three-day average values of the baseline widths derived from the first 300 bins of the high-gain SSD PMT traces for the first batch of 31 stations are shown. Therein, the stations LS20 and LS22 are listed on the top of the diagram due to their significantly higher event rate as a consequence of being part of the SD-433 array. Overall, the SSDs and UUBs display a stable performance over the more than one year of data acquisition. Nevertheless, in certain time intervals in the first and the last months of the acquisition period, we can observe a repeating feature. In these time intervals, a large fraction of the SSD PMTs show a substantially higher average baseline-width values when compared to regular time intervals. These outliers can be related with thunderstorms and lightning events appearing over the SD array creating noise signals with large standard deviations in the PMT traces. A more detailed analysis of thunderstorm effects on the AugerPrime stations is given in Section 5.4.1, including the responses of the three LPMTs of the WCDs.

In addition, for a better analysis of the uniformity between the electronics boards, we determined the distribution of the average values of a single time interval, i.e., in the case of the UUB PPA of one three-day period. In the diagrams in Fig. 5.14 the distributions of the average baseline widths for the last time interval in the data set from March 2022 for the more than 250 the station are shown. The left diagram displays the distribution for the LPMTs with the ID 2 of all WCDs, while the in the diagram on the right, the values for the SSD PMTs are given. In both diagrams, the peak of the distribution representing the noise level is slightly below 2 confirming the results of the performance tests of the pre-production UUBs which
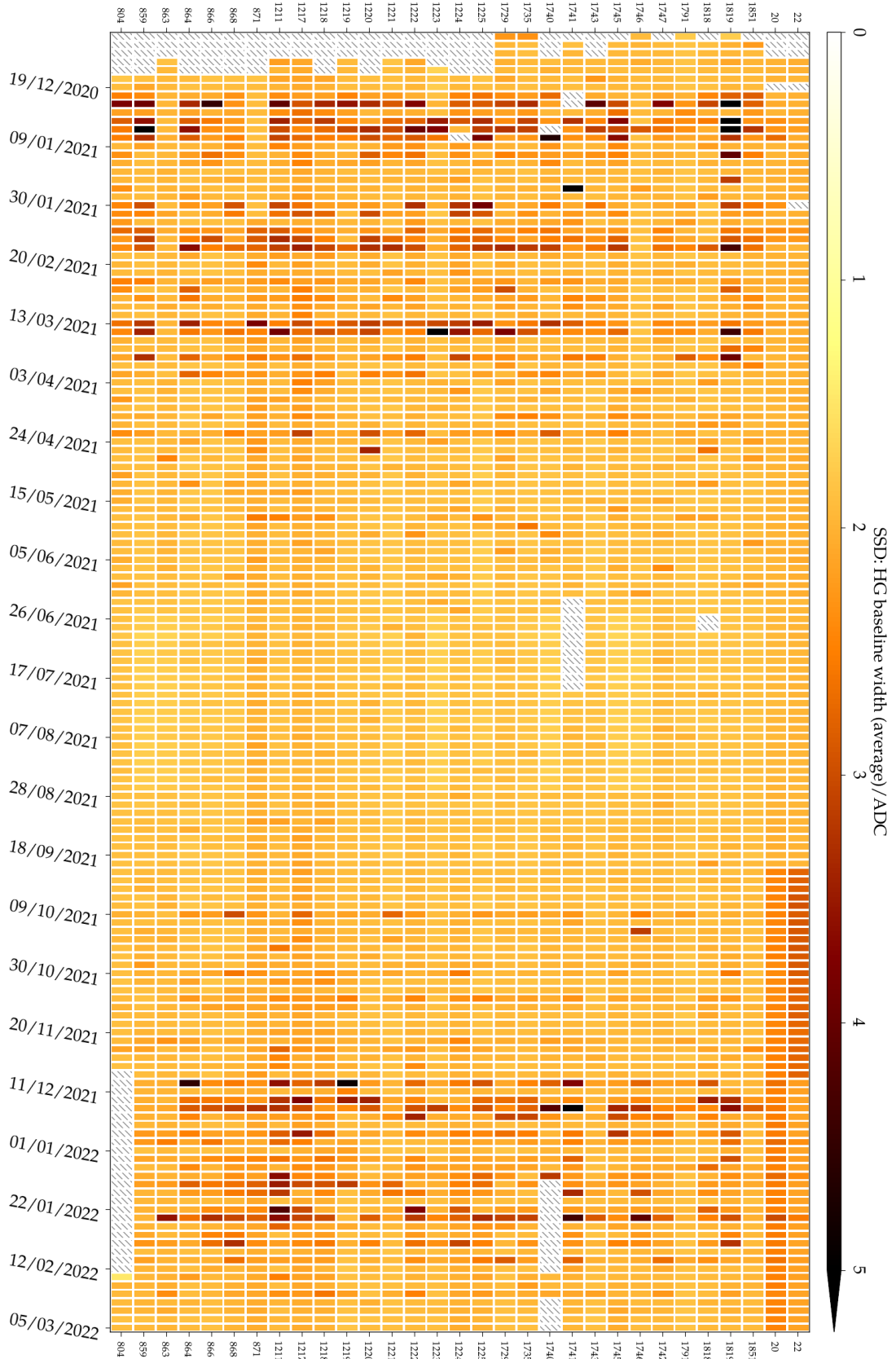
Figure 5.13: Three-day averages of baseline-distribution widths for the SSD PMT high-gain (HG) channels of the first batch of 31 UUB PPA stations.
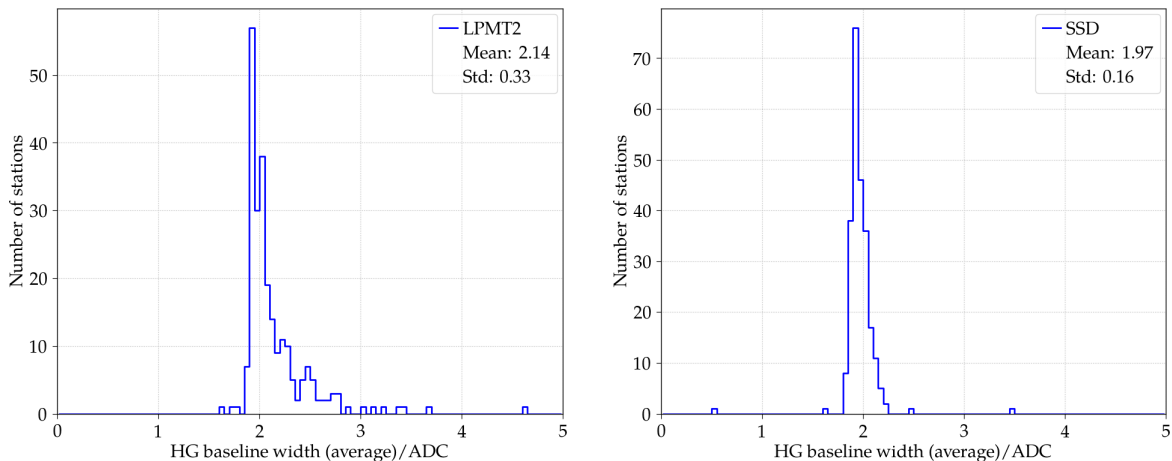
Figure 5.14: Distributions of three-day average baseline widths (March 2022) of all working stations in the UUB PPA. *Left:* For all LPMTs with the ID 2. *Right:* For all SSD PMTs.
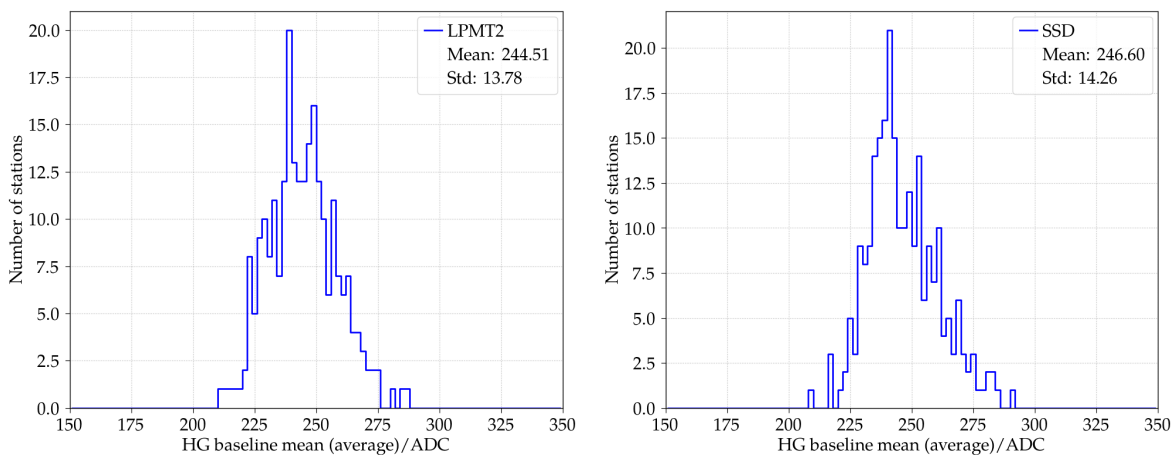
Figure 5.15: Distributions of three-day average baseline means (March 2022) of all working stations in the UUB PPA. *Left:* For all LPMTs with the ID 2. *Right:* For all SSD PMTs.

have been already presented in the electronics board comparisons in Section 5.1.4. The mean values provided in the legend of the diagrams are biased towards a higher noise level due to the fact that a few stations show an increased baseline width for this interval. This can also be seen on the overview plot by the darker colors for these respective stations. As a reason for the increased average values, we can propose local external noise sources, e.g., RFI, or statistical fluctuations due to the low number of events in the interval for the UUBs in the standard SD-1500 array. In addition, we can conclude from the comparison of the shape of distribution that the spread for the SSD PMTs is slightly larger than for the LPMTs which also matches the observations presented in the electronics comparisons.

Besides the baseline widths, the mean values of the baseline traces provide important information about the individual PMT settings and the uniformity of the electronics boards. Therefore, we analyzed the three-day averages of the baseline means in the same way than the width values. By selecting one time interval, i.e., the last period in the data set, and determining the distributions of individual PMTs for all stations, we observe a similar behavior for all four PMTs. The resulting distributions for the LPMTs with the ID 2 and for the SSD PMTs are displayed in the left and right diagram in Fig. 5.15, respectively. The relative spread for

the baseline-mean distributions for all PMTs is between 5 % and 7 % which is a factor of 2 to 3 smaller compared to the relative spread of stations equipped with the original UB and SSD connected (see Section 5.3.1).

5.3   Surface Scintillator Detector pre-production array

When we describe the performance of the AugerPrime upgrade components in the Observatory, we have to mention a third array configuration, the so-called Surface Scintillator Detector pre-production array (SSD PPA), which was deployed at the end of 2018 and beginning of 2019 to serve as an intermediate test array for in-depth studies of the scintillation detectors under field conditions. In October 2021, the majority of these stations were further upgraded and added to the new UUB PPA marking the end of data acquisition of the SSD PPA.

At this point a question might arise: Why is this station configuration introduced separately from the other two test arrays? The answer lies in the usage of the original UBs, instead of the UUBs, due to the fact that in 2019, the new electronics boards were still in the development and testing phase while a large fraction of SSDs had already been produced and mounted in the field. The SSD PPA consisted of 76 stations and was located in front of the Coihueco Fluorescence Detector (FD) building to the left of the AugerPrime EA station hexagon and the UUB PPA, as shown by the blue circles in Fig. 5.12. The array spanned an area of ~120 km^2 and contained stations which belong to all three SD grids with the majority of the stations on positions of the standard SD-1500 array. Only five stations (LS1570, LS1574, LS1622, LS1765, and LS1773) were not counted to the SD-1500 array, but were exclusively part of the denser SD sub-arrays. With the deployment of additional pre-production UUBs in October 2021, the stations of the SSD PPA have been upgraded to AugerPrime stations are from that time on assigned to the UUB PPA. Thereby, the test phase of SSD PPA was terminated.

The method of coupling the SSD PMT to an UB comes with a disadvantage related to the design of the original electronics boards, the necessity of disconnecting one of the LPMT of the WCD. As mentioned in Section 5.1.1, the UB contains six identical signal input channels of which always two channels are connected to the two gains of one PMT, using separate cables. The SSD PMT base electronics is designed for the connection to an UUB, and therefore only provides the single output channel of the anode, i.e., a single signal cable, assuming the gain splitting and amplification is executed on the station electronics board. Hence, an adapter tool is needed to connect the SSD PMT to the UB. This is realized with the UB-SSD interconnection box containing a simple electronics board that serves two purposes. On one hand, the adapter board is splitting the PMT signal into two paths which then can be connected to the two UB input channels. On the other hand, the interconnection box amplifies one of the signal paths by the factor of 32 to reproduce the high-gain amplification of the dynode. The power support and slow control for the adapter box, as well as for the active base of the SSD PMT is provided by splitting the standard multipole cable of the UB.

The disconnection of LPMTs creates certain drawbacks on the data acquisition. For example, the event trigger threshold of the WCD changes depending on the number of running LPMTs, i.e., the detection threshold increases, the fewer LPMTs are participating in the event determination. This leads to systematic shifts in the observed energies of air showers for events measured with the SSD PPA stations. Additionally, with a smaller number of running LPMTs, the chances of a station failure due to the malfunction of the remaining LPMTs is increased. A second disadvantage of the disconnection is the artificially introduced asymmetry in the determination of the total WCD signals. The positioning of the individual LPMT 1, LPMT 2, and LPMT 3 in a triangle around center is identical inside all WCDs to reduce asymmetry effects on the signal calculation depending on the azimuth angle of the incoming air shower.

Finally, the selection procedure of LPMTs to disconnect was organized by following
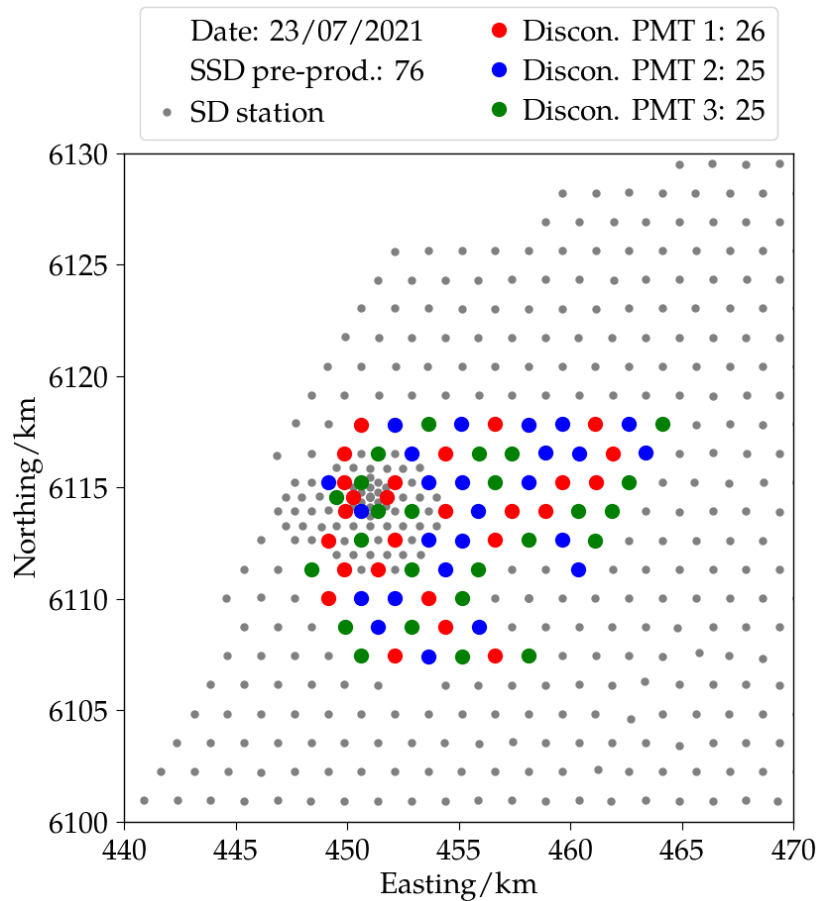
Figure 5.16: Surface detector station map of disconnected LPMTs in the SSD PPA.

certain criteria to suppress the drawbacks as much as possible. If one of the WCDs contained a non-functioning LPMT, then this device was chosen to be disconnected to reduce the loss of well performing devices. For stations with three functioning LPMTs, the devices were chosen in a way that in total, an equal amount of each of the LPMT IDs was disconnected. And if possible, neighboring stations would not have LPMTs with the same ID disconnected, and thus an asymmetric behavior of the whole array depending on the azimuth angle of the air shower can be avoided. The final PMT selection for the disconnection is shown in Fig. 5.16.

5.3.1 Station performance

Despite the fact that the deployment of the SSD PPA started already in October 2018, the official launch of the data acquisition was defined after the last chosen SD-1500 station received the upgrade with an SSD and its PMT in March 2019. A first short report about the performance of the SSD PPA stations was given three months after the launch of the data acquisition in Ref. [101]. In July 2021, an update on the SSD data quality was provided in Ref. [146] containing results of the analyses presented in this Dissertation. To display the performance of the test array, especially of the SSDs, we present in the diagram in Fig. 5.17 the weekly average values of the baseline widths of the SSD PMTs of all SSD PPA stations. Similarly to the overview diagrams of the AugerPrime arrays above, the stations are grouped by their respective SD sub-array classification, the SD-1500 stations on the bottom, the SD-750 stations in the center, and the stations belonging to the SD-433 on the top. If a stations is assigned to multiple sub-arrays, it is listed in the group with the denser spacing.

In the diagram, we can observe that the weakly average baseline widths for most of the
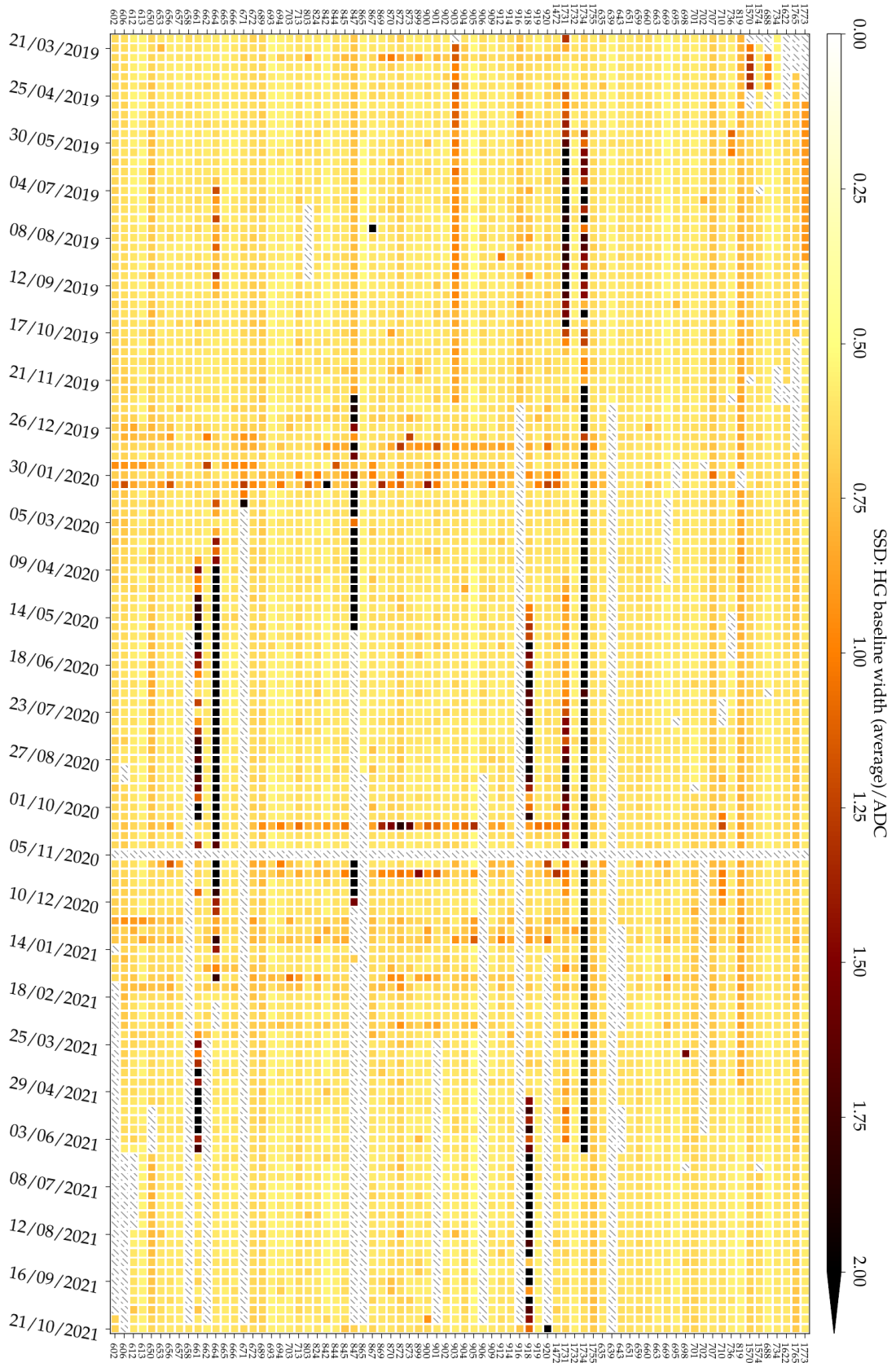
Figure 5.17: Weekly averages of baseline-distribution widths for the SSD PMT high-gain (HG) channels of all SSD PPA stations.
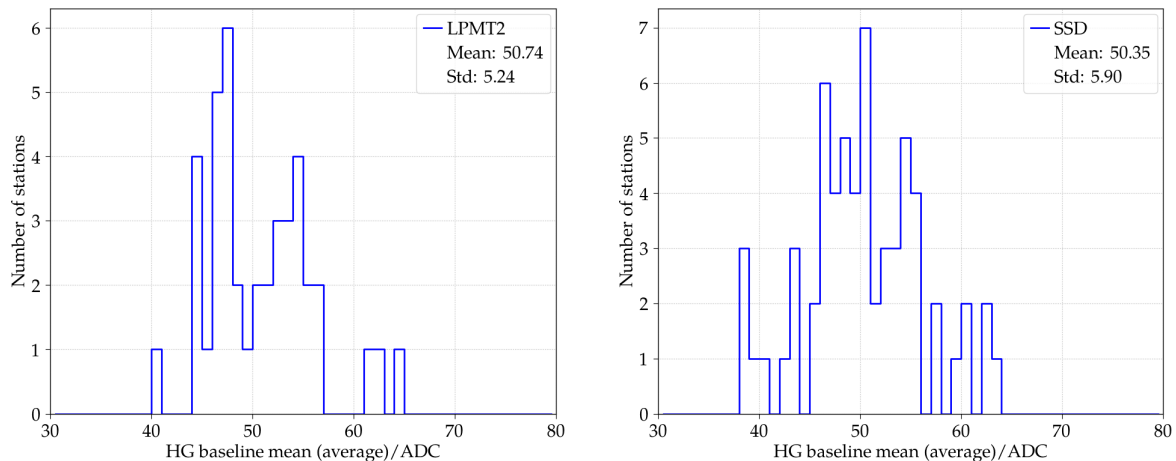
Figure 5.18: Distributions of weekly average baseline means (October 2021) of all working stations in the SSD PPA. *Left:* For all LPMTs with ID 2. *Right:* For all SSD PMTs.

SSD PMTs were stable over time, at values between 0.5 and 0.6 ADC which matches the general noise level of the UB input channels. Only a few stations, e.g., LS1731 and LS1734, show increased average values. This might indicate an issue with the respective electronics board channel or with the PMT and its active base. Another explanation might be a light tightness problem of the SSD, resulting in external photons entering the detector and creating noise pulses in the baseline traces. Besides the stations with increased baseline widths, several stations were not sending data for more than one year, for instance LS639 and LS916, and the number of malfunctioning stations was increasing with time. This observation can be related with the reduction of the station maintenance caused by the restrictions due to the Covid pandemic and lead to a decrease in the event detection with the SSD PPA. Analogously to the vertical features in the UUB PPA summary diagram, we can also see the certain weeks with slightly increased average values for a large fraction of the stations. Due to the fact that this feature is more distinct for stations of the SD-1500, i.e., stations from the lower group in the diagram which have a significantly lower event detection rate than stations from the denser sub-arrays, we can assume that the origin for the increased number of noise pulses are thunderstorm and lightning events. This argument is supported by the matching appearance time of the coincidence features with the thunderstorm periods observed with the UUB PPA stations.

Analogously to the UUB arrays, we are interested in the uniformity of the signals from the stations in the SSD PPA. For this reason, we analyzed the weekly averages of the mean values of the baseline traces and determined the distribution of these average values for all stations using the data of a single week, here from last time week in the data set from October 2021. Equivalent to the UUB test array introduced in the previous section, the distributions are very similar for all four PMTs, but the relative spread with values between 10 % and 15 % is significantly larger compared to the results of the PMTs connected to a UUB, shown in Section 5.2.2. In Fig. 5.18, the distribution of the LPMTs with the ID 2 is presented in the left diagram, while on the right side the distribution of the SSD PMTs is displayed.

5.3.2 Light tightness tests

During the main assembly process of the SSDs at the different production sites, issues with light leakage have been observed during the validation tests which were performed for each detector shortly after its assembly. The majority of these problems have been brought in relation with the procedure of sealing and gluing the enclosure, majorly the corners of the

detector, and lead to the optimization and improvement of the general assembly procedure. In Section 4.2.3 the light tightness analysis of the SSDs from the main production at the KIT is presented. Therein, no SSD with a visible light leakage was found.

Nevertheless, the mechanical stress on the scintillation detectors during the transport from the production sites to the Observatory can be a potential source of damage of the aluminum enclosure and the silicone-glue sealing, and ultimately results in a light leakage when the detector is deployed in the field. For this reason, a procedure to search for light leakage utilizing the data acquired with the SSDs in the Observatory has been carried out using the SSD PMT event traces and investigating once again the widths of the baseline distributions.

In contrast to the calculation of daily, weekly, or monthly averages of the data in the sections above, we split the baseline-width values of the whole data set into two groups. For one group, we only select events that appeared in a time window during nighttime, i.e., after the sunset and before the sun rise, from 23:00 to 04:00. The other group is formed by events measured during daytime, i.e., when the sun is shining, from 11:00 to 16:00. If the detector suffers light leakage issues, we expect increased baseline-width values in the day events compared to night the events, i.e., more visible noise during the day produced by external photons entering the SSD. This search procedure was applied to all the stations in the SSD PPA with the result that the majority of SSD PMT traces are on a very similar noise level for day and night events which was already published in [146]. Only a small fraction of stations show an irregular behavior when comparing day events to night events indicating a potential light leakage.

To further analyze the light tightness, we chose the candidate station LS903 to determine the day and night baseline widths for the mounted SSD, including single event values, as well as the overall distributions. In the diagrams in Fig. 5.19 the baseline-width information for the selected station LS903 are shown. On the left all individual events falling into one of the two chosen time intervals over the lifetime of the SSD PPA are presented. The diagram on the right shows the distributions of both event groups of the total data set. In both diagrams, the day events and their distribution are displayed in orange, while the night events are represented by the color black.

Analyzing the individual baseline-width values, we can observe that at the beginning of the data acquisition, the baseline-width values from events appearing during daytime are systematically higher compared to the events during nighttime. At the end of 2019, the values of the day events begin to decrease and finally reach the same level than the night events. Both event groups then stay on a similar level until the end of the data set.

The difference between day and night events can also be seen in the two distributions in the diagram on the right. The second peak around 1.5 ADC in the distribution of the day events is created by the events of the first seven months of the data acquisition. This observation strongly indicates a light leakage problem, potentially created by a small hole in the silicone sealing. But the downwards trend of the widths values of the day events with time is unexpected and difficult to explain with the data from the field. At that time, several explanations have been discussed, for example a self-sealing effect which closed the potential hole and the light tightness was reestablished. Another origin of the increased width values during daytime might be an external noise sources, e.g., RFI from nearby devices and machines or electric fields from thunderstorms. The amount of hypotheses and wide range of interpretations of the data summarizes the problem of analyzing the standard deviation as baseline quality criterion, due to the fact that the shape of the pulses cannot be distinguished. The standard deviation represents the size of the noise pulses, but separating symmetric pulses, usually created by external RFI sources or malfunctioning electronics components, from asymmetric pulses, potentially created by single photons reaching the photocathode and producing small signals, is challenging.
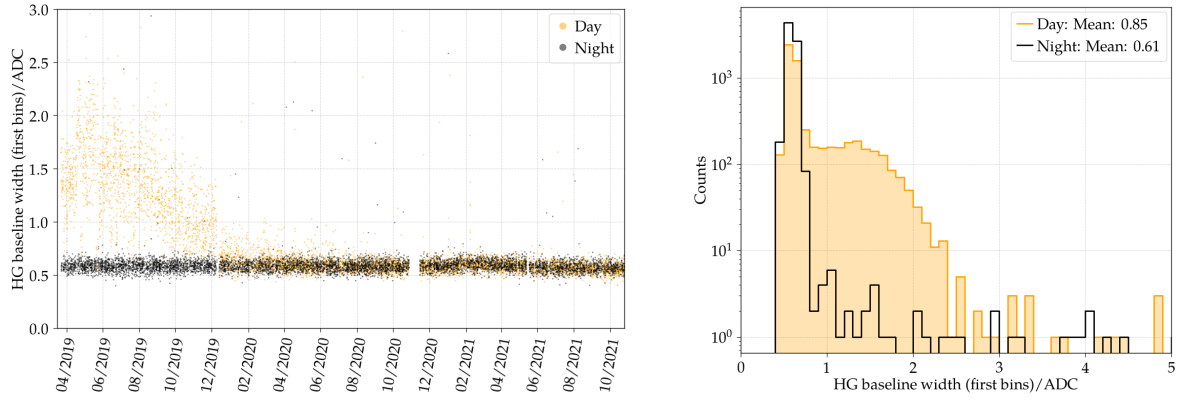
Figure 5.19: Baseline-distribution width values of the high-gain (HG) channel of the SSD PMT of station LS903 separated for events acquired during daytime and nighttime. *Left:* Individual width values over SSD PPA lifetime. *Right:* Distribution of both event groups for the total data set.

In the search for electrical transients in Section 5.1.3, a simple peak finding algorithm was used to distinguish the shape of the pulses appearing in the baseline traces. Here, we chose a different approach by utilizing a different baseline quantity, the so-called skewness S, that provides a measure to describe the shape of the pulses. The skewness S of a sample is defined as the ratio of the third central moment over the cube of the standard deviation σ_b resulting in

$$S = \frac{\frac{1}{N}\sum(b(t)-\overline{b})^3}{\sigma_b^3} = \frac{\frac{1}{N}\sum(b(t)-\overline{b})^3}{\left(\frac{1}{N-1}\sum(b(t)-\overline{b})^2\right)^{\frac{3}{2}}} \tag{5.10}$$

with N defining the number of baseline bins, i.e., 100 in the case of the UB, and $\overline{b}$ representing the mean of the baseline trace.

Similarly to the analysis of the baseline widths, we calculated the skewness for all stations of the SSD PPA. Hereby, we observed that some stations which have been classified as candidates for a light leakage issue do not indicate differences between day and night events within the skewness values. In addition, the average skewness is around 0 for both event groups indicating that the high baseline-width values have been produced by symmetric pulses, i.e., are not created by leaking photons.

In the case of station LS903 the situation is different. The calculated skewness values for individual events are shown in the left diagram in Fig. 5.20, and their distributions from the total acquisition period in the diagram on the right. In both diagrams, we can observe that the skewness values of day events are significantly higher than for night events, at least in the first seven months since the launch. Additionally, the skewness values are positive and larger than 0 which implies that the pulses are asymmetric and above the baseline mean. These indicators are a strong evidence for a light leakage problem of the SSD of station LS903, but still no explanation is given why the values of the day events decrease at the end of 2020 towards a similar level than the events observed at night.

This mystery was only solved by a manual check of the SSD including an opening of the PMT housing. During this check, a significant amount of water was found inside the detector. This time not just inside the aluminum protection box for the cable connectors which has been reported for other SSDs beforehand. But also inside the aluminum tube housing the PMT and its electronics which is supposed to be sealed, and thereby protected from external influences. The fact that water was found directly at the PMT matches the hypothesis of an untight sealing which can also result in an entering of external photons detectable in the event trace data. The decrease in the day events after seven months can be related to a slow
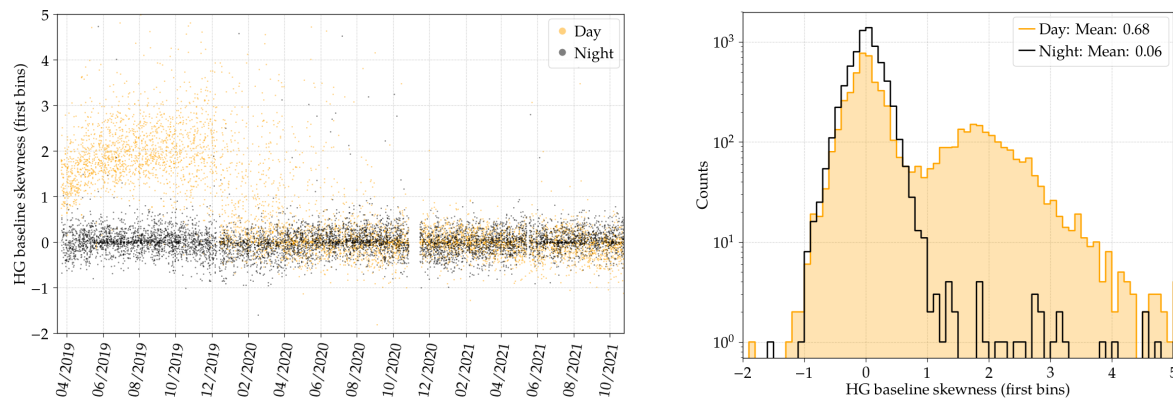
Figure 5.20: Baseline-distribution skewness values of the high-gain (HG) channel of the SSD PMT of station LS903 separated for events acquired during daytime and nighttime. *Left:* Individual skewness values over SSD PPA lifetime. *Right:* Distribution of both event groups for the total data set.

damaging of the PMT and its photocathode by the high light exposure, or the damaging of the base electronics by the surrounding water. In any case, both effects ultimately resulted in the malfunction of the PMT. The baseline width and skewness values that were measured after the malfunction of the PMT are then just representing the noise level of an empty UB channel. For this reason, the difference between events measured during daytime and nighttime vanishes.

After the water was detected inside the SSD of station LS903, the sealing of the critical enclosure components has been improved and the PMT has been exchanged. Overall, we can conclude that the analysis of the baseline traces by determining the distribution width and skewness is a valid procedure to describe the performance of the deployed detectors and to search for potential light tightness issues of the current and new detectors.

5.4   Environmental effects

Besides the studies of the performance and the intrinsic properties of the electronics and detector components, we analyze in this Chapter the influences of environmental effects on the data acquired with the three test arrays equipped with AugerPrime components. Here, two major effects are presented. At first, the detector response to pulses induced by electric fields created by thunderstorm events is analyzed. Secondly, we analyze and present the temperature dependence of the embedded electronics components.

5.4.1   Lightning and thunderstorm events

During the analysis of the first months of UUB PPA data after the launch in December 2020, we observed a feature appearing in nearly all stations and for all PMTs at the same time. The average baseline-width values for certain time intervals were significantly increased compared to the regular values on the majority of days of the acquisition period. This can be seen in the two-dimensional overview diagram of the SSD PMTs in Fig. 5.13 by the vertical lines with a darker color, i.e., with larger baseline-width averages for individual time intervals, for example in the first week of January 2021. Due to the fact that in the Summer season in Malargüe, i.e., from December to February, the appearance probability of thunderstorms with numerous lightnings and strong electric fields is generally increased, and actually multiple large storms have been reported during the chosen data period, the correlation of the observed feature with thunderstorms was very likely.
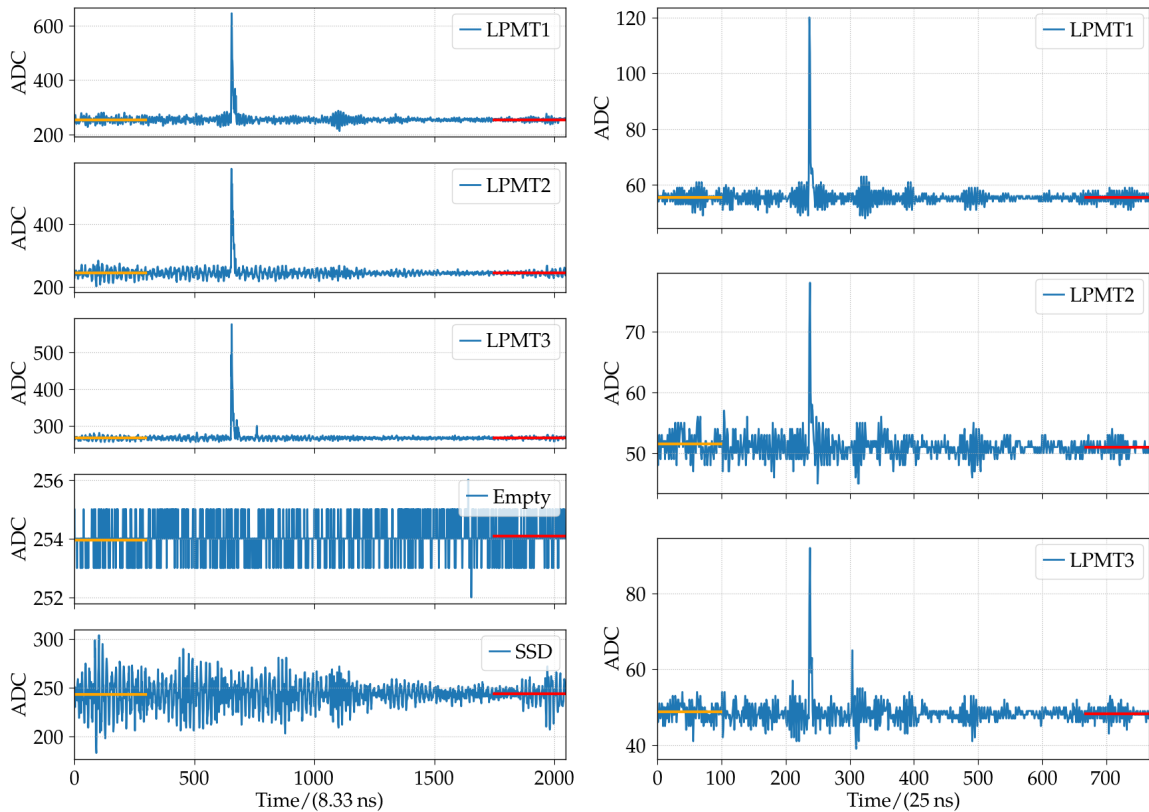
Figure 5.21: High-gain channel traces of two stations participating in the SD event "SD61568654". *Left:* Traces of the AugerPrime station LS1222. *Right:* Traces of the non-upgraded station LS826.

One indication to confirm this hypothesis can already be seen in the two-dimensional overview diagram. The high average values of the baseline widths are created by rare outliers which appear only during a few hours of the day, and therefore can only be seen, if the number of events inside the chosen time bin is not too large. This means that for stations which have an increased event rate, e.g., the stations LS20 and LS22 in the SD-433 array with approximately one order of magnitude more events compared to the SD-1500 stations, the change in the average baseline widths due to rare events is suppressed, as can be seen in the diagram. Analogously, when selecting longer time intervals, e.g., weeks or months as in the case of the two-dimensional overview diagrams of the other AugerPrime test arrays, the visibility of the feature vanishes.

Nevertheless, the influences of thunderstorm events on the input-channel traces of all the connected devices and electronics generations can be observed on an individual event level. To further exclude noise related issues of the new electronics components, a qualitative comparison between the input-channel data from AugerPrime stations and data from non-upgraded stations, i.e., stations equipped with an original UB and without additional AugerPrime components, has been analyzed for individual candidate events. In Fig. 5.21 the high-gain PMT traces of two stations, which are approximately 11 km apart from each other, and participating in the same SD event "SD61568654" are shown. On the left, the five PMT traces of the AugerPrime station LS1222 can be seen, while on the right, the three LPMT traces of the non-upgraded station LS826 are displayed. For both stations, multiple symmetric pulses can be observed for all connected devices at various positions in the time trace. The coincident arrangement of the pulses indicates that their origin seems to be independent of the respective electronics configuration, but relates with an externally induced phenomenon,
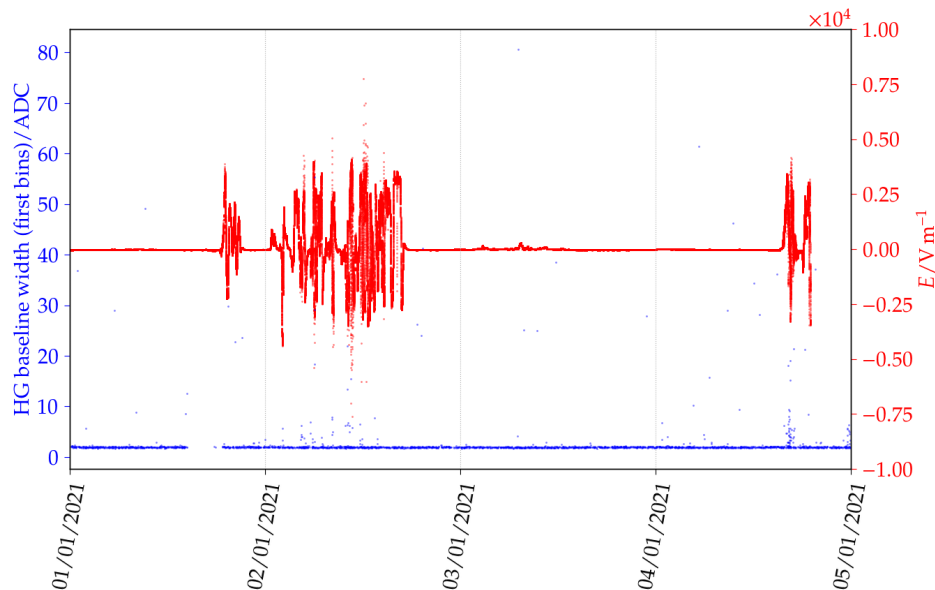
Figure 5.22: Baseline-distribution width values of the high-gain channel of the SSD PMT of station LS20 (blue markers). The red markers display the electric field values measured with a sensor located at the central radio station in the Observatory.

for example with a thunderstorm event.

Finally, as additional study on the correlation of the appearing noise pulses with thunderstorm events, we analyzed the data acquired with sensors installed in the SD array which are able to measure the electric field strength in the atmosphere. Two of these so-called "electric field mills" are currently installed in the Observatory, more precisely, one at the Auger Engineering Radio Array (AERA) weather station, and the other one at the central radio station. These sensors are of the type CS110 produced by Campbell Scientific [147] and provide measurements of the vertical component of the atmospheric electric field close to the surface of the Earth. The embedded data logger stores every second the measured field strength value. Subsequently, the data is readout and transferred to the Auger monitoring database [139].

In the analysis, we chose to use the data of the sensor at the central radio station for the correlation determination, due to the shorter distance to the nearest UUB PPA stations, here the stations LS20 and LS22. Although the electric field mills in the Observatory are currently not calibrated, they still provide a high sensitivity to changes in the local electric fields which are usually created by lightnings and thunderstorm events. These events can be observed as spikes in the sensor data as it is shown in the diagram in Fig. 5.22. Therein, the electric field values for a time period of four days in the first week of January 2021 are presented, highlighted by the red markers. The blue markers represent the baseline-width values determined on the high-gain traces of one of the LPMTs of station LS20. For certain days and hours, we can observe an systematic increase in the width values which often correlates with spikes in the electric field sensor data. This observation strongly enforces the hypothesis that thunderstorms are viable sources of coincident noise pulses in the measured event traces. We can also conclude that the new electronics boards show a very similar behavior compared to the original UBs for all the different connected devices.

In the near future, the number of electric field sensors in the Observatory will be increased by several new devices to further improve the investigation and measurement of the atmospheric electric field conditions. With the installation and an accompanying calibration of the sensors, a precise estimation of the effects of electric fields on the responses of the AugerPrime components will be possible which is especially of high importance for the sensitivity and
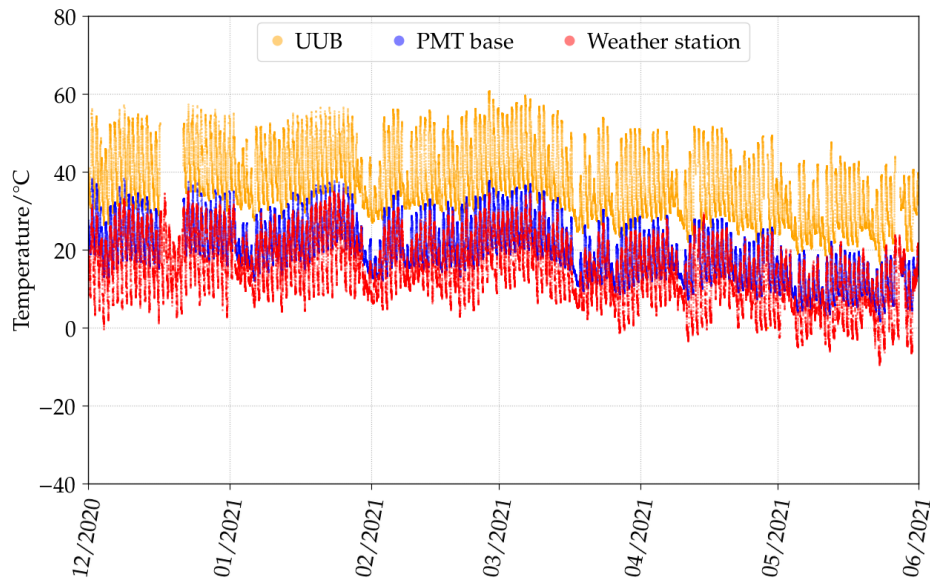
Figure 5.23: Temperature values of three sensors over the total time period of the UUB PPA data acquisition. The UUB sensor data (orange) is obtained from the board installed in station LS20, the PMT base data (blue) represents the LPMT with the ID 1 of station LS20.

performance studies for the upcoming RD antennas.

5.4.2 Temperature dependence

The dependence of the performance and behavior of electronics components on the temperature is a well known relation. Therefore, the study of the temperature dependence of the UUBs, especially of the pre-production version, as well as of the new active base electronics of the SSD PMTs is very important for the success of the AugerPrime upgrade. Before the new electronics boards are send to Argentina for the deployment in the Observatory, each UUB is tested in several laboratory experiments, such as stress screening and temperature cycling procedures inside a climate chamber. These test have been presented in Ref. [148] and in Ref. [96].

In this work, we analyzed the temperature dependence of the PMT and station electronics by utilizing the values of three different temperature data sets. Two sets were received from the monitoring data stream which is acquired and sent together with the event data. While one of these sets was obtained by sensors on each base electronics of the LPMTs and the SSD PMT, the second set was received from a sensor mounted on-board the UUBs. The third set of temperature values was extracted from the atmospheric database collected with several weather stations which are distributed in the Observatory [149]. Following the approach of the previous analyses, we used the baseline-trace quantities, here the mean of the individual baseline traces, to describe the performance of the PMTs and electronics boards, as well as to search for correlations with the temperature data.

Before the analysis of the PMT behavior, the values of the three temperature data sets were compared, and finally, one data set has been selected to be used for the signal-to-temperature correlation studies. With this comparison of the temperature values, the performance and quality of the different sensors can be analyzed. The diagram in Fig. 5.23 shows the temperature values acquired with the three different sensors over the first six months of data acquisition with the UUB PPA. Therein, the combined data of the weather stations is represented by the red markers, and the orange markers indicate the data of the sensor on-board
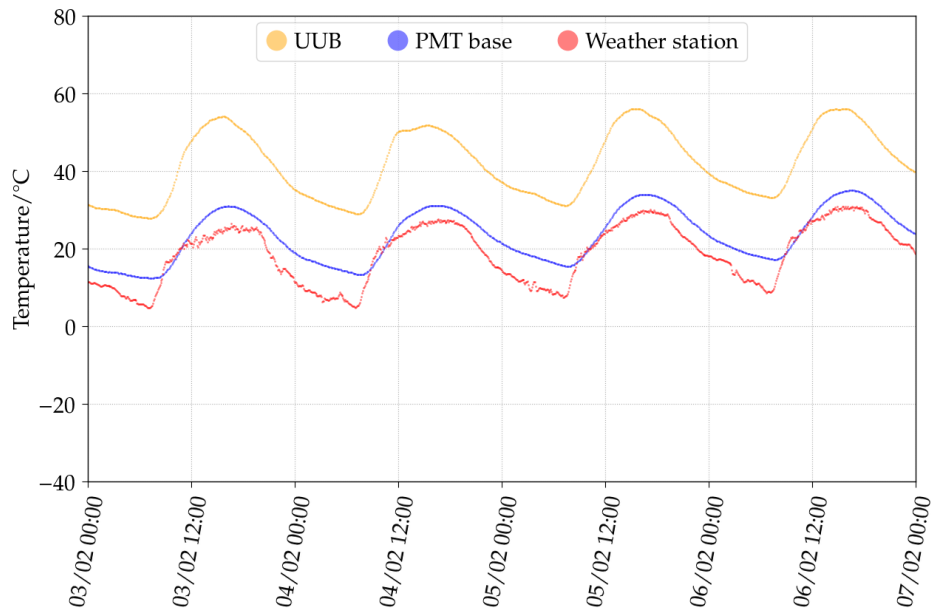
Figure 5.24: Temperature values of three sensors over the time period of three days (3 to 6 February 2021). The UUB sensor data (orange) is obtained with the board installed in station LS20, the PMT base data (blue) represents the LPMT with the ID 1 of station LS20.

the UUB installed in the station LS20. The blue markers show the temperatures measured with the sensor on the base electronics of the LPMT with the ID 1 of the station LS20.

In the diagram, we can observe that all three sensors display a very similar behavior with time. On the large scale, the temperatures follow the seasonal cycle, i.e., the average temperature has its maximum for all data sets in the summer months December and January, and then decreases over the Fall period to reach the general minimum in the Winter months June and July. When comparing the absolute temperatures from the three temperature sensors, the values of the sensors on the PMT base electronics appear for the majority of devices close or only slightly above to the external air temperatures acquired with the sensors on the weather stations. This indicates that temperatures inside the WCDs, and also inside the PMT tube of the SSDs do not exceed critical limits that might lead to a damage of the hardware. The temperatures obtained with the sensors directly installed on the UUBs represent the values inside the electronics board housing in the electronics dome of the station. Compared to the data of the other two sensor types, the temperatures are systematically shifted to higher values. But similarly, the maximum temperatures do not surpass a critical temperature threshold and a stable operation and performance is expected. Here, we also have to note that the comparisons of the absolute temperature values depend on the proper conversion of the raw monitoring values to physical temperature units, in this case °C, defined in the slow-control settings.

Besides the seasonal behavior of the average temperature values, we are able to analyze the expected daily fluctuations depending on the daytime. To receive a more detailed view on the short-scale temperature values, the diagram in Fig. 5.24 displays the data of the three data sets for three consecutive days, from 3 to 6 February 2021. Analogously to the temperature curves of the six months of data from the UUB PPA, the values of the base electronics of the device show a comparable amplitude and absolute scale to the weather station data, while the temperatures from the UUB sensors are shifted towards higher values. Overall, all three curves follow the expected solar cycle with the highest temperatures in the hours after midday, and the lowest in the early mornings.
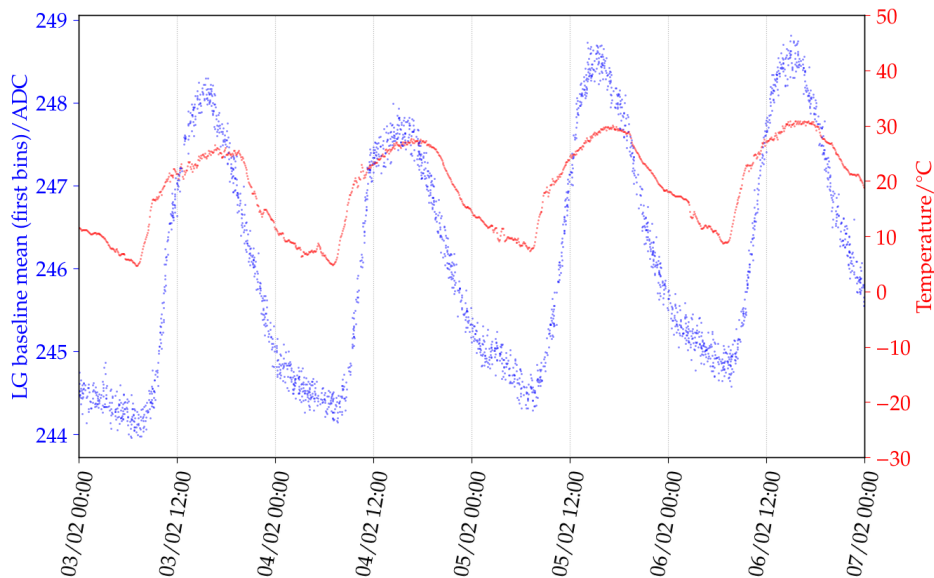
Figure 5.25: Baseline-distribution mean values of the low-gain (LG) channel of the LPMT with the ID 1 of station LS20 (blue) and the external temperature obtained with weather stations sensors (red) over the time period of three days (3 to 6 February 2021).

Finally, the weather station temperature values are chosen to be used in the PMT behavior studies due to the fact that the overall time-dependent behavior of all three sensors is similar and the weather station data has the advantage to be independent of the general data stream of the SD stations. This can be seen in the middle of December 2020, when both data sets from the monitoring database are missing temperature values for several days related to an issue caused by an update of the SD data acquisition software, while the weather stations provide data over the complete period.

In the first months of the UUB PPA, various updates and tests of the station firmware and data acquisition software have been carried out. For this reason, the baseline-mean values show several discontinuities with increases and decreases depending on the current station settings. Therefore, we were not able to carry out a correlation study of the baseline-mean values with the average temperatures in the time period of the UUB PPA. This might be possible in the future when a larger number of events will be obtained under stable conditions.

Contrarily, the correlation of the baseline distribution with the daily temperature fluctuations can be observed. This is shown in the diagram in Fig. 5.25 by the baseline-mean values of the low-gain channel of the LPMT with the ID 1 of station LS20 over three days (blue markers), as well as by the external temperature values (red markers). Hereby, we chose one of the two UUB stations in the SD-433 array which provides a sufficient event rate to observe clear structures on a time scale of single days. When comparing the baseline-mean values with the daily temperatures, we can observe a strong correlation with the external temperature, i.e., with the solar cycle. The higher the temperature rises over the day, the larger the measured baseline means can become. The minimum baseline-mean values are reached when the external temperature reaches its daily minimum. On average, the daily fluctuations show an amplitude of approximately 2 ADC.

5.5 Summary and conclusions

After the promising results from the laboratory tests and simulation studies of the SSDs in the previous Chapter, the performance and operation stability of the main components under field conditions in the Observatory is of high importance for the success of the AugerPrime upgrade and the future data acquisition of the SD. Therefore, we addressed in this Chapter one crucial question: Are the AugerPrime components, i.e., the UUBs in their latest version in combination with the original WCDs and the newly deployed SSDs ready to define the baseline SD stations of the measurement stage Phase II of the Pierre Auger Observatory?

To answer this question, we analyzed the data acquired with AugerPrime stations equipped with the four different versions of electronics boards since 2016. Thereby, the focus was set on the intrinsic properties of the electronics boards and their behavior in the signal sampling and digitization process. By analyzing the event traces, more precisely the baseline traces at the beginning and the end of the event trace, for the different connected devices, a search procedure for misbehaving electronics components was carried out, detecting electrical transients appearing in the data. Contrarily to the first prototype UUB which suffered from frequent noise spikes in the signals, in later versions of the UUB, the measured rate of transient pulses has reached a low and stable level. When we compare the latest UUB version with the results for the original UB, the spike-appearance rates seem to be slightly increased, especially for the SSDs PMT. A potential explanation might be the biasing of the transient rates by an increased number of externally induced spikes as a result of the uncommonly high number of thunderstorms during the first months of the data acquisition with the pre-production UUBs.

In addition to the electrical transient search, the general noise levels of all input channels for all four versions of UUBs have been performed including a comparison with the values obtained for the original UBs. This was realized by determining the average values of the distributions of the baseline-width values. In this analysis, we observed that for the prototype V1 the general noise level were significantly higher compared to the later versions of electronics boards. For the latest UUB version, an average noise level of approximately 2 ADC or slightly below for the high-gain channels of the majority of the PMTs can be determined which matches the pre-assigned requirements on the electronics. In comparison, the absolute noise levels of the UB for the high-gain channels are significantly lower, with values of 0.5 ADC or slightly below. However, if the relative noise levels are compared, we can conclude that latest UUB version reaches similar or even better values than the UB

In the acquisition of air-shower events, the dynamic range of the detection set-up is very important. For this reason, the input channels of the electronics boards are split into a low and a high gain which provide different signal amplification factors. Due to the fact that these factors are given by the electronics components, their accuracy is of interest for the precision of the later data acquisition. In this Chapter, a data-driven method has been developed to derive the amplification factors directly from the analysis of the event traces for the low- and high-gain channels. For the latest UUB version, the resulting amplification factors match the expected nominal values when the statistical uncertainties of the method are considered. Especially for the SSD channels, large uncertainties in the amplification factor determination can be observed

Additionally, the responses of the new UUBs towards environmental effects has been analyzed. Signals of the UUBs obtained during thunderstorm events have been compared to the data of UBs measured at the same time. Herein, we observed a comparable sensitivity of both electronics generations to the electric fields created by thunderstorms. Finally, the temperature dependence of the new electronics boards has been studied resulting in the expected correlation of the trace baselines with the external temperature.

Besides the new electronics boards, the performance of the SSDs installed at the SD stations in the Observatory has been analyzed in this Chapter, majorly under the topic of

light tightness tests of their mechanical enclosure. These tests were carried out by studying the baseline traces of the SSD PMTs, and separating the data into events measured during daytime and others during nighttime. With this strategy, one SSD has been found showing a significantly higher baseline noise during the daytime compared to the night events which indicated an issue with external photons entering the detector. This leakage issue has been confirmed after the detector was opened and water was found in the proximity of the PMT potentially caused by an untight silicone sealing. For the other SSDs, a similar behavior has not been detected.

Furthermore, we have introduced and described the different SD station and array configurations related with the AugerPrime upgrade which have been operated in the past or are still acquiring data. One of these configurations is the Upgraded Unified Board pre-production array (UUB PPA) which was deployed and launched in 2020 as the successor of the Auger-Prime Engineering Array (EA) originally installed in 2016. In parallel, the Surface Scintillator Detector pre-production array (SSD PPA) was established in 2019 to test a larger number of SSDs under the environmental conditions in the Observatory. An overview of the current status of the SD upgrade at the submission date of this Dissertation is shown in Fig. 5.26. In the final configuration, all SD stations except the most outer rows will be equipped with an SSD. The deployment of the UUBs together with the SPMTs inside the WCDs is foreseen for all the available SD stations in the Pierre Auger Observatory.

From the point of the data acquisition and detector performance, we can finally positively answer the aforementioned question asking if the latest hardware for the AugerPrime upgrade is ready for the use in all the SD stations. When analyzing the data of both generations of electronics boards regarding their respective noise and dynamic range properties, a smooth transition from the measurement stage Phase I towards Phase II seems to be achievable. Nevertheless, further studies and comparisons of the respective array trigger algorithms and event timing information are necessary to prevent a loss of observed extensive air shower (EAS) events.

In parallel to the analyses presented in this Chapter, additional performance studies of the AugerPrime components have been performed using the SD-433 AugerPrime multiplet stations equipped with prototype UUBs and SSDs of the EA design [110]. These studies include the analysis of the timing resolution of multiplet stations equipped with UUBs, as well as tests of the baseline and signal stability in dependence of the temperature.
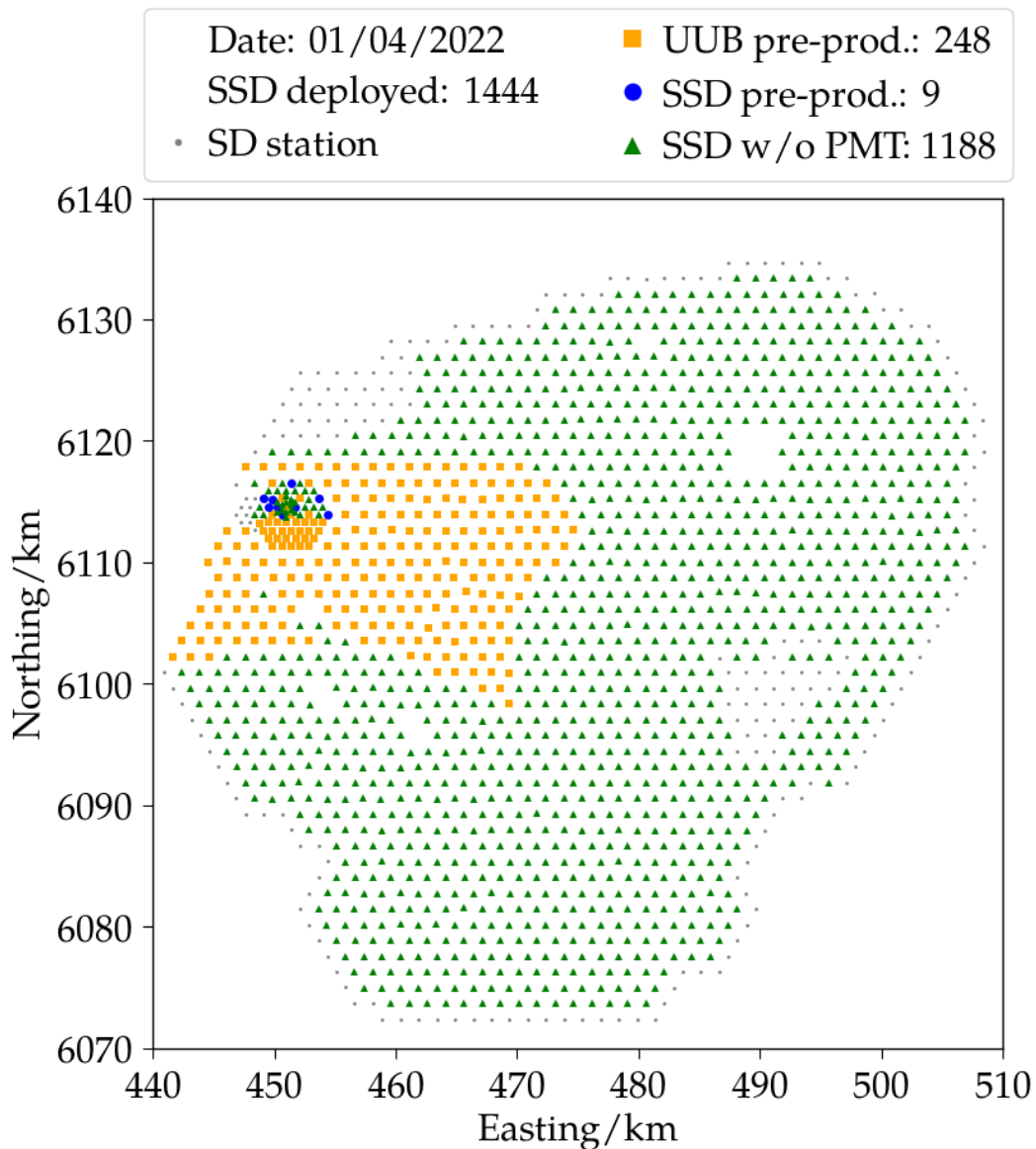
Figure 5.26: Current status (May 2022) of the AugerPrime deployment for the SD. Each gray dots represents a non-upgraded station, the green triangles depict the stations with a mounted SSD which is not yet equipped with an PMT. The SSD PPA containing SSDs connected to an original UB is shown by the blue circles. The orange squares display the stations of the UUB PPA which represent the final AugerPrime stations, only missing the radio antenna.
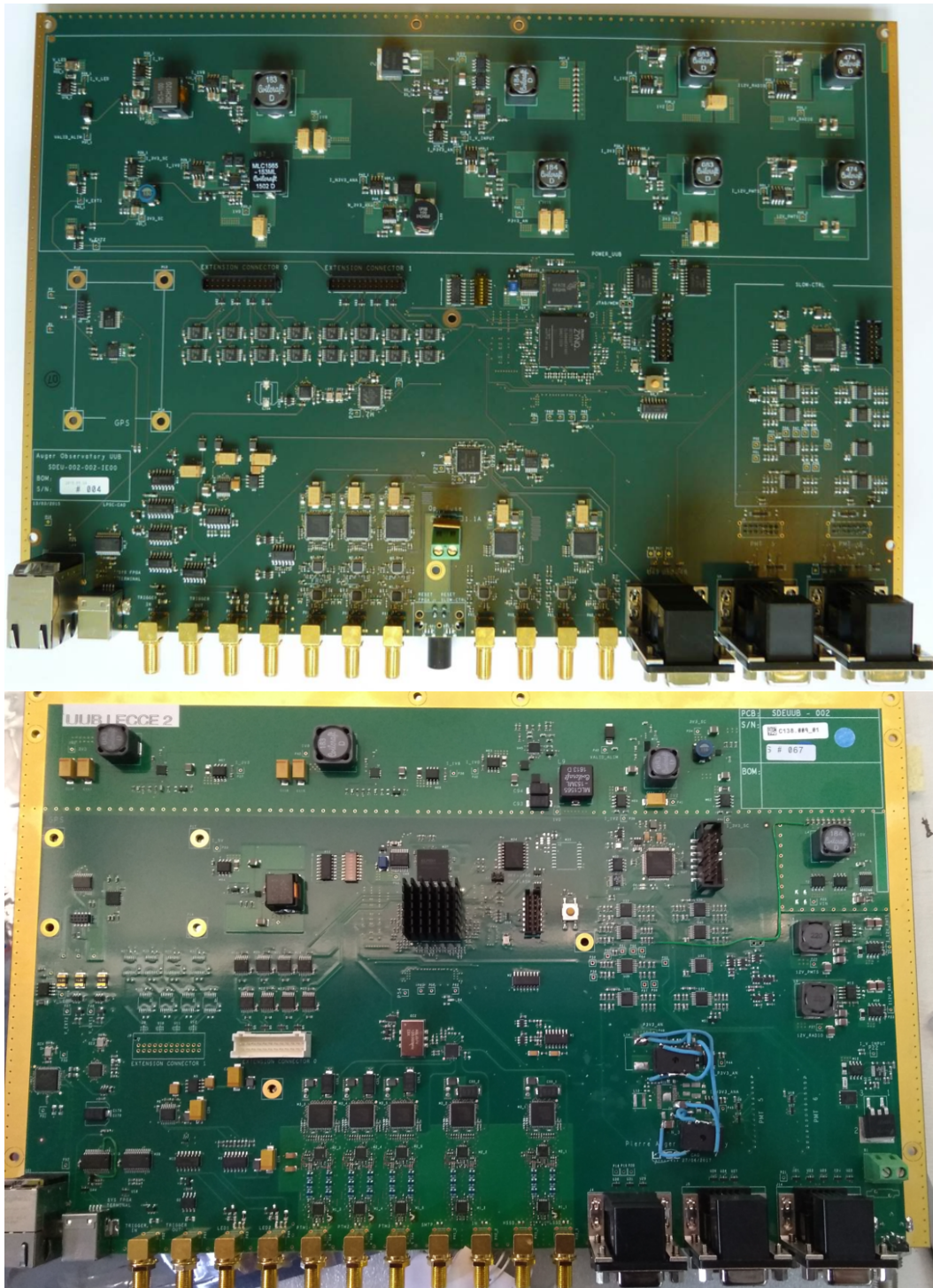
Figure 5.27: Photos of different UUB versions. *Top:* Prototype version V1 from 2016. *Bottom:* Prototype version V2 from 2018. Credits: [150].
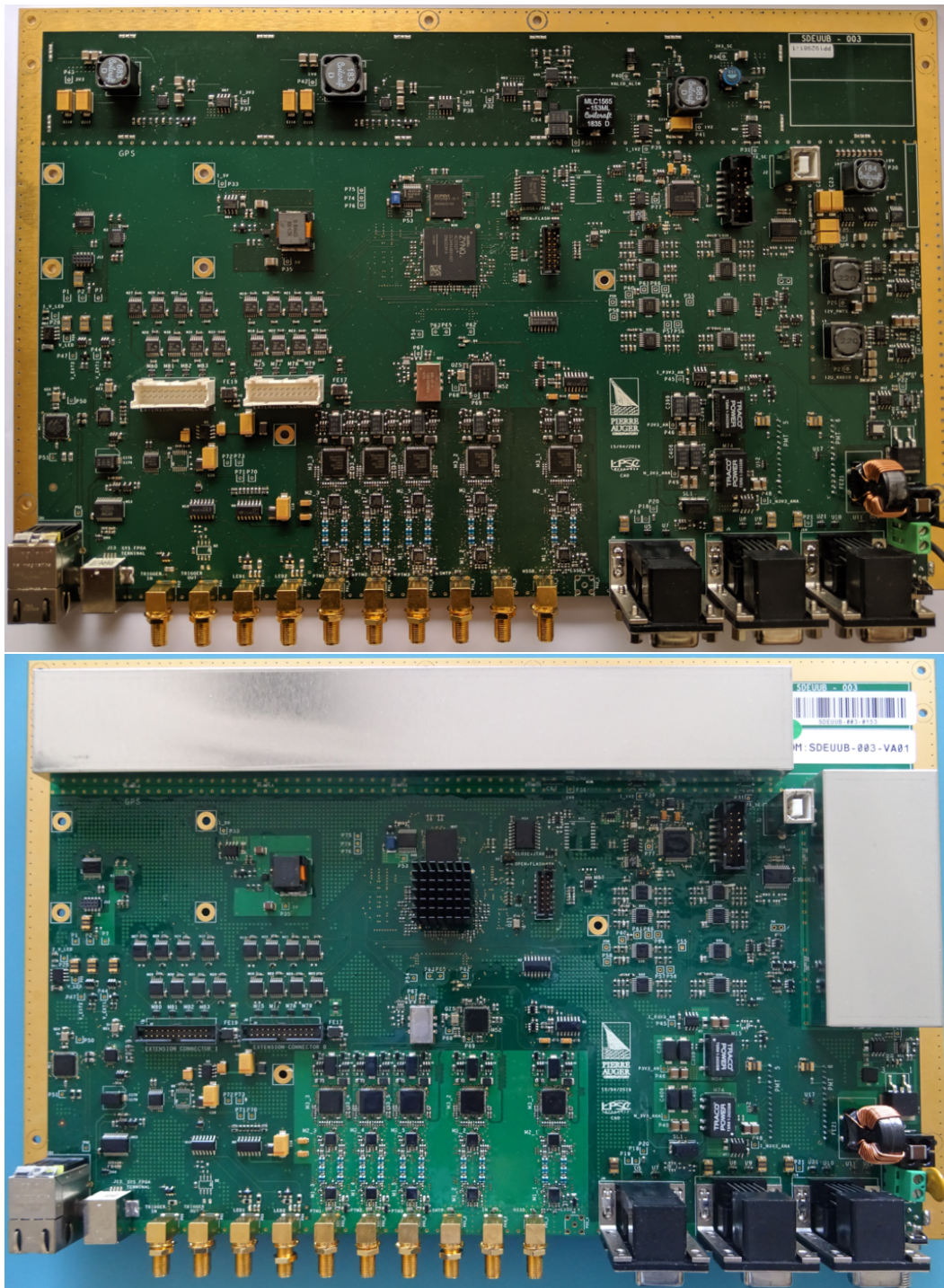
Figure 5.28: Photos of different UUB versions. *Top:* Prototype version V3 from 2019. *Bottom:* Pre-production version from 2021. Credits: [150].

Chapter

6

Calibration of the Surface Detector Signals

Understanding and interpreting the measured detector signals is mandatory for the determination and derivation of physical concepts and natural laws. In general, a calibration process can be described by comparing measurement values and their accompanying uncertainties to a calibration standard of pre-known accuracy. For this process, the calibration of each single detection device is of high importance and requires an advanced knowledge of its properties and behavior to understand the systematic uncertainties driven by the calibration process.

Due to the fact that the Surface Detector (SD) of the Pierre Auger Observatory consist of a large number of autonomously running stations, which themselves contain multiple detection devices, a unified and automatic calibration procedure is necessary. Thereby, this procedure is required to be fast, robust, and executable on the local-station electronics, i.e., on the electronics of a single SD station, without negatively influencing the continuous data acquisition. Additionally, the use of extended device information provides the opportunity to perform a software calibration at the later stage of the data analysis, independently from the electronics configuration and the data acquisition process. Due to the design of the SD stations and their operation settings, a calibration of the individual devices to their intrinsic responses for each event is not feasible. Thus, a calibration of each photomultiplier tube (PMT) to the number of produced photoelectrons, as a measure of the deposited energy, for example presented in the laboratory measurements in Chapter 4, cannot be achieved. This is simple by the fact that single particles passing through the water-Cherenkov detector (WCD) are not distinguishable, nor are the devices operated under conditions to directly measure intrinsic properties, for instance single photoelectrons (SPEs). As an alternative, a relative calibration is in place converting the measured deposited charges into an unified average reference unit which then is used to quantify the signals of the stations in the subsequent air-shower reconstruction procedure. Even so, the identical method is applied to all the PMTs, individual calibration factors for each device are determined by utilizing the information from the event and monitoring data stream in combination with general detector properties which have been determined in preceding laboratory tests and studies of simulations.

To provide an overview on the calibration of the SD of the Pierre Auger Observatory, this Chapter commences with a general description of the calibration information provided

by the station electronics, and continues with a presentation of the modules of the $\overline{\text{Off}}\underline{\text{line}}$ analysis framework participating in the event signal calibration. This includes an analysis of the performance of the currently implemented offline SD calibration algorithm and its reliability and stability over the total data acquisition period from 2004 until 2021. From the results of the studies of the stably running WCDs, we infer optimization possibilities to increase the flexibility of the algorithm, and thereby ensure a successful calibration of the newly added Surface Scintillator Detectors (SSDs), as well as of all the AugerPrime stations containing the next generation electronics boards, the Upgraded Unified Boards (UUBs). A detailed introduction of the modified calibration algorithm, together with an analysis of its performance, and a comparison with the currently available procedures is given in the second part of this Chapter. In addition, we study the long-term behavior of calibration-related quantities of both detectors, the WCDs and the SSDs, to gain insights on the material aging behavior of the individual hardware components, as well as the accompanying influences on the future data acquisition. Finally, an outlook on the calibration performance of the signals from the AugerPrime stations is provided.

6.1   Calibration information stream

Following basic experimental concepts, the data acquisition of the SD of the Pierre Auger Observatory can be divided into two parallel main processes. On the one hand, the design of the detectors and the implementation of the local-station trigger logic provide the measurement of particles from extensive air showers (EASs) with a predefined rate including the "physics" events, i.e., the EAS events produced by ultra-high energy cosmic rays (UHECRs) arriving at the Earth's atmosphere, as described in Section 3.1.2. In addition, to match the expected trigger rates, a continuous adaptation procedure of the trigger thresholds defines the online calibration of each individual device and determines estimates of various quantities describing the current operation and calibration status. On the other hand, continuously and uniformly arriving air showers from low-energy primary cosmic rays (CRs), mostly consisting of muons due to the attenuation and the decay of the other shower components, are used to derive additional calibration information. These air showers are often called "background showers" or "muon showers".

In general, the set-up and calibration of the SD stations and their respective devices follow a well-defined strategy which can be split in several sub-processes. At first, we shortly introduce the rate-based procedure for the determination and application of the proper power settings for each individual detection device. After the operation status of the PMTs reaches an acceptable level, the automatic calibration process implemented on the local-station software is launched, and from that point on, continuously executed on each station electronics board. This process includes the methods for the adaptation of the trigger thresholds to provide a uniform trigger condition for the entire SD array, and simultaneously, determines certain quantities and rates relevant for the later event reconstruction. Subsequently, we describe the additional calibration information acquired from the background shower data which is stored and transmitted in the so-called calibration histograms.

6.1.1   Operation settings

Before an SD station is added to the trigger and data acquisition system, all devices, i.e., the three large photomultiplier tubes (LPMTs) of the WCD, and in the case of the AugerPrime stations, also the SSD PMT and the small photomultiplier tube (SPMT) have to be set up with the proper power configuration to provide the expected sensitivity and dynamic rage. Thereby, a rate-based method for all the devices except the SPMT is used in a 1-fold coincidence, i.e., on each individual device separately, to set the respective voltage levels on the electronics

bases, and consequently match the gain factors of the devices [151, 152]. With this procedure, a uniform response of the three LPMTs is guaranteed resulting in an equivalent treatment of the three devices in the local coincidence event trigger of the WCD.

In the case of the LPMTs, the gain adjustment is realized by measuring the signal rate of frequently arriving air-shower particles utilizing a simple threshold trigger mode implemented in the local-station electronics, the so-called "singles mode" or "scaler mode". After an LPMT is connected to the electronics board, the configuration script is launched with pre-defined start parameters to obtain the scaler trigger counts for the currently applied voltage. Thereby, the scaler trigger is used in a 1-fold condition, contrarily to the regular 3-fold scaler mode. Preceding test measurements during the engineering phase of the Observatory, delivered an optimal detection rate of 100 Hz for a defined threshold which is then set as the target value for the adjusting procedure. If for an individual LPMT the detection rate for a fixed threshold is below or above the expected optimal value, the applied voltage is increased or decreased in small steps, respectively. This process is iteratively repeated until the expected rate is reached and remains stable for a certain time period. For setting the voltages of the SSD PMTs, the same procedure is applied utilizing the standard full-bandwidth single bin trigger due to the missing implementation of a "scaler mode". Contrarily, in the case of the SPMT, the low sensitivity towards the arriving low-energy muons prevents the application of the rate based method, and therefore the power settings are chosen by visually estimating the optimal operation conditions.

6.1.2 Online calibration procedure

Although the detection rate for a constant threshold can alter due to temperature and material aging effects, the voltage settings of all devices are not changed after the initial power configuration is terminated and the station enters the regular data acquisition mode. From this point on, another method is applied to compensate for shifts in the responses of the devices by adjusting the individual trigger thresholds with a continuous online calibration procedure, and thereby retaining a uniform trigger behavior and dynamic range of the SD stations [151, 152]. Due to the payload limitation of 1200 bits per second for the data transmission of the SD stations to the communication units at the Fluorescence Detector (FD) sites, the procedure cannot be performed remotely, but has to be executed by the station electronics to provide a fast adaptation to changes in the measurement conditions. The procedure was developed in extensive studies of the LPMT responses inside the WCD during the engineering phase of the SD and utilizes the single LPMT information, as well as the multi-device coincidence conditions.

As already introduced in Section 3.1.2, the WCD is expected to provide a first local trigger stage with an expected trigger rate of 100 Hz for the single bin trigger condition (TH-T1). Thereby, the TH-T1 condition is defined in a 3-fold coincidence on the signals of the LPMTs stored in dedicated memory buffers, the so-called "shower buffers", of the station electronics with a trigger threshold of $1.75\, I_{\mathrm{VEM}}^{\mathrm{est}}$. For the case that the WCD contains malfunctioning LPMTs, the coincidence trigger thresholds are increased, i.e., when two functioning LPMTs are participating in the local-station trigger to $2.00\, I_{\mathrm{VEM}}^{\mathrm{est}}$, and for a single LPMT station to $2.85\, I_{\mathrm{VEM}}^{\mathrm{est}}$. When the data acquisition of a station is started, a first estimate of the threshold factor $I_{\mathrm{VEM}}^{\mathrm{est}}$ is derived.

Despite the fact that the T1 trigger condition is applied in a 3-fold coincidence, the threshold factor I_{VEM} is determined on the single device level. After a first estimate of the factor is set and the T1 trigger condition is applied, a check of the trigger rate of the single devices is performed. Out of the T1 triggers detected in approximately one minute for each individual device, the rate of triggers above $2.5\, I_{\mathrm{VEM}}^{\mathrm{est}}$ is expected to be 70 Hz [151, 152]. This correlation was determined during test measurements in the engineering phase and is internally referred to as "T70" condition. If the current rate does not match the expected value, the threshold

factor is iteratively decreased or increased, utilizing a so-called "sigma-delta method" until the required 70 Hz is reached. Similarly to the 3-fold T1 condition, the T70 threshold depends on the number of participating devices and is increased to $2.6\,I_{\text{VEM}}^{\text{est}}$ and $3.3\,I_{\text{VEM}}^{\text{est}}$ for two and one functioning LPMTs, respectively. The resulting factor $I_{\text{VEM}}^{\text{est}}$ represents the average maximum pulse height of the obtained signals and is also referred to as "average signal amplitude" or "amplitude calibration factor". Internally, the term "peak calibration factor" is occasionally used which can potentially lead to a confusion with the general meaning of the word "peak", especially when functional relations are described.

Besides the average signal amplitude, a second quantity with a very high priority for the calibration and reconstruction procedure is determined by the local-station software on the shower buffer data. This quantity is the average signal area $Q_{\text{VEM}}^{\text{est}}$, also frequently referred to as "average signal charge" or "charge calibration factor". Thereby, the charge calibration factor $Q_{\text{VEM}}^{\text{est}}$ is determined by selecting the signal areas calculated by the field-programmable gate array (FPGA) for signals with an average signal amplitude in-between a defined window above the T1 threshold.

In case of the AugerPrime stations which have been added to the data acquisition in 2016, the threshold trigger condition TH-T1 is performed on the compatibility mode traces which are also stored in the shower buffers, i.e., using the filtered and down-sampled traces, to emulate a similar trigger behavior compared to the Unified Board (UB) trigger system. Regarding the calibration quantities, the implementation of the calculation of the local-station software estimates, especially the average signal area $Q_{\text{VEM}}^{\text{est}}$ of the LPMTs, still has to be adapted to the different responses and thresholds of the devices connected to the final UUB version. In the case of the SSD PMTs, a modified algorithm is necessary to determine the analogous quantities, the average signal amplitude $I_{\text{MIP}}^{\text{est}}$, as well as the average signal area $Q_{\text{MIP}}^{\text{est}}$.

Completing the calibration information stream of the local-station estimates, several additional quantities representing the current electronics and detector performance are provided. For example, the online estimate of the flash analog-to-digital converter (FADC) trace baseline is transmitted calculated as the average of the first bin entry of each T1 trace. In addition, the dynode-to-anode ratio (D/A), i.e., the factor between the high- and low-gain channels, is included in the stream, as well as rates of local triggers determined in the calibration intervals.

6.1.3 Calibration histograms

Besides the online calibration algorithm of the event trigger thresholds, a second source of calibration information is available for each T3 event [151, 152]. This information is merged into in the raw data files created by the Central Data Acquisition System (CDAS) and is obtained by the local-station software analyzing the data from the so-called "muon buffers". These memory buffers are filled by acquiring the signals of low-energy background showers which mostly contain muon signals, hence the naming of the buffer. In contrast to the event single bin threshold trigger (TH-T1) which uses a method to continuously adapt the threshold factors depending on the observed trigger rates, the thresholds for the muon triggers are set to constant values. While the trigger uses the full-bandwidth traces from the high-gain input channels and is performed in a 1-fold coincidence, i.e., on each LPMT independently, the readout of all devices is realized with a logical OR condition between the three LPMTs. When the muon trigger is fulfilled, several calibration-relevant quantities are determined by the local-station software. These quantities are monitored in the so-called calibration histograms over the time window of 61 s, and then are sent together with the event trigger information when a readout request is sent to the station. Only for stations which have been operated with a certain calibration software version (8 or lower) these additional calibration histograms are not available in the T3 event files. From the obtained quantities, the histograms of the maximum signal amplitudes and the signal areas are the most relevant for the subsequent
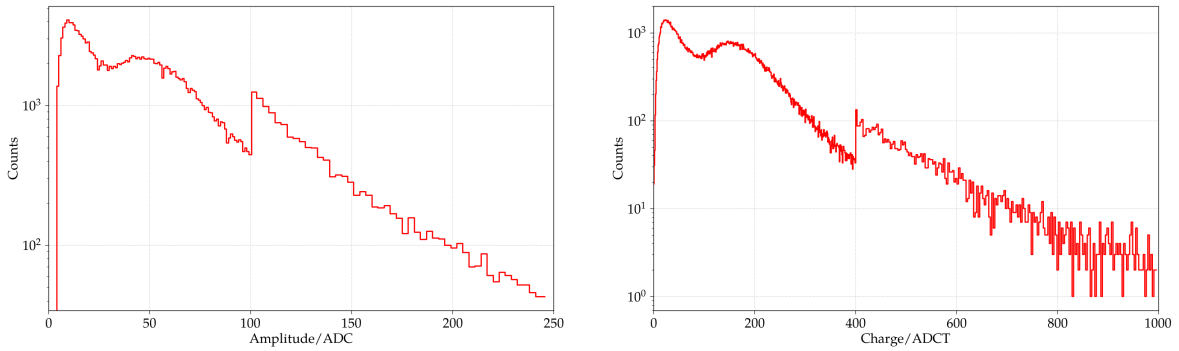
Figure 6.1: Examples of raw calibration histograms for an LPMT connected to an
UB. *Left:* Signal-amplitude histogram. *Right:* Signal-area histogram.

event signal calibration which is performed offline.

In general, the raw signal-amplitude histograms of the LPMTs display a defined shape
with several extreme values, as shown in the left diagram in Fig. 6.1:

- A first maximum at low ADC values can be seen which is created by air-shower particles
  with low-energies, e.g., electrons or positrons, which enter the WCD and deposit all
  the energy therein. Additionally, corner clipping muons can produce low amplitude
  signals which are filled in the histograms. On the left flank of the peak, the convolution
  with the trigger condition is visible.

- At higher amplitude values, around 50 ADC, a second maximum is visible which
  contains the calibration-relevant information. This maximum is the result of the flux
  of through-going background muons, and therefore can be named "muon peak". The
  position of the maximum defines the signal amplitude factor $I_{\mathrm{VEM}}^{\mathrm{peak}}$ for omnidirectional
  muons passing through the detector and is equivalent to the online estimated average
  signal amplitude $I_{\mathrm{VEM}}^{\mathrm{est}}$.

- Besides the two maxima, a third feature can always be seen at a defined bin number,
  for the signal-amplitude histograms starting at the 101st of the 150 bins. To reduce
  the amount of the transmitted data, the sizes of the bins from number 101 to 150 are
  increased by a scaling factor resulting in the merging of several bins of the original
  size and a summation of their respective bin entries. This procedure of splitting the
  histogram in "normal" and "big" bins is viable due to the fact that if the device is set
  up properly, the expected muon peak position is assumed to be always located in a
  bin before the 101st. Therefore, the information content of the last bins is rather low
  compared to the first 100 bins.

In the context of the AugerPrime upgrade, the total number of histogram bins, as well
as the transition bin position is identical for the amplitude histograms determined with the
UBs and the UUBs. Only the scaling factors for the "normal" and "big" bins vary between
the electronics generations. The signal amplitudes are stored in values of their raw units of
FADC counts or short just "ADC".

Analogously, the histograms of the signal areas of the LPMTs can be described by a general
shape with two maxima, one at lower signal-charge values produced by low-energy particles,
while at higher signal charges the peak from through-going muons can be observed defining
the signal area $Q_{\mathrm{VEM}}^{\mathrm{peak}}$ for muons arriving at the detector from all angles. When comparing the
muon charge peak to the average signal area from the online calibration procedure, a scaling
factor between $Q_{\mathrm{VEM}}^{\mathrm{peak}}$ and $Q_{\mathrm{VEM}}^{\mathrm{est}}$ is needed. The signal-charge histograms contain more bins
than the signal-amplitude histograms, in detail, always 600 bins are available, independently
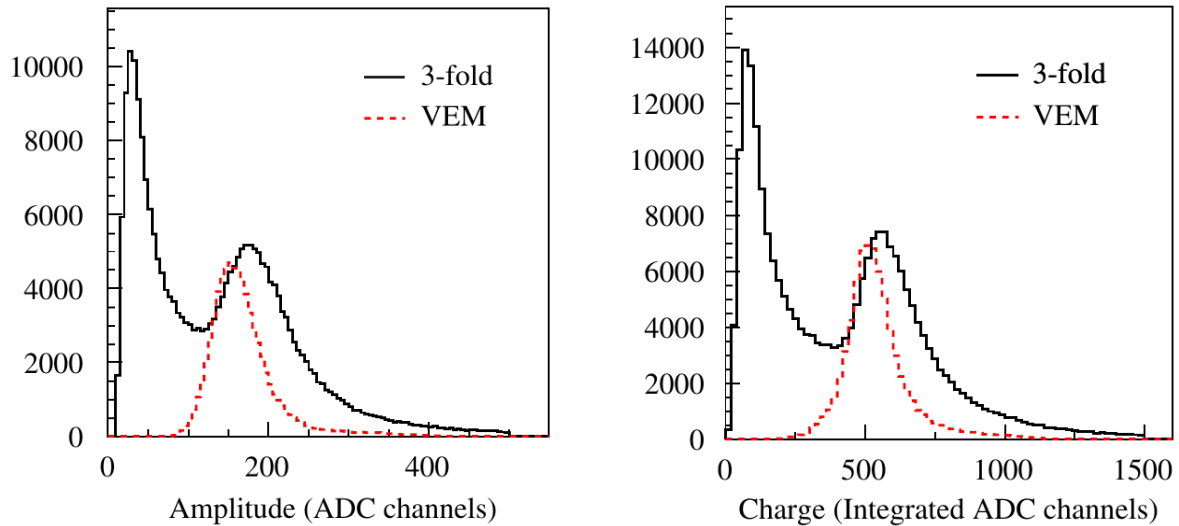
Figure 6.2: 3-fold calibration histograms of the LPMTs (black) obtained with a trigger threshold of 5 ADC. The red histograms display the signals of vertical central through-going muons selected with an external muon telescope. Both taken from Ref. [152]. *Left:* Signal-amplitude histograms. *Right:* Signal-area histograms.

of the electronics board generation. Following the same principle, the bins can be split into the "normal" bins, here the first 400 bins with the standard bin size, and the remaining 200 bins with the additional electronics dependent scaling factor for the merging of the bin entries. All features of the signal-area histogram are shown for an LPMT connected to a UB in Fig. 6.1 in the diagram on the right. Similarly to the signal amplitudes, the signal areas, i.e., charges, are provided in their raw units which are the time integrated FADC counts resulting in "ADCT", matching the naming in Ref. [153].

Finally, geometrical correction factors are necessary to convert the muon peak amplitudes and charges obtained from omnidirectional muons, i.e., muons arriving with different zenith angles, to values vertical central through-going muons would provide. These conversion factors have been determined in preceding experiments during the engineering phase of the SD using a muon telescope consisting of scintillator panels above and below the WCD to determine the response to selected single muons [151, 154, 152]. The results of these experiments are shown in Fig. 6.2 by the histograms of signal amplitudes and charges. In both diagrams, the black histogram indicates the signals from omnidirectional particles, while the red histogram only contains signals of vertical and central through-going muons. From the position of the muon peaks, the conversion factors can be obtained. After the conversion from $I_{\text{VEM}}^{\text{peak}}$ to I_{VEM}, the average signal amplitude I_{VEM} defines the reference factor for the conversion of the raw FADC traces to the normalized vertical-equivalent muon (VEM) traces used in determination of the total station signal and the subsequent event reconstruction. The converted average signal area Q_{VEM} is used in the normalization of the PMT signals into charge units of a VEM which are then used in the calculation of the total station signals. Nearly 15 years after the determination of the conversion factors, the experiment was repeated to study potential variations in the detector behavior due to aging of the components [155]. This time, a hodoscope consisting of two planar modules of resistive plate chambers (RPCs) with a similar design than the modules of the Muon Array with RPC for Tagging Air showers (MARTA) detector have been used, one module above and one below the WCD. The resulting conversion factors agree with the values obtained one and a half decades ago and will be further used in the signal calibration.

With the AugerPrime upgrade data, another set of histograms for all the introduced
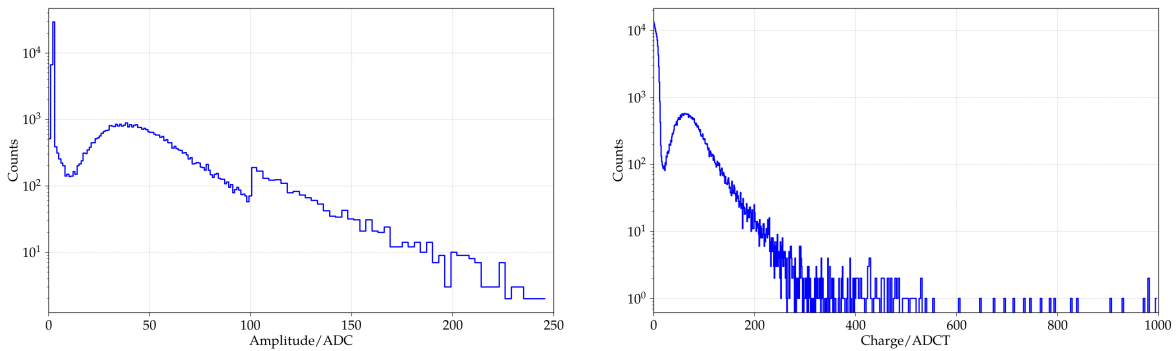
Figure 6.3: Examples of raw calibration histograms for an SSD PMT connected to an UB. *Left:* Signal-amplitude histogram. *Right:* Signal-area histogram.

quantities has been added in the data stream to provide calibration information for the newly deployed SSD PMTs. In contrast to the LPMTs, the SSD PMTs are not participating in the 1-fold coincidence trigger condition, but are only read out when the muon trigger by one of the LPMTs is fulfilled. This leads to a slightly different shape of the amplitude histograms of the SSD PMT, especially for very low amplitude values. This is displayed in the left diagram in Fig. 6.3 for an SSD PMT connected to an original UB. Due to the different detector geometries, a large fraction of events that trigger the WCD are not producing a signal in the SSD, and therefore the muon buffer traces of the SSD PMTs often contain only the electronics baseline noise. The result is visible in an increased first maximum for very low amplitude values. Similarly to the LPMTs, a second maximum can be observed in the SSD histograms which is produced by particles with energies of a minimum ionizing particle (MIP) passing through the detector and defining the signal-amplitude factor $I_{\mathrm{MIP}}^{\mathrm{peak}}$ for omnidirectional particles. This can be explained with the similar response of the SSD towards electromagnetic and muonic particles which deposit on average the same energy when traversing. Ultimately, the step induced by the transition of the bin sizes can be observed.

In the case of the signal-area histograms of the SSD PMTs, similar features can be seen, i.e., a high peak close to zero from the integration of traces without a signal pulse, as well as the charge peak created by the MIPs, both visible in the right diagram in Fig. 6.3. The transition between the "normal" and the "big" bins is not visible in the SSD PMT charge histograms obtained with an UB due to the very low bin entries at higher signal areas. Up to the submission date of this Dissertation, the conversion factors from the omnidirectional particles $Q_{\mathrm{MIP}}^{\mathrm{peak}}$ to vertical particles Q_{MIP} have been derived from simulation [156]. To validate these factors in the future, measurements with a defined test set-up similar to the previous tests of the WCD geometry factors have to be carried out.

In addition to the previously introduced histograms, two other quantities are monitored in the calibration histograms and transmitted if a T3 request is sent. On the one hand, for the calculation of the signal amplitude and area, the baselines of the muon traces are determined. These baseline values are then stored and sent in the baseline histograms. On the other hand, a fourth type of histogram is obtained which is named "shape histogram". This histogram contains all the muon traces measured in the calibration time window of 61 s stacked on top of each other, and thereby represents the general shape of a muon trace. By analyzing the shape histograms, estimates of the decay time of muons in the detectors can be obtained.

In the following sections, we use the two terms "entries" or "counts" to describe the content of a bin of the calibration histograms. Furthermore, the quantities determined by the local-station software are referred to as "online" values, in contrast to the "offline" values obtained by processing the calibration histograms in the analysis software frameworks.

6.2　Current offline calibration

The offline calibration procedure implemented in both analysis software frameworks can be divided into two major steps. After the event information is read from the raw data files, initial checks of the data quality and operation status of each PMT are performed utilizing certain online estimated calibration quantities. In this filter process, miscalibrated devices can be easily detected and removed before the actual calibration procedure is commenced. This procedure then defines the second stage in the offline applied signal analysis. In this Section, we present the status of the device quality checks and describe in detail the currently implemented calibration algorithm in the $\overline{\text{Off}\underline{\text{line}}}$ software framework [70].

6.2.1　PMT quality checks

When an WCD is deployed and initialized, the detector contains three functioning LPMTs whose settings are defined following the procedure described in Section 6.1.1. Additionally, in the case of an AugerPrime station, the SPMT and the SSDs PMT are set in an analogous way. But after a time, the PMTs of both detector types can start to show an unusual behavior induced by chemical and physical alterations of the hardware due to environmental influences, for instance, temperature or weather effects. These effects can lead to irreversible damage distorting the observed signals, or in the most severe case, producing the malfunction of the device. In addition, software failures can be sources of shifts and resets of the proper device settings or can cause losses of data packages during the transmission. This interferes with the signal analysis and can lead to an incorrect determination of the reconstructed quantities. For this reason, these malfunctioning devices have to be detected and removed during, or shortly after, the data acquisition to avoid a miscalibration of the measured signals and a distortion of the following reconstruction procedure.

In the procedure for the SD event reconstruction, information about malfunctioning devices are obtained from the various data streams and several quality checks are performed. Hereby, the quality assurance process is only launched if the respective SD station is not marked with an error flag, and therefore is not rejected in total. If a station is classified as an "error station", e.g., due to data package losses during the transmission, the necessary single device information is not provided and the station information is not included in the data pool for the quality analysis. This also holds true for the other following analyses in the upcoming sections of this Dissertation.

The first step of the data quality checks is performed already during the mapping of the raw station and device information from the event data stream to the respective software classes in both of the utilized analysis software frameworks, the CDAS analysis software and the $\overline{\text{Off}\underline{\text{line}}}$ framework. Each PMT provides a flag in the raw event data which indicates its general functioning status. For example, PMTs which are knowingly malfunctioning or purposely disconnected, are flagged as "bad" PMTs and can be easily rejected before the calibration procedure is initialized.

In addition, the PMTs can be tagged with different quality flags during the event merging process when the information of the different detectors and the monitoring data streams are synchronized. For example, devices with anomalously high noise levels caused by electronics issues can be distinguished using the monitoring information.

In the $\overline{\text{Off}\underline{\text{line}}}$, the module called "SdPMTQualityChecker" contains the methods and functions to check the monitoring quality flags of the three LPMTs of the WCDs and is able to potentially remove individual PMTs from the subsequent signal calibration. For the case that all of the three LPMTs are classified as "bad", the station is added to the list of rejected station and is not sent to the calibration module. Besides the check of the additional flags achieved from the monitoring data, the module performs comparisons of three quantities estimated
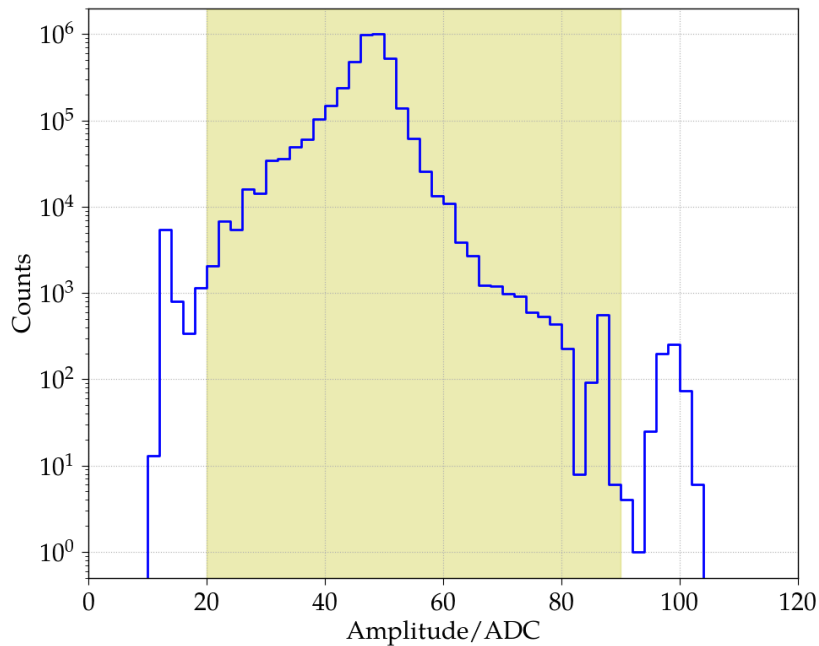
Figure 6.4: Distribution of average amplitude values estimated by the local-station software of all non-upgraded SD stations in August 2021. The PMTs with values outside the expected value range, indicated by the yellow background, are rejected from the calibration procedure.

by the local-station software with their respective expected value ranges. These quantities are the dynode-to-anode ratio (D/A) ratio, i.e., the ratio between the low- and the high-gain signal defining the dynamic range of the device, the trigger threshold factor I_{VEM}, and the width, i.e., standard deviation, of the muon-trace baseline as measure for the noise level of the device. Hereby, to ensure an identical pre-selection of properly functioning PMTs, both Auger analysis frameworks apply the identical quality conditions on the selected quantities. As an example, the histogram in Fig. 6.4 displays the distribution of the individual device average signal amplitudes estimated by the local-station software for all events acquired with the non-upgraded SD stations in August 2021. Non-upgraded stations define the original SD stations containing an UB and an WCD, i.e., no AugerPrime component is installed. The area indicated by the yellow color defines the range of accepted online estimates, i.e., devices with estimates outside the highlighted range are flagged as "bad" and are not further used in the calibration procedure.

When analyzing the signal quality data of the LPMTs of all non-upgraded stations over the SD data acquisition period from January 2004 until October 2021, variations in the fractions of rejected devices due to certain criteria can be seen, as it is displayed in Fig. 6.5. In this diagram, the number of calibration histograms of LPMTs flagged with a respective quality status are shown as monthly fractions of the total number of available charge histograms of individual LPMTs which surpasses already the enormous number of ~720 million histograms. Therein, the black markers indicate the total fraction of rejected calibration histograms which are prevented from passing to the subsequent calibration process. The main contribution to the total rejection fraction are the LPMTs which are already flagged as "bad" by the local-station software, in this diagram in red. Contrarily, the number of LPMTs rejected by one of the subsequent checks of the online estimated quantities defines only a small fraction of the total amount of rejected devices.

Overall, we can observe that the total fraction of flagged LPMTs is slowly increasing from the start of the data acquisition in 2004 until the middle of 2012, to a final average
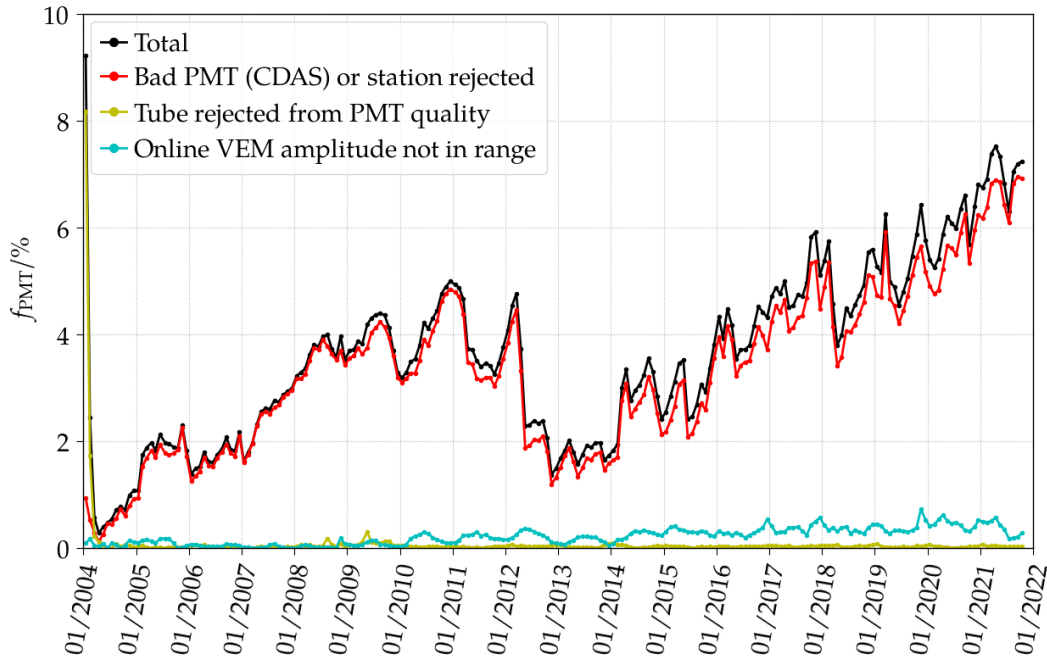
Figure 6.5: Monthly fractions of rejected histograms over time. The main contribution of the total fractions of rejected histograms is generated by the "bad" PMTs flagged by CDAS, highlighted by the red markers.

value of ~4 %. In 2012, the number of "'bad" PMTs decreased significantly and stayed at a lower level of ~2 % until another increase towards the end of the data set in October 2021 with values above 6 % are reached. These nearly constant increases of rejected devices can be explained by the aging processes of the hardware components leading to an increased amount of malfunctions, while the amount of LPMTs which can be manually maintained and recovered by the team of technicians stays rather constant over time [68]. Thereby, a further increase of the number of rejected PMTs with a similar rate of malfunctions is expected in the future.

The large decrease in 2012 might be related to the installation of the SD-750 array stations as part of the Auger Muon Detectors for the Infill Ground Array (AMIGA) extension, introduced in Section 3.1.2. The deployment process was launched in 2008 and finalized in 2012 matching the period during which changes in the behavior of the fraction of rejected devices can be seen. With the extension of the detection range towards lower energies, the number of events detected with stations inside or near the SD-750 array was significantly increased compared to stations in the standard SD-1500 array. This also reflects in the increased amount of available PMT quality status information, and therefore, although their number is rather small, the total rejection fraction of calibration histograms can be driven by the newly installed and well-performing stations. To further improve the maintenance of the devices and electronics in the Observatory, several campaigns of repairing and replacing the malfunctioning hardware have been performed in the lifetime of the experiment. These campaigns have been able to recover a certain number of "bad" PMTs and are the candidates for the multiple small decreases in the total rejection fraction which appear on annual intervals. A third effect on the fraction of malfunctioning devices can be observed after station reboots due to the fact that incorrect settings, e.g., drifting power supply values, can be corrected when the recalibration procedure is performed.

In the context of the AugerPrime upgrade, the pre-selection of devices using the locally estimated quantities is still under evaluation, and therefore, up to the submission date of this Dissertation not fully implemented yet. Due to the significant differences in the signal

responses of the SSD PMTs compared to the LPMTs, the quality ranges have to be adjusted to match the different average values. In addition, due to the increased resolution of the new UUBs, the average estimates strongly vary from the usual values obtained with the original UBs. With future studies of the average behavior of the new electronics boards and connected devices, the PMT quality checks have to be optimized and adapted.

6.2.2 Current calibration algorithm

Subsequently to the device and station filtering by the PMT quality checker module, all remaining stations are then sent to the main module in the $\overline{\text{Offline}}$ calibration and reconstruction sequence, the so-called "SdCalibrator". This module serves multiple purposes and performs all necessary calculations to prepare the detector data for the following air-shower reconstruction. At the start, the calibration procedure is commenced by the rejection of stations which do not provide the necessary trigger and timing information, or are tagged with an error status during the data transmission. Afterwards, within the second major process, the determination of the calibration factors for each individual device is executed using information from both data buffers, the online estimated calibration quantities from the shower buffers, as well as the calibration histograms obtained from the muon buffers. These normalization factors are then used to determine the average signals of the detectors, which on the other hand are utilized in the reconstruction of the air-shower properties. The processes which follow directly after the actual determination of the calibration factors, are performed on the physics event time traces stored in the shower buffers and can be further separated. They include the estimation of the baseline traces, i.e., the values for the correction of each individual trace bin, the search for trace bin segments containing potential pulse information, the definition of the integration window for the signal pulses in coincidence of all participating devices, and finally the calculation of the total detector signal.

To draw conclusions on the quality and stability of the current calibration procedure, i.e., on the determination of the calibration factors, we perform a detailed analysis of the performance and reliability of all the involved steps of the process. In general, several calibration factors of the individual PMTs are determined, including the charge calibration factor Q_{VEM} or Q_{MIP}, the amplitude calibration factor I_{VEM} or I_{MIP}, as well as the muon decay factors from the general pulse shape histograms. Out of these list of factors, the charge conversion values have the highest priority for the calibration of the PMT signals in the $\overline{\text{Offline}}$, and therefore an overview of their determination procedure is given in this Dissertation. The current algorithm can be divided into multiple sub-processes which are performed sequentially on each individual device of each station participating in the event:

1. At first, after a general check of the PMT functionality, the online estimated values are used to define an initiation of the charge calibration factor Q_{VEM} or Q_{MIP}. In case of events that do not provide any calibration histogram information, especially from the beginning of the official SD data acquisition when an early calibration software version was used, these initialized values are directly sent to the subsequent signal calculation.

2. If a charge histogram is available, another check is performed if the bin with the maximum number of entries exceeds a fixed threshold value (in case of the UB charge histograms: 500 counts) to ensure that the histogram is filled to a sufficient amount.

3. The main procedure in the search for the maximum position created by the through-going muons is started at the last bins of the histogram and continues in reverted bin order. Thereby, the last five bins are excluded from the search procedure, due to their use as containers for meta information. To further reduce the number of bins that have to be processed, the actual peak finding process is launched at the first bin (from the

back) which surpasses a fixed bin entry threshold (in case of the UB charge histograms: 300 counts).

4. In a bin-to-bin comparison (still in reverted bin order) the search for a local maximum bin is performed. When this maximum bin was found, a method to determine two limits around the maximum bin is applied. In this method, the counts of the bins to the left of the maximum are compared to the counts of the maximum itself and when three consecutive bins fall below the threshold of $0.75\,\mathrm{count}_{max}$, the left limit, also called "left shoulder" is determined. The same procedure is then applied to the bins on the right side of the maximum using the identical threshold condition and resulting in the "right shoulder" position. Thereby, in the search for the maximum bin, as well as in the shoulder determination method, the bin entries have been normalized by the respective bin size beforehand.

5. If the maximum bin, as well as the left and right shoulder have been successfully determined, a check is performed if the online estimated charge calibration factor lies inside the shoulder range. If this condition is not fulfilled, the calibration procedure is terminated and the online estimate is used as a fallback in the subsequent signal calibration.

6. If the online estimate matches the shoulder limits, a fit of the bin centers between the shoulders is initialized. To ensure a fast calibration process, no numerical minimizing procedure is in place to determine the position of the muon peak, but rather an analytical quadratic fit following the function

$$y(z) = (c_2 z + c_1)z + c_0 \tag{6.1}$$

with $z = x - x_0$ is performed, returning the function coefficients c_2, c_1, c_0, as well as the position of the maximum x_0.

7. The charge peak value obtained in the fit is then corrected for the potential shift induced by a change of the baseline values from one calibration time window to another. This correction is realized with the estimated baseline from the local-station software and the baseline value received during the filling process of the histograms.

8. As the final step, the conversion factor for the transition from the omnidirectional muon peak to the average charge of the vertically passing muons is applied, resulting in Q_{VEM} or Q_{MIP}.

A successful determination of the charge calibration factor of a LPMT charge histogram using the currently implemented algorithm is shown in the left diagram in Fig. 6.6, including the online estimate indicated by the purple arrow, the starting threshold which initiates the bin-to-bin comparison as cyan horizontal line, the left and right shoulders represented by the dashed and solid gray vertical lines, and the position of the fit named "offline". In contrast, the diagram on the right displays a histogram which failed the muon peak determination procedure. In this histogram, the shoulder finder was unable to determine the correct maximum position due to a low count difference to the minimum bin on the left of the muon peak, i.e., the condition for the left shoulder has not been fulfilled for the muon peak. Finally, the online estimate was selected as the charge calibration factor indicated by the "offline" arrow pointing at the identical charge position. When analyzing the charge histogram that fails the muon peak determination, the strong dependence of the algorithm on variations of the expected shape of the histogram becomes visible. Due to aging effects altering the PMT photocathode sensitivity and the liner reflectivity, the amount of measured light for the same amount of deposited energy decreases over time, thus the charge position
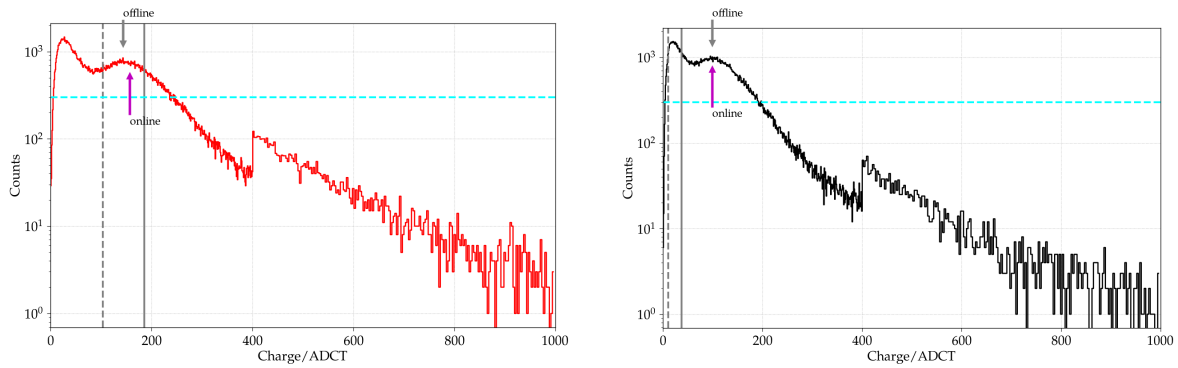
Figure 6.6: Current calibration procedure applied to charge histograms for different LPMTs connected to an UBs. *Left:* Histogram with a successful fit, i.e., the "offline" arrow points to the maximum of the quadratic fit of the muon peak. *Right:* Fallback to the online estimate due to the misdetermination of the shoulder positions. The "offline" and "online" arrow point to the identical value).
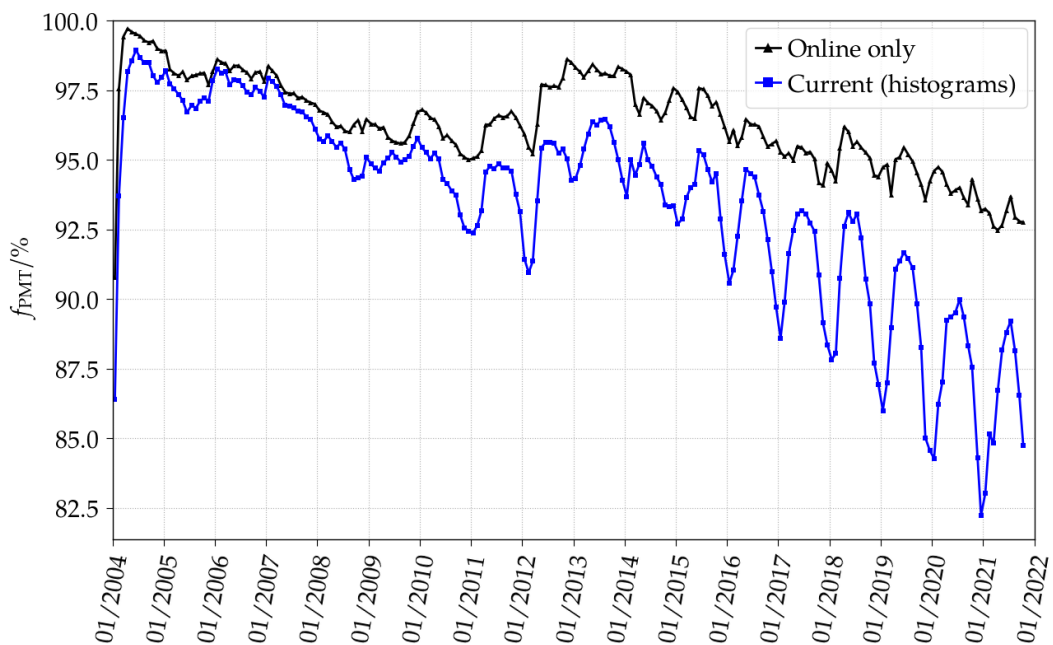
Figure 6.7: Monthly fractions of non-rejected devices over time (black). These devices always provide an online estimate and the histograms are sent to the calibration module. The blue curve shows the fractions of charge histograms which actually provide a successful fit of the muon peak when the current algorithm is applied.

and bin entries of the muon peak and of the minimum to the left slowly approach identical values. To receive an insight on the behavior of the current calibration algorithm we further analyzed in detail the individual steps of the calibration procedure by adding a status flag to the calibration-related modules in the $\overline{\text{Offline}}$ that indicates for each individual calibration histogram the point of failure or success in the algorithm.

When analyzing the calibration status for all the histograms of the LPMTs of all non-upgraded stations over the SD data acquisition period from January 2004 until October 2021, a significant change in the number of histograms successfully passing the current calibration algorithm with time can be observed. This is shown in the diagram in Fig. 6.7 by the blue markers displaying the monthly fractions of successful fits of the charge histograms, in the
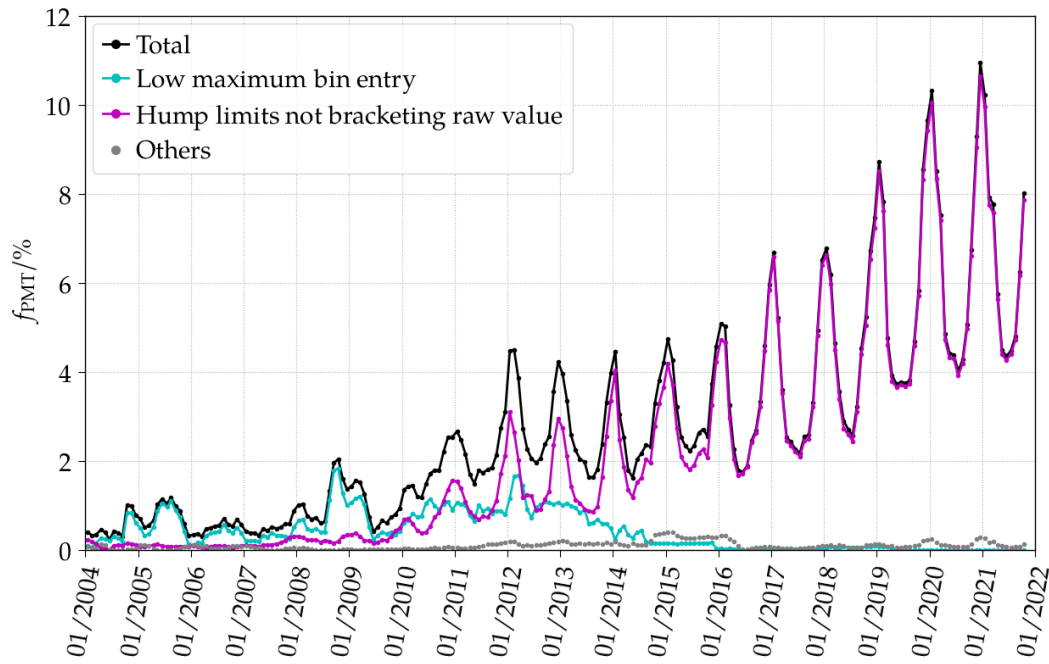
Figure 6.8: Monthly fractions of histograms that fail the current histogram fit procedure over time. The dominating failure sources are insufficiently filled histograms in the early years highlighted by the cyan markers, and the mismatch of the online estimate and the determined muon peak shoulder limits represented by the color magenta.

following also called "success fractions". In the first years after the start of the data acquisition the success fractions follow very closely the fractions of non-rejected calibration histograms, i.e., the fractions of devices that provide at least an online estimate, indicated by the black markers. This means that nearly all charge histogram that have been sent to the calibration module passed the algorithm with a good fit. But latest since 2012, the number of successful fits decreases and the average difference between the non-rejected and the successful fit histograms increases.

In addition, a second behavior in the time development of the success fractions can be observed. In 2010, the success fractions started to develop an oscillation pattern which reduces or enhances the monthly success fraction depending on the season. In the Winter months, the fraction of successful fits of the charge histograms is significantly increased and reaches values above 96 % for the histograms sent to the calibration module in 2021. Contrarily, during the Summers, the success fraction reaches an annual minimum with only ~89 % of successful fits.

To get further insight on the origin of the failing histogram fits, we analyzed the calibration status information and searched for the respective algorithm steps responsible for the failure. The results are displayed in the diagram in Fig. 6.8, showing the fractions of different failing conditions over time. We can observe that the total fractions of failing histogram fits, i.e., the black markers, are dominated by two unfulfilled conditions. At the beginning of the data acquisition, histograms that do not provide a sufficient number of entries, i.e., that do not contain a bin whose entry surpasses the necessary threshold, contribute the most to the total fractions of failures, as indicated by the cyan markers. Since 2012, the failure type changed and the condition that the determined muon peak shoulder limits have to bracket the online charge estimate becomes the dominant source, while the issues with insufficiently filled histograms seems to disappear. This is shown by the magenta markers nearly fully forming the shape of the total fraction of failure rates.
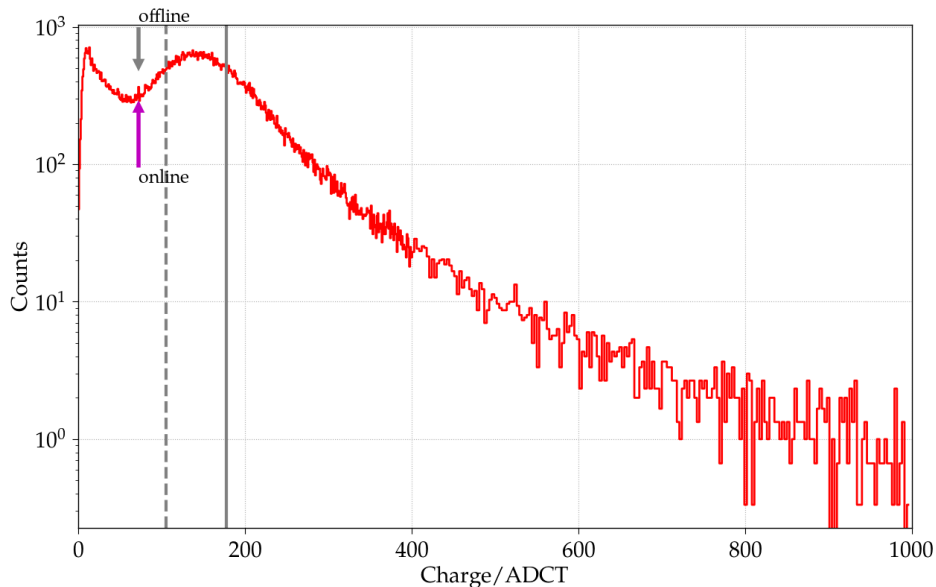
Figure 6.9: Example of a charge histogram of an LPMT connected to the UB of the station LS24. The shoulder range around the muon peak is correctly determined by the currently implemented algorithm, but the limits are not bracketing the online estimate. The online estimate is selected as signal calibration factor.

Currently, if a charge histogram is successfully fit, the position of the fit maximum is selected as the charge calibration factor with a higher priority than the online estimated charge. This default approach was chosen due to the higher information content provided by the histograms in contrast to the plain signal area estimation obtained by the local-station software. Thereby, this procedures expects a very high fraction of successful fits. From this analysis, we can observe that this condition is not fulfilled anymore for the current offline calibration algorithm showing a significant increase of failures in the recent years. For the case that the fit of the histogram fails, the local-station estimate of the average signal area Q_{VEM} or Q_{MIP} is selected as charge calibration factor. Thereby, this fallback method assumes that the online estimate is always a non-zero value in the event data. Furthermore, no measure for the quality of the online estimate is provided, i.e., the estimate has to be accepted as the "true"value. A positive example of the fallback procedure can be seen in the histogram in the right diagram in Fig. 6.6.

If the online value does not provide a proper estimation of the muon peak, the entanglement with the histogram fit algorithm utilizing the online estimate as quality criterion for the determination of the fit ranges can lead to an incorrect calibration factor. An example of this effect is displayed in Fig. 6.9, wherein a charge histogram with a peculiar shape is shown. The online estimate position does not represent the position of the muon maximum, while the search algorithm determined the proper shoulder range. Due to the range condition of the shoulders, the online value is chosen over the value from the offline procedure. This indirectly changes the priority of the methods in the selection of the final calibration factor.

To study the behavior and quality of both, the values obtained from the fits of the charge histograms and the online estimates, a modification of the current calibration algorithm in necessary to disentangle the determination of both values, and thereby enable a direct comparison. In the following section, we present a modified and optimized algorithm which is proposed to serve as the future calibration procedure in the $\overline{\text{Off}}\underline{\text{line}}$ framework.

Besides the cases of failing calibration processes for the non-upgraded SD stations, the calibration of the events obtained with the stations containing AugerPrime components with the current algorithm requires certain workarounds and shows a high rate of failures. As
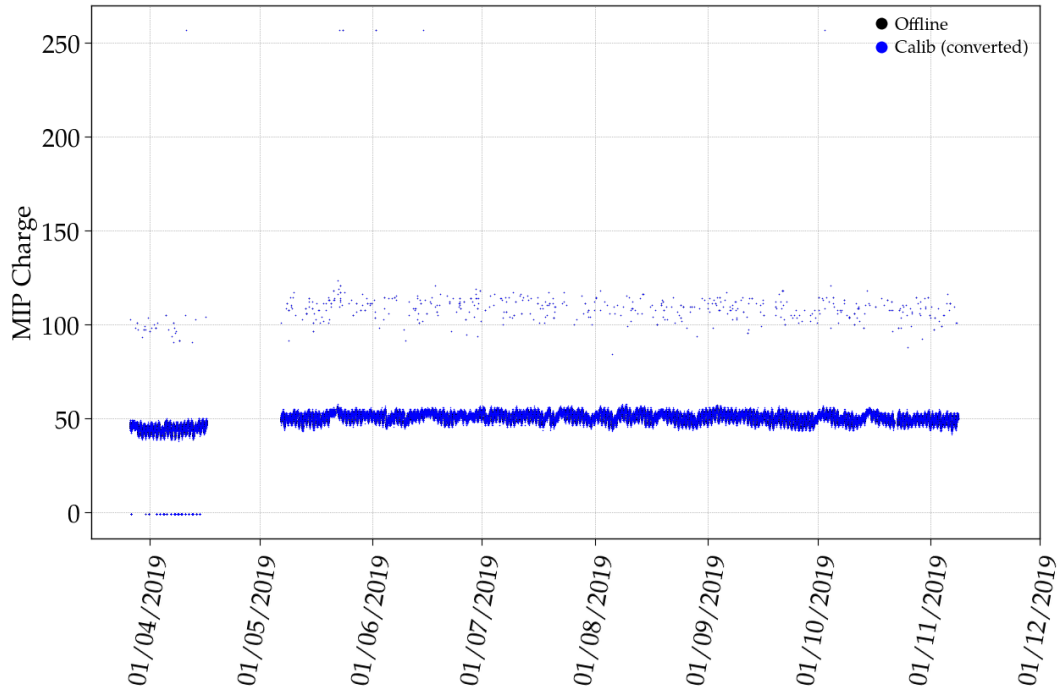
Figure 6.10: Charge normalization factors of the SSD PMT of the station LS688 over the time period of approximately seven months. Besides the true charge value population at ~50 ADC and the rejected events at 0 ADC, a third population of incorrectly determined charges at higher values can be observed which is related to the recovery module.

mentioned previously, in the case of the AugerPrime stations, the local-station software is not yet adapted to provide the necessary calibration quantities. For this reason a module called "CalibrationFiller" has been established to recover several of the required quantities and to prepare the data for the calibration and reconstruction process. This includes the calculation of the missing baseline estimations on the event traces for both, the high and the low gain, as well as the assignation of the gain amplification factor to their nominal values provided by the UUB.

In the case of the signal calibration, the missing local-station estimates for the average signal amplitude and area are needed to be recovered. This is realized for the signal area by applying a simple fit procedure to the charge calibration histograms, identical to the former fit procedure implemented in the analysis software framework built on top of the CDAS data management. With this pre-determination, rough charge estimates can be obtained for a large fraction of events which are then used as the initial start values for the subsequent offline calibration. Do to the use of various constant thresholds and ranges in the pre-determination process of the necessary quantities, the recovery module is very sensitive to modifications in the raw data, for example changes of scaling factors in the building of the calibration histograms.

In addition, the applied pre-fit of the charge histograms can introduce new features in the final calibration results. One of these features is shown in Fig. 6.10. Therein, we display the charge calibration factor (here called MIP Charge) of each event obtained for the SSD PMT of the station LS688 over the time period of approximately seven months. Although this station is part of the Surface Scintillator Detector pre-production array (SSD PPA), introduced in Section 5.3, and the SSD PMT is connected to an original UB, the recovery module is necessary to provide an SSD PMT charge estimate for the calibration algorithm in the $\overline{\text{Offline}}$. In the

diagram, three different populations are visible, the largest at a charge value of ~50 ADC which defines the proper charge calibration result, and a smaller population at the beginning of the data acquisition at 0 ADC representing events that have been rejected. The third population at around 110 ADC is the result of the incorrect determination of the charge estimate by the recovery module. For these events, the simple algorithm obtains the fit on fluctuations appearing in the histogram at higher charge values. This incorrect charge estimate is propagated to the calibration procedure in the $\overline{\text{Off}}\underline{\text{line}}$, creating the failure of the current fit algorithm, and ultimately resulting in the selection of the incorrect charge normalization factor. Analogously to the case of the non-upgraded stations, a modification of the current calibration algorithm might provide an improvement of the signal calibration of the devices from the AugerPrime stations and prohibit miscalibrated events passing to the subsequent air-shower reconstruction.

6.3 Modified calibration algorithm

Since the number of successful charge calibrations for the non-upgraded stations is significantly decreasing over the last years and the implementation of the AugerPrime detectors is not in its final state, we present in this Section the modifications and optimizations applied to the calibration algorithm. The modified algorithm was designed to replace the current implementation in the standard calibration and reconstruction chain in the $\overline{\text{Off}}\underline{\text{line}}$ software framework serving two purposes, enable a stable calibration for the upcoming data of the measurement stage "Phase II" and provide the opportunity to reanalyze the data of the current measurement stage "Phase I" with an improved performance. Thereby, we focused on several criteria that should be improved and realized with the new algorithm.

Due to the differences in the shapes of the charge histograms, the increase of the general flexibility is one main criteria for the modification. Then, histograms from PMTs connected to an original UB or to a new UUB, which provide different histogram binnings, can be fit utilizing the same algorithm. Instead of fixed thresholds, we chose a statistics-based approach which provides the opportunity to adapt to the respective shape of each individual histogram. The second major motivation is the implementation of a purely histogram-driven algorithm, i.e., only the information achieved from the muon buffer is used in the offline procedure. In this case, an independent comparison of the offline results with the online estimates from the shower buffers is possible and a quality measure between both can be obtained. Another criterion is related to the improvement of the accuracy of the charge determination. Instead of just finding the first maximum which matches the condition, the new algorithm is thought to be able to determine the correct extreme position, i.e., the muon peak, but should fail if the first maximum at lower charges was obtained by the procedure. This can be realized by expecting a minimum to the left of the muon peak whose determination is also required in the modified algorithm.

In general, different approaches to implement a new algorithm have been thought of, for instance a modification of the current bin-to-bin comparison, an extreme value search by calculating the derivatives and searching for zeros, or a peak finding algorithm using certain quantities like the sample mean and the standard deviation to determine the standard score $z = (x - \overline{x})/\sigma$. In the end, we selected the first proposal, staying with a bin-to-bin comparison approach due its simplicity and fast execution, as well as remaining closest to the current implementation. Similarly to the current implementation, the new algorithm is supposed to be fast and stable, and therefore the use of numerical minimizers is not desired. Only the fast analytical quadratic fit will be performed in a range around the detected extreme positions.

Overall, all of the mentioned methods suffer from fluctuation effects between neighboring bins. This can be addressed by flattening, i.e., smoothing the histogram, before the peak finding algorithm is initiated. The here mentioned modification are designed to optimize
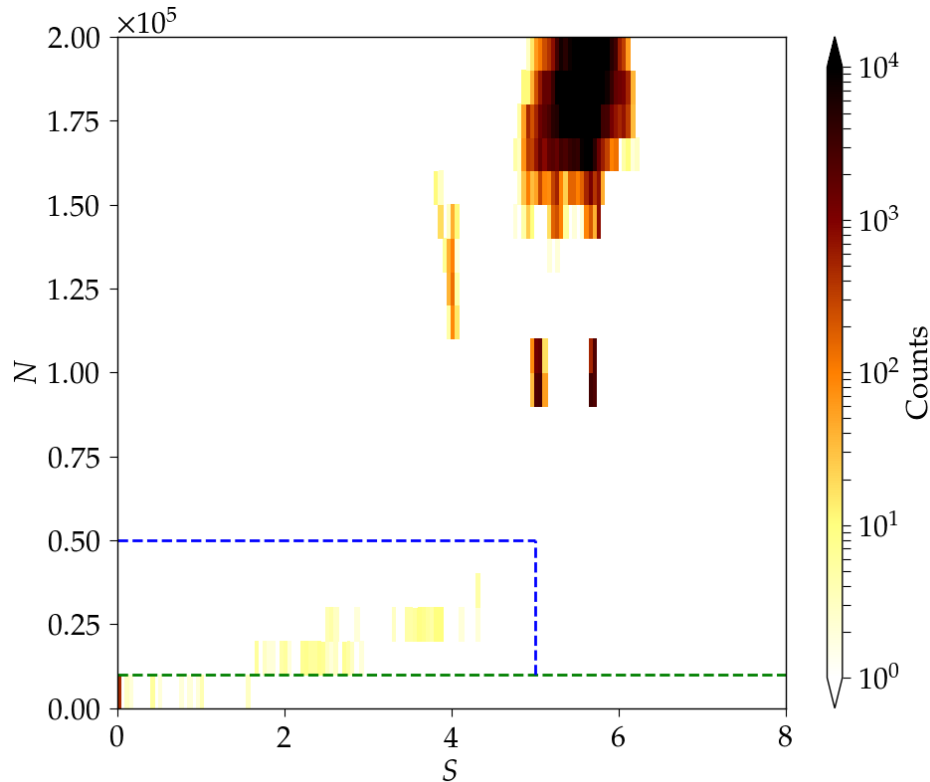
Figure 6.11: Distribution of the total number of entries over the entropy distribution for the LPMTs connected to UBs obtained in August 2021. The green and blue dashed lines represent thresholds for the histogram rejection on the total sum of the bin entries and on the entropy.

the calibration procedure in the $\overline{\text{Off}\underline{\text{line}}}$ framework which is based on the original procedure to determine the charge calibration factor. In the parallel analysis software framework, a modified procedure is implemented since 2015, described internally in Ref. [157]. This algorithm contains several of the improvement concepts mentioned above, such as a smoothing procedure of the bin counts to suppress bin fluctuation effects or the search for two extreme values in the histograms, the muon peak and the additional minimum to the left. Within the algorithm, the fit range is adapted with an iterative method until the extreme values are determined, and uses the online charge estimate as first guess at the beginning of the procedure. For the case that the charge estimate is missing or is not matching the position of the muon peak, the algorithm is able to recover an estimate but is strongly optimized for the binning and shape of the histograms of the LPMTs obtained with an UB, and therefore limited to fixed ranges.

The changes to the calibration algorithm presented in this Section can be divided into three stages. In the beginning, a new pre-selection or pre-filtering of histograms is introduced, followed by the description of the determination of the extreme positions, i.e., the charge positions of the muon peak and the minimum. The third stage is the post-selection of histograms and the calculation of the charge normalization factor. After the description of the new algorithm, we present the performance and comparisons with the currently implemented version.

6.3.1 Pre-selection of charge histograms

Before the histograms are send to the actual determination algorithm of the extreme values, the current calibration algorithm applies a check of the filling status of the histogram. This is performed by analyzing the bin with the maximum number of entries and comparing it to a fixed threshold value. This check can be influenced by artificial high bin entries, for example in the case that certain bins are used as container for the transmission of meta information as mentioned previously. For this reason, in the modified calibration procedure, instead of the maximum bin entry, a check of the total sum of the bin entries is performed, disregarding the entries of the last bin. With this approach, the selection of histograms with single high bins is prohibited. To pass the pre-selection, all histograms have to fulfill the condition of a total sum of entries $N > 1 \times 10^4$ counts. If this threshold is not surpassed, the histogram is defined as "empty" and is rejected from the calibration process. The total entry threshold is highlighted in the in the diagram in Fig. 6.11 by the green horizontal dashed line. The histograms in this diagram have been acquired from all non-upgraded stations, i.e., from the stations with UBs and no SSD, in the example month August 2021. While the dominating majority of histograms contains 10^5 counts or more, a small fraction of histograms have been classified as empty, and therefore are not propagated to the peak finding algorithm. In the diagram, we can also observe a second population of histograms around a total entry of 2.5×10^4 counts. These histograms are not necessarily underfilled and might provide a muon peak. For these histograms, another check has to be performed to get insight on the quality of these candidates.

The introduction of a total number of entries condition already increased the number of properly rejected histograms, but no further implications on the general shape or symmetry of the histogram can be drawn. Therefore, a second quantity is determined by the modified algorithm, the Shannon's information entropy S. With this entropy, already introduced in Section 4.1.3, a measure for the regularity of the filling status of the individual bins is given. For the histograms, the probabilities p_i are defined by each entry of the one-dimensional histograms, i.e., the count of each bin c_i, normalized to the total sum of all counts N resulting in

$$p_i = \frac{c_i}{\sum c_j} = \frac{c_i}{N}. \tag{6.2}$$

The histogram entropy is then defined as

$$S = -\sum_i \frac{c_i}{N} \ln \frac{c_i}{N} = -\frac{\sum c_i \ln c_i}{N} + \ln N. \tag{6.3}$$

The entropy values can be used to assure that the histograms contain a certain amount of structure, i.e., potential maxima and minima, but no information about the actual positions of these extreme values can be obtained, due to the insensitivity to the ordering of the individual bins. The distribution of entropy values for the non-upgraded stations from August 2021 is shown in the diagram in Fig. 6.11. While the majority of histograms depicts entropy values of approximately 5 or slightly above, the histograms with low number of total entries also show low entropy values. This is a strong indication for a missing muon peak in these histograms. Therefore, to further reduce the number of misshaped histograms, we established a second criterion. This filter rejects histograms inside a two-dimensional window defined by a threshold on the total entries of $N < 5 \times 10^4$ and a threshold on the entropy of $S < 5$, as indicated by the blue vertical and horizontal dashed lines.

In the case of the SSD PMT connected to the UB in the stations of the SSD PPA, the identical selection on the total number of bin entries has been implemented. But in contrast to the LPMTs, the mean of the entropy distribution is at lower values, between $S = 3$ and $S = 4$, as can be seen in the diagram in Fig. 6.12 for the SSD PMT histograms obtained in
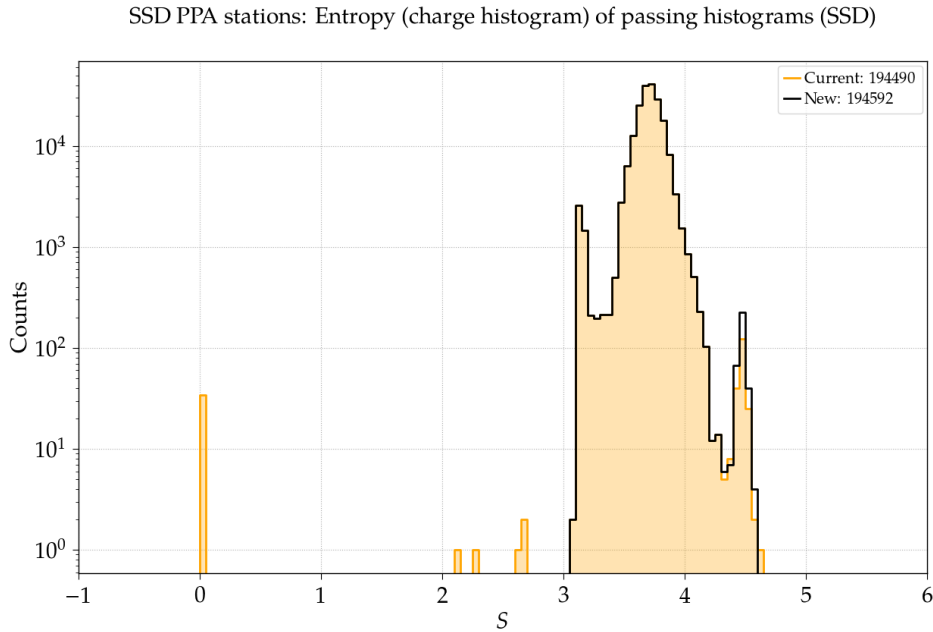
Figure 6.12: Entropy distribution for the SSD PMTs connected to UBs obtained in August 2021. The majority of histograms show entropy values above $S = 3$.

August 2021. For this reason, the rejection threshold of $S < 3$ is applied before the extreme value determination is initiated.

6.3.2 Extreme value determination

After the filtering of empty or incorrectly filled histograms, the main process of determining the muon peak and its accompanying minimum follows. For simplicity reasons, the general procedure of the modified extreme position finder follows the major concepts of the currently implemented algorithm implemented in the $\overline{\text{Off}}\underline{\text{line}}$, which have been introduced previously. But instead of starting the bin-to-bin comparison at the first bin that surpasses a fixed bin entry threshold, described in the third item in Section 6.2.2, the new algorithm already commences the procedure in the back of the histogram after the last five bins are excluded. In this region, the "big" bins with increased bin sizes are present. Therefore, the normalization of the bin entries is of high importance for a successful determination of the extreme values. Especially for the histograms acquired with the new UUBs, the bin normalization by the respective sizes becomes essential. With this concept the identical algorithm can be applied to the histograms of both types of PMTs, the LPMTs and the SSD PMTs.

To reduce the effects of triggering on large bin fluctuations of neighboring bins, we introduce a pre-processing step, a so-called "smoothing" process. In this process a sliding average of 3 consecutive normalized bin entries is calculated, i.e., for each of the histogram bins, the average with the bin before and the bin after is calculated. Only for the bins on the edges of the histogram, this averaging is not performed. In the following, the newly defined quantity is named bin density d_i. An example density histogram calculated for an LPMT connected to an UB is shown in Fig. 6.13.

For the pre-processing procedure, the weighted sum of the histogram entries is generally defined as

$$x_i = \sum_i w_i c_i. \tag{6.4}$$
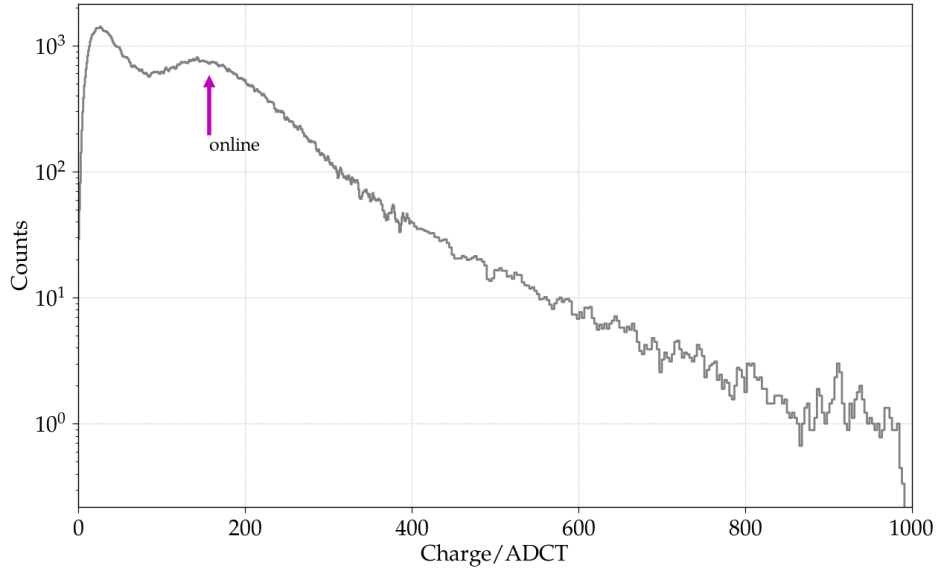
Figure 6.13: Example of a density histogram for an LPMT connected to an UB. Compared to the original histogram, the bin-to-bin fluctuations are suppressed. The step at the transition of the bin sizes is smoothed by the normalization process.

We can then calculate the histogram density d_i of each bin with

$$d_i = \frac{1}{3}\left(\frac{1}{\Delta_{i-1}}c_{i-1} + \frac{1}{\Delta_i}c_i + \frac{1}{\Delta_{i+1}}c_{i+1}\right) \tag{6.5}$$

where c_i and Δ_i define the count and size of the i-th bin, respectively.

In addition, the uncertainty σ_{d_i} of each density bin is calculated. With this quantity, the conditions for the search of the shoulder limits is later implemented. In general, the variance and standard deviation of a weighted sum of entries is given by

$$\sigma_{x_i}^2 = \sum_i w_i^2 \sigma_{c_i}^2 = \sum_i w_i^2 c_i \rightarrow \sigma_{x_i} = \sqrt{\sum_i w_i^2 c_i}, \tag{6.6}$$

assuming a Poisson uncertainty of each respective bin count with $\sigma_{c_i} = \sqrt{c_i}$. Then, the standard deviation of each density can be calculated with

$$\sigma_{d_i} = \frac{1}{3}\sqrt{\frac{1}{\Delta_{i-1}^2}c_{i-1} + \frac{1}{\Delta_i^2}c_i + \frac{1}{\Delta_{i+1}^2}c_{i+1}}. \tag{6.7}$$

After the determination of the density histogram and its accompanying density uncertainty histogram, the bin-to-bin comparison algorithm is initiated.

Analogously to the current muon peak finder, the modified algorithm begins at the end of the density histogram, skipping the last five bins. The bin-to-bin comparison is performed in reverted bin order by searching for the first maximum density value (muon peak). When a local maximum density is found, the bins to the left and to the right have to fulfill a certain condition to define the maximum as the actual muon peak. Here, the left and the right limits around the maximum are determined when the density of three consecutive bins fall below a defined threshold. But in contrast of using a fixed proportion of the maximum bin entry for this threshold, a relative condition is implemented which utilizes the density uncertainty of the local maximum.
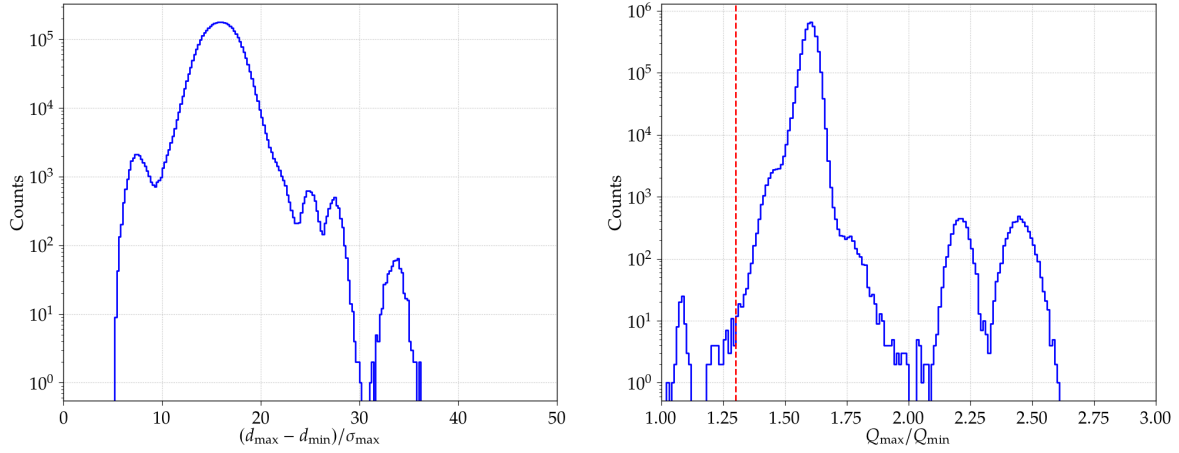
Figure 6.14: Distributions of calibration-related quantities obtained from the histograms of the LPMTs connected to UBs in August 2021. *Left:* Relative density differences of the muon maximum and the accompanying minimum. *Right:* Charge position ratio of the muon maximum and the accompanying minimum. The red vertical dashed line displays the lower limit for the selection of successful calibrations.

In a first step, the threshold is set to a multiple of the density uncertainty of the maximum bin $th_{max} = f\sigma_{max}$, with $f = 10$ as the starting factor. If either the left or the right limit condition is not fulfilled, the check is repeated iteratively with two lower threshold factors, here chosen $f = 8$ and $f = 5$. For the case that the limits are still not determined after applying the lowest threshold condition, the search for the muon peak is terminated and the histogram is rejected in the charge calibration. However, if both limits are obtained, the identical analytical second order polynomial fit is performed on the raw histogram entries using

$$y(x - x_0) = (c_2(x - x_0) + c_1)(x - x_0) + c_0. \tag{6.8}$$

Besides the check of the goodness of the fit, identically implemented compared to the current algorithm, an additional inspection of the curvature c_2 is performed, and thereby the determination of a maximum is assured.

To imply a certain shape on the charge histograms, the modified algorithm searches in a second step for another extreme position, the minimum to the left of the muon peak. The search utilizes the identical bin-to-bin comparison on the density histogram and is initiated one bin to the left of left limit of the muon peak to avoid the fit on fluctuations. A minimum position is defined when its left and right limit conditions are fulfilled. These conditions use analogous threshold definitions, i.e., a limit is found when three consecutive bins surpass the relative threshold of $th_{min} = f\sigma_{min}$. Thereby, the identical scaling factors $f = 10, 8, 5$ are iteratively tested. To further assure that the minimum is correctly positioned, its right limit is prohibited to surpass the bin position of the previously determined muon peak. The actual position of the minimum is received by performing the analytical quadratic fit and assuring a positive curvature, i.e., $c_2 > 0$.

In case of the SSD PMT charge histograms, the minimum to the left of the muon peak provides a very narrow shape as can be in the right diagram in Fig. 6.3. Therefore, the determination of the limits can result in a very small range of bins which strongly suppresses a successful execution of the fit. To compensate for this effect, the analytic quadratic fit of the minimum for all types of PMTs is only applied when the determined limits span a range of more than 10 bins. For the histograms with a lower limit range, the charge value from the bin-to-bin comparison process is used as the position of the minimum without any further fit.

6.3.3 Post-selection and conversion

After the positions of the muon maximum and the accompanying minimum are determined, the majority of charge histograms provide a successful calibration. At this point the question arises if the histograms passing the modified algorithm actually show the expected shape and extreme positions, and if the general quality of these histograms can be described. With the new procedure, various additional quantities can be derived to further analyze the histograms and the performance of the calibration procedure.

One quantity the describes the stability of the extreme value determination is the difference between the density values of the maximum d_{max} and the minimum d_{min} determined by the bin-to-bin comparisons. When normalizing this difference with the density uncertainty σ_{max}, resulting in

$$D = \frac{d_{\text{max}} - d_{\text{min}}}{\sigma_{\text{max}}}, \tag{6.9}$$

the search condition for the left limit condition of the muon peak can be analyzed. In the left diagram in Fig. 6.14, the relative density differences for the LPMTs connected to UBs obtained in August 2021 are shown. The majority of the histograms indicate a relative density difference of around 18 which is significantly larger than the highest threshold factor ($f = 10$) applied in the limit search. For these histograms, the separation between the muon maximum and the minimum is easily possible. On the left side of the distribution, we can observe the effect of reaching the lowest threshold condition of $f = 5$. The density of the minimum defines the lowest possible condition to determine the limit, and therefore no histograms with a relative density difference below 5 can be seen. On the other side of the distribution, the values of individual LPMTs with very large separations between the muon maximum and the minimum are prominent. These values can be an indication of incorrect power settings for these device which might ultimately result in a reduction of the dynamic range. Overall, the relative density difference provides a measure to monitor the performance of the fit procedure over time which is presented in the long-term studies in Section 6.5.2.

In addition, a second quantity is utilized to ensure a high quality level of the charge normalization factor determination. This quantity is the ratio of the charge positions of the muon maximum Q_{max} and its accompanying minimum Q_{min}, i.e.,

$$R = \frac{Q_{\text{max}}}{Q_{\text{min}}}. \tag{6.10}$$

The distribution of the charge ratios for our chosen data set is displayed in the right diagram in Fig. 6.14. Therein, we can see that the majority of histograms deliver a charge ratio above 1.5. Only a few histograms seem to provide a very low charge ratio, i.e., seem to have the minimum and the muon maximum very close to each other. When looking at individual of these low ratio histograms, we can observe that their shape does not match the expected form, but still the determination of both extreme values has been successful. This is possible in rare cases in which fluctuations or oscillations create various maxima and minima in the histogram that are then accidentally recognized as muon peak and its accompanying minimum. An example for one of these histograms with multiple extreme positions is given in the left diagram in Fig. 6.15. To clean the final data set from these misdetermined charge positions, we impose a selection of histograms with a charge ratio above 1.3, as shown by the red vertical dashed line in the charge ratio diagram in Fig. 6.14.

Finally, if the positions of the minimum and maximum fulfill their ratio requirements, the signal normalization factor Q_{VEM} or Q_{MIP} is obtained by applying the baseline correction to the muon peak position from the fit. Here we have to note that this correction is not yet implemented for the histograms obtained with the PMTs of the AugerPrime stations due to the missing local-station estimate necessary for the calculation. As the last step, the factor to convert the responses from omnidirectional to vertical passing muons is multiplied. The
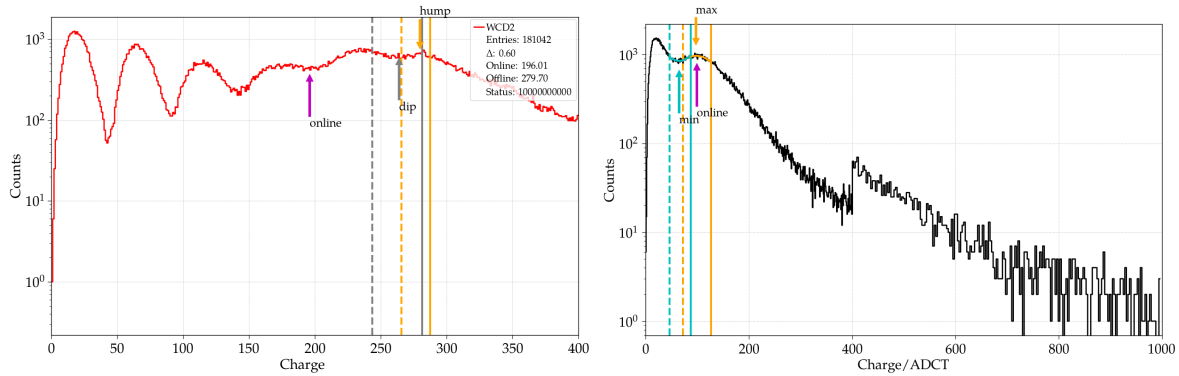
Figure 6.15: *Left:* Example of a charge histogram of an LPMT connected to an UB. The histogram shows an unusual PMT behavior. This histogram can only be rejected by imposing a minimum distance between the relevant extreme positions. *Right:* Example of a charge histogram with a successful fit by the new calibration algorithm. This histogram failed the calibration with the current algorithm, as shown in the right diagram in Fig. 6.6.

histogram is then accepted and the algorithm is terminated with success. In the right diagram in Fig. 6.15, a successful fit of a charge histogram of an LPMT connected to an UB is presented, including the muon maximum and the accompanying minimum with their respective limits. This diagram shows the enhanced success rate of the modified algorithm due to the fact that the same histogram failed the current calibration procedure presented in the right diagram in Fig. 6.6.

6.4 Algorithm performance and discussion

With the modified calibration algorithm, we gain the opportunity to further analyze the performance of the WCDs and SSDs and investigate the currently implemented online and offline signal calibration procedures. By selecting histograms that deliver a successful charge determination fit in the current and the modified algorithm, a direct comparison between the two offline procedures can be carried out. In addition, due to the fact that the modified algorithm only relies on the charge histogram information, i.e., does not rely on the charge estimates determined by the local-station software, a comparison between the online estimated charge values and the ones determined by the $\overline{\text{Off}\underline{\text{line}}}$ algorithm can be drawn. In the following, several comparisons are presented using the data of the LPMTs of all non-upgraded stations obtained in August 2021. In this data set, a total number of approximately 4.25 million histograms are contained. Out of these histograms, 6.67 % have been rejected before the charge determination algorithm is initialized. The non-rejected histograms then define the basis for the comparisons.

6.4.1 Charge factors: new vs. current

When comparing the two algorithms, the first numbers to determine are the fractions of successful fits for the respective procedure. For the current algorithm, 94.83 % of the non-rejected histograms in the data set are properly fit which is a relative high success fraction compared to other months due to selection of a Winter month. In contrast, with the improved flexibility, the success fraction for the modified algorithm reaches a significantly increased value of 99.66 % for the identical data set. This corresponds to a difference of ~190 thousand histograms and highlights the enhanced performance of the future algorithm towards changes in the histogram shapes.
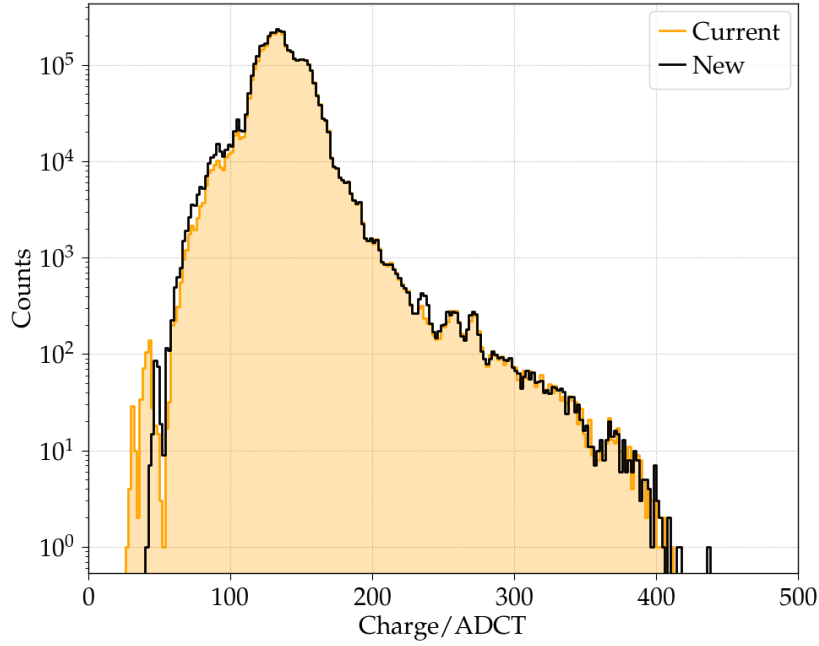
Figure 6.16: Charge distributions obtained with the current (orange) and the new (black) calibration algorithm.

Besides the fractions of successful fits, the direct comparisons of the charge distributions of both algorithms after the final conversion to vertical muon factors are very important for the estimation of the quality of the new procedure. In the diagram in Fig. 6.16, the resulting charge distributions obtained with the two algorithms are shown. Therein, we present the results of the current algorithm in orange, while the charges obtained with the new algorithm are drawn in black. Overall, both distributions provide a very similar shape with the majority of charges between 100 and 200 ADCT. Only at lower charge values, a difference between a small number of histograms is visible. Nevertheless, the black distribution of the new algorithm contains as significantly increased number of histograms. Due to the fact that the total number of included histograms varies between both distributions, it is rather complicated to draw conclusions on the respective performance. This can be achieved when we compare the results of both algorithms on a single histogram level, i.e., we analyze the relative differences $\Delta Q_{\text{offline}}$ between the charge values for histograms that have been successfully determined by both algorithms. The relative difference is given by

$$\Delta Q_{\text{offline}} = \frac{Q_{\text{offline}}^{\text{new}} - Q_{\text{offline}}^{\text{current}}}{Q_{\text{offline}}^{\text{current}}}. \tag{6.11}$$

The distribution of the relative charge difference between the algorithms for all the histograms in the selected data set are shown left diagram Fig. 6.17. In this diagram we can observe that the new calibration procedure is not introducing a significant bias in the determination of the charge factors when compared to the results of the current algorithm. Thereby, the spread of the differences is below 1 %. To further analyze the two algorithms, the diagram on the right displays the two-dimensional distribution of the relative charge differences in dependence of the charge factors from the current algorithm. Therein, a larger spread in the charges can be observed for values below 150 ADCT, while for larger charges, the differences approach zero.

In general, we can conclude that the new algorithm provides nearly identical charge factors for individual charge histograms compared to the current procedure when both are terminated successfully. But due to the significantly increased number of successful fit
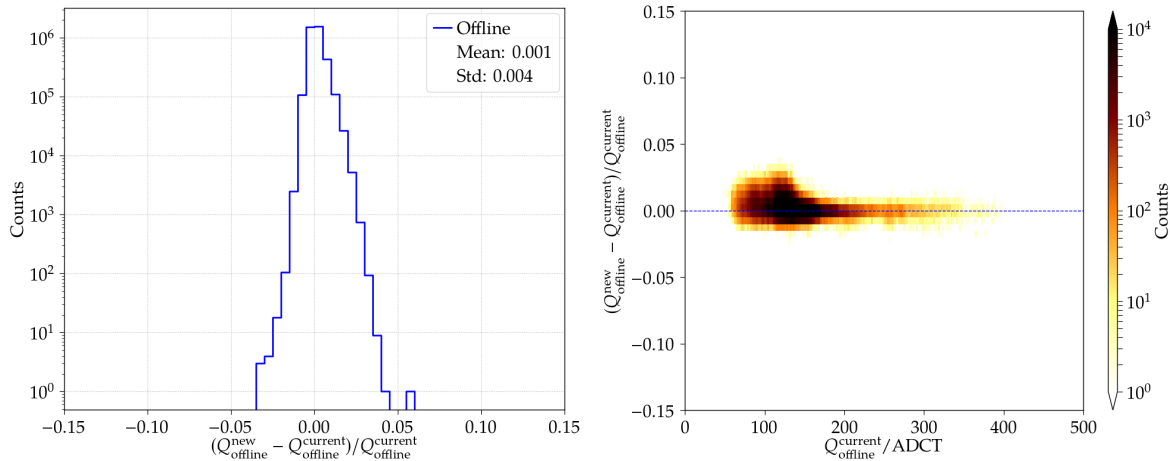
Figure 6.17: Relative differences of the charge values obtained with the current and the new calibration algorithm. *Left:* Distribution of the total data set. The spread between the two algorithms is below 1 %. *Right:* Two-dimensional distribution of the relative differences in dependence on the charge factors determined with the current algorithm.

procedures of 5 % or higher, the new algorithm represents the superior method. For this reason, the new algorithm is proposed as a replacement in the $\overline{\text{Off}}\underline{\text{line}}$ software framework.

6.4.2 Detector signals: new vs. current

After the promising results of the comparison of the offline calibration algorithms for individual charge histograms, i.e., for individual devices, the impact of the modified calibration algorithm on the signals of the WCDs and SSDs is of high importance for the future detector performance. These signals of the sub-detector of each participating SD station are calculated after the charge calibration values of the devices are determined. They define the starting point for the event reconstruction, presented in the following Chapter. In general, during the signal calculation, the pulse information of the event traces that passed the necessary trigger conditions are associated with the calibration information read out at the time of the event. Thereby, an identical procedure is applied to the three LPMTs of the WCDs, as well as to the single PMT of the SSDs. Up to the submission date of this Dissertation, the calibration of the SPMT and its use in the determination of the WCD signals is not available due to the missing implementation in the $\overline{\text{Off}}\underline{\text{line}}$ analysis software.

The signal determination of air-shower events measured with the WCD utilizes the event trace information of all three LPMTs, as well as their charge calibration factors $Q_{\text{VEM},i}$ obtained from the matching calibration data in the offline calibration process [158, 153, 156]. Therein, the signal of each individual device S_i is calculated before the total signal of the WCD S_{WCD} is determined. After the integration of the pulse bins, the signals are given in the electronics unit ADCT and are then converted into the unified relative unit VEM by normalizing with the calibration factor. In these unified units, the signals can be used to reconstruct the lateral air-shower properties, described in Chapter 7.

As an initial step, the baselines of both gains, the low- and the high-gain channel, are obtained. Instead of using a simple estimation to receive a constant baseline value for the total trace, as described and utilized in Section 5.1.2, a baseline value for each bin of the trace is determined. The result is the so-called "baseline trace" $b_i(t)$ that allows variations in the baseline along the trace matching large amplitude shifts of the observed pulses, e.g., undershoot effects of the PMTs [153]. The baseline procedure searches for trace segments that
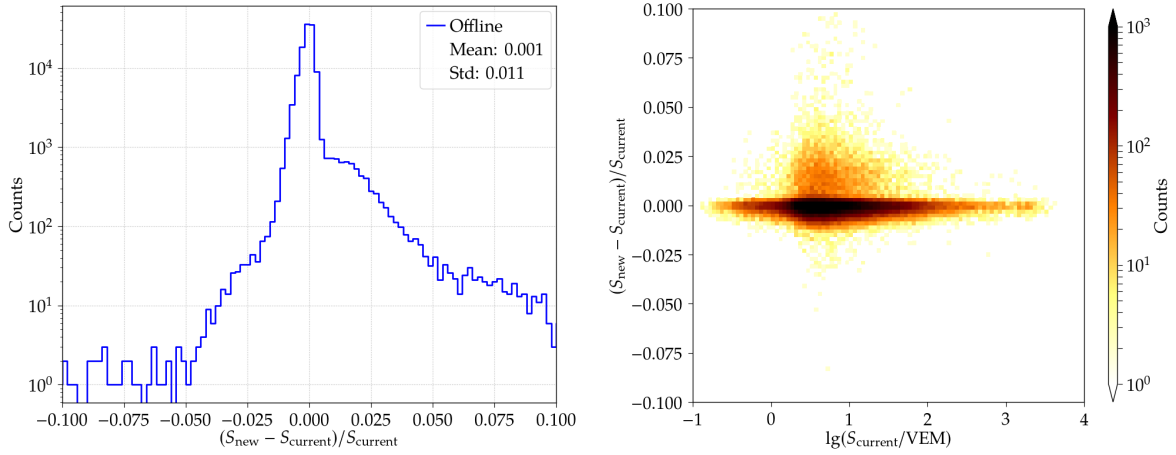
Figure 6.18: Relative differences of the WCD signals obtained by using the calibration factors determined with the current and the new calibration algorithm. *Left:* Distribution of the total data set with a spread of ~1 %. *Right:* Two-dimensional distribution of the relative differences in dependence on the logarithmic WCD signals determined with the charge values of the current algorithm.

do not contain pulses and defines these as baseline trace elements. For the bins that do contain pulses, the baseline in each bin is obtained by an interpolation process. Currently, an optimization of the baseline trace determination is intensively studied and will be implemented in the near future.

After the baseline traces have been obtained, the start bin t_{start} and stop bin t_{stop} for each event pulse are determined on the high-gain traces which later define the range for the integration of the signal bins. Analogously to the segment search for the baseline traces, the time traces are examined searching for segments that contain entries above a well-defined threshold which then can be classified as potential signal segments. From the bin entries of these potential signal segments, the baseline values are subtracted and the segments are merged or rejected using certain criteria resulting in the signal segment s_i of the individual LPMT trace. Afterwards, the signal segments of all the participating LPMTs are averaged and the signal segment with the largest signal is chosen to define the integration range. Finally, the total signal of the station is determined by the integration of the averaged signal trace between the start and the stop bin. The signal of one of the LPMTs can be depicted as

$$S_i = \frac{1}{Q_{\text{VEM},i}} \sum_{t_{\text{start}}}^{t_{\text{stop}}} \left(s_i(t) - b_i(t) \right). \tag{6.12}$$

The total signal of the WCD can then be calculated with

$$S_{\text{WCD}} = \frac{1}{N} \sum_i S_i \tag{6.13}$$

with N defining the number of the participating LPMTs.

With the introduction of the modified calibration algorithm, different results in the calculation of the signals of individual LPMTs are possible, and therefore changes in the total signal of the WCD can appear. To analyze the effects of the modified calibration procedure, the WCD signals obtained with the current and the new calibration algorithm are compared for the given data set. Especially for stations with large signals, the performance of the calibration is of high importance. For these stations which usually appear in the event close to the core of the air shower, the uncertainties of the calibration dominate the determination of the lateral
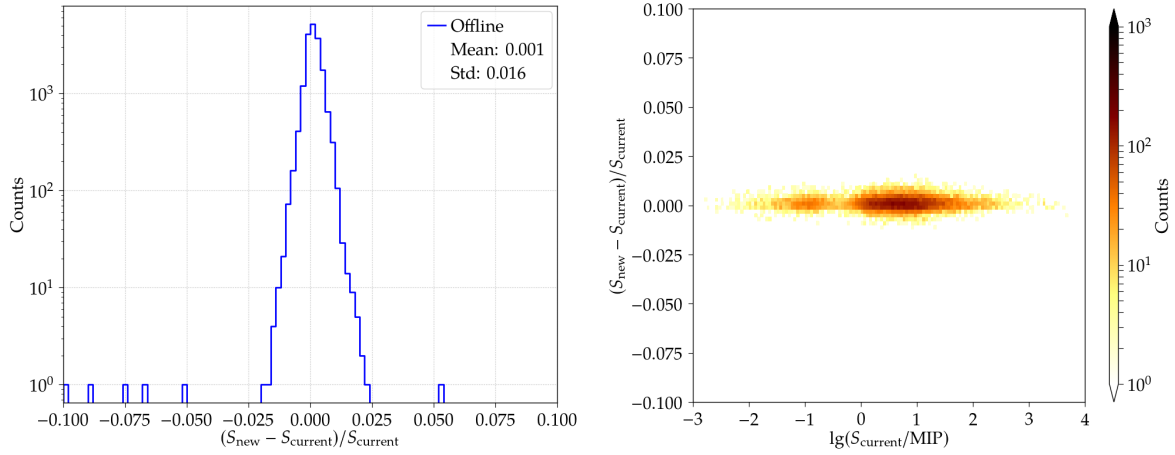
Figure 6.19: Relative differences of the SSD signals obtained by using the calibration factors determined with the current and the new calibration algorithm. *Left:* Distribution of the total data set with a spread of slightly above 1 %. *Right:* Two-dimensional distribution of the relative differences in dependence on the logarithmic SSD signals determined with the charge values of the current algorithm.

profile of the air shower. Contrarily, for stations with lower signals, the calibration resolution plays only a secondary role. At positions further away from the air-shower core, the sampling fluctuations define the uncertainties in the fit of the lateral distribution.

In the left diagram in Fig. 6.18, the distribution of the relative differences of the individual WCD signals from both algorithms ΔS for the over ~150 thousand detector events are shown. This is generally defined as

$$\Delta S = \frac{S_{\text{new}} - S_{\text{current}}}{S_{\text{current}}}. \tag{6.14}$$

Therein, we can observe that for the majority of detectors the differences of the signals is ~1 %, matching the results from the comparisons on a single device level. Analogously, we present in the diagram on the right the two-dimensional distribution of the relative signal differences in dependence of the signals from the current algorithm for the WCDs. As in the case of the individual histogram analysis, a larger spread in the signals can be observed for smaller absolute signal values. Thereby, for a small fraction of WCDs, the signal differences can reach values of up to 10 % or more. These outliers can be explained with the fallback mechanism of the current calibration algorithm which uses the charge estimates of the local-station software for the case that the histogram fit fails. Despite the fact that the fallback option is activated in both calibration algorithms, the appearance in the current algorithm is significantly higher due to the increased number of failures on the histogram fit procedure. The difference in the signals is then created by large differences between the charge value from the histogram fit and the online estimate for individual PMTs. In general, understanding the influences of the fallback method is crucial for the upcoming final implementation of the procedures for the AugerPrime detectors. Hence, in Section 6.4.3, the variations between the online and offline charge values are investigated.

In contrast to the WCDs, the SSDs only contain a single PMT to measure the scintillation light, and therefore the total SSD signal S_{SSD} is defined by the trace information of the respective PMT. Analogously to the LPMTs of the WCD, the baseline trace $b(t)$ and the merged signal segments are determined. Then, the total SSD signal can be calculated using

the signal trace $s(t)$ and the charge calibration factor Q_{MIP} resulting in

$$S_{\mathrm{SSD}} = \frac{1}{Q_{\mathrm{MIP}}} \sum_{t_{\mathrm{start}}}^{t_{\mathrm{stop}}} \left(s(t) - b(t) \right). \tag{6.15}$$

Therein, the integration range of the SSD defined by the start and end bins fully includes the WCD integration window, and can be additionally extended in both directions by the algorithm performing the search for the signal segments. This adaptation method for the SSD has been implemented to compensate for the unknown timing differences in the signals of the two detector types, and their varying average trace shapes for the same air-shower event [156].

Analogously to the WCD, the signals of the SSD strongly depend on the calibration values, and therefore on the algorithm used for the determination of these factors. To analyze the influences of the modified calibration procedure on the SSD signal determination, we present in the left diagram in Fig. 6.19 the distribution of the relative differences of the SSD signals ΔS when comparing the current and the new calibration algorithm. Similarly to the WCDs, the majority of the SSD signals are distributed close to a difference of zero, with a spread of slightly above 1 %. Additionally, the diagram on the right displays the two-dimensional distribution of the relative signal differences in dependence of the signals from the current algorithm. In contrast to the WCDs, the signals obtained with both calibration algorithms show a high agreement. The cases in which the histogram fit fails and the current algorithm utilizes the charge which is incorrectly determined by the recovery module are not visible in this diagram, due to their rare appearance and the limitation of the data set. Nevertheless, the new algorithm prevents the requirement of the recovery module and provides the determination of the calibration factors for properly functioning PMTs in nearly 100 % of the cases.

6.4.3 Charge factors: new offline vs. online estimate

With the implementation of a purely histogram-driven approach to determine the charge values in the new algorithm, a comparison between the online charge estimates obtained by the local stations and the values from the offline calibration can be carried out. This comparison is in principle also possible using the charge values determined by the current offline algorithm, but due to its interconnection to the online estimates when performing the search for the muon peak, i.e., the check of the inclusion inside the bin range for the fit as explained in Section 6.2.2, the number of histograms in the comparison is reduced. Especially for the histograms we are mainly interested in, i.e., the histograms that failed the current fit procedure, no information about the actual peak determination is provided. In these cases, the current offline procedure uses the fallback option to the online estimate without terminating all necessary steps in the calibration module.

For this reason, we focus in the following online-to-offline comparisons on the offline values obtained with a successful termination of the new calibration procedure. Despite the fact that the fallback mechanism to the online estimate for the cases in which the extreme value determination fails has also been implemented in the new algorithm, this option is rarely triggered due to the very high success fractions. For the majority of histograms sent to the calibration module, i.e., more than 99 %, two charge values are available, the online estimate from the local-station software and the offline charge value from the modified calibration algorithm. To provide an absolute comparison of the charge values on an individual histogram level, the online estimates obtained with the procedure introduced in Section 6.1.2 are converted with the geometrical factors from the responses of omnidirectional muon to the values vertical through-going muons would produce.

When comparing the charge values from both procedures, we use the relative differences
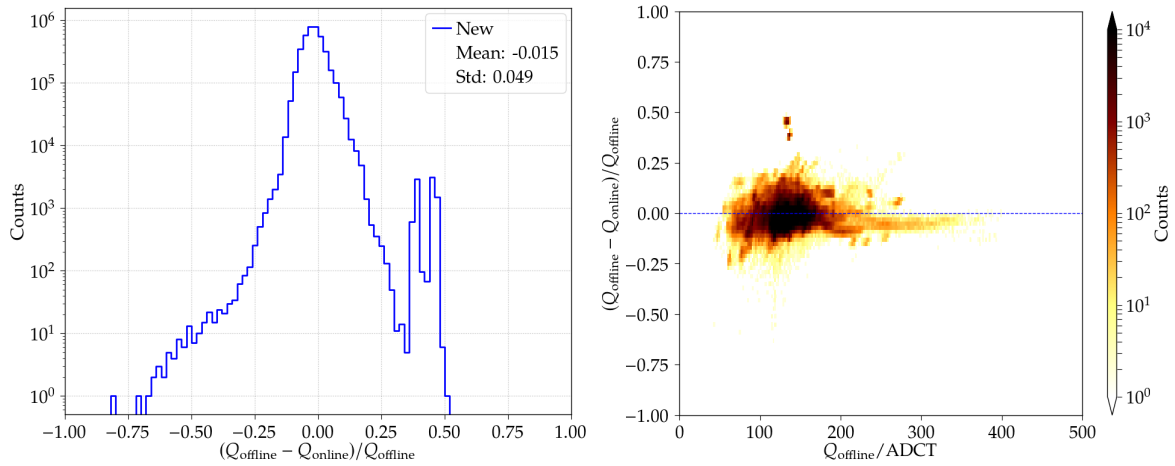
Figure 6.20: Relative differences of the charge values obtained with the online calibration procedure and the new offline algorithm. *Left:* Difference distribution of the total data set showing a small average bias and a spread of ~5 %. *Right:* Two-dimensional distribution of the relative differences in dependence on the charge values determined with the offline calibration algorithm. Populations with larger differences of the charge values from individual PMTs can be observed.

between the online and offline charges ΔQ_{proc} as a sensitive measure which is formulated as

$$\Delta Q_{\mathrm{proc}} = \frac{Q_{\mathrm{offline}} - Q_{\mathrm{online}}}{Q_{\mathrm{offline}}}. \tag{6.16}$$

In the left diagram in Fig. 6.20, the distribution of the relative differences between the online and offline charge in the data set shown. Therein, we can observe a small systematic shift of ~1 % of the offline charges towards lower charge values when compared to the online estimates. This might be a first indication that the conversion factors between the online estimates and the offline charges which have been acquired during the engineering phase of the SD have slightly changed over the total measurement period of the Observatory. Furthermore, an overall spread of the distribution of the order of 5 % can be seen which further indicates a potential small mismatch between the charges determined by the local-station software and from the calibration histograms. For a small number of histograms, a rather large charge difference has been determined represented by the two peaks in the right tail of the distribution. These peaks are produced by two single PMTs repeatedly showing an unusual behavior when they appear in the data.

To further investigate the relative charge differences of the different calibration procedures, the dependence of the differences on the respective absolute charge values is analyzed. The results for the selected data set of August 2021 are shown in the right diagram in Fig. 6.20. Therein, the two-dimensional distribution of the relative differences of the charge values displays the average spread between the two calibration methods. In contrast to the comparisons of the two offline calibration algorithms with rather small resulting charge differences, a non-negligible fraction of histograms shows a spread of ~5 %, as already observed in the one-dimensional distribution. Additionally, we can observe small populations of values at large distances from the mean of up to 50 % which are the result of individual devices showing an unusual behavior. For example the histograms producing the two small peaks at the higher difference values in the one-dimensional histogram are created by two PMTs, one of the station LS24, and the other installed in the station LS32. One histogram of the identified PMT of the station LS24 is presented in Fig. 6.21. The new calibration algorithm determines the charge value at the position of the peak which is assumed to be
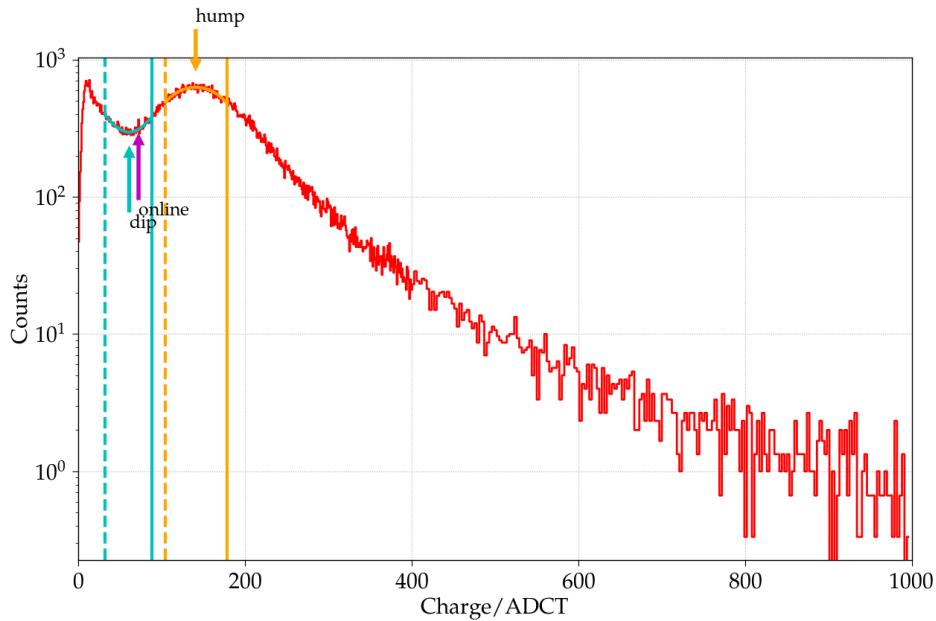
Figure 6.21: Example charge histogram of an LPMT connected to the UB of the station LS24. The modified calibration algorithm determines the muon peak position depending on the shape of the histogram and independent of the position of the online estimate. A larger difference between the online and offline charges is visible. This histogram failed the calibration with the current algorithm, and in this case the online estimate was selected as shown in Fig. 6.9.

the muon maximum, while the online estimate is pointing towards a lower charge. Thereby, the identical histogram has been already shown in Fig. 6.9 during the introduction of the currently implemented offline calibration procedure, highlighting the failure of the maximum determination and the fallback to the online estimate as final charge value. This example emphasizes the advantage of the modified calibration algorithm to be independent of the online estimates, and thereby providing a second measure of the charge normalization factor.

Nevertheless, the actual origin for the differences when comparing the online and offline charge values cannot be fully determined within the scope of this analysis. On the one hand, the values from the online calibration procedure strongly depend on the present trigger system settings. Therein, correlations between the 3-fold and the 1-fold PMT responses in combinations with firmware implementations are used which have been obtained in detector studies using the WCDs of the engineering phase nearly 20 years ago. Due to aging effects, potential shifts in these correlations are possible, and therefore remeasurements of the most relevant quantities for the aged detectors appear to be necessary to reject the online calibration procedure as the source of uncertainties.

On the other hand, the calibration histograms depend on certain software algorithms to calculate the respective quantities. Changes in the shapes of the charge histograms and fluctuations of the baseline values can lead to shifts of the extreme values, ultimately resulting in a potential misinterpretation of the muon peak position. Even so the question about the origin of the charge differences cannot be answered, their general evolution over time provides information of the aging behavior of the hardware components and enables extrapolations towards the future performance. Furthermore, a stable and precise online calibration procedure is very important for events which do not provide calibration information from the muon buffers. This can appear in rare cases in which the transmission of the calibration information is lost due to the limited bandwidth of the SD communication. The general time development of the differences between the online and offline charges are presented and
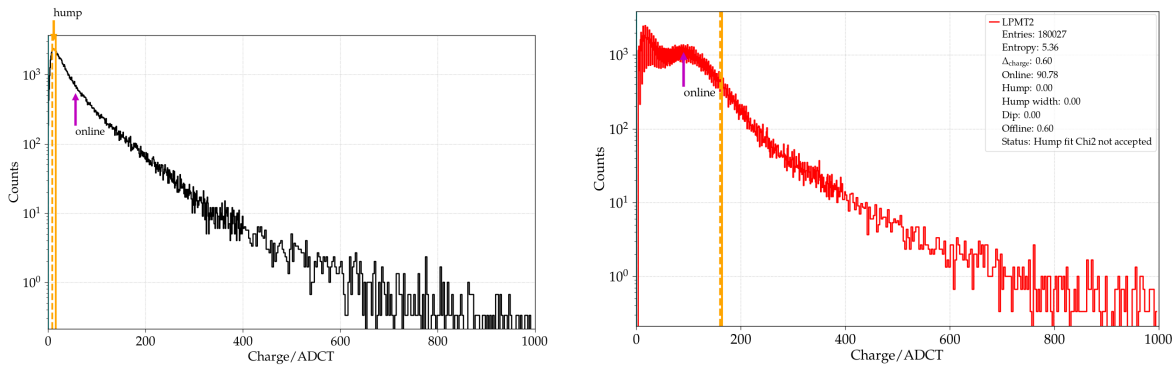
Figure 6.22: Examples of charge histograms of LPMTs connected to UBs. For both histograms, the new calibration algorithm is failing and the optional fallback to the online estimate can be chosen. *Left:* No muon peak is visible due to an incorrect power setting or a potential PMT or electronics malfunction. *Right:* Appearance of high-frequent bin fluctuations prevent a successful muon peak determination with the both offline calibration algorithms.

analyzed in Section 6.5.3.

6.4.4   Rejected histograms

Despite the fact that the number of successful fits is significantly increased using the modified calibration procedure, a small fraction of histograms of approximately 0.5 % in the recent years are still failing the extreme value determination of the new algorithm. For the majority of these failing histograms, the requirement to find a minimum to the left of the muon maximum is not fulfilled. This is the case when the shape of the histogram is rather flat, i.e., the bin entries of the muon peak and of the minimum are too close to each other. In the most extreme case, the muon peak is just visible as a shoulder of the exponentially falling flank of the low energy particle peak, or not visible at all, as can be seen for example in the left diagram in Fig. 6.22. These charge histograms indicate an incorrect power setting of the respective PMT or a potential electronics malfunction, and therefore the device cannot be successfully calibrated. For the histogram on the right in Fig. 6.22, the calibration procedure has also been terminated unsuccessfully. In this case, the modified algorithm is incapable to determine the limits of the muon maximum due to the appearance of high-frequent bin fluctuations. Although the expected shape is visible including a muon peak, and furthermore the online estimate is determined at a viable position, this histogram is rejected by the new algorithm. Here, the alternating bin entries might be an indication of a malfunction of the PMT or the connected base electronics, and therefore the device should be excluded from the total signal calculation of the WCD signal. Nevertheless, the fallback to the online estimate is also available and selectable in the new offline calibration algorithm.

6.5   Calibration long-term performance

After the introduction of the modified calibration algorithm in Section 6.3 and its performance applied to the charge histograms obtained in August 2021 in Section 6.4, we intensively studied the evolution of the calibration-related quantities over a longer time period to estimate the long-term stability of the different calibration procedures. By reanalyzing the total SD data set of the measurement stage Phase I, consisting of the large number of ~720 million histograms, benchmarks can be defined to describe the past, current and future performance of the WCDs and SSDs concerning their calibration. With the long-term performance studies, the
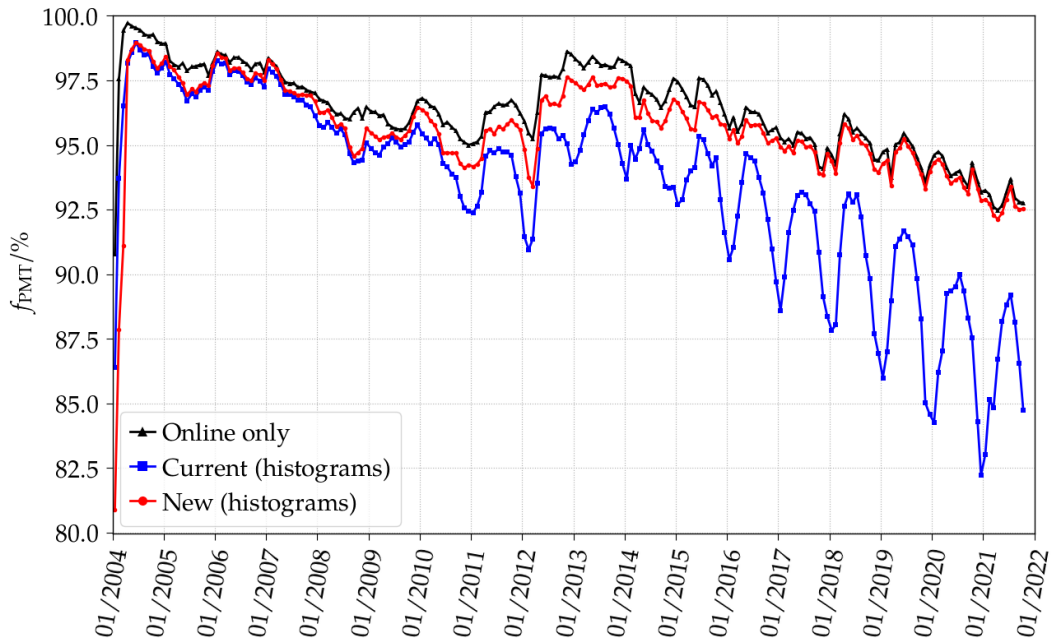
Figure 6.23: Monthly fractions of histograms over the total data acquisition time of the SD. Analogously to Fig. 6.7, the black markers represent the fractions of non-rejected devices which always provide an online estimate for the charge value and thus define the maximum reachable fraction of calibrated devices. The success fraction of the current offline calibration algorithm is given by the blue markers. The red markers represent the monthly success fraction of the new algorithm. Except for the first months in 2004 when a large number of histograms have not been filled sufficiently, the new algorithm provides increased success rates compared to the current procedure, especially in the most recent years.

influences of aging effects on the various hardware components can be analyzed which manifest in changes of the shapes of the obtained calibration histograms and require a highly flexible algorithm to determine the calibration factors. Additionally, assumptions on the future performance and operation status of the detectors and devices can be drawn.

In the following, the general calibration status is presented by the comparisons of the success fractions of the two calibration algorithms for the total time period of the SD data acquisition. Subsequently, the performance of the new calibration procedure is evaluated by analyzing the time development of the extreme-value search condition for the PMTs of the WCDs, as well as the variations in the position determination of the muon maximum and its accompanying minimum. Finally, we present the general aging behavior of the detectors of the SD stations by comparing the results of the determination of the charge values with the two calibration methods, the online charge estimation and the offline calibration algorithm. Furthermore, evolution of the charge calibration factors for both types of PMTs, the LPMTs and the SSD PMTs are studied.

6.5.1 General calibration status

When analyzing the data of the non-upgraded stations from August 2021, the modified algorithm provides a significant improvement in the determination quality of the charge factors compared to the current algorithm resulting in ~5 % more successfully calibrated histograms. But the calibration procedure has to perform equally well on the LPMT data of the total lifetime of the Pierre Auger Observatory, i.e., starting from 2004 up to the latest acquired events in our data set at the end of 2021. For this reason, the monthly fractions of the
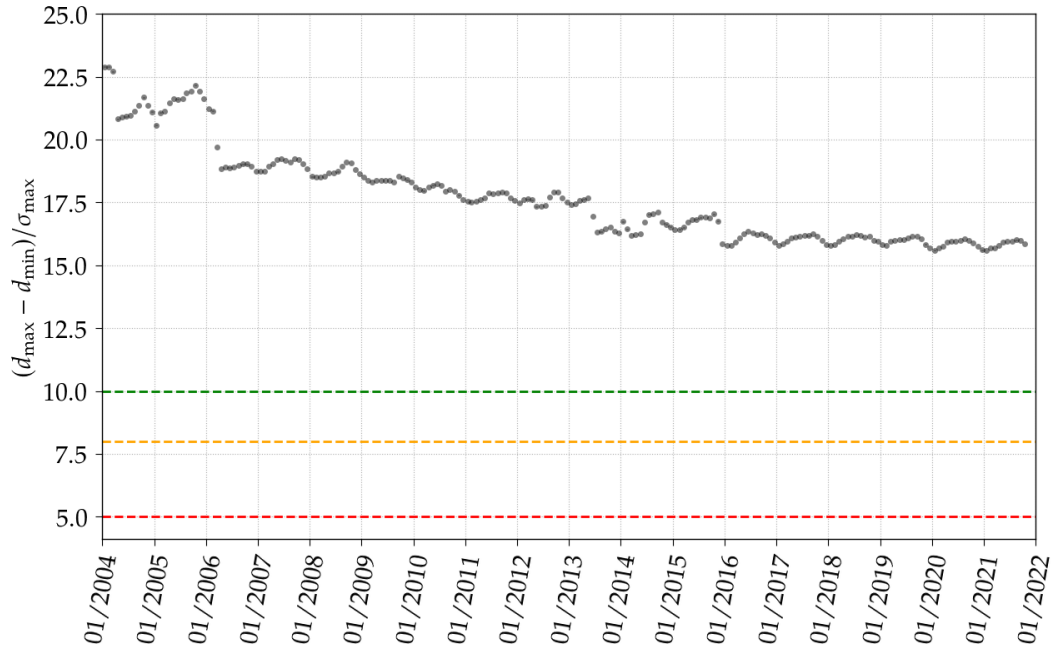
Figure 6.24: Monthly averages of relative density differences of the muon maximum and its accompanying minimum for all the histograms of all the devices in the data set. The green, orange, and red horizontal dashed lines highlight the threshold factors for the search condition of the limits around the extreme values with $f = 10, 8, 5$. Despite the fact that a decrease of the density difference with time can be observed, the curve flattens in the recent years and is not expected to reach the lowest algorithm threshold.

histograms successfully passing the modified offline calibration procedure are determined. In the diagram in Fig. 6.23, these success fractions of the new algorithm are displayed in red together with the monthly success fractions of the current algorithm in blue and the fractions of non-rejected histograms in black, both taken from Fig. 6.7. When comparing the fractions of the two calibration algorithms, we can observe that for the grand majority of the months, the success fraction of the new algorithm lies above the values of the current algorithm, indicating the enhanced flexibility and stability after the modifications. Thereby, the number of successful charge factor determinations with the new algorithm nearly reaches the maximum possible fraction defined by the online estimates of the non-rejected histograms. Only in the first months in 2004 and between 2008 and 2014 an increased fraction of histograms failed the new calibration algorithm due to an increased number of histograms which have not been filled sufficiently by the local-station software. This effect appears in coincidence with the deployment of the new stations in the SD array, and therefore can be related to an adaptation of the local-station software after the initially incorrect settings. In the other months, the success fraction of the new algorithm reaches success values of 99 % and higher.

Overall, for all months except the first three in 2004, the new algorithm provides increased calibration success compared to the current one. Especially in the most recent years, the differences between the two algorithms are significantly increasing, resulting in values between 5 % and 10 %, depending on the season. The continuous decrease of the success fractions with time cannot be observed for the new calibration algorithm, and the seasonal variations seen in the fractions of the current algorithm are suppressed when the modified calibration algorithm is applied. From this direct comparison we can conclude that the superior flexibility of the modified algorithm significantly improves the offline calibration of the PMT signals and that the new algorithm is a valid candidate to be used as standard

Figure 6.25: Monthly averages of relative density differences of the muon maximum and its accompanying minimum for the three LPMTs of the station LS324. The green, orange, and red horizontal dashed lines highlight threshold factors for the search condition of the limits around the extreme values with $f = 10, 8, 5$.

calibration procedure in the $\overline{\text{Off}}\underline{\text{line}}$ framework assuring a successful calibration of the past and the future data.

6.5.2 Modified algorithm

Besides the analysis of the general evolution of the success fractions, the performance of the new algorithms can be further studied in detail utilizing certain quantities to describe the quality of the calibration. With this obtained information, extrapolations and assumptions of the future behavior and performance of the detectors can be derived. Thereby, the two quantities introduced in Section 6.3.3 to analyze the shape of the charge histograms have been determined for all histograms in the total data set. With the relative density differences D, the stability of the extreme value determination over time can be described and expectations on the change of the histogram shape can be formulated. In the diagram in Fig. 6.24, the monthly averages of the relative density differences of the muon maximum and its accompanying minimum for all the devices in the data set are displayed. Therein, we can observe that average values follow a decrease over time indicating the slow flattening process of the shape of the histograms. Especially in the first years of the data acquisition larger decreases in the density differences between the two extremes are prominent, while in the recent years the averages appear to stabilize towards constant values. Nevertheless, for the average of all devices in the SD array, the muon peak finder condition is fulfilled for the total time period, i.e., a sufficiently large difference between the muon maximum and the minimum to the left is given. To highlight these necessary requirements for a successful determination of the limits around the muon peak, the three chosen relative threshold factors are included in the diagram represented by the three horizontal dashed lines. Thereby, the green line shows the strongest applied criterion with the relative threshold of $th_{max} = 10\sigma_{max}$. The orange and red lines display the intermediate and the lowest criteria with the threshold factors of $f = 8$ and $f = 5$, respectively. If the relative density difference reaches the lowest threshold
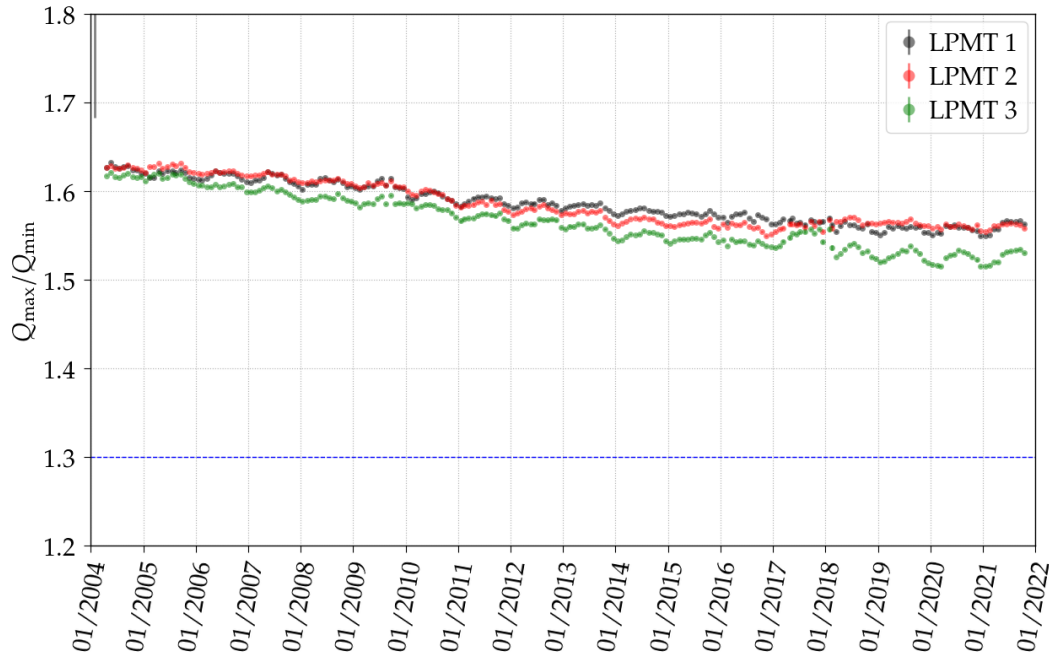
Figure 6.26: Monthly averages of the charge position ratios of the muon maximum and its accompanying minimum for the three LPMTs of the station LS324. The blue dashed line at a ratio value of 1.3 represents the minimum threshold for the post-selection criterion of the new calibration algorithm.

condition, i.e., the red dashed line in the diagram, due to changes in the histogram shapes, the determination of the muon peak fails and the calibration process is terminated. In the case of the average values of all stored histograms, the density differences are always located above the strongest peak search condition and a successful determination of the muon peak by the new calibration algorithm is provided.

Despite the fact that the average device calibration results in a successful determination of the muon peak, for individual PMTs the situation might be different. For this reason we searched for and selected a station which was deployed at the beginning of the SD data acquisition in 2004 and is still in operation at the end of the data set in 2021. One of the few stations that fulfill this requirement is the station LS324. To analyze the time evolution of the calibration performance of the new algorithm, we determined the monthly averages and compared the values for the individual devices of this station. The results for the relative density difference is shown in the diagram in Fig. 6.25, containing the monthly averages for the three LPMTs. Similarly to the curve of all devices, the individual LPMTs depict the general decrease of the density differences with time. When compared to the values of all averaged histograms, the absolute values reach lower levels, especially the LPMT with the ID 3, but all devices fulfill the required peak search condition for the muon maximum at any time. The lowest density difference values at the end of 2021 still fulfill the strongest criterion of $f = 10$.

By analyzing the behavior of the stations with the longest operation period in the Observatory, and under the assumption of a continuation of the current trend of the monthly averages of the density differences, we can expect that for the large majority of the devices, this calibration condition will be fulfilled regarding the search of the fit limits for the muon maximum, and therefore a successful calibration in the upcoming years can be achieved.

Additionally to the density difference, the ratio R of the charge positions of the muon maximum and its accompanying minimum, provides insight into the past and future performance of the detectors. The charge ratio is used in the post-selection process of the modified
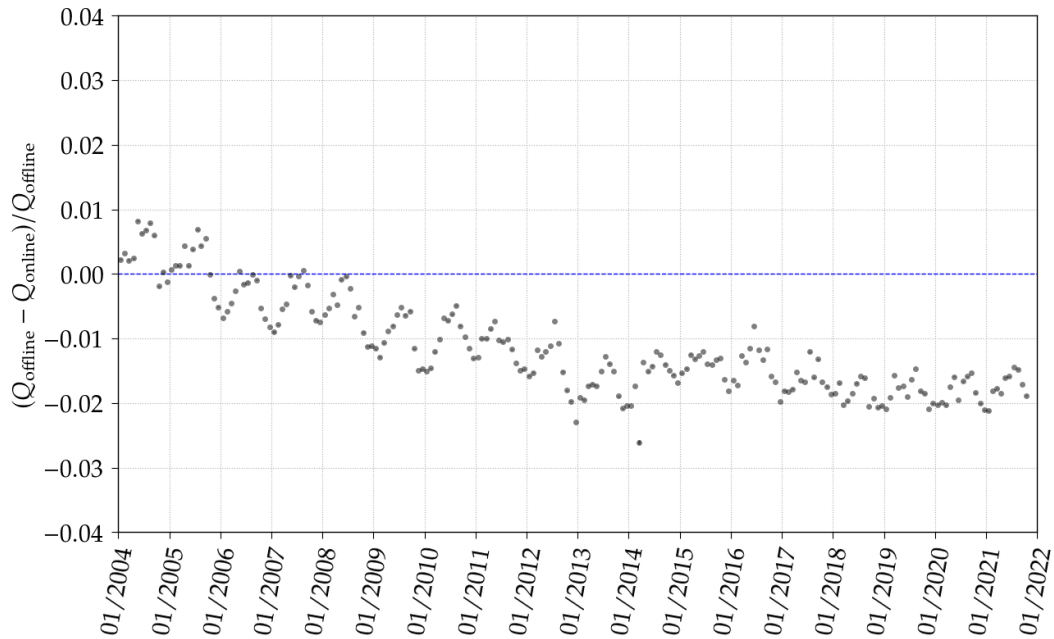
Figure 6.27: Monthly averages of the relative differences of the online and offline charges for all the histograms of all the devices in the data set.

algorithm and defines a measure to filter and reject histograms with oscillating appearances of extreme values or short-frequent fluctuations which undesirably succeed the muon peak and minimum determination. In the post-selection step, a minimum threshold of 1.3 is applied to the charge ratio. In the case that the charge histograms change their shape due to material aging effects and the maximum-to-minimum charge ratio decreases, the filter threshold can be reached at a certain time and the histograms of the device might not succeed the calibration process anymore.

For this reason we determined the monthly average charge ratios of the individual devices of the chosen station LS324 which are displayed in Fig. 6.26. Therein, all three LPMTs show a decrease of the charge ratio with time, starting with a ratio of above 1.6 in 2004 and developing to values of around 1.55 after 18 years of data acquisition. Analogously to the density differences, the continuous decrease reflects the aging induced changes of the shapes of the histograms, but the minimum threshold for a successful calibration, indicated by the blue dashed line, is not reached and will not be reached in the near future when we expect a constant slope of the decrease.

6.5.3 Detector Aging

For a further analysis of the impact of material aging on the calibration factors, and thereby on the signals of the individual detectors, we studied the time evolution of the differences between the charge values obtained with the modified calibration procedure and the online charge estimates calculated by the local-station software. By comparing the results of the different calibration methods, the intrinsic behavior of the devices can be analyzed and conclusions on the performance of the two procedures can be drawn. In the diagram in Fig. 6.27, the time development of the relative differences of the online and offline charges ΔQ_{proc} are displayed. For the comparisons, the monthly averages including the histograms of all the devices have been determined. Whereas in the first years after the start of the data acquisition in 2004, the average charge differences between the procedures were fluctuating with the seasonal variations around the mean difference of zero, a drift in the mean value with time can be observed. This leads to a final shift of 1.5 to 2 % at the end of 2021 matching
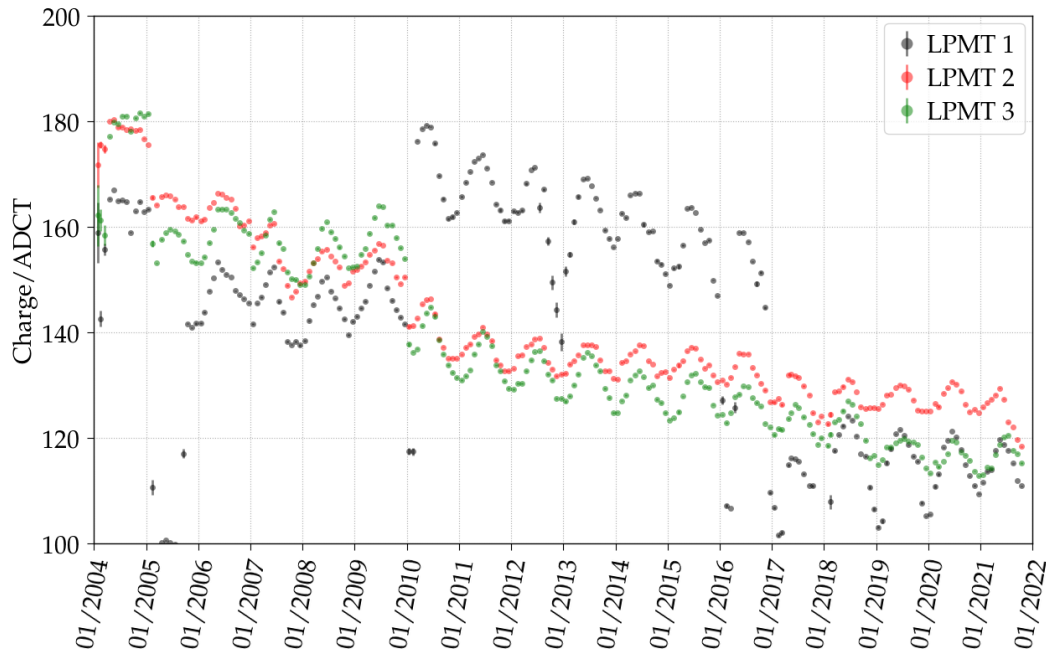
Figure 6.28: Monthly averages of the charge values obtained with the new calibration algorithm for the three LPMTs of the station LS324. A decrease of the average values for all PMTs can be seen. Changes in the power settings for the PMT with ID 1 in 2010 and 2017 result in discontinuities of the charges.

the results obtained in the analysis of a single month of data in Section 6.4.3. The spread of the seasonal fluctuations remains rather stable over the total time period.

From the shift in the average behavior of the online and the offline calibration procedures, we can conclude that the material aging effects impact the methods in different ways. Thereby, without any additional studies on the algorithm for the determination of the online estimates, we are not able to separately distinguish the direct influences on the procedures. Nevertheless, the use of two parallel precise calibration methods is highly beneficial to recover failures in one of the procedures. For this reason, potential adaptations of the conversion factors between the two methods to reduce the detectable shift might be advisable.

When analyzing the long-term behavior of the LPMTs, the calibration procedure related quantities provide measures to describe the quality of the data and the general performance of the applied calibration methods. But besides these variables, the resulting charge conversion factors define the most important value to determine the success and the precision of the calibration procedure of the detected air-shower events. Therefore, we have analyzed the time evolution of the charge conversion factors of the three LPMTs of the station LS324, presented in the diagram in Fig. 6.28. Therein, the monthly averages of the charge values obtained with the new calibration algorithm are shown for the three PMTs of the station LS324. These charge factors already include the conversion to vertical through-going muon responses and represent the values used in the determination of the signals of the WCDs as presented in Section 6.4.2. For all three PMTs, a downwards trend of the charge values can be observed, with an faster decrease in the early years of the data acquisition period. In addition, the seasonal fluctuations of the average charge values are visible which can be related to the correlations with the external temperatures. For the PMT with the ID 1, two discontinuities can be seen. These can be explained with changes in the power settings in 2010 and 2017. When studying the evolution of all the charge values of all the devices, we can conclude that the majority of LPMTs show a very similar behavior than the devices of the example station.

Additionally to the WCDs, the calibration results of the SSD PMTs can be analyzed
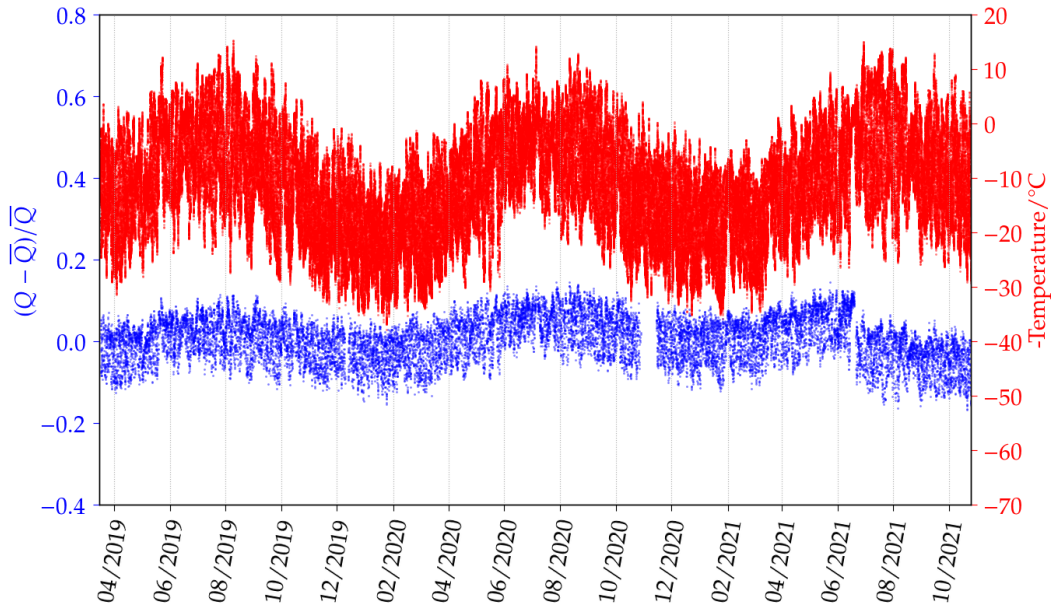
Figure 6.29: Relative charge differences of all histograms obtained with the SSD PMT of the station LS1732, indicated by the blue markers. The red markers display the negative external temperature obtained with the weather station in the Observatory. Thereby, a strong correlation between the two distributions can be observed which can be related to the temperature dependence of the shape of the charge histograms.

to study potential material aging effects leading to decreases in the light production, and therefore to changes in the detected signals. Despite the fact that the first SSDs have already been deployed in the AugerPrime Engineering Array (EA) in 2016, we present the long-term studies which have been carried out using data obtained with the scintillation detectors connected to the original UBs in the SSD PPA, introduced in Section 5.3. This decision was taken due to the significantly higher stability in the operation conditions of the SSD PPA detectors during the nearly three years of their data acquisition when compared to the first AugerPrime stations. For the calibration of the SSD PMT signals, the modified algorithm has been applied to the charge histograms including the final conversion from omnidirectional to vertical through-going particles. To enhance the visibility of small variations or trends in the charge values, the relative charge differences ΔQ are determined utilizing the charge values from each histogram Q and the mean charge of the total time period $\overline{Q}$ for each SSD PMT individually. The differences can be calculated with

$$\Delta Q = \frac{Q - \overline{Q}}{\overline{Q}}. \tag{6.17}$$

In the diagram in Fig. 6.29, the blue markers present the relative charge differences of all histograms obtained with the SSD PMT of the station LS1732. Therein, we can observe that the relative charge differences follow a regular oscillation pattern with an amplitude of ~5 %. Due to the fact that this pattern indicates a periodicity with the alternation of the seasons, the diagram also contains the time evolution of external temperature values to further investigate a potential dependence. Thereby, similarly to the temperature dependence analysis of the electronics input channels in Section 5.4.2, we use the temperatures obtained with the weather station in the Observatory [149] as measure of the environmental effects due to their independence of the SD electronics status. But in contrast, in this diagram, the negative temperatures are displayed. When comparing the charge differences and the negative temperature values, a strong correlation between the two distributions can be seen.
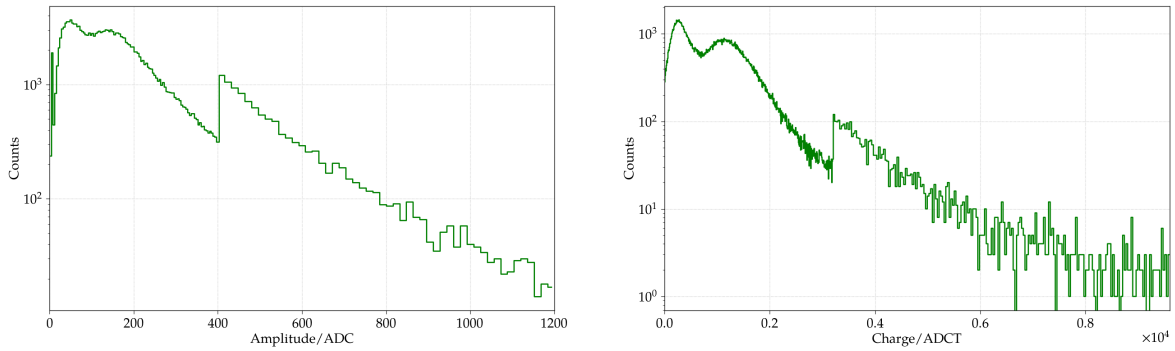
Figure 6.30: Examples of calibration histograms for an LPMT connected to an UUB. *Left:* Signal-amplitude histogram. *Right:* Signal-charge histogram.

This relation is a strong indication of a temperature dependence of the shape of the charge histograms, i.e., a variation of the position of the muon peak for different daytimes and seasons can be measured. In contrast to the LPMTs of the WCDs, no general decrease of the charge values which can be associated with material aging effects is observed for the SSDs. This might be explained with the rather short time period of analysis compared to the nearly two decades of the WCD data acquisition. Furthermore, small aging effects can be hidden in larger signal variances produced by changes of the power settings.

To exclude a malfunction of the device or station electronics, the analysis has been performed for all SSD PMTs in the SSD PPA, resulting in very similar temperature dependence for all the devices which has been already published for several PMTs including the one presented here in Ref. [146]. Nevertheless, the origin of the temperature dependence remains unclear. One explanation might be the temperature influences on the baseline values of the traces in the muon buffers. These baselines are used to calculate the signal amplitudes and areas which are then stored in the calibration histograms. If the baseline values are changing with the external temperatures while the amount of light produced by the through-going particles remains the same, an indirect dependence of the muon peak position with the temperature will be derived. To confirm this hypothesis, an in-depth study of the calculation of the signal properties is necessary which cannot be carried out within the scope of this Dissertation.

6.6 Calibration of AugerPrime stations

While in the previous section the analyses of the performance and stability of the calibration procedures have been performed on the data acquired with SD stations equipped with the original UBs, this section presents the general situation of the calibration for the devices connected to AugerPrime electronics boards, the UUBs. Due to the fact that until the submission date of this Dissertation the adaptations of the local-station software to provide the necessary online estimates is still pending, the calibration of the PMTs in the AugerPrime stations requires a recovery module to successfully pass the current implementation of the calibration procedure, as already described in Section 6.2.2. In contrast, the modified algorithm is designed to use only the information of the streamed calibration histograms, and therefore is independent of online estimated quantities. In the following, we evaluate the performance of the new calibration algorithm applied to histograms acquired with the UUBs connected to both types of PMTs, the LPMTs of the WCDs and the PMTs of the SSDs.

Analogously to the local-station software of the UBs, the locally implemented algorithms of the UUBs utilize the muon buffer traces to calculate certain calibration-relevant quantities which are then stored in the calibration histograms containing the values obtained in the
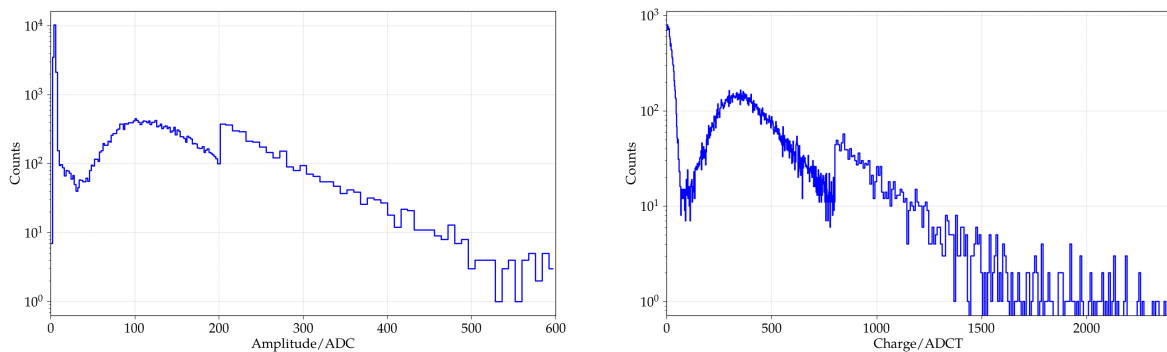
Figure 6.31: Examples of calibration histograms for an SSD PMT connected to an UUB. *Left:* Signal-amplitude histogram. *Right:* Signal-charge histogram.

61 s time windows. Despite the fact that the bin sizes and scaling factors in the calibration histograms vary between the two generations of electronics boards due to the differences in the sampling frequency and signal readout resolution, the general shape of the histograms remains similar.

In the signal-amplitude and -area histograms of the LPMTs inside an AugerPrime stations, two maxima are visible, one at lower amplitude or charge values created by mostly electromagnetic particles entering the WCD, and a second one defined by the through-going muons. An example of both types of histograms for an LPMT connected to an UUB is shown in Fig. 6.30 with the amplitude histogram on the left and the charge histogram on the right. Additionally, in both histograms we can observe the transition between the different bin sizes to reduce the amount of transmitted information, analogously to the implementation in the software fore the original UBs.

In the case of the SSD PMTs connected to an UUB, the situation of the calibration histograms is very similar. Analogously to the implementation on the UBs, the calculation of the calibration variables and the storing of the values in the histograms is performed when the trigger condition on the LPMTs of the WCD is fulfilled. This results in large entries for bins with a low number, due to the determination of the quantities on traces which only provide baseline fluctuations. The result is a larger pedestal peaks close to zero, as can be seen in the amplitude and charge histograms in Fig. 6.31. Similarly to the histograms acquired with the UBs, the bin entry difference of the muon maximum to its accompanying minimum is significantly larger for the histograms of the SSD PMTs compared to the histograms obtained with the LPMTs which strongly increases the success fraction of the calibration.

With the new calibration algorithm, the extreme value determination has been significantly improved by increasing the flexibility of the bin-to-bin comparison procedure and implementing a purely histogram-driven procedure. When applying the new algorithm to the charge histograms of the devices in the AugerPrime stations, the majority of properly functioning PMTs can be calibrated, determining the muon peak and the accompanying minimum. Two examples of successful fits of the charge histograms are shown in Fig. 6.32, on the left for one of the LPMTs and on the right for the SSD PMT of the same station. After the successful determination of the muon peak position in the histograms, the same geometry factors compared to the UBs are applied to finally receive the charge calibration factors Q_{VEM} or Q_{MIP} for vertical passing particles. At this point we have to note that due to missing implementations in the UUB software to enable the transmission of certain online calibration information, potential shifts induced by changes of the baselines are not corrected in the latest version of the new calibration algorithm. These corrections have to be included when the necessary local-station information will be available in the future. In addition, due to the unavailability of certain online estimated quantities, no quality checks are currently
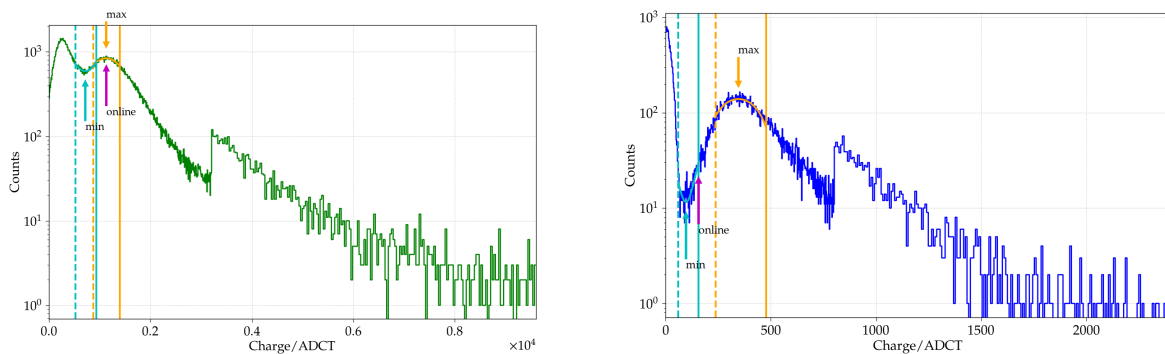
Figure 6.32: Charge calibration histograms with successful determination of the muon maximum and the accompanying minimum obtained with an UUB. *Left:* For an LPMT. *Right:* For an SSD PMT.

performed for the UUB devices before the actual charge calibration process commences.

To further analyze the general performance of the new calibration procedure, we can investigate the time evolution of the charge factors determined for the PMTs connected to an UUB. To carry out this study, we selected an AugerPrime station of the Upgraded Unified Board pre-production array (UUB PPA) installed in December 2020 and calculate the daily averages of the resulting charge values from the calibration process. In the diagram in Fig. 6.33 the charges of all four devices of the station LS1222 from the start of the data acquisition phase in December 2020 until October 2021 are shown. Therein we can observe that for one of the LPMTs and the SSD PMT the daily average charges are very stable, while for the other LPMTs increases and decreases due to small changes in the power setting are visible. At the end of June 2021, a discontinuity in the charges of all devices can be observed. The origin of this feature was an initiation of the reconfiguration procedure of the power settings (shortly introduced in Section 6.1.1) of all the SD stations due to a preceding shutdown of the whole detector. Together with the shutdown and reinitialization process, a hotfix of the power configuration software has been rolled out, resulting in large discontinuities in the charges of all the SSD PMTs.

6.7   Summary and conclusions

The performance results of the AugerPrime hardware presented in the previous Chapter indicate the readiness of the various detector components for the use as the standard configuration for the future SD stations. To complete the upgrade process and guarantee a precise reconstruction of the EAS events, the analysis software frameworks of the Pierre Auger Collaboration, as well as the software for the data acquisition process in the Observatory have to be prepared to handle the increased amount of data of the original and all the new detectors. Thereby, the complex calibration process of the various detectors plays a major role in the successful outcome of the AugerPrime upgrade. For this reason, we present in this Chapter, the in-depth analysis and studies of the calibration procedures of the two main sub-detectors of the SD stations, the WCDs and the SSDs, by addressing one crucial question: Is the current software implementation of the detector calibration capable to properly handle the signals of the AugerPrime detectors, and furthermore, can the procedure be used for the new and the original detector configuration at the same time?

To get an insight into the available general calibration procedures for the SD, we introduced at the beginning of this Chapter the different methods to determine the necessary calibration information of the individual PMT signals. Thereby, the two currently implemented calibration procedures are presented and described. One is the online calibration
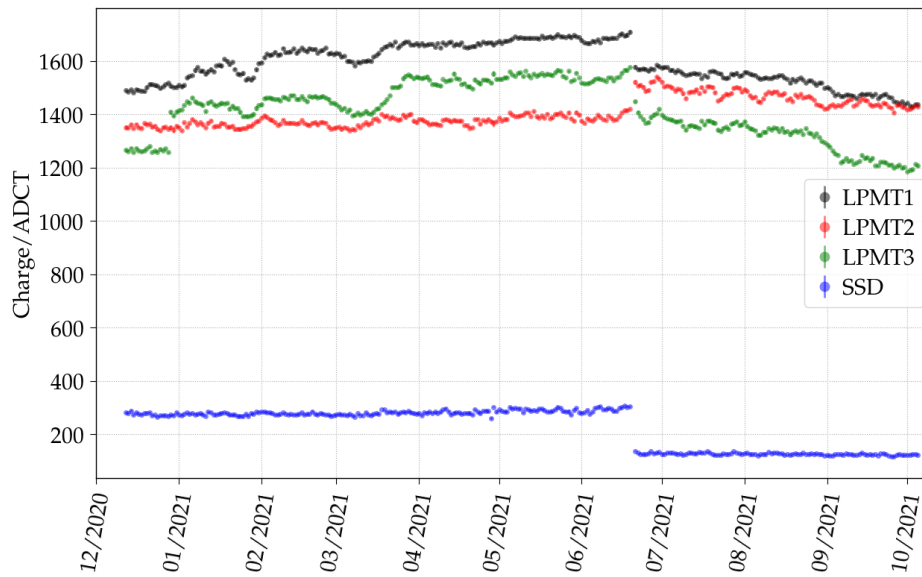
Figure 6.33: Daily averages of the charge calibration factors for the individual PMTs of the AugerPrime station LS1222. The discontinuity in June 2021 is related with a reconfiguration of the power settings of all SD stations after a preceding detector shutdown.

procedure implemented in the software of the local-station electronics which is used to define the local event trigger thresholds and further determines the estimates of various quantities including the factors necessary to calibrate the signal pulses of the devices. Besides the online procedure, a second set of calibration information, contained in the so-called "calibration histograms", is streamed from the stations to the CDAS. From these histograms, the most probable signals of vertical through-going single muons can be derived which are then used as relative calibration units for the respective device signals. This procedure defines the offline calibration and is preceded by a data quality check which is capable of rejecting malfunctioning PMTs before the actual calibration is initiated.

To answer the addressed question about the readiness of the current calibration implementation, we analyzed in the second part of this Chapter the performance of the offline calibration procedure. Due to limitation of the number of measured events from AugerPrime stations, we focused at first on the results when the method is applied to histograms obtained with the non-upgraded SD stations over the more than 18 years of data acquisition, resulting in the check of the calibration status of the enormous number of ~720 million histograms. In these studies, we observed a decrease of the number of successfully terminated calibration processes with advancing time, as well as an increasing seasonal oscillation pattern. Both behaviors can be tracked back to the changes of the general shape of the histograms due to material aging effects and environmental influences. In addition, the entanglement of the current calibration algorithm with the results from the online estimation procedure leads to failures of the offline calibration and a potential miscalibration of the devices. In the case of the AugerPrime detectors, an additional recovery module is required to enable the current offline calibration method, but due to its inflexibility towards changes in the histogram settings, the failure rate can reach high levels. With these major drawbacks, we can conclude that the current software implementation of the detector calibration is not ready for the application to the AugerPrime data, and even the calibration of the devices of non-upgraded stations is limited.

For this reason, we developed and presented a new calibration procedure which is able to replace the current implementation and increases the amount of successful terminations of the

offline procedure. Thereby, three major motivations have been addressed to design the new algorithm. The overall flexibility of the procedure has to be enhanced to be able to determine the relevant quantities on histograms with changing shapes. Additionally, the new algorithm assures higher quality requirements on the individual histograms, by not only searching for the calibration-relevant muon maximum, but also for the accompanying minimum. With this implementation, misdetection of the low-energy maximum in the histograms can be avoided. Finally, the modified procedure is designed to be purely histogram-driven to provide the independence of the online estimates, offering the opportunity of comparisons between the complementary procedures. Especially in the case of the AugerPrime stations, the calibration with the histograms is necessary due to the missing transmission of the required online estimates. The new algorithm calculates the density of the histogram bins, determined with a sliding average window, and uses a relative condition in the bin-to-bin comparisons based on the density uncertainty of the extreme value to determine the fit ranges. In addition, new pre- and post-selection criteria for the histograms have been included to further enhance the quality of the selected data.

Subsequently, we analyzed the performance of the modifications on the data of the original WCDs, first on the histograms obtained in a single month, then on the total data set since the start of the data acquisition in 2004. To validate the performance of the new algorithm, the monthly fractions of histograms which have been successfully fit can be determined for both algorithms. While the current method results for the example month in ~94.8 % of successful fits of the non-rejected histograms, the modified algorithm significantly rises this number to values above 99.5 %. In general, for all months in the SD data except the first three in 2004, the new algorithm results in significantly higher fractions of successful fits with values up to 10 % compared to the current procedure in the most recent years and depending on the season. Furthermore, by comparing the charge values for histograms which have been successfully fit with both algorithms, we determined the potential bias introduced by the modified procedure. As a result, both algorithms deliver nearly identical charge factors for individual charge histograms with overall differences below 1 %. This minimal bias also holds true, when the detector signals for the WCDs and SSDs are analyzed.

In additional long-term performance studies of various quantities describing the performance of the new algorithm, the changing shape of the histograms produced by the aging effect has been further analyzed. With the time evolution of the trigger condition of the extreme value finder and the post-selection criteria, we have been able to present the quality and stability of the new procedure for the past and present histograms. Furthermore, under the assumption of a continuation of the current trend of these sensitive quantities, an extrapolation towards the future calibration performance can be provided. Thereby, the new algorithm is expected to perform successfully for the large majority of devices in the upcoming years.

Due to the purely histogram-driven approach, the new offline calibration algorithm provides an independent second measure of the charge calibration factors and enables comparisons with the online estimates determined by the local-station software. When analyzing the differences of the charge values from the online and the offline procedures, a change over time can be observed. While at the beginning of the SD data acquisition, both methods deliver nearly identical values, a small shift of the average difference in the most recent years is detectable. This indicates that the material aging impacts the methods differently and suggests adaptations of the conversion factors between the two procedures which have been determined in the engineering phase of the SD.

Ultimately, the efficiency of the new calibration algorithm is even more important when the data of the new AugerPrime stations is analyzed. These stations define the SD of the measurement stage Phase II and require an adapted offline calibration procedure to handle the different calibration histograms of the original and the new devices. Due to the fact

that at the submission date of this Dissertation the AugerPrime components are still in the installation phase, various calibration information are not available in the data analysis. For instance, the algorithms for the determination of the online calibration estimates is still under investigation, and therefore no quality selections of individual devices are in place. While the current calibration algorithm requires the use of a recovery module, and thereby introduces miscalibrated events, the new algorithm is purely histogram-driven, resulting in significantly higher fractions of properly calibrated histograms. With the new procedure, we have also determined the long-term behavior of the SSDs installed in the SSD PPA in 2019. Thereby, no aging related changes in the signals have been found in the first three years of data acquisition.

In general, we can conclude that the new algorithm developed in this Dissertation significantly improves the calibration process of the PMT signals obtained with both generations of SD stations, the non-upgraded stations with UBs and the AugerPrime stations containing the new UUBs and additional detectors. This is achieved by the superior flexibility of the new algorithm towards changes of the shape of the histograms when compared to the current calibration procedure, resulting in nearly 100 % of successful fits of the histograms of properly functioning PMTs. Furthermore, no bias in the determined charge distributions is introduced by the new calibration procedure and the independence from the online estimated values is provided. The time evolution of calibration-related quantities indicate a stable calibration performance which can also be expected in the upcoming years if the aging velocity stays constant. After evaluating these arguments, we propose the new algorithm to be used as the standard calibration procedure in the $\overline{\text{Off}}\underline{\text{line}}$ software framework assuring a successful calibration of the past and the future SD data.

Nevertheless, the use of different parallel calibration methods is highly beneficial for the data analysis due to the potential to recover failures in one of the procedures. For this reason, the optimization of the online calibration procedure, especially for the AugerPrime stations, will further enhance the precision of the signal reconstruction in the future and can lead to additional adaptations in the offline calibration process. These might be necessary due to the continuous aging of the hardware. With the additional detectors of the AugerPrime stations, an additional approach to improve the determination of the muon peak in both relevant calibration histograms, the signal amplitude and the signal area, has been internally proposed in Ref. [159]. Therein, the transmission of two extra calibration histograms is suggested containing coincidence events of the SSD PMT and one of the LPMTs when both types of PMTs detect a pulse above a defined amplitude threshold. By the selection of particles that deposit a sufficiently large signal in the SSD PMT trace, the shape of the LPMT histograms changes and a suppression of the low-charge maximum produced by the electromagnetic particles is achieved. Consequently, the muon peak is enhanced, and thereby a successful calibration is provided. In the case of the stations in the most outer rows of the SD array which will not receive an SSD, these coincidence histograms will not be available and the standard offline algorithm is required.

Chapter

7

Reconstruction of Surface Detector Events

The reconstruction of extensive air showers (EASs) and the determination of the properties of the primary cosmic ray (CR) particles arriving at the Earth defines the ultimate goal of the current and the future detectors of the Pierre Auger Observatory. With the telescopes of the Fluorescence Detector (FD), the longitudinal profile of the EASs developing in the atmosphere can be determined, and thereby a first estimate of the energy and mass of the primary particle can be obtained. But due to their design and background light sensitivity, the measurements are only possible in clear and moonless nights, hence the number of detected events above $10^{19.5}$ eV is strongly limited.

In contrast, the measurement of air-shower particles reaching the ground utilizing the stations of the Surface Detector (SD) is independent of the daytime and background light, but only depends on the general operation status of the individual detector stations. This leads to a significantly larger number of observations of EASs, enabling studies of the properties of ultra-high energy cosmic rays (UHECRs) in the energy region of the flux suppression. Despite the fact that the SD stations sample only a fraction of the total number of secondary particles, and therefore the total calorimetric energy of the EAS is not directly obtainable, a general shower-size estimator can be determined for each air shower. By utilizing a cross calibration technique derived from the data set of EAS events that have been successfully reconstructed with both of the main detectors, the so-called "golden hybrid events", the shower-size estimator can be converted into an estimate of the calorimetric energy of the primary CR. With this method a well-defined energy scale for all events which are successfully reconstructed with the SD can be achieved.

Besides the energy, the determination of the primary CR mass is highly relevant for the UHECR research constraining the proposed source models and describing propagation effects. Due to the limited capability to reconstruct the muon content of individual EAS using the original SD stations, and thereby their incapability to properly determine the CR mass composition, each station will be upgraded with additional sub-detectors in the context of the AugerPrime upgrade. By providing complementary measurements of the secondary particles of the air showers on an event-by-event basis, the mass sensitivity of the SD is significantly enhanced. This increases the importance of a stable and reliable SD reconstruction procedure which itself strongly depends on the signal acquisition using the proper calibration of the

various devices.

After the photomultiplier tube (PMT) time traces of air-shower events measured in the Observatory have been studied in Chapter 5, and the detailed analyses of the calibration procedures of the individual detection devices and the detector signal have been carried out in Chapter 6, the event reconstruction procedure is presented in this Chapter. Similarly to the previous chapters, we focus on the data obtained with the water-Cherenkov detectors (WCDs) and the Surface Scintillator Detectors (SSDs). The signal determination and calibration performance of the other AugerPrime components, for instance the small photomultiplier tube (SPMT) or the antennas of the Radio Detector (RD), are not analyzed in the scope of this Dissertation.

The standard Auger reconstruction procedure starts at the smallest scale, the digitized currents of the individual PMTs, and ultimately evolves into a large scale array reconstruction of the air-shower footprints using the signals of multiple SD stations. Thereby, primary particles with the highest energies can produce air-shower footprints on the ground which can exceed areas of $25 \, \text{km}^2$. The first step in the reconstruction process, the determination of the signals of the WCDs and the SSDs, has been already introduced in Section 6.4.2. The resulting detector signals of each station then define the starting point of the subsequent air-shower reconstruction procedure which defines the first part of this Chapter. Thereby, the focus is set on the three main processes of the reconstruction of events with zenith angles below 60°, the so-called "vertical" events. After the geometry of the air shower is determined using the timing information of the SD stations, the lateral distribution, i.e., the profile of the air shower on the ground, is obtained, for both sub-detectors individually. With the resulting shower-size estimators, the last step in the event reconstruction chain can be performed, the determination of the primary CR energy.

Additionally, the modification of the calibration procedure influences the calculation of the individual detector signals, and therefore impacts the determination of the reconstruction-related quantities. For this reason we presented in the second part of this Chapter the analysis dependence of the shower-size estimators on the chosen algorithm for the device calibration. Finally, the last chapter part is dedicated to the comparison of the performance and behavior of the different SD array configurations related to the AugerPrime upgrade which have been installed in the Observatory. These include stations from varying stages of the upgrade process and provide the opportunity to evaluate the readiness of the upgrade components, as well as enable predictions of the future data acquisition and EAS reconstruction performance at the Pierre Auger Observatory.

7.1   Reconstruction of air showers

Subsequently to the calibration of the individual devices and the determination of the WCDs and SSDs signals, introduced in the previous Chapter, the reconstruction of the EASs can be performed. Thereby, the reconstruction procedure of vertical EAS events detected with the stations of the SD contains three major stages which are executed sequentially [158, 153, 156]. At the beginning, the geometry of the air shower is reconstructed by determining the azimuth and zenith angle, as well as the timing between the triggers of the participating stations. In a second step, the lateral distribution of the EAS is obtained by fitting a so-called lateral distribution function to the station signals. After the shower size is estimated by the lateral distribution function (LDF) fit, an energy estimate can be derived by applying a correction for atmospheric attenuation effects and converting the previously obtained shower size with the energy calibration from the golden hybrid event analysis [3]. In the following, we describe the current implementation of the reconstruction modules in the software frameworks of the Pierre Auger Collaboration. In the case of inclined air-shower events, a different procedure is applied, presented in Ref. [160].
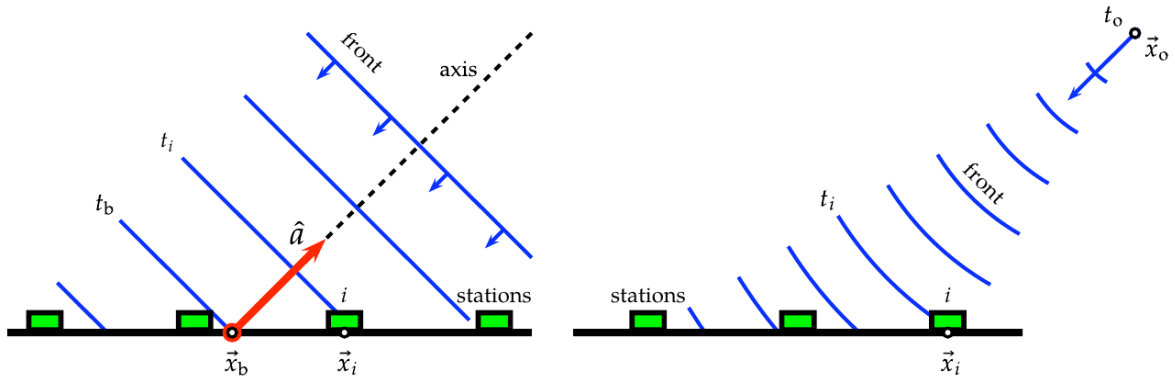
Figure 7.1: Schematics of the air-shower front models containing the relevant quantities to characterize the EAS geometry. Both taken from Ref. [153]. *Left:* For a planar air-shower front. *Right:* For a spherical air-shower front.

7.1.1 Geometry of air showers

The geometry of air showers can be obtained using the relative timing information and time structures of the SD stations, i.e., the WCDs. As already introduced in the trigger description in Section 3.1.2, on the T4 trigger level, the condition of a planar air-shower front moving with the speed of light is applied to the participating stations enforcing a removal of accidental triggers in the event data. With this condition, the seed of the air shower is determined by the three neighboring stations which provide the highest signals, and first estimates of the geometric quantities are obtained. This procedure is illustrated in the left schematic in Fig. 7.1, including the relevant quantities for the description of the air-shower front. In general, the timing analysis using a planar air-shower front propagating along the axis $\hat{a}$ with the speed of light c can be written by

$$c\,t_{\mathrm{sh}}(\vec{x}) = c\,t_{\mathrm{b}} - \hat{a}(\vec{x} - \vec{x}_{\mathrm{b}}). \tag{7.1}$$

Therein, $\vec{x}_{\mathrm{b}}$ describes the signal-weighted barycenter which defines a first estimate of the air-shower core arriving at the ground at the time t_{b}. The timing of the air-shower front passing each point $\vec{x}$ is then defined by the time t_{sh}.

After the first shower geometry estimates are obtained, and a list of minimum four participating SD stations is produced, the geometry of the air shower is properly determined by using a spherical air-shower front fit on the timing information of the stations. In the right schematic in Fig. 7.1 the concept of a spherically shaped air-shower front is shown. For any point $\vec{x}$, the arrival time of the air-shower front $t_{\mathrm{sh}}(\vec{x})$ is then described by

$$c\,t_{\mathrm{sh}}(\vec{x}) = c\,t_0 + |\vec{x} - \vec{x}_0|. \tag{7.2}$$

The virtual point of the air-shower origin is given by $\vec{x}_0$ at the time t_0. At the end of the geometry analysis, the axis and core impact position at the ground of the respective air shower is obtained. To visualize the result, an example air-shower footprint for a high-energy primary particle is shown in the left diagram in Fig. 7.2. Therein, the participating stations are displayed by the colored circles, while the small gray circles represent stations that did not trigger. The color of the station markers indicate the arrival time of the air shower, from early triggers in blue to the late triggered stations in green. In addition, the projection of the axis (black line) and the impact position with the ground (red square) of the air shower obtained by the geometry reconstruction are displayed. The sizes of the station markers indicate the respective measured station signal sizes which are utilized in the subsequent reconstruction stage determining the total shower size and the lateral air-shower distribution.
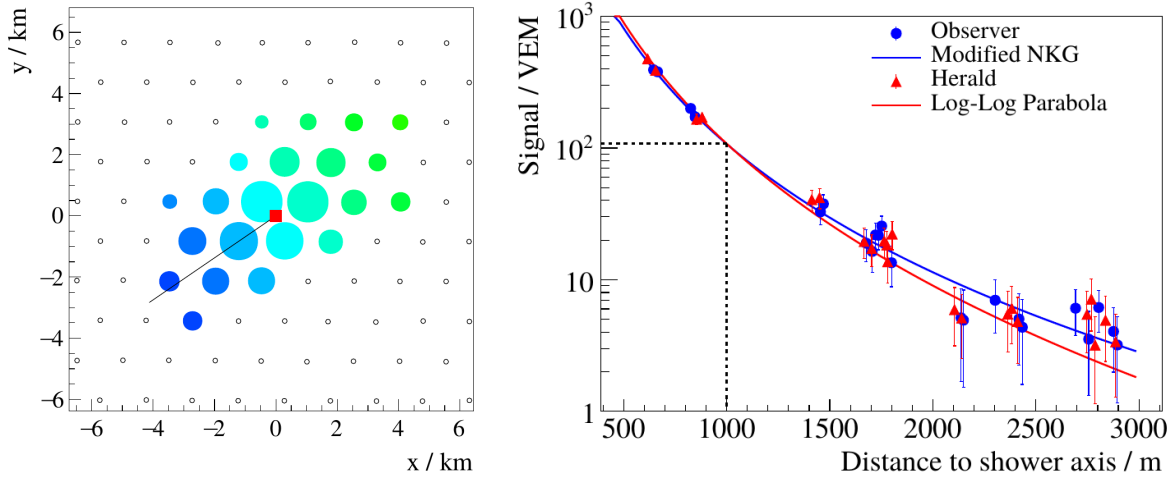
Figure 7.2: *Left:* Air-shower footprint containing the timing and the signal information as color and size indications, respectively. The black line shows the projection of the air-shower axis, the red square displays the air-shower core impact position at the ground level. Taken from Ref. [153]. *Right:* Signals of individual stations depending on their distance to the air-shower core (blue and red markers). These signals are fit with an LDF function depending on the chosen analysis software (blue and red lines). Taken from Ref. [153].

7.1.2   Lateral distribution function

After the air-shower geometry has been obtained, the lateral dependence of the air-shower signals at the ground is determined to receive an estimate of the total shower size [158, 153, 156]. By utilizing the shower direction and the impact position of the core at the ground, the signals of the WCDs can be examined depending on their distances to the air-shower core in the shower-detector plane of the SD, i.e., the plane perpendicular to the air-shower core. Due to the large distances in-between individual stations, the direct measurement of the total shower size is not possible. Therefore, a fit is applied to the signals of the participating stations which utilizes an average functional shape derived from previously acquired data. The signal in dependence of the radial distance r can then be written as

$$S(r) = S(r_{\mathrm{opt}}) f_{\mathrm{LDF}}(r) \tag{7.3}$$

with $S(r_{\mathrm{opt}})$ representing the shower-size estimator and $f_{\mathrm{LDF}}(r)$ defining the functional form of the LDF. To minimize the uncertainties of the shower-size estimator produced by shower-to-shower fluctuations, the optimal distance r_{opt} has to be selected. This distance depends on the spacing of the SD stations and their triangular arrangement, and is set to $r_{\mathrm{opt}} = 1000\,\mathrm{m}$ for the standard SD-1500 array. The resulting shower-size estimator can be written as $S(1000)$ or S_{1000}. In the case of the reconstruction of the denser SD arrays, i.e., the SD-750 and the SD-433 array, the optimal distances are adjusted to the respective spacing of the individual stations.

The functional shape of the LDF is described by $f_{\mathrm{LDF}}(r)$ and varies in the reconstruction chains of the two analysis software frameworks used within the Pierre Auger Collaboration. While in the framework implemented on top of the Central Data Acquisition System (CDAS) software, a log-log parabola fit is performed, the modules in the $\overline{\text{Off}\underline{\text{line}}}$ framework use a modified version of the Nishimura-Kamata-Greisen (NKG) function [25, 26, 27]. In the analyses in this Dissertation the latter one is used which can be describe by

$$f_{\mathrm{LDF}}(r) = \left(\frac{r}{r_{\mathrm{opt}}}\right)^{\beta} \left(\frac{r + r_{\mathrm{s}}}{r_{\mathrm{opt}} + r_{\mathrm{S}}}\right)^{\beta + \gamma}. \tag{7.4}$$

While β provides a measure of the slope of the LDF for closer distances to the air-shower core, the second term with the additive slope γ is designed to improve the description of the lateral distribution at larger distances. The changes in the slope of the LDF depending on the distance to the core can be explained with the transition from a region which is dominated by electromagnetic particles near the air-shower core, to a region far away from the core which contains signals of nearly pure muonic origin. The transition point is chosen for the SD-1500 array at a distance of $r_s = 700\,\text{m}$. An example of an LDF fit for an EAS event is displayed in the right diagram in Fig. 7.2. Therein, the signals of the individual stations depending on the distance to the air-shower core are shown by the blue and red markers, depending on the chosen analysis software. The lines highlight the fit of the LDF using the different functional forms. The fit of the LDF is performed with a maximum likelihood approach which assumes uncertainties for each measured signal. As mentioned previously, the signal uncertainties are dominated by different effects depending on the distance of the station to the core. While close to the air-shower core, the calibration uncertainties produce the largest contribution to the signal uncertainties, for the stations further away from the core the sampling fluctuations are the most relevant factor. These sampling fluctuations can be be estimated from measured or simulated data of multiplet stations, i.e., stations which are separated by only a few meters [161]. The signals from the same air shower measured with these stations slightly vary due to particle sampling effects. The uncertainties σ_S in the signals depict a Poisson behavior, and therefore can be noted as

$$\sigma_S(\theta, S) = f_S(\theta)\sqrt{S} = (a + b \sec \theta)\sqrt{S}. \tag{7.5}$$

Thereby, the uncertainties depend on the zenith angle θ and can be parametrized with a well-defined functional form. In the case of the event reconstruction with the AugerPrime SD stations, two LDFs are determined, one with the signals of the WCDs and the second using the signals of the SSDs from the same set of stations. The LDF of the SSDs has been developed and analyzed in Ref. [109] and uses an analogous functional form compared to the WCD LDF. Thereby, the determined LDFs vary in the steepness of the curves, i.e., in the slope parameters β and γ, which is the result of the different responses of the detectors towards the air-shower components. Due to the lower number of signals measured with the SSDs compared to the WCDs as the consequence of the geometrical detection efficiency, the LDFs determination for the SSDs requires only a single participating detector, while in contrast, the LDFs for the WCDs is only determined if at least three detector signals are available. Furthermore, to reduce the effect of uncertainties due to the imprecise determination of the shower core impact positions, a correction is implemented propagating the position errors to the station signal uncertainty which is relevant in the likelihood fit procedure of the LDF [156].

7.1.3 Energy calibration

Finally, the standard Auger reconstruction procedure for vertical events estimates the energy of the primary particle using the energy scale which was determined with the FD energy E_{FD} from the golden hybrid events [3]. Before the actual energy can be derived from the shower sizes, the attenuation effects of the atmosphere have to be estimated. By utilizing a constant-intensity-cut procedure, the shower sizes $S(1000)$ are converted into an zenith-independent quantity which represents the shower size of a primary particle that arrived with a zenith angle of 38°. The zenith-independent energy estimator is defined as

$$S_{38} = \frac{S(1000)}{f_{\text{CIC}}(\theta)}. \tag{7.6}$$

The correction function is parametrized with a third-order polynomial, assuming that the flux is isotropic in $\cos^2(\theta)$, i.e., the variable x can be defined as $x = \cos^2(\theta) - \cos^2(38°)$. Then
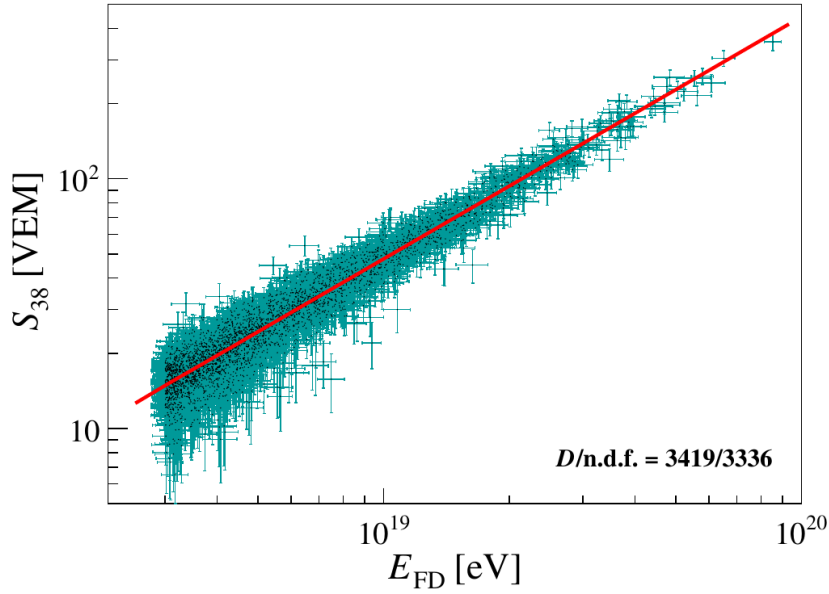
Figure 7.3: Energy scale derived from the correlation diagram between the reconstructed FD energy E_{FD} and the zenith-independent energy estimator S_{38} utilizing the golden hybrid events. The red line defines the best fit assuming a certain functional form between the two quantities. Taken from Ref. [3].

the correction function can be written as

$$f_{\text{CIC}}(\theta) = 1 + ax + bx^2 + cx^3 \tag{7.7}$$

Finally, the method derives the energy from the energy estimator S_{38} using a power-law calibration obtained in correlation studies using the golden hybrid data set, as shown in Fig. 7.3. The data is fit with the general functional form indicated by

$$E_{\text{FD}} = A \left(\frac{S_{38}}{\text{VEM}} \right)^B \text{ EeV}. \tag{7.8}$$

The best fit is displayed by the red line in the diagram, defined by the parameters A and B. The latest SD energy scale was determined in Ref. [3] and can be written as

$$E_{\text{FD}} = 0.186 \left(\frac{S_{38}}{\text{VEM}} \right)^{1.031} \text{ EeV} \tag{7.9}$$

with a total uncertainty of approximately 14 %.

Despite the fact that the standard Auger reconstruction of SD events is implemented in both analysis software frameworks, we utilize in this Dissertation the current procedures and modules in the $\overline{\text{Off}}\underline{\text{line}}$ framework [70].

7.2   Impact of detector calibration

Analogously to the comparisons of the charge factors obtained with the two offline calibration algorithms presented in Section 6.4.1, and the analysis of the impact of the calibration procedures on the detector signal calculations in Section 6.4.2, we have the opportunity to study the influences of the calibration procedure on the reconstruction of EAS events. This can be realized by the analysis of reconstruction-related quantities, like the shower sizes, and the determination of the differences between the two calibration methods, when the identical
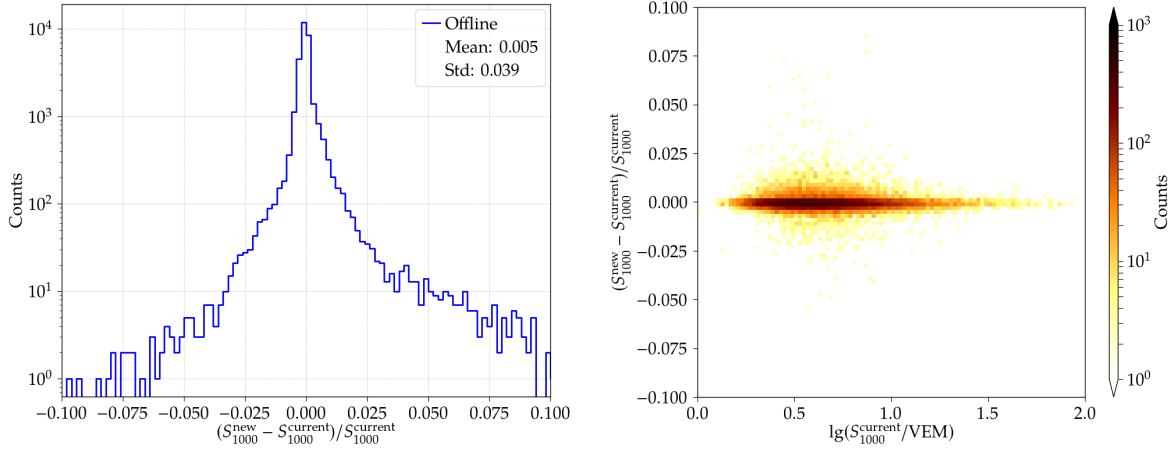
Figure 7.4: Relative differences of the WCD shower sizes obtained with the current and the new calibration algorithm. *Left:* Distribution of the total data set with a spread of ~4 %. *Right:* Two-dimensional distribution of the relative differences in dependence on the logarithmic WCD shower sizes determined with the current algorithm.

events are examined. Thereby, the determination of the shower sizes in the reconstruction chain can be affected by the changing detector signals as a result of the modifications in the calibration procedure. The detector signal changes on the other hand, are the result of changes in the charge factors from the single device calibration. In the case of the WCDs the signals are defined as the average of the maximum three participating large photomultiplier tubes (LPMTs). For the SSDs, differences in the determination of the charge values for the single PMT are directly propagated to the detector signal. Especially for stations which appear in the event close to the air-shower core, the impact of the signal changes are highly relevant for the fit of the LDF and the determination of the shower sizes. Therefore, we present the impact of the different calibration procedures on the shower sizes for the WCDs and for the SSDs separately. For both detectors, the standard reconstruction for the SD-1500 array was chosen. To maximize the number of participating devices, both calibration procedures utilize the fallback method to the online estimate when the offline calibration fails.

7.2.1 Water-Cherenkov detector

For the analysis of the impact of the modifications in the calibration procedure on the WCD LDF determination, we reconstructed the EAS events detected with the non-upgraded stations for the chosen month, August 2021, which includes more than 33 thousand events. To examine the results for the different calibration algorithms, the new and the current procedure, the event data was reconstructed once for each algorithm and the comparisons have been carried out by selecting identical events which appear in both data sets. This is realized by determining the relative differences of the shower sizes ΔS_{1000} obtained with the two calibration algorithms. The relative difference can be formulated with

$$\Delta S_{1000} = \frac{S_{1000}^{\text{new}} - S_{1000}^{\text{current}}}{S_{1000}^{\text{current}}}. \qquad (7.10)$$

In the left diagram in Fig. 7.4, we display the distribution of the relative differences of the shower sizes for the events reconstructed with the WCDs for the chosen data set. Therein, we can observe that for the majority of events, the differences are very small, i.e., a spread in the WCD shower sizes of ~4 % can be seen while the average difference is close to zero. This
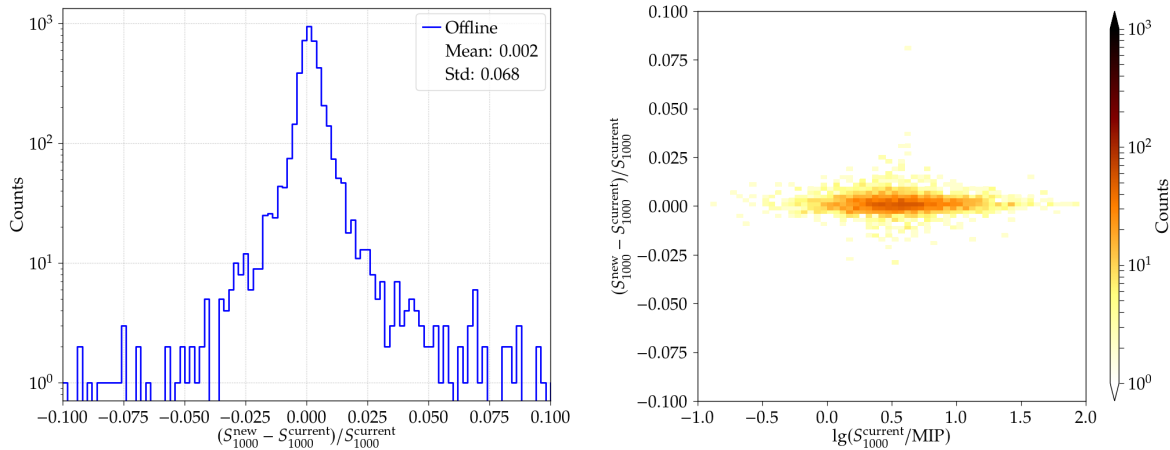
Figure 7.5: Relative differences of the SSD shower sizes obtained with the current and the new calibration algorithm. *Left:* Distribution of the total data set with a spread of ~7 %. *Right:* Two-dimensional distribution of the relative differences in dependence on the logarithmic SSD shower sizes determined with the current algorithm.

indicates that the modified calibration algorithm is not introducing a significant bias during the reconstruction process of the WCD LDFs. The symmetric behavior can also be seen in the right diagram in Fig. 7.4 by the two-dimensional distribution of the relative differences in dependence on the WCD shower sizes obtained with the current calibration algorithm. The rare events with larger differences in the shower sizes might be explained with the use of the online estimates as the fallback method in the calibration of one or more devices, which can show increased differences from the offline determined calibration factors, as presented in Section 6.4.3.

7.2.2 Surface Scintillator Detector

Analogously to the shower-size comparisons for the WCDs, we are able to analyze the reconstruction differences for the two calibration algorithms by comparing the resulting shower sizes from the fits of the SSD LDFs. Due to the significantly smaller number of SSDs in the SD array, events obtained with the stations of the Surface Scintillator Detector pre-production array (SSD PPA) of four months are chosen as the data set for this study. The resulting distribution of the relative shower-size differences ΔS_{1000} is shown in the left diagram in Fig. 7.5. In this diagram, the relative differences of SSDs shower sizes show a similar behavior when compared to the WCDs, but the spread of the distribution of ~7 % is slightly larger. This is also visible in the two-dimensional distribution of the relative shower-size differences in dependence of the SSD shower size determined with the current calibration algorithm, displayed in the right diagram in Fig. 7.5. This increased spread might be explained by the implementation of the LDF determination for the SSDs. Due to the minimum condition of a single participating SSD in the fits of the LDFs, a non-negligible number of these single SSD events can be observed in the data set. In the case of a charge value difference of the PMT induced by the modification of the calibration procedure, the SSD signal is shifted, and therefore a shift of the shower size can be observed. This might lead to larger spread in the shower-size differences compared to the WCDs values which are the averages of the device responses. For SSD LDFs obtained from single detectors, the change of the calibration factor results in a upwards or downwards shifting of the total LDF.

7.3 Comparisons of array configurations

In the extensive studies of the general performance of the new calibration procedure in the previous Chapter and the analysis of its impact on the standard reconstruction process in the previous Section, the significantly improved applicability to data obtained with the Auger-Prime stations containing the latest upgrade components, as well as the superior calibration efficiency has been presented. Therefore, the use of the new algorithm for the comparisons of the performance and behavior of different configurations of SD stations is strongly recommended. Furthermore, with the continuous deployment of upgrade components in the Observatory starting at the end of 2020, the number of events detected with the upgraded SD stations has been significantly increased since then. In the presented comparisons, three different array combinations are presented which are introduced in the following section. Thereby, for all array configurations the EAS events have been reconstructed with the standard SD-1500 procedure for vertical events which is currently implemented in the $\overline{\text{Off}}\underline{\text{line}}$ software framework. Due to the missing online estimates for AugerPrime stations equipped with the new Upgraded Unified Boards (UUBs), the fallback option in the new calibration procedure is disabled for all arrays.

7.3.1 Array configurations

Since the deployment of the first AugerPrime prototype components in 2016, different configurations of stations equipped with AugerPrime components have been installed in the Observatory. A general overview of all the station and array configurations which are related to the AugerPrime upgrade is given in this Dissertation in Chapter 5. For the performance and reconstruction comparisons, the three main array configurations have been selected, each varying in the number of installed upgrade components.

Up to submission date of this Dissertation, the largest number of SD stations still do not contain an active AugerPrime component and form the array of non-upgraded stations which represents the original SD consisting of WCDs which are read out with Unified Boards (UBs). Due to the large number of included stations, a short time period was selected, from of April to October 2021, resulting in ~140 thousand reconstructed events.

The second array in this comparisons is the SSD PPA, introduced in Section 5.3, which represents an intermediate stage of the AugerPrrime upgrade. The array consists of stations which provide a new SSD mounted on top the WCD, but still use the original UBs to operate and read out the signals of the two sub-detectors. Due to the limited number of input channels of the UB, the SSD PPA stations require the continuous disconnection of one of the LPMTs of the WCD to be able to connect the SSD PMT. Furthermore, a so-called interconnection box is needed to split the signal of the single cable of the SSDs. The intermediate upgrade solution was chosen at that time to provide a test array for the already deployed SSDs before the main production of the new UUBs was commenced. In the performance comparisons, we analyze in total ~14 thousand events acquired with the 76 SSD PPA stations from March 2019 until October 2021.

Finally, the Upgraded Unified Board pre-production array (UUB PPA) described in Section 5.2.2 represents the array with the latest versions and the largest number of upgrade components, thus it describes the final AugerPrime array in this comparison. The stations are equipped with the latest version of UUBs, a SPMTs inside the WCDs, and the majority of stations also contain an SSD on the top. To avoid a regular update of the array configuration due to the continuous deployment of AugerPrime components, we selected a fixed configuration of 79 stations defined by the first two UUB batches, shown in Fig. 5.12 by the orange squares. In the time period from April 2021 until February 2022 approximately 4600 events have been determined and reconstructed. Due to the appearance of a synchronization error in the in Global Positioning System (GPS) clocks of various UUBs starting in December 2021,
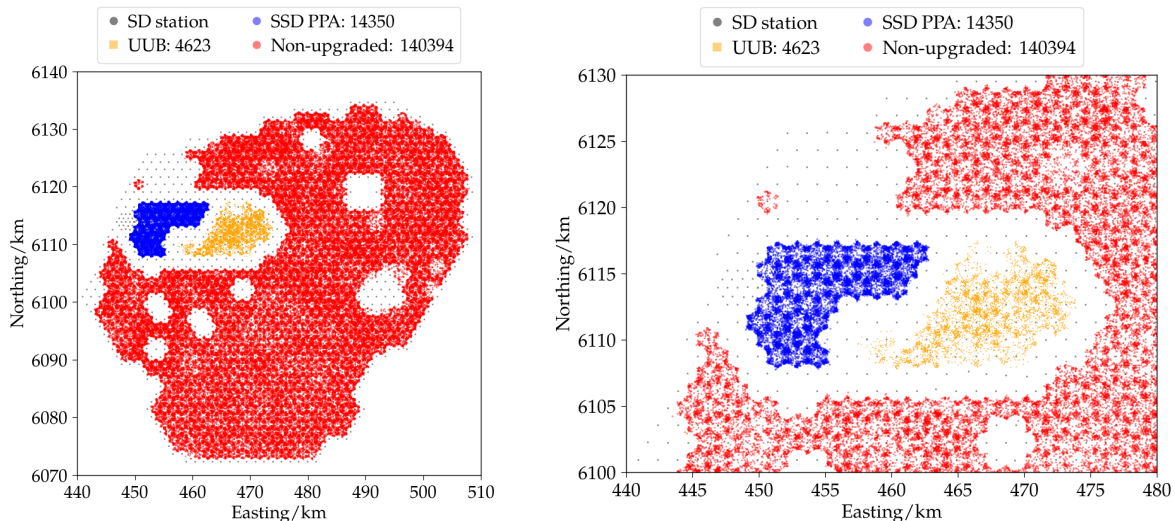
Figure 7.6: Distributions of impact positions of the reconstructed air-shower cores with the ground for the three different arrays. In addition, the number of events reconstructed with the respective configuration is given. *Left:* For the total SD. *Right:* Zoom into the region of the AugerPrime sub-arrays.

the number of reconstructed events was unfortunately not significantly extendable in the last months. Therefore, the statistics of the AugerPrime stations in this comparison remain limited.

To provide an independent analysis of the respective array configurations, the reconstruction was performed separately by selecting only the stations which belong to the respective array. In this process, we additionally applied the "6T5" condition for each array which requires six working stations in a hexagon surrounding the station with the largest signal of the event. The resulting distributions of the impact positions of the reconstructed air-shower cores with the ground for the three different arrays are displayed in the left diagram in Fig. 7.6. Therein, the reconstructed core impact positions of the non-upgraded stations are shown by the red markers, of the SSD PPA stations by the blue markers, and of the UUB PPA by the orange markers. To further enhance the distributions in the region of the AugerPrime arrays, the right diagram shows a zoom into the area of interest. In the depicted distributions, we can observe the effect of separately selecting the stations of the arrays and applying the 6T5 criterion, leading to a clear separation of the reconstruction events of the respective arrays. With these separated event data sets the comparisons of reconstruction-related quantities are enabled.

7.3.2   Shower size and energy

As already presented in the previous Section, the determination of the shower sizes for the WCDs and the SSDs by the fit of the detector signals with the LDF function defines a first quantity to describe the reconstruction performance. In the case of the WCD shower sizes, all three chosen arrays can be compared by determining the respective shower-size distributions. The results are shown in the left diagram in Fig. 7.7. To enable the presentation of all three distributions in the same diagram, all data sets have been normalized by the respective integrated shower sizes of the events with the highest values, i.e., by the summed shower sizes above 10 VEM. For all distributions we can observe a sharp rise at lower shower sizes which is the result of the limited detection efficiency defined by the trigger implementation of the WCDs. When comparing the SSD PPA with the non-upgraded array, the increased trigger threshold due to systematic disconnection of one of the LPMTs in the SSD PPA stations can
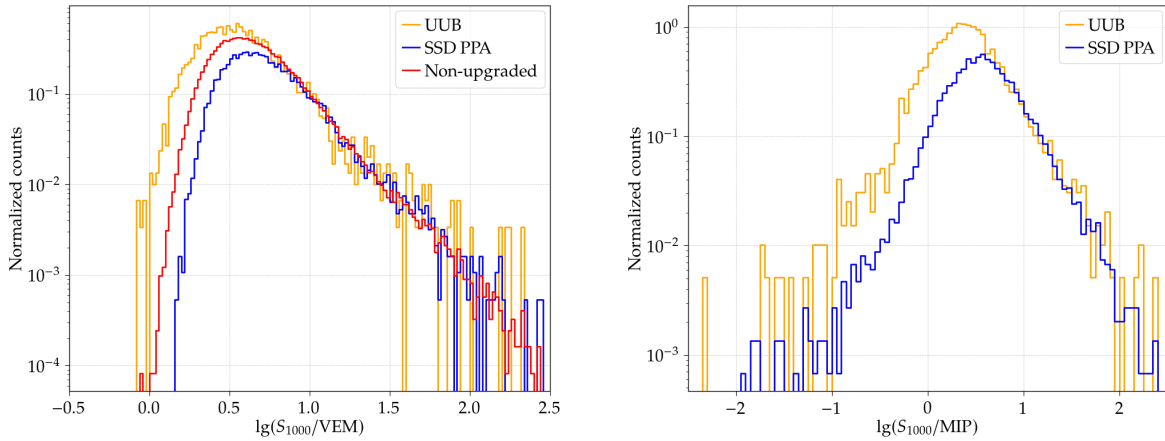
Figure 7.7: *Left:* Distributions of WCD shower sizes of all three array configurations, the non-upgraded array in red, the SSD PPA in blue, and the UUB PPA in orange. The counts of the distributions have been normalized by the respective integrated shower sizes above 10 VEM. *Right:* Distributions of SSD shower sizes of all the SSD PPA in blue and the UUB PPA in orange. The counts of the distributions have been normalized by the respective integrated shower sizes above 10 MIP.

be observed, indicated by the shifted start of the blue distribution towards higher shower sizes. Furthermore, when the new UUB PPA is compared with the original SD array, we can detect a shift towards smaller shower sizes. This leads to the estimation of an even lower threshold for the UUB PPA stations. Thereby, we cannot exclude potential trigger on noise signals resulting in rather small detectors signals and shower sizes. The increased appearance for stations with UUBs is currently investigated in the analysis of thunderstorm events which are prominent in the chosen data period. At the high shower-size flank, all three distributions show a very similar behavior indicating a well-performing reconstruction of UHECRs with the AugerPrime stations.

In the context of the AugerPrime upgrade, the newly installed SSDs provide a second set of shower sizes from the separate determination of the SSD LDFs. This results in the SSD shower-size distributions shown in the right diagram in Fig. 7.7, for the SSD PPA in blue and for the UUB PPA in orange. Analogously to the WCD shower sizes, the distributions have been normalized with the respective integrated shower sizes above 10 MIP. In contrast to the WCD distributions, the SSD shower sizes do not provide a steep flank on the lower value side. This is due to the fact that the SSD signals are not used in the local-station trigger, but serve in a slave mode to the WCD, and therefore the SSD shower sizes are determined even when the SSDs do not contain a signal pulse in the event trace, resulting in very small shower sizes. Similarly to the WCD distributions, the stations equipped with UUBs appear to measure a larger fraction of low SSD shower sizes which further supports the assumption of an increased number of noise pulses in the event data.

Analogously to the shower sizes, the final reconstruction-related quantity can be determined for all three array configurations, the reconstructed energy of the primary particle. The energy values have been obtained with the functional form presented in Section 7.1.3 using the most recent parameters presented in Ref. [3]. The resulting energy distributions of all three array configurations is shown in the diagram in Fig. 7.8. Following the concept of the shower-size analysis, the distributions have been normalized by the respective integrated energies above $10^{18.5}$ eV. Due to the exponential correlation of the reconstructed energy with the energy estimator, and therefore with the shower size obtained from the WCD LDF, the resulting distributions show a very similar shape and behavior to the WCD shower-size distributions .
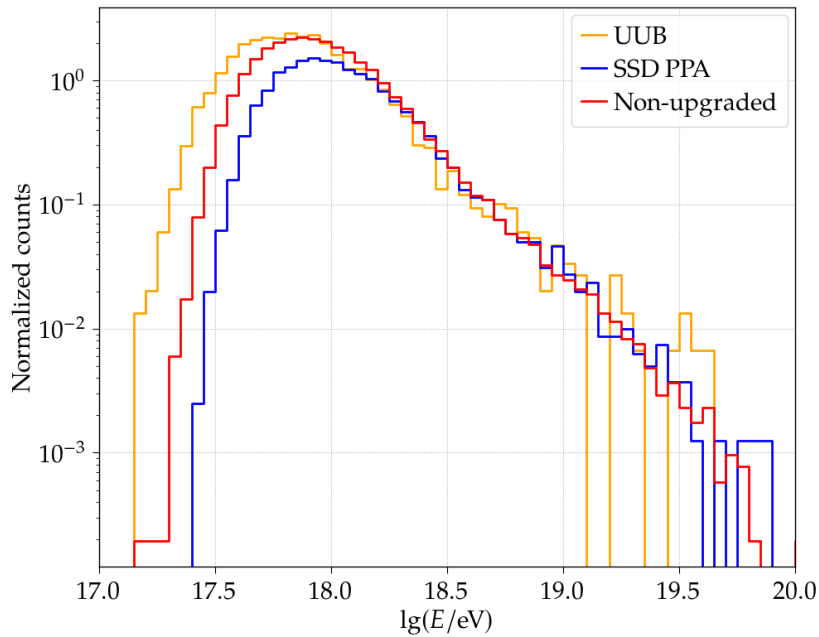
Figure 7.8: Reconstructed energy distributions of all three array configurations, the non-upgraded array in red, the SSD PPA in blue, and the UUB PPA in orange. The counts of the distributions have been normalized by the respective integrated energies above $10^{18.5}$ eV.

7.3.3 Signal ratios

While all the previous analyses presented in this Chapter depend on the SD reconstruction process, the final comparisons between the different array configurations are carried out by determining the detector signals of each individual SD station, i.e., no air-shower reconstruction-related quantities are required. Thereby, we investigate the sensitivity of the SSDs and WCDs concerning the detection and determination of the electromagnetic and muonic component of the EASs which results in a first estimation of the mass sensitivity of the upgraded SD stations. While in the SSD, electrons and muons deposit on average a similar amount of energy when passing through the detector reflected by the energy unit MIP, the observed signals from the WCD are dominated by the energy deposit of the muons. With these detector characteristics, we can define a quantity to describe the varying detector responses on an individual station level. This is achieved with the determination of the signal ratios of the SSDs and WCDs which can be expressed with

$$R = \frac{S_{\mathrm{SSD}}}{S_{\mathrm{WCD}}}. \tag{7.11}$$

In the case of the selected array configurations, the signal ratios can be determined for the arrays which provide the air-shower detection with an SSDs, i.e., the stations of the SSD PPA, as well as the UUB PPA stations.

To analyze the sensitivity of the signal ratios towards the respective components of the EAS we have determined the values for both array configurations. In the diagrams in Fig. 7.9, the signal ratio profiles in dependence of the distance of the stations to the air-shower core are given. The left diagram displays the values for the stations equipped with UBs, whereas in the diagram on the right, the signal ratios of the AugerPrime stations are presented. When analyzing the diagrams, we can observe that the signal ratios obtained with both station configurations show a similar behavior. While for stations close to the air-shower core the signal ratios are close to values of 1, the ratio values decrease with an increasing distance.
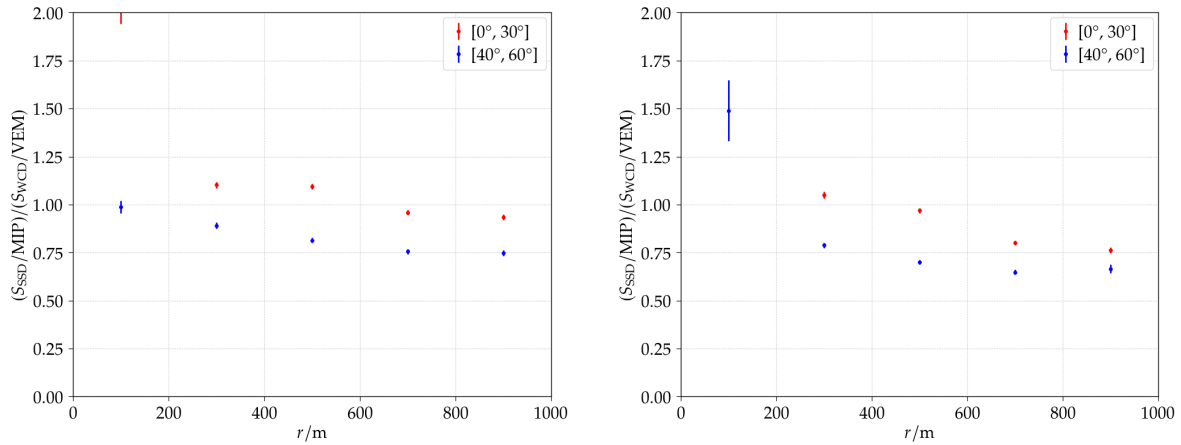
Figure 7.9: Ratios of the signals of the SSDs and WCDs over the distance to the air-shower core. The ratios are determined for two zenith angle groups. The decreasing signal ratios with increasing distances are related to the changes of the dominating EAS component and the different responses of the SSDs and WCDs. *Left:* For the SSD PPA. *Right:* For the UUB PPA.
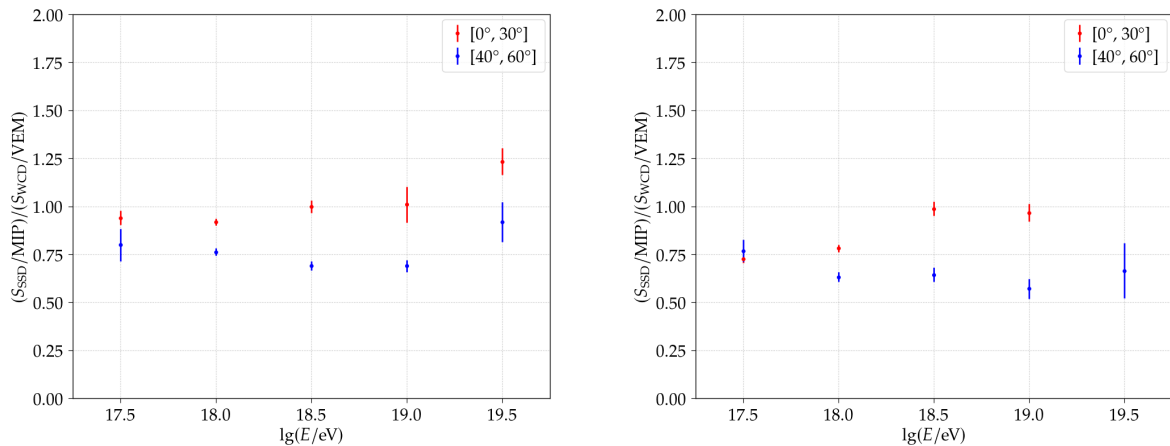
Figure 7.10: Ratios of the signals of the SSDs and WCDs for stations selected in a distance range of $800\,\text{m} < r < 1000\,\text{m}$ to the shower core over the reconstructed energy. These ratios are determined for two zenith angle groups. The increasing signal ratios with increasing energies indicate a sensitivity to the EAS components. *Left:* For the SSD PPA. *Right:* For the UUB PPA.

This can be explained with the changes of the composition of the EAS particles depending on the distance to the air-shower core. In the region near the air-shower core, the detector signals are dominated by the electromagnetic particles which then diminish with increasing distance. This decrease of the electromagnetic component results in a decrease of the measured SSD signal, and ultimately in the decrease of the signal ratio, as can be seen in both diagrams. Furthermore, we can observe that the absolute ratio value depends on the zenith angle. By separating the data set into two zenith angle ranges, one from 0° to 30° highlighted by the red markers, and the other from 40° to 60° represented by the blue markers. The more inclined events provide a smaller signal ratio due to the smaller SSD signals. These values are the consequence of the increased attenuation of the electromagnetic component for more inclined events. In both diagrams, the first bin at 100 m distance to the air-shower core is not analyzed in the sensitivity studies of the signal ratios due to the saturation of the signals of the detectors.

For a further check of the sensitivity of the signal ratios on the composition of the measured EASs, we apply an additional selection criterion to obtain only the stations which appear in the events within a certain distance range, more precisely inside the range of $800\,\mathrm{m} < r < 1000\,\mathrm{m}$. The remaining signal ratios are then displayed as profiles over bins of the reconstructed energy. This is shown in the diagrams in Fig. 7.10, again for the SSD PPA on the left, and for the UUB PPA on the right. In these diagrams, we expect an increase of the signal ratios with increasing energies due to the faster rise of the electromagnetic component compared to the muonic component. This relation can be seen for the nearly vertical events measured with the stations of the SSD PPA indicated by the red markers, especially for the largest energy bin at $10^{19.5}$ eV. For the inclined events highlighted by the blue markers, the increase of the signal ratios with increasing energy appears less apparent. In the case of the AugerPrime stations containing both detectors connected to the UUBs, the expected trend of the signal ratios with the reconstructed energies can be assumed for the vertical events. Similarly to the results for the SSD PPA stations, the inclined events stay rather constant with increasing energies. For the highest energy bin, the number of events detected with the UUB PPA is strongly limited.

Generally, we can conclude that by analyzing the signals of the upgraded SD stations, first estimations on the particle components of EASs can be derived which enables first assumptions on the mass composition of the arriving primary particles on a single station level. This might be further advanced by combining the energy dependent analysis of this Section with studies of the depths of the air-shower maxima X_{max} obtained in hybrid measurements which are beyond the scope of this Dissertation. When comparing the detector signals for the two generations of electronics boards, a very similar behavior can be observed.

7.4   Summary and conclusions

After the detailed presentation of the studies of the calibration performance of the non-upgraded and AugerPrime detectors in the previous Chapter, the ultimate processes in the measurement of EASs from UHECRs are provided in this Chapter, the reconstruction of the air-shower geometry and the determination of certain properties of the primary particle. Thereby, the capability to precisely reconstruct EAS events defines the major goal of the SD of the Pierre Auger Observatory. For this reason, at the beginning, an overview and description of general procedure to reconstruct air-shower events with the SD stations is presented. This includes the three main steps, the determination of the air-shower geometry using the different shapes of air-shower fronts, the fit process of the LDF resulting in the size of the air shower, and finally the derivation of the primary CR energy from the shower-size estimator.

Subsequently to the introduction of the EAS reconstruction procedure, two different major studies have been carried out in this Chapter. The first analysis defines a follow-up study of the impact of the modification of the calibration procedure on the obtained reconstruction quantities. Thereby, we can address one pending question: Will the use of the new calibration algorithm in the reconstruction process result in variations of the shower sizes of the WCDs and SSDs? Contrarily, the second analysis part examines the comparisons of the reconstruction performance of SD arrays with stations from varying stages of the upgrade process when the standard procedure from the $\overline{\text{Off}}\underline{\text{line}}$ software framework is applied. This leads to the following question: How will the future array of fully upgraded AugerPrime stations perform compared to the well-known SD array of non-upgraded stations?

To provide an answer to the first question, we applied the standard reconstruction procedure for the SD-1500 array implemented in the $\overline{\text{Off}}\underline{\text{line}}$ framework to the data obtained with the non-upgraded stations and analyzed the resulting WCD shower sizes S_{1000} from the fits of the LDFs. Thereby, the events have been reconstructed twice, using the current and the new calibration procedure once. When comparing the results for the two algorithms, no significant bias was observed and an overall spread of ~4 % was detectable. The obtained

difference distribution matches the observations in the comparisons of the calibration procedures on the single detector or single device level of the previous Chapter. Furthermore, the behavior of the event reconstruction with the SSDs was compared using the two different offline calibration algorithms. In this analysis, events acquired with the stations of the SSD PPA were used resulting in a similar distribution of shower-size differences compared to the WCDs. While the bias of the distribution can be neglected, a slightly larger spread of approximately 7 % were determined for the SSD shower sizes. This might be explainable with the determination of the SSD LDFs with a minimum criterion of a single participating detector. For this reason, changes in the signals of the SSD PMTs in these events result in significantly stronger impacts on the determined shower sizes than in the case of the WCDs which use the average signal of the functioning devices. Finally, we can conclude that the new calibration algorithm qualifies for the use as the default procedure in the complete SD reconstruction process. In addition, for the AugerPrime detectors, only the use of the new calibration algorithm provides a reliable reconstruction of the EAS events due to its independence of the online estimated calibration factors which cannot be determined due to the missing adaptations of the local-station software.

These advantages of the new calibration procedure can then be used to enable a comparison of the reconstruction performance of the non-upgraded stations with the newly installed AugerPrime stations, and thereby the second raised question is addressed. In these studies, we analyzed the results of three selected array configurations which have been separately reconstructed using the standard Auger reconstruction procedure for vertical events and applying a posterior quality criterion on the functionality of the respective stations. These three arrays are defined on stations which contain different components of the AugerPrime upgrade. While the non-upgraded stations do not contain any upgraded component, as the name highlights, the second array is represented by the SSD PPA stations which provide a functioning SSD, but are still operated with the UBs. The AugerPrime array is defined by the stations of the UUB PPA which contain the latest UUB version, a SPMT inside the WCD, an SSD on the top of the station. For these arrays, the reconstruction-related quantities were determined, in detail, the shower-size distributions for both detectors, the WCD and the SSD, as well as the energy distribution. In case of the WCD distributions, the trigger effects at low energies, i.e., at low shower sizes, events can be observed. Due to the increased trigger threshold for the SSD PPA stations, the rise of the distribution is shifted towards higher energies compared to the non-upgraded stations. In contrast, the WCD distributions of the UUB PPA indicate an increased detection rate of lower energy events. A similar behavior can be observed when the shower-size distributions for the SSDs are compared. Do to the fact that the enhanced detection of low shower-size values appears for both detectors, an external origin might be responsible for the unexpected behavior. One potential candidate are thunderstorm events which have been observed in the data period of the AugerPrime array. Current studies in the Pierre Auger Collaboration analyzing the responses of the upgraded detectors during lightning and thunderstorm events indicate a strongly enhanced response of the new UUBs when thunderstorm events are detected, matching our observations in the array comparisons.

In the studies of the signal ratios for the detectors of the AugerPrime SD stations, we presented an approach to determine the composition of the air-shower particles by utilizing station-level information. Therein, the effect of the expected differing responses of the WCDs and SSDs towards different air-shower components was analyzed. These detector signals can in the future serve as the starting point to improve mass composition sensitive methods, for instance the matrix-formalism or approaches based on deep neural networks. Furthermore, with additional hybrid measurements of the EAS events, and thereby the determination of the air-shower maxima X_{max}, more precise mass estimates will be achieved.

Chapter

8

Summary and conclusions

The scientific and technical evolution of any experiment is a difficult and time consuming process which demands an extensive amount of resources and workload to finally reach the new configurations. This sentence holds true for the Pierre Auger Observatory which is currently undergoing a major upgrade phase of its main detectors for the preparation of the next measurement stage in the upcoming decades. With the AugerPrime upgrade, the detection and characterization of extensive air showers (EASs) produced by ultra-high energy cosmic rays (UHECRs) entering the Earth's atmosphere will be strongly enhanced, and major progress in the UHECR research is foreseen by addressing the various open questions in the field, including the unknown mass composition and origin of the arriving particles.

This Dissertation has been carried out in the context of the AugerPrime upgrade and focuses on the evaluation of the performance and quality of the newly constructed hardware components for the upgrade of the Surface Detector (SD). Thereby, we demonstrate the evolution of the integration of the new detectors, from the first operation measurements in the laboratory directly after the construction process up to their final implementation into the EAS reconstruction process in the Observatory. This includes studies of the particle detection properties and the general operation stability of the new detector components in two measurement scenarios. On the one hand, validation measurements of the performance of the newly assembled Surface Scintillator Detectors (SSDs) in a test set-up under laboratory conditions are analyzed. On the other hand, the performance of crucial hardware components are studied in extensive tests under the regular data-acquisition conditions in the Observatory. Besides the hardware analyses, we present the modifications and optimizations of the calibration procedures implemented in the analysis software frameworks which significantly improve the accessibility and interpretation of the data obtained with the AugerPrime detectors. Finally, conclusions on the readiness of the AugerPrime hardware and software for a continuous operation in the Pierre Auger Observatory are drawn.

As one of the major components of the AugerPrime upgrade, the assurance of the quality of the SSDs plays an important role for their later performance as complementary particle detector on top of the water-Cherenkov detectors (WCDs) at the majority of the SD stations. Out of the over 1500 SSDs produced at six sites in the Pierre Auger Collaboration, the large number of 661, i.e., approximately 44 % of the detector units, have been assembled at the Karlsruhe Institute of Technology (KIT). Over the total production period of nearly three

years, the performance and general operation status of each SSD was analyzed in extensive laboratory tests, ultimately leading to a total amount of nearly 20 thousand measurement hours. These validation tests have been performed inside the "muon tower" set-up which offers a precise reconstruction of the trajectories of through-going charged particles, and thereby enables the analysis of the spatial detection efficiency and signal uniformity of the SSDs. In the validation measurements we focused on three main quantities to describe the general detector performance. By analyzing the light yields of the individual SSDs which represent the average signal sizes for single particles passing through the detectors, we observed a stable performance when comparing all the assembled SSDs, resulting in a variance of below 10 % between individual detectors. Furthermore, with the particle-trajectory information, the spatial homogeneity of the SSDs has been analyzed. This was realized by determining the spatial signal distributions, as well as their projections along and across the scintillator bars. With these distributions the signal responses of individual scintillator bars and the inserted fibers can be resolved and potentially malfunctioning components might be detected. Analyzing the data of all SSDs, no detector with spatial inhomogeneities above the expected fluctuations of up to ~10 % was observed. To study the stability of the mechanical enclosure of the scintillation detector and search for a potential light leakage, we analyzed the appearance rate of random pulses in the measured time traces. Thereby, a small number of detectors with increased rates of noise pulses have been detected, but for none of these candidates, light leakage was identified as origin of the noise. Finally, the muon tower measurements have been compared with the results from detector simulations, validating the expected geometrical behavior of the SSDs by comparing the obtained light yield values, as well as the signal pulse shapes. Overall, we can conclude that the requirements on the new scintillation detectors have been fulfilled by all detectors produced at the KIT, and that a constant high-quality level and stable production has been achieved.

After the validation measurements of the SSDs in the laboratory, we moved our focus towards the analysis of the AugerPrime components under the regular operation conditions in the Observatory. Thereby, the performance of two of the main upgrade components, the Upgraded Unified Boards (UUBs) and the SSDs, have been extensively studied. In the case of the UUB, the four different versions which have been installed in the Observatory since the deployment of the first prototype in 2016 have been tested regarding their intrinsic electronics properties, as well as their behavior in the signal sampling and digitization process. By analyzing the baseline traces at the beginning and the end of the event traces for all UUB versions and all connected devices, we determined several characteristics of the electronics boards to describe their overall performance. This includes the development of a fast algorithm to search for transient electrical pulses which indicate malfunctioning hardware components. While for the first UUB prototypes frequent noise spikes in the signals were visible, our analysis of the latest UUB version, the so-called "pre-production version", displays a low and stable appearance rate of noise pulses which are on a comparable level to the values of the original Unified Board (UB). Furthermore, we determined the general noise levels of the input channels of the UUBs and observed that with the evolution of the electronics boards over the different versions, the noise levels have been reduced, finally reaching absolute values of ~2 ADC for the latest version of UUBs. This corresponds to a similar relative noise level when compared to the results for the original UB. With the additional determination of the amplification factors between the two gains of each input channel, the dynamic range of the new electronics boards was evaluated. By developing a data-driven method, we were able to derive the amplification factors directly from the analysis of the event traces. With the comparison of the determined factors with the nominal values of the hardware components, conclusions on the accuracy of these pre-defined values, as well as on the uncertainty of the data-driven method can be drawn. In the case of the latest UUB version, we were able to show that under the consideration of the uncertainties, the amplification factors match the

expectations. Ultimately, tests of the AugerPrime electronics boards have been carried out analyzing the influences of environmental effects, e.g., thunderstorm events or temperature fluctuations on the detected signals. In conclusion, we can state that from the hardware point of view, the latest version of the UUBs fulfills the necessary requirements regarding the noise levels and dynamic range properties, and shows its readiness for the deployment on the large scale.

Besides the new electronics boards, the performance of the SSDs in the Observatory is essential for the later operation as sub-detectors of the SD stations. For this reason, we performed a follow-up study to the stability of the mechanical enclosure. This time, the analysis was based on the baseline traces of the SSD photomultiplier tubes (PMTs) obtained from the scintillation detectors in the Observatory. By determining baseline quantities which are sensitive to the pulse shapes, in this case the skewness, we analyzed the event traces of the SSDs, splitting the data into events measured during daytime and events obtained during nighttime. With this method only one candidate detector was discovered with an increased pulse rate during daytime, indicating a potential light leakage. This behavior was later confirmed by the observation of water inside the SSD after manually opening the PMT housing.

For the completion of the upgrade process, studies of the performance of the current software frameworks are substantial to guarantee the access and interpretation of the data obtained with the new hardware components. This includes the analysis software frameworks of the Pierre Auger Collaboration, as well as the software for the data acquisition process in the Observatory. Thereby, the complex calibration process of the various detectors plays a major role in the successful outcome of the AugerPrime upgrade. For this reason, we performed an in-depth analysis of the calibration procedures for the WCDs and the SSDs concerning their efficiency and stability when applied to the data of the different detectors. Especially the performance of the offline procedure which is designed to handle the calibration information streamed together with the event data is of high importance for the subsequent air-shower reconstruction process. Due to the availability, a first analysis of the offline calibration procedure was carried out using the calibration histograms obtained with the WCDs of the non-upgraded SD stations. In the studies of the calibration performance of the ~720 million histograms obtained in 18 years of data acquisition, we determined a decrease of the number of successfully terminated calibration processes with advancing time, majorly in the most recent years, accompanied by a seasonal oscillation pattern. Both of these behaviors can be tracked back to the changes of the general shape of the histograms due to material aging effects and environmental influences. Furthermore, the entanglement of the calibration algorithm with the online determined estimates obscures the search for sources of miscalibration. In the case of the AugerPrime detectors, an increased rate of failures during the calibration process can be related to the use of a recovery module which is necessary to compensate for missing calibration estimates.

Due to these drawbacks of the current calibration procedure, we developed a new algorithm to replace the current implementation, and thereby increase the amount of successful calibration processes. This goal was achieved by introducing three major design concepts, the increase of the flexibility to enable the determination of the calibration factors on histograms with changing shapes, the search for certain features in the histograms to assure a more precise determination of the calibration-relevant positions, as well as a purely histogram-driven implementation to provide the independence of the online estimated quantities. To evaluate the performance of the new calibration algorithm, several comparisons between the new and the currently implemented procedure were carried out concerning the efficiency of the calibration process and the resulting calibration factors. Except for a short time at the beginning of the data acquisition in 2004, the new algorithm delivers significantly higher fractions of successful calibration processes compared to the current procedure. Theses differences

reach values of up to 10 % in favor of the new algorithm in the most recent years, depending on the season. Furthermore, by comparing the charge values for histograms which have been successfully fit with both algorithms, we demonstrated that no bias is introduced by the new procedure. Both algorithms provide nearly identical values with overall differences below 1 % in the case of individual charge histograms, as well as for the detector signals of the WCDs and SSDs. In further long-term studies of different quantities which describe the performance of the new algorithm, we analyzed the changing shape of the histograms produced by the aging effects on the WCD components. Therein, a stable calibration of the past and present histograms with the new algorithm was obtained and a positive extrapolation towards the future calibration performance can be given, assuming a continuation of the current trend of the histogram shapes. Additionally, the new calibration algorithm provides an independent measure of the calibration factors and enables comparisons with the online estimates determined by the local-station software using pre-determined conversion factors. In these comparisons, a small shift of the average difference in the most recent years can be observed which indicates a different reaction of the calibration methods towards the material aging effects. While the conversion factors between the online and offline method have been determined more than 18 years ago with well matching results, adaptations of these factors seem to be necessary for the histograms obtained in the last years. Furthermore, the impact of the new calibration algorithm on the reconstruction procedure was studied. Thereby, we determined a stable performance of the new procedure and concluded that the modifications to create an independent procedure have been highly beneficial for the applicability of the new algorithm to data of the AugerPrime stations.

Finally, we analyzed the general performance and efficiency of the new calibration procedure on histograms obtained with the AugerPrime stations. Due to the independence of the online estimated calibration factors, the new algorithm provides the calibration of the AugerPrime detectors without the use of a recovery module, resulting in significantly higher fractions of successfully calibrated histograms when compared to the current offline calibration procedure. This enables the precise determination of the WCD and SSD signals which are used in the subsequent air-shower reconstruction to determine the lateral distribution functions for events observed with the AugerPrime stations. With the new procedure, we have also determined the long-term behavior of the SSDs installed in the Observatory in the deployment campaign in 2019. In contrast to the WCDs, no aging related changes in the signals have been found in the three years of data acquisition. We concluded that the new algorithm developed in this Dissertation significantly improves the calibration process for the detectors of the non-upgraded stations, as well as of the new AugerPrime stations. The superior procedure is obtained by the enhanced flexibility towards aging induced changes resulting in nearly 100 % of successful calibrations for properly functioning devices. Furthermore, the time evolution of calibration-related quantities indicates a stable performance in the upcoming years if the aging velocity remains constant. Ultimately, we proposed the new algorithm to be used as the standard calibration procedure in the $\overline{\text{Off}}\underline{\text{line}}$ software framework assuring a successful calibration of the past and the future SD data. With the new calibration procedure, comparisons of the different array configuration have been carried out regarding the performance of the reconstruction procedure. From these comparisons, we can conclude that the stations with the latest AugerPrime components provide promising results for a future operation as the default station of the SD.

Despite the fact that the performance is very promising, further adjustments and tests of the hardware components together with their associated software will be necessary to guarantee a stable operation in the upcoming years. A continuous monitoring of the hardware stability of the newly installed detectors is required to search for potential mechanical malfunctions. Thereby, issues like the water leakage into the SSD due to the untight sealing can potentially reappear and might lead to a significant damage of the vulnerable electronics.

When analyzing the noise levels and properties of the two generations of electronics boards, the new UUBs provide a similar or improved performance compared to the original UBs. From this point of view, a smooth transition from the measurement stage "Phase I" with the original SD stations to the AugerPrime stage "Phase II" seems to be achievable. Nevertheless, further studies and comparisons of the array trigger algorithms and event timing information are necessary to validate this statement. Especially in the current transition phase, unexpected effects and features can appear and need to be accounted for. This can be realized studying a hexagon of station doublets which has been deployed in the SD array at the beginning of 2022. Each doublet contains one station with the original UB and the second station with the new electronics board. With this station configuration, timing offsets between the two electronics boards, as well as trigger efficiency variances can be studied and further optimizations of the hardware and software settings can be carried out.

In general, the mechanical aging of the devices and detectors in the Observatory, especially of the components of the WCDs, will continue in the future leading to further changes in the detector responses and measured data. During the analysis of the offline calibration procedures, we determined the influences of the aging processes on the calibration histograms and were able to significantly improve the flexibility of the procedure by developing the new algorithm. Nevertheless, to guarantee a stable calibration in the future, a continuous monitoring of the detector signals will be crucial. One possibility to recover the miscalibration of individual devices is the simultaneous application of several different calibration methods to the same events. For this reason, an implementation of the online calibration procedure for all the AugerPrime detectors in the near future will be highly beneficial. Furthermore, with the development of new calibration procedures, the aging effects can be compensated and the situation can be improved. One candidate procedure is the currently tested coincidence calibration which utilizes the signals of the WCD and the SSD at the same time.

With the results from the analyses presented in the main chapters of this Dissertation, and the consideration of the previously mentioned suggestions for improvement, we can conclude that a successful outcome of the AugerPrime upgrade is expected. By the replacement of the original electronics boards with the new UUBs, the signal handling capabilities of the originally installed WCDs will be significantly enhanced. Additionally, the complete installation of the new SSDs over the total SD area, will provide a complementary measurement and reconstruction of EASs from vertical events. By combining the signals of the sub-detectors of the SD, mass composition sensitive quantities can be determined and with the help of the multi-hybrid event reconstruction, the determination of the properties of the UHECRs will be possible. With the optimized calibration procedure developed in this Dissertation, the signal determination is improved and adapted for the use on the data obtained with both main AugerPrime detectors. By analyzing the combined signals of the SD sub-detectors, a disentanglement of the components of EASs can be achieved, and thereby the determination of the mass composition of individual UHECRs becomes possible. This can be realized with different methods and approaches which will be further improved in the upcoming years using the increasing amount of AugerPrime data. While some of these procedures utilize the signals of the different sub-detectors on a single station level, for example matrix-formalism-based methods, others are defined on air-shower models and parametrizations, such as the "Universality" approach or general deep learning algorithms. For the case of inclined EAS events, the detection efficiency of the SSDs is significantly reduced. However, to recover the hybrid reconstruction, these events will be measured and reconstructed with the antennas of the Radio Detector (RD). The first antenna prototypes have been installed in the field, but a large scale implementation and analysis will be carried out in the near future. Ultimately, the reconstruction of the properties of the primary cosmic rays (CRs) will be enhanced even further when the reconstruction results of the AugerPrime SD are combined with the data obtained with the Underground Muon Detector (UMD) and the Fluorescence Detector (FD),

and any additional type of detector which might be added in the future.

When we take a glance outside the UHECR research, the new detectors and hardware components will also enhance the detection sensitivity of the Pierre Auger Observatory on phenomena of other fields of physics, e.g., geophysics. In this Dissertation, we demonstrated that the SSDs provide a high sensitivity on thunderstorm events and electromagnetic fields, and therefore these detectors might be integrated into the general thunderstorm analyses. Additionally, the extended buffers of the new electronics boards can be utilized to perform additional algorithms for various purposes, for instance, lightning triggers which can detect the particular signal shapes of thunderstorm events, or trigger algorithms for the specialized search of air-shower events induced by neutral particles, such as cosmogenic and astrophysical photons and neutrinos.

Bibliography

[1]   T. K. Gaisser, R. Engel, and E. Resconi, "Cosmic Rays and Particle Physics," 2nd ed., Cambridge University Press, (2016), DOI: 10.1017/CB09781139192194

[2]   A. Aab et al., "The Pierre Auger Cosmic Ray Observatory," Nucl. Instrum. Meth. A **798** (2015) 172–213, DOI: 10.1016/j.nima.2015.06.058, arXiv: 1502.01323 [astro-ph.IM]

[3]   A. Aab et al., "Measurement of the cosmic-ray energy spectrum above 2.5×10^{18} eV using the Pierre Auger Observatory," Phys. Rev. D **102** (2020) 062005, DOI: 10.1103/PhysRevD.102.062005, arXiv: 2008.06486 [astro-ph.HE]

[4]   A. Aab et al., "Depth of Maximum of Air-Shower Profiles at the Pierre Auger Observatory: Measurements at Energies above $10^{17.8}$ eV," Phys. Rev. D **90** (2014) 122005, DOI: 10.1103/PhysRevD.90.122005, arXiv: 1409.4809 [astro-ph.HE]

[5]   A. Aab et al., "The Pierre Auger Observatory Upgrade - Preliminary Design Report" (2016), arXiv: 1604.03637 [astro-ph.IM]

[6]   V. F. Hess, "Über Beobachtungen der durchdringenden Strahlung bei sieben Freiballonfahrten," Phys. Z. **13** (1912) 1084–1091

[7]   R. A. Millikan and G. H. Cameron, "The Origin of the Cosmic Rays," Phys. Rev. **32** (1928) 533–557, DOI: 10.1103/PhysRev.32.533, URL: https://link.aps.org/doi/10.1103/PhysRev.32.533

[8]   P. A. Zyla et al., "Review of Particle Physics," PTEP **2020** (2020) 083C01, DOI: 10.1093/ptep/ptaa104

[9]   A. M. Hillas, "Cosmic Rays: Recent Progress and some Current Questions," Conference on Cosmology, Galaxy Formation and Astro-Particle Physics on the Pathway to the SKA, (2006), arXiv: astro-ph/0607109

[10] D. Allard, "Extragalactic propagation of ultrahigh energy cosmic-rays," Astropart. Phys. **39-40** (2012) 33–43, DOI: 10.1016/j.astropartphys.2011.10.011, arXiv: 1111.3290 [astro-ph.HE]

[11] K. Greisen, "End to the cosmic ray spectrum?" Phys. Rev. Lett. **16** (1966) 748–750, DOI: 10.1103/PhysRevLett.16.748

[12] G. T. Zatsepin and V. A. Kuzmin, "Upper limit of the spectrum of cosmic rays," JETP Lett. **4** (1966) 78–80

[13] D. Hooper and A. M. Taylor, "On The Heavy Chemical Composition of the Ultra-High Energy Cosmic Rays," Astropart. Phys. **33** (2010) 151–159, DOI: `10.1016/j.astropartphys.2010.01.003`, arXiv: `0910.1842 [astro-ph.HE]`

[14] R. Alves Batista et al., "Open Questions in Cosmic-Ray Research at Ultrahigh Energies," Front. Astron. Space Sci. **6** (2019) 23, DOI: `10.3389/fspas.2019.00023`, arXiv: `1903.06714 [astro-ph.HE]`

[15] E. Fermi, "On the Origin of the Cosmic Radiation," Phys. Rev. **75** (1949) 1169–1174, DOI: `10.1103/PhysRev.75.1169`

[16] A. M. Hillas, "The Origin of Ultrahigh-Energy Cosmic Rays," Ann. Rev. Astron. Astrophys. **22** (1984) 425–444, DOI: `10.1146/annurev.aa.22.090184.002233`

[17] E. S. Seo et al., "CREAM: 70 days of flight from 2 launches in Antarctica," Adv. Space Res. **42** (2008) 1656–1663, DOI: `10.1016/j.asr.2007.03.056`

[18] O. Adriani et al., "The PAMELA experiment on satellite and its capability in cosmic rays measurements," Nucl. Instrum. Meth. A **478** (2002) 114–118, DOI: `10.1016/S0168-9002(01)01726-0`

[19] J. Chang et al., "The DArk Matter Particle Explorer mission," Astropart. Phys. **95** (2017) 6–24, DOI: `10.1016/j.astropartphys.2017.08.005`, arXiv: `1706.08453 [astro-ph.IM]`

[20] R. Battiston, "The antimatter spectrometer (AMS-02): A particle physics detector in space," Nucl. Instrum. Meth. A **588** (2008) 227–234, DOI: `10.1016/j.nima.2008.01.044`

[21] A. Haungs, H. Rebel, and M. Roth, "Energy spectrum and mass composition of high-energy cosmic rays," Rept. Prog. Phys. **66** (2003) 1145–1206, DOI: `10.1088/0034-4885/66/7/202`

[22] W. Heitler, "The quantum theory of radiation," Oxford University Press, (1954)

[23] J. Matthews, "A Heitler model of extensive air showers," Astropart. Phys. **22** (2005) 387–397, DOI: `10.1016/j.astropartphys.2004.09.003`

[24] T. K. Gaisser and A. M. Hillas, "Reliability of the Method of Constant Intensity Cuts for Reconstructing the Average Development of Vertical Showers," International Cosmic Ray Conference, **8**, (1977) 353

[25] K. Kamata and J. Nishimura, "The Lateral and the Angular Structure Functions of Electron Showers," Progress of Theoretical Physics Supplement **6** (1958) 93–155, DOI: `10.1143/PTPS.6.93`

[26] K. Greisen, "Progress in elementary particle and cosmic ray physics," **3**, Amsterdam: North-Holland Publishing, (1956)

[27] K. Greisen, "Cosmic ray showers," Ann. Rev. Nucl. Part. Sci. **10** (1960) 63–108, DOI: `10.1146/annurev.ns.10.120160.000431`

[28] A. V. Olinto et al., "POEMMA: Probe Of Extreme Multi-Messenger Astrophysics," PoS **ICRC2017** (2018) 542, DOI: `10.22323/1.301.0542`, arXiv: `1708.07599 [astro-ph.IM]`

[29] F. G. Schröder, "Radio detection of Cosmic-Ray Air Showers and High-Energy Neutrinos," Prog. Part. Nucl. Phys. **93** (2017) 1–68, DOI: `10.1016/j.ppnp.2016.12.002`, arXiv: `1607.08781 [astro-ph.IM]`

[30] P. Auger et al., "Extensive cosmic ray showers," Rev. Mod. Phys. **11** (1939) 288–291, DOI: `10.1103/RevModPhys.11.288`

[31] J. Linsley, "Evidence for a primary cosmic-ray particle with energy 10**20-eV," Phys. Rev. Lett. **10** (1963) 146–148, DOI: `10.1103/PhysRevLett.10.146`

[32] M. A. Lawrence, R. J. O. Reid, and A. A. Watson, "The Cosmic ray energy spectrum above 4x10**17-eV as measured by the Haverah Park array," J. Phys. G **17** (1991) 733–757, DOI: `10.1088/0954-3899/17/5/019`

[33] S. Yoshida et al., "The Cosmic ray energy spectrum above 3 x 10**18-eV measured by the Akeno Giant Air Shower Array," Astropart. Phys. **3** (1995) 105–124, DOI: `10.1016/0927-6505(94)00036-3`

[34] P. Sokolsky, "Final Results from the High Resolution Fly's Eye (HiRes) Experiment," PoS **ICHEP2010** (2010) 444, DOI: `10.22323/1.120.0444`, arXiv: `1010.2690 [astro-ph.HE]`

[35] T. Antoni et al., "The Cosmic ray experiment KASCADE," Nucl. Instrum. Meth. A **513** (2003) 490–510, DOI: `10.1016/S0168-9002(03)02076-X`

[36] W. D. Apel et al., "The KASCADE-Grande experiment," Nucl. Instrum. Meth. A **620** (2010) 202–216, DOI: `10.1016/j.nima.2010.03.147`

[37] H. Kawai et al., "Telescope array experiment," Nucl. Phys. B Proc. Suppl. **175-176** (2008) 221–226, DOI: `10.1016/j.nuclphysbps.2007.11.002`

[38] P. Abreu et al., "Energy spectrum of cosmic rays measured using the Pierre Auger Observatory," PoS **ICRC2021** (2021) 324, DOI: `10.22323/1.395.0324`

[39] A. Aab et al., "Features of the Energy Spectrum of Cosmic Rays above 2.5×10^{18} eV Using the Pierre Auger Observatory," Phys. Rev. Lett. **125** (2020) 121106, DOI: `10.1103/PhysRevLett.125.121106`, arXiv: `2008.06488 [astro-ph.HE]`

[40] P. Abreu et al., "The energy spectrum of cosmic rays beyond the turn-down around 10^{17} eV as measured with the surface detector of the Pierre Auger Observatory," Eur. Phys. J. C **81** (2021) 966, DOI: `10.1140/epjc/s10052-021-09700-w`, arXiv: `2109.13400 [astro-ph.HE]`

[41] R. Abbasi et al., "Joint analysis of the energy spectrum of ultra-high-energy cosmic rays as measured at the Pierre Auger Observatory and the Telescope Array," PoS **ICRC2021** (2021) 337, DOI: `10.22323/1.395.0337`

[42] V. Berezinsky, A. Z. Gazizov, and S. I. Grigorieva, "On astrophysical solution to ultrahigh-energy cosmic rays," Phys. Rev. D **74** (2006) 043005, DOI: `10.1103/PhysRevD.74.043005`, arXiv: `hep-ph/0204357`

[43] A. Aab et al., "Depth of maximum of air-shower profiles at the Pierre Auger Observatory. II. Composition implications," Phys. Rev. D **90** (2014) 122006, DOI: `10.1103/PhysRevD.90.122006`, arXiv: `1409.5083 [astro-ph.HE]`

[44] A. Yushkov, "Mass Composition of Cosmic Rays with Energies above $10^{17.2}$ eV from the Hybrid Data of the Pierre Auger Observatory," PoS **ICRC2019** (2020) 482, DOI: `10.22323/1.358.0482`

[45] A. Aab et al., "Measurement of the Fluctuations in the Number of Muons in Extensive Air Showers with the Pierre Auger Observatory," Phys. Rev. Lett. **126** (2021) 152002, DOI: `10.1103/PhysRevLett.126.152002`, arXiv: `2102.07797 [hep-ex]`

[46] A. Aab et al., "Direct measurement of the muonic content of extensive air showers between 2×10^{17} and 2×10^{18} eV at the Pierre Auger Observatory," Eur. Phys. J. C **80** (2020) 751, DOI: `10.1140/epjc/s10052-020-8055-y`

[47] A. Aab et al., "Observation of a Large-scale Anisotropy in the Arrival Directions of Cosmic Rays above 8×10^{18} eV," Science **357** (2017) 1266–1270, DOI: `10.1126/science.aan4338`, arXiv: `1709.07321 [astro-ph.HE]`

[48] A. Aab et al., "Large-scale cosmic-ray anisotropies above 4 EeV measured by the Pierre Auger Observatory," Astrophys. J. **868** (2018) 4, DOI: `10.3847/1538-4357/aae689`, arXiv: `1808.03579 [astro-ph.HE]`

[49] A. Aab et al., "An Indication of anisotropy in arrival directions of ultra-high-energy cosmic rays through comparison to the flux pattern of extragalactic gamma-ray sources," Astrophys. J. Lett. **853** (2018) L29, DOI: `10.3847/2041-8213/aaa66d`, arXiv: `1801.06160 [astro-ph.HE]`

[50] P. Abreu et al., "The ultra-high-energy cosmic-ray sky above 32 EeV viewed from the Pierre Auger Observatory," PoS **ICRC2021** (2021) 307, DOI: `10.22323/1.395.0307`

[51] L. A. Anchordoqui, "Acceleration of ultrahigh-energy cosmic rays in starburst superwinds," Phys. Rev. D **97** (2018) 063010, DOI: `10.1103/PhysRevD.97.063010`, arXiv: `1801.07170 [astro-ph.HE]`

[52] G. E. Romero, A. L. Müller, and M. Roth, "Particle acceleration in the superwinds of starburst galaxies," Astron. Astrophys. **616** (2018) A57, DOI: `10.1051/0004-6361/201832666`, arXiv: `1801.06483 [astro-ph.HE]`

[53] A. L. Müller, G. E. Romero, and M. Roth, "High-energy processes in starburst-driven winds," Mon. Not. Roy. Astron. Soc. **496** (2020) 2474–2481, DOI: `10.1093/mnras/staa1720`, arXiv: `2006.12259 [astro-ph.HE]`

[54] P. Abreu et al., "Indication of a mass-dependent anisotropy above $10^{18.7}$ eV in the hybrid data of the Pierre Auger Observatory," PoS **ICRC2021** (2021) 321, DOI: `10.22323/1.395.0321`

[55] A. Aab et al., "Search for photons with energies above 10^{18} eV using the hybrid detector of the Pierre Auger Observatory," JCAP **04** (2017) 009, DOI: `10.1088/1475-7516/2017/04/009`, arXiv: `1612.01517 [astro-ph.HE]`

[56] J. Rautenberg, "Limits on ultra-high energy photons with the Pierre Auger Observatory," PoS **ICRC2019** (2021) 398, DOI: `10.22323/1.358.0398`

[57] P. Abreu et al., "Testing effects of Lorentz invariance violation in the propagation of astroparticles with the Pierre Auger Observatory," JCAP **01** (2022) 023, DOI: `10.1088/1475-7516/2022/01/023`, arXiv: `2112.06773 [astro-ph.HE]`

[58] P. Abreu et al., "Follow-up Search for UHE Photons from Gravitational Wave Sources with the Pierre Auger Observatory," PoS **ICRC2021** (2021) 973, DOI: `10.22323/1.395.0973`

[59] A. Castellina, "Highlights from the Pierre Auger Observatory," PoS **ICRC2019** (2021) 004, DOI: `10.22323/1.358.0004`, arXiv: `1909.10791 [astro-ph.HE]`

[60] A. Aab et al., "Probing the origin of ultra-high-energy cosmic rays with neutrinos in the EeV energy range using the Pierre Auger Observatory," JCAP **10** (2019) 022, DOI: `10.1088/1475-7516/2019/10/022`, arXiv: `1906.07422 [astro-ph.HE]`

[61] A. Aab et al., "Limits on point-like sources of ultra-high-energy neutrinos with the Pierre Auger Observatory," JCAP **11** (2019) 004, DOI: `10.1088/1475-7516/2019/11/004`, arXiv: `1906.07419 [astro-ph.HE]`

[62] I. A. Caracas et al., "A tau scenario application to a search for upward-going showers with the Fluorescence Detector of the Pierre Auger Observatory," PoS **ICRC2021** (2021) 1145, DOI: `10.22323/1.395.1145`

[63] P. W. Gorham et al., "Observation of an Unusual Upward-going Cosmic-ray-like Event in the Third Flight of ANITA," Phys. Rev. Lett. **121** (2018) 161102, DOI: `10.1103/PhysRevLett.121.161102`, arXiv: `1803.05088 [astro-ph.HE]`

[64] A. Aab et al., "Ultrahigh-Energy Neutrino Follow-Up of Gravitational Wave Events GW150914 and GW151226 with the Pierre Auger Observatory," Phys. Rev. D **94** (2016) 122007, DOI: `10.1103/PhysRevD.94.122007`, arXiv: `1608.07378 [astro-ph.HE]`

[65] B. P. Abbott et al., "Multi-messenger Observations of a Binary Neutron Star Merger," Astrophys. J. Lett. **848** (2017) L12, DOI: `10.3847/2041-8213/aa91c9`, arXiv: `1710.05833 [astro-ph.HE]`

[66] A. Albert et al., "Search for High-energy Neutrinos from Binary Neutron Star Merger GW170817 with ANTARES, IceCube, and the Pierre Auger Observatory," Astrophys. J. Lett. **850** (2017) L35, DOI: `10.3847/2041-8213/aa9aed`, arXiv: `1710.05839 [astro-ph.HE]`

[67] "Web page of Darko Veberič," (2023), URL: `https://web.iap.kit.edu/darko/`

[68] R. Caruso et al., "Operations of the Pierre Auger Observatory," PoS **ICRC2021** (2022) 238, DOI: `10.22323/1.395.0238`

[69] P. Abreu et al., "Monte Carlo simulations for the Pierre Auger Observatory using the VO auger grid resources," PoS **ICRC2021** (2021) 232, DOI: `10.22323/1.395.0232`

[70] S. Argiro et al., "The Offline Software Framework of the Pierre Auger Observatory," Nucl. Instrum. Meth. A **580** (2007) 1485–1496, DOI: `10.1016/j.nima.2007.07.010`, arXiv: `0707.1652 [astro-ph]`

[71] P. Abreu et al., "Update of the Offline Framework for AugerPrime," PoS **ICRC2021** (2021) 250, DOI: `10.22323/1.395.0250`

[72] G. Medina-Tanco, "Astrophysics Motivation behind the Pierre Auger Southern Observatory Enhancements," 30th International Cosmic Ray Conference, **5**, (2007) 1101–1104, arXiv: `0709.0772 [astro-ph]`

[73] T. H.-J. Mathes, "The HEAT telescopes of the Pierre Auger Observatory: Status and first data," 32nd International Cosmic Ray Conference, **3**, (2011) 153, DOI: `10.7529/ICRC2011/V03/0761`

[74] P. Abreu et al., "The XY Scanner - A Versatile Method of the Absolute End-to-End Calibration of Fluorescence Detectors," PoS **ICRC2021** (2021) 220, DOI: `10.22323/1.395.0220`

[75] J. Abraham et al., "Properties and performance of the prototype instrument for the Pierre Auger Observatory," Nucl. Instrum. Meth. A **523** (2004) 50–95, DOI: `10.1016/j.nima.2003.12.012`

[76] A. Etchegoyen, "AMIGA, Auger Muons and Infill for the Ground Array," 30th International Cosmic Ray Conference, **5**, (2007) 1191–1194, arXiv: `0710.1646 [astro-ph]`

[77] F. Sánchez, "The AMIGA detector of the Pierre Auger Observatory: overview," 32nd International Cosmic Ray Conference, **3**, (2011) 149–152, DOI: `10.7529/ICRC2011/V03/0742`

[78] D. Ravignani, "Measurement of the energy spectrum of cosmic rays above 3×10^{17} eV using the AMIGA infill detector of the Pierre Auger Observatory," 33rd International Cosmic Ray Conference, (2013) 0693

[79] P. Abreu et al., "Performance of the 433 m surface array of the Pierre Auger Observatory," PoS **ICRC2021** (2021) 224, DOI: `10.22323/1.395.0224`

[80] J. Abraham et al., "Trigger and Aperture of the Surface Detector Array of the Pierre Auger Observatory," Nucl. Instrum. Meth. A **613** (2010) 29–39, DOI: `10.1016/j.nima.2009.11.018`, arXiv: `1111.6764 [astro-ph.IM]`

[81] P. Billoir, "Proposition to improve the local trigger of Surface Detector for low energy showers," Auger internal note GAP-2009-179, (2009)

[82] P. Billoir et al., "First results of the ToTd trigger in the test hexagon," Auger internal note GAP-2011-032, (2011)

[83]   P. Billoir, "New proposal to improve the local trigger of the Surface Detector," Auger internal note GAP-2011-089, (2011)

[84]   A. Coleman, "The New Triggers Settings," Auger internal note GAP-2018-001, (2018)

[85]   J. L. Kelley, "AERA: The Auger Engineering Radio Array," 32nd International Cosmic Ray Conference, **3**, (2011) 112, DOI: `10.7529/ICRC2011/V03/0556`

[86]   P. Abreu et al., "Antennas for the Detection of Radio Emission Pulses from Cosmic-Ray," JINST **7** (2012) P10011, DOI: `10.1088/1748-0221/7/10/P10011`, arXiv: `1209.3840 [astro-ph.IM]`

[87]   T. Huege, "Radio detection of cosmic rays with the Auger Engineering Radio Array," EPJ Web Conf. **210** (2019) 05011, DOI: `10.1051/epjconf/201921005011`, arXiv: `1905.04986 [astro-ph.IM]`

[88]   A. Aab et al., "The FRAM robotic telescope for atmospheric monitoring at the Pierre Auger Observatory," JINST **16** (2021) P06027, DOI: `10.1088/1748-0221/16/06/P06027`, arXiv: `2101.11602 [astro-ph.IM]`

[89]   R. Engel, "Upgrade of the Pierre Auger Observatory (AugerPrime)," PoS **ICRC2015** (2016) 686, DOI: `10.22323/1.236.0686`

[90]   A. Letessier-Selvon et al., "Layered water Cherenkov detector for the study of ultra high energy cosmic rays," Nucl. Instrum. Meth. A **767** (2014) 41–49, DOI: `10.1016/j.nima.2014.08.029`, arXiv: `1405.5699 [astro-ph.IM]`

[91]   P. Abreu et al., "MARTA: a high-energy cosmic-ray detector concept for high-accuracy muon measurement," Eur. Phys. J. C **78** (2018) 333, DOI: `10.1140/epjc/s10052-018-5820-2`, arXiv: `1712.07685 [physics.ins-det]`

[92]   B. Pont, "A Large Radio Detector at the Pierre Auger Observatory - Measuring the Properties of Cosmic Rays up to the Highest Energies," PoS **ICRC2019** (2021) 395, DOI: `10.22323/1.358.0395`

[93]   D. Martello, "The Pierre Auger Observatory Upgrade," PoS **ICRC2017** (2018) 383, DOI: `10.22323/1.301.0383`

[94]   T. Suomijärvi, "New electronics for the surface detectors of the Pierre Auger Observatory," PoS **ICRC2017** (2018) 450, DOI: `10.22323/1.301.0450`

[95]   D. F. Nitz, "New Electronics for the Surface Detectors of the Pierre Auger Observatory," PoS **ICRC2019** (2020) 370, DOI: `10.22323/1.358.0370`

[96]   P. Abreu et al., "AugerPrime Upgraded Electronics," PoS **ICRC2021** (2021) 230, DOI: `10.22323/1.395.0230`

[97]   "SITAEL," (2023), URL: `https://www.sitael.com/`

[98]   A. Castellina, "The dynamic range of the AugerPrime Surface Detector: technical solution and physics reach," PoS **ICRC2017** (2018) 397, DOI: `10.22323/1.301.0397`

[99]   "Hamamatsu R8619," (2023), URL: `https://www.hamamatsu.com/jp/en/product/type/R8619/index.html`

[100] "CAEN A7501B," (2023), URL: `https://www.caen.it/products/a7501b/`

[101] A. Taboada, "Analysis of Data from Surface Detector Stations of the AugerPrime Upgrade," PoS **ICRC2019** (2020) 434, DOI: `10.22323/1.358.0434`

[102] A. Aab et al., "Muon counting using silicon photomultipliers in the AMIGA detector of the Pierre Auger observatory," JINST **12** (2017) P03002, DOI: `10.1088/1748-0221/12/03/P03002`, arXiv: `1703.06193 [astro-ph.IM]`

[103] A. Aab et al., "Design and implementation of the AMIGA embedded system for data acquisition," JINST **16** (2021) T07008, DOI: `10.1088/1748-0221/16/07/T07008`, arXiv: `2101.11747` [`astro-ph.IM`]

[104] P. Abreu et al., "Status and performance of the underground muon detector of the Pierre Auger Observatory," PoS **ICRC2021** (2021) 233, DOI: `10.22323/1.395.0233`

[105] J. R. Hörandel, "Precision measurements of cosmic rays up to the highest energies with a large radio array at the Pierre Auger Observatory," EPJ Web Conf. **210** (2019) 06005, DOI: `10.1051/epjconf/201921006005`

[106] P. Abreu et al., "Expected performance of the AugerPrime Radio Detector," PoS **ICRC2021** (2021) 262, DOI: `10.22323/1.395.0262`

[107] P. Abreu et al., "First results from the AugerPrime Radio Detector," PoS **ICRC2021** (2021) 270, DOI: `10.22323/1.395.0270`

[108] D. Schmidt, "Sensitivity of AugerPrime to the masses of ultra-high-energy cosmic rays (GAP-2019-030)," PhD thesis, Karlsruher Institut für Technologie (KIT), 2018

[109] Á. Taboada Núñez, "Analysis of the first data of the AugerPrime detector upgrade (GAP-2020-002)," PhD thesis, Karlsruher Institut für Technologie (KIT), 2019

[110] S. Mayotte, "Study of the cosmic ray composition sensitivity of AugerPrime: probing the prospects of the upgrade to the Pierre Auger Observatory with a deep learning approach (GAP-2021-042)," PhD thesis, Bergische Universität Wuppertal, 2021

[111] R. Šmída, "Scintillator detectors of AugerPrime," PoS **ICRC2017** (2018) 390, DOI: `10.22323/1.301.0390`

[112] A. Streich, "Scintillator Surface Detector for the Upgrade of the Pierre Auger Observatory (GAP-2017-045)," MA thesis, Karlsruher Institut für Technologie (KIT), 2017

[113] I. Yashin et al., "Scintillation hodoscope for muon diagnostics," 31st International Cosmic Ray Conference, ICRC 2009 (2009)

[114] Z. Zong et al., "Study of light yield for different configurations of plastic scintillators and wavelength shifting fibers," Nucl. Instrum. Meth. A **908** (2018) 82–90, DOI: `10.1016/j.nima.2018.08.029`

[115] A. Pla-Dalmau, A. D. Bross, and V. V. Rykalin, "Extruding plastic scintillator at Fermilab," (2003)

[116] A. Dyshkant et al., "About NICADD extruded scintillating strips" (2005)

[117] D. G. Michael et al., "The Magnetized steel and scintillator calorimeters of the MINOS experiment," Nucl. Instrum. Meth. A **596** (2008) 190–228, DOI: `10.1016/j.nima.2008.08.003`, arXiv: `0805.3170` [`physics.ins-det`]

[118] "Wavelength Shifting Fibers," (2023), URL: `http://kuraraypsf.jp/psf/ws.html`

[119] "Plastic Scintillating Fibers (Materials and Structures)," (2023), URL: `http://kuraraypsf.jp/psf/index.html`

[120] "Hamamatsu R9420," (2023), URL: `https://www.hamamatsu.com/us/en/product/type/R9420/index.html`

[121] "ISEG PHQ," (2023), URL: `https://iseg-hv.com/en/products/detail/PHQ`

[122] J. Rautenberg et al., "Development of bases and qualification tests of Photomultiplier Tubes for the AugerPrime scintillation detectors," PoS **ICRC2021** (2021) 265, DOI: `10.22323/1.395.0265`

[123] Z. Zong, "First results from the AugerPrime engineering array," PoS **ICRC2017** (2018) 449, DOI: `10.22323/1.301.0449`

[124] N. Barenthien et al., "Scintillator Surface Detectors of the Engineering Array: Production and Validation," Auger internal note GAP-2016-040, (2016)

[125] J. Pkala, "Production and Quality Control of the Scintillator Surface Detector for the AugerPrime Upgrade of the Pierre Auger Observatory," PoS **ICRC2019** (2020) 380, DOI: `10.22323/1.358.0380`

[126] P. Doll et al., "Muon tracking detector for the air shower experiment KASCADE," Nucl. Instrum. Meth. A **488** (2002) 517–535, DOI: `10.1016/S0168-9002(02)00560-0`

[127] J. Zabierowski and P. Doll, "Front-end readout boards for streamer tube muon tracking detector in the KASCADE EAS Experiment," Nucl. Instrum. Meth. A **484** (2002) 528–532, DOI: `10.1016/S0168-9002(01)02027-7`

[128] "Raspberry Pi," (2023), URL: `https://www.raspberrypi.org/`

[129] F. G. Schroeder et al., "The Surface Array planned for IceCube-Gen2," PoS **ICRC2021** (2021) 407, DOI: `10.22323/1.395.0407`, arXiv: `2108.00364 [astro-ph.HE]`

[130] A. Haungs et al., "Cosmic-Ray Studies with the Surface Instrumentation of Ice-Cube," PoS **ICRC2021** (2021) 336, DOI: `10.22323/1.395.0336`, arXiv: `2108.07164 [astro-ph.HE]`

[131] T. Bretz et al., "The Aachen Muon Detector for testing the local production of Scintillating Surface Detectors for AugerPrime," PoS **ICRC2019** (2021) 203, DOI: `10.22323/1.358.0203`

[132] "Hamamatsu R11102," (2023), URL: `https://www.hamamatsu.com/us/en/product/type/R11102/index.html`

[133] "PicoScope 6000 Series," (2023), URL: `https://www.picotech.com/oscilloscope/6000/picoscope-6000-overview`

[134] "SSD database," (2023), URL: `https://auger-sdeu.farm.particle.cz/db-ssd/`

[135] D. Schmidt, "AugerPrime implementation in the Offline simulation and reconstruction framework" (2017) 185–192, DOI: `10.22323/1.301.0353`

[136] S. Agostinelli et al., "GEANT4–a simulation toolkit," Nucl. Instrum. Meth. A **506** (2003) 250–303, DOI: `10.1016/S0168-9002(03)01368-8`

[137] "Pierre Auger Electronic Logbooks page," (2023), URL: `https://www.auger.org.ar/Elog/`

[138] "Pierre Auger Parts Management System," (2023), URL: `https://pms.auger.org.ar/`

[139] "Pierre Auger Monitoring Database (Mirror)," (2023), URL: `http://paomon.physik.uni-wuppertal.de/`

[140] "I-Lotus M12M," (2023), URL: `http://www.ilotus.com.sg/m12m_timing_oncore/`

[141] "Synergy Systems SSR," (2023), URL: `https://synergy-gps.com/synergy-products/ssr-6t-gps-receiver/`

[142] "Photomultiplier Tubes," (2023), URL: `https://www.hamamatsu.com/content/dam/hamamatsu-photonics/sites/documents/99_SALES_LIBRARY/etd/PMT_handbook_v4E.pdf`

[143] "Hamamatsu R6094," (2023), URL: `https://www.hamamatsu.com/jp/en/product/type/R6094/index.html`

[144] "ET Enterprise 9107B," (2023), URL: `https://et-enterprises.com/products/photomultipliers/product/p9107b-series`

[145] T. Bretz et al., "An integrated general purpose SiPM based optical module with a high dynamic range," JINST **13** (2018) P06001, DOI: `10.1088/1748-0221/13/6/P06001`, arXiv: `1803.04841 [physics.ins-det]`

[146] G. Cataldi et al., "The upgrade of the Pierre Auger Observatory with the Scintillator Surface Detector," PoS **ICRC2021** (2021) 251, DOI: `10.22323/1.395.0251`

[147] "Campbell Sientific CS110," (2023), URL: `https://www.campbellsci.com/cs110`

[148] M. Bohacova, "Test benches for the upgrade of the Pierre Auger Observatory electronics," PoS **ICRC2019** (2021) 199, DOI: `10.22323/1.358.0199`

[149] "Pierre Auger Weather and Monitoring," (2023), URL: `http://auger.uis.edu.co/data/`

[150] "Great thanks to Patrick Stassi and Martina Boháčová for providing the photos"

[151] P. Allison et al., "Surface Detector calibration in the Engineering Array," Auger internal note GAP-2002-028, (2002)

[152] X. Bertou et al., "Calibration of the surface array of the Pierre Auger Observatory," Nucl. Instrum. Meth. A **568** (2006) 839–846, DOI: `10.1016/j.nima.2006.07.066`, arXiv: `2102.01656 [astro-ph.HE]`

[153] A. Aab et al., "Reconstruction of events recorded with the surface detector of the Pierre Auger Observatory," JINST **15** (2020) P10021, DOI: `10.1088/1748-0221/15/10/P10021`, arXiv: `2007.09035 [astro-ph.IM]`

[154] D. Dornic et al., "Calibration Analysis: CAPISA data," Auger internal note GAP-2005-101, (2005)

[155] A. Aab et al., "Studies on the response of a water-Cherenkov detector of the Pierre Auger Observatory to atmospheric muons using an RPC hodoscope," JINST **15** (2020) P09002, DOI: `10.1088/1748-0221/15/09/P09002`, arXiv: `2007.04139 [astro-ph.IM]`

[156] P. Abreu et al., "Reconstruction of Events Recorded with the Water-Cherenkov and Scintillator Surface Detectors of the Pierre Auger Observatory," PoS **ICRC2021** (2021) 218, DOI: `10.22323/1.395.0218`

[157] P. Billoir et al., "Never Too Late to Change the SD VEM Calibration," Auger internal note GAP-2015-050, (2015)

[158] D. Mockler, "Reconstruction of Vertical Events Recorded by the Surface Detector of the Pierre Auger Observatory," PoS **ICRC2019** (2020) 353, DOI: `10.22323/1.358.0353`

[159] I. C. Mariş, R. Sato, and O. Zapparrata, "Using the AugerPrime scintillators for improving the calibration of the water Cherenkov detectors," Auger internal note GAP-2021-046, (2021)

[160] A. Aab et al., "Reconstruction of Inclined Air Showers Detected with the Pierre Auger Observatory," JCAP **08** (2014) 019, DOI: `10.1088/1475-7516/2014/08/019`, arXiv: `1407.3214 [astro-ph.HE]`

[161] M. Ave et al., "The accuracy of signal measurement with the water Cherenkov detectors of the Pierre Auger Observatory," Nucl. Instrum. Meth. A **578** (2007) 180–184, DOI: `10.1016/j.nima.2007.05.150`, arXiv: `2101.06158 [astro-ph.IM]`

Acknowledgments

First, I would like to express my deepest gratitude towards Prof. Dr. Johannes Blümer and Prof. Dr. Hernán Asorey for supporting and reviewing this thesis and for giving me the chance to participate in two extraordinary programs between Germany and Argentina, the Double Doctoral degree in Astrophysics (DDAp) and the Helmholtz International Research School for Astroparticle Physics and Enabling Technologies (HIRSAP).

I am especially thankful to Prof. Dr. Ralph Engel for supervising my work and for providing me guidance and outstanding support since my first day at the IAP. I am deeply grateful to my advisor and good friend Dr. Darko Veberič for his endless help, fruitful discussions, and sharing of valuable life lessons. My special thanks to Dr. Markus Roth for the encouraging supervision of my work and the immense support during my time at the institute.

I would like to dearly express my gratitude towards Prof. Dr. Alberto Etchegoyen and Dr. Aníbal Gattone for organizing and promoting the DDAp program and for providing me help during my time in Argentina. Many sincerest thanks to Sabine Bucher and Marie-Christine Mundt for all their help and support with the overwhelming bureaucracy and organization, and for always having an open ear to problems.

I would like to thank my good friends and long-term office mates Martin, David, and Alvaro for countless unforgotten moments, endless discussions, and all the fun we shared that made my time at the IAP a wonderful experience. In the same way, I am very thankful to Christoph for helping me with my work, especially at the end of my thesis, and always be available for discussions.

Many thanks to Fabio, Tobias, and Allan who had an immense impact on the progress and finalization of my work. To all the people I had the pleasure to share the office with, Nicolás, Johan, Maximilian, and Thomas, having together lively exchanges about work, life, and many other topics.

I am very grateful to Ana Martina, Ewa, Sarah, Gaia, Marina, Isabel, Flavia, Steffen, Maximilian, Felix, Joaquín, Carmina, Luciano, Emily, Kathrin, Varada and to all the former and new fellows in the DDAp and the HIRSAP for all the amazing memories and fun, as well as the faith and trust in me as representative of the doctoral students.

Many thanks to all my colleagues and friends at the IAP and the Campus Nord, as well as to everyone involved in the detector production at the KIT. My special thanks to Michael Riegel, Heike Bolz, Günter Wörner, Heiko Kern, and Murat Toron for helping me over my whole time at the institute and for teaching me skills which I would never have imagined to learn.